DOCTOR OF PHILOSOPHY

Magnetic Characterisation of Nanostructured Magnetic Systems Using SQUID Magnetometry

Bennington-Gray, Suzanne

Award date:
2019

Awarding institution:
Queen's University Belfast

Magnetic Characterisation of Nanostructured Magnetic Systems Using SQUID Magnetometry

Thesis submitted for the degree of

Doctor of Philosophy (PhD)

in the

Faculty of Engineering and Physical Sciences

by

Suzanne Bennington-Gray

School of Mathematics and Physics

Queen's University Belfast

March 2018

For Mum, Dad and James

Thank you!

Acknowledgements

First and foremost I wish to acknowledge my supervisor Dr Solveig Felton, without whose continued tuition and support this thesis would not have come to fruition. Secondly I would like to acknowledge Dr Peter Nockemann for supplying and conducting the structural analysis on the ionic liquid samples in Chapter 5, and magnetic crystals in Chapter 6. My thanks is also extended to Dr Katherine McBride for the synthesis, structural characterisation and magnetic heating analysis of the lanthanum manganate magnetic nanoparticles investigated in Chapter 4. I would also like to acknowledge Dr William Hendren for his continued support throughout the course of this thesis and maintenance of the super conducting quantum interference device (SQUID) magnetometer. Finally I would like to acknowledge my family, friends and husband James, for all of their support over the past 5 years. Their belief has made this thesis possible.

The financial contribution of the EPSRC is greatly acknowledged.

Abstract

In this thesis SQUID magnetometry was employed as the main characterisation tool to investigate the magnetic behaviour of a number of materials on the bulk, nano- and atomic scale. In particular magnetic characterization was conducted on a selection of doped lanthanum manganate (LMO) magnetic nanoparticles (MNPs), a family of lanthanide ionic liquids, and finally on three distinct magnetic crystals synthesized using an acetate ionic liquid in place of a more conventional solvent.

Investigation into the effect of doping on the magnetic properties of LMO MNPs was conducted with the aim of synthesizing a suitable mediator for magnetic hyperthermia treatment. The magnetic heating exhibited by the MNPs was shown to be enhanced when the dopant ion radius was larger than that of the La^{3+} ion, and reduced when the dopant ion radius was smaller. $La_{0.60}Sr_{0.40}MnO_3$ proved to show the most promise as a potential mediator for mild hyperthermia, showing magnetic heating of 36.5°C and a specific absorption rate (SAR) of $46Wg^{-1}_{Mn.}$ Further investigations into the effect of strontium dopant concentrations on the magnetic properties of the MNPs showed that as the dopant concentration was increased the magnetic heating achieved also increased until a maximum was reached for $La_{0.65}Sr_{0.35}MnO_{3.}$ Maximum heating of 46.7°C and an SAR of $56Wg^{-1}_{Mn}$ was achieved for this material. Finally the effect of using microwave heating compared with conventional heating techniques during the synthesis process of the MNPs was investigated. This synthesis process was shown to improve the crystallinity of the MNPs over samples prepared using conventional heating. The improved crystallinity of the MNPs resulted in enhanced magnetic properties, which made them more attractive as potential mediators for mild hyperthermia treatments.

Magnetic characterization of a family of monomeric lanthanide ionic liquids showed them to possess magnetic moments comparable with those of their constituent ions, as quoted in the literature. Further studies into Dy and Nd dimeric ionic liquids showed these materials to exhibit antiferromagnetic interactions between neighbouring atoms below 100K.

In the final section of this thesis, three distinct magnetic complexes, a hexameric Ni(II) complex, trimeric Co(II) complex and polymeric Mn(II) complex, were all synthesized using the same process, employing the 1-methyl-3-ethylimidazolium ionic liquid. All three magnetic crystals exhibited splitting of the isofield lines in the reduced magnetization measurements, suggesting the presence of sizeable zero-field splitting. Fitting to the data returned values of D=-2.34 cm^{-1} and D=16.66 cm^{-1} for the Ni(II) and Co(II) complexes respectively. Fitting to the susceptibility data of these two

complexes confirmed these results and returned a spin ground state of 2 for the Ni(II) complex and 1.5 for the Co(II) complex. Stepping of the hysteresis loop of the Ni(II) complex was observed in the temperature range 1.8-10K, suggesting that this complex exhibits single molecule magnet behaviour.

The work in this thesis leverages the flexibility of SQUID magnetometry to characterise interesting magnetic materials across a variety of size regimes and fields of interest. The results presented provide a firm foundation for further work in the area of ionic liquids, single molecule magnetism (SMM) and also demonstrate a convincing case for the application of LMO MNPs for magnetic hyperthermia treatment.

Table of Contents

Chapter 1

Introduction

Super conducting quantum interference device (SQUID) magnetometry is considered the most accurate commercially available instrument for the measurement of magnetic behaviour, with the ability to achieve resolutions of 10^{-17} T or better [1-2]. In this thesis SQUID magnetometry is used to characterise magnetic behaviour on the bulk, nano- and atomic scale. This magnetic measurement technique is the common thread that runs through this thesis, which delves into three quite distinct subject areas. In Chapter 4 SQUID magnetometry is used to investigate magnetisation on the nano-scale. A family of lanthanum manganate (LMO) magnetic nanoparticles (MNPs) for potential use in mild hyperthermia treatment is investigated. SQUID magnetometry was used to investigate changes in the magnetic behaviour of the MNPs, when the material is doped with a range of alkaline metal ions. Further investigation specifically into the change in magnetic behaviour with different levels of strontium doping is then conducted. Finally the effects of using microwave heating during the synthesis process, in place of conventional heating methods, on the magnetic properties of the MNPs is investigated. In Chapter 5 SQUID magnetometry is used to investigate magnetic behaviour on the bulk scale, when it is employed to measure the magnetisation of a family of lanthanide ionic liquids. Finally in Chapter 6, SQUID magnetometry is employed to investigate magnetisation on the atomic scale. In this chapter the atomic interactions of a Nickel, Cobalt and Manganese crystal complex, synthesised using ionic liquids in place of conventional solvents, is investigated. Although

SQUID magnetometry has proven to be an extremely useful tool for magnetic characterisation, there are limitations and complications with using this device, which must be addressed. These are detailed throughout this thesis.

The structure of this thesis is detailed below;

Chapter 2 – The relevant background theory in the field of magnetism for easy comprehension of this thesis is presented.

Chapter 3 – The SQUID magnetometer is introduced and experimental considerations used throughout the course of the thesis are presented. An introduction to the two magnetic fitting programmes used throughout this thesis is also given.

Chapter 4 – Investigation of the effects of dopant ion, dopant concentration and synthesis process on the magnetic properties of a family of LMO MNPs is investigated.

Chapter 5 – Magnetic characterisation of a family of monomeric lanthanide ionic liquids and a Dy and Nd dimeric ionic liquid is conducted.

Chapter 6 – The magnetic behaviour of nickel, manganese and cobalt magnetic crystals are investigated. Fitting to the data is conducted to calculate a range of magnetic parameters.

Chapter 7 – Conclusions from the three experimental chapters are summarised and potential future work is presented.

References

[1] Fagaly, R.L, "Superconducting quantum interference device instruments and applications", (2006), *Review of Scientific Instruments*, Vol **77**, 10, 101101

[2] Martínez-Pérez, M. J. and Koelle, D., "NanoSQUIDs: Basics & recent advances", (2017), *Physical Sciences Reviews*, Vol **2**, 8

Chapter 2

Background Theory

2.1 Outline

In order to fully understand the analysis conducted in this thesis it is necessary to have some fundamental knowledge on the field of magnetism and magnetic materials. A brief overview of some of the necessary components of this field is detailed in this chapter, so that the subsequent work presented may be easily interrupted by the reader. The two main units system used in the field are introduced and their conversion explained before a brief overview of the field of magnetism is discussed. Finally there is a brief discussion of the relevant theory required to understand the interpretations made in the three experimental chapters included in this thesis.

2.2 Units Systems

There are two main units systems commonly used in the literature to describe the magnetic behaviour of materials: The System International (SI) and the Centimetre-Gramm-Second or Gaussian System (cgs). Although there has been a move towards the new standardised SI system, a lot of twentieth century literature still uses the CGS system, or indeed a combination of both [1]. As this thesis delves into three quite distinct subject areas, each of which with their own conventions as to which unit system is prominent in the field, a combination of both systems is used throughout this thesis. As such a brief overview of the two systems and the conversion between them is detailed below.

In the SI system the five basic quantities and their corresponding base units are, mass – kilograms, length – metres, time – seconds, current – ampere and temperature - Kelvin. Comparatively the cgs system uses the following base units, mass – grams, length – centimetres, time – seconds, current – biot and temperature - Kelvin. The biggest discrepancy between the two systems is however in the way in which they define the magnetic field [2]. In the SI system the definition of the magnetic flux (**B**) includes a term, which describes the magnetic constant of the material, μ_o. This term is omitted from the cgs system definition of magnetic flux;

$$\boldsymbol{B} = \mu_o\,(\mathbf{H} + \mathbf{M}) \qquad \text{(SI)} \qquad \textbf{Equation 2.1}$$

$$\boldsymbol{B} = \boldsymbol{H} + 4\pi\boldsymbol{M} \qquad \text{(cgs)} \qquad \textbf{Equation 2.2}$$

The difference in the definition of the magnetic flux in these two systems arises due to a discrepancy in how they define the magnitude of the magnetic field (**H**), (Equations 2.3 and 2.4).

$$\boldsymbol{H} = \frac{q}{4\pi r^2} \qquad \text{(SI)} \qquad \textbf{Equation 2.3}$$

$$\boldsymbol{H} = \frac{q}{r^2} \qquad \text{(cgs)} \qquad \textbf{Equation 2.4}$$

where q is the magnetic monopole charge and r is the distance of the monopole from the field.

In the SI unit system, **H** is defined in terms of current, whereas in the cgs unit system **H** is defined according to monopoles, where a unit monopole produces a field of one Oersted a distance of one centimetre away. This difference in the definition of **H**-fields leads to a factor of 4π, which often has to be considered when converting between the two unit systems. In the SI system the factor 4π often appears in equations as a reminder that the field from a point magnetic monopole has spherical symmetry. A list of the conversion factors required to move from one unit system to the other are summarised in Table 2.1 [3].

Magnetic Term	Symbol	SI Unit	CGS Unit	Conversion Factor
Magnetic induction	B	tesla (T)	gauss (G)	1 T = 10^4G
Magnetic field	H	A m^{-1}	oersted (Oe)	1 A m^{-1} = 4π x 10^{-3}Oe
Magnetization	M	A m^{-1}	emu cm^{-3}	1 A m^{-1} = 10^{-3}emu cm^{-3}
Magnetic polarisation	J	T	G	1 T = $10^4/4\pi$ emu cm^{-3}
Magnetic moment	m	A m^2	emu = G cm^3	1 A m^2 = 10^3emu
Magnetic moment per unit mass	σ	A m^2 kg^{-1}	emu g^{-1}	1 A m^2 kg^{-1} = 1 emu g^{-1}
Volume magnetic susceptibility (κ=M/H)	κ	dimensionless	dimensionless	1 (SI) = 1/4π (cgs)
Mass magnetic susceptibility (χ= κ/ρ)	χ	m^3 kg^{-1}	emu Oe^{-1} g^{-1}	1 m^3 kg^{-1} = $10^3/4\pi$ emu Oe^{-1} g^{-1}
Molar magnetic susceptibility (χ_m = χM)	χ_m	m^3 mol^{-1}	emu Oe^{-1} g^{-1} mol^{-1}	1 m^3 mol^{-1} = $10^5/4\pi$ emu Oe^{-1} g^{-1} mol^{-1}
Magnetic permeability (μ=B/H)	μ	H m^{-1}	G Oe^{-1}	1 H m^{-1} = $10^7/4\pi$ G Oe^{-1}
Magnetic flux	Φ	Weber (Wb)	maxwell (Mx)	1 Wb = 10^8Mx
Magnetic scalar potential; Magnetomotive force	ϕ	A	gilbert	1 A = 4π/10 gilbert
Magnetic vector potential	A	Wb m^{-1}	emu = G cm	Wb m^{-1} = 10^6emu
Magnetic pole strength	p	A m	emu = G cm^2	1 A m = 10 emu
Demagnetizing factor	N	dimensionless	dimensionless	1 (SI) = 4π (cgs)
Magnetostriction constant	Λ	dimensionless	dimensionless	1 (SI) = 1 (cgs)
Anisotropy constant	K	J m^{-3}	erg cm^{-3}	1 J m^{-3} = 10 erg cm^{-3}
Magnetostatic energy	E_m			
Energy product	$(BH)_{max}$			

Table 2.1: Summary of the conversion factors used to convert magnetic measurements between the SI and cgs unit systems, taken from reference 3.

2.3 Magnetism

Magnetism is defined as a physical phenomenon resulting from the motion of electron charges, which results in either an attractive or repulsive force between objects. Although the properties of magnetic materials can only be fully described in the context of quantum mechanics, a simplified knowledge of the base principles described using classical electrodynamics is essential.

Consider a current flowing through a wire. As electron movement generates magnetism, the motion of the electrons through the wire must therefore generate a magnetic field. This was discovered to be true by Hans – Christian Oersted in 1820. Oersted successfully demonstrated that a current-carrying wire produced a circumferential field capable of deflecting a compass needle [4]. Subsequent work by André – Marie Ampère, Dominique – François Argo and Michael Faraday eventually inspired James Clark Maxwell's formulation of a unified theory of electricity, magnetism and light in 1864 [5]. This formulation is most notably referenced as Maxwell's equations (Equations 2.5-2.8) and is fundamental to the understanding of electromagnetism [6].

$$\boldsymbol{\nabla} \cdot \boldsymbol{B} = 0 \qquad \textbf{Equation 2.5}$$

$$\varepsilon_0 \boldsymbol{\nabla} \cdot \boldsymbol{E} = \rho \qquad \textbf{Equation 2.6}$$

$$\frac{1}{\mu_0} \boldsymbol{\nabla} \times \boldsymbol{B} = \boldsymbol{j} + \varepsilon_0 \frac{\delta \boldsymbol{E}}{\delta t} \qquad \textbf{Equation 2.7}$$

$$\boldsymbol{\nabla} \times \boldsymbol{E} = \frac{\delta \boldsymbol{B}}{\delta t} \qquad \textbf{Equation 2.8}$$

where : $\boldsymbol{B}$ is the magnetic induction field

$\boldsymbol{E}$ is the electric field

ε_0 is the electric permittivity of free space

μ_0 is the magnetic permeability of free space

ρ is the electric charge density

$\boldsymbol{j}$ is the electric current density

$\boldsymbol{\nabla}$ is the gradient operator

Equation 2.6 shows that the divergence of electric fields in a system can be non-zero, that is to say electric fields can diverge away from positive charges and converge on negative charges. In contrast to this Equation 2.5 shows that the divergence of magnetic fields must be zero, therefore the existence of magnetic monopoles is impossible and magnetic field lines must always form closed loops. Equation 2.8 shows that loops of electric field are created in regions of space where there is a changing magnetic field, as described by Faraday's Law of Electromagnetic Induction [7]. Finally Equation 2.7 shows that in the absence of a changing magnetic field, loops of magnetic induction are found around electric currents. Ampère's approach, regarding electric current as the source of magnetic fields and Maxwell's Equations form the foundation of understanding classical magnetism. However in order to gain a comprehensive view of magnetism one must build on these basic principles.

2.3.1 The Magnetic Dipole Moment

The fundamental quantity in solid state magnetism is the magnetic moment, μ. In accordance with Ampère's Law we can consider a magnet as equivalent to an electric current circulating around a tiny loop [8]. If a current, I, circulates around an infinitesimally small loop of area $|dS|$ then the magnetic moment is given by Equation 2.9 and will have units of Am^2 (Figure 2.1).

$$\boldsymbol{d\mu = I\, dS} \qquad \textbf{Equation 2.9}$$

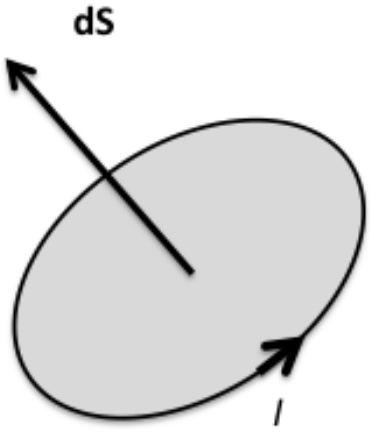

Figure 2.1: Schematic of an elementary magnetic moment due to a current loop

The length of the vector ***dS*** is equal to the area of the current loop, and the relation of the directions of vectors *du* and *I* are given by the Right-Hand Corkscrew Rule, whereby when the tip of one's right thumb is extended from a closed fist to point in the direction of the current *I* and the hand is rotated in a clockwise fashion, the direction of the remaining digits point along ***dμ***. The magnetic moment can be considered as a magnetic dipole. Analogous to the electric dipole, the magnetic dipole can be considered as two magnetic monopoles of opposite magnetic charge separated by a small distance in the same direction as ***dS***. If we consider a circuit loop of finite size, we can calculate the magnetic moment by

summating the magnetic moments of many infinitesimal current loops distributed throughout the area of the loop. The neighbouring current loops all cancel and as a result only a current running along the exterior of the loop remains [2]. Hence we can calculate the magnetic moment according to:

$$\mu = \int \boldsymbol{d\mu} = I \int \boldsymbol{dS} \qquad \textbf{Equation 2.10}$$

2.3.2 Precession

The current loop outlined above occurs because of the motion of a charged particle. As these particles possess mass, there is an angular momentum associated with their motion around the current loop. Consider the particular case of atoms, where electrons orbit the nucleus. The magnetic moment associated with an orbiting electron lies along the same direction as its angular momentum and can be described by Equation 2.11, where γ represents a quantity known as the gyromagnetic ratio.

$$\mu = \gamma L \qquad \textbf{Equation 2.11}$$

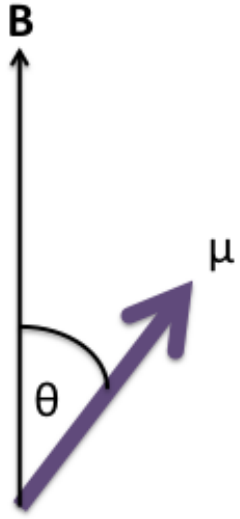

Figure 2.2: Schematic of a magnetic moment, μ, in a magnetic field **B**.

The presence of angular momentum is key to the intricacies of why different materials exhibit different magnetic properties. It also results in the characteristic motion or precession of a magnetic moment in an applied field as detailed below. Consider a magnetic moment, μ, in a magnetic field, $\boldsymbol{B}$ (Figure 2.2). The energy of the magnetic moment, E, is given by [2]:

$$E = -\boldsymbol{\mu} \cdot \boldsymbol{B} \qquad \textbf{Equation 2.12}$$

The energy of the system is minimised when the magnetic moment aligns along the B-field. Therefore a torque acts on the magnetic moment as described by:

$$\boldsymbol{G} = \boldsymbol{\mu} \times \boldsymbol{B} \qquad \textbf{Equation 2.13}$$

If it were not for the presence of angular momentum, the magnetic moment would simply align to the magnetic field. However, as the magnetic moment is associated with angular momentum in accordance with Equation 2.11, Equation 2.13 can be rewritten as:

$$\frac{d\boldsymbol{\mu}}{dt} = \gamma\boldsymbol{\mu} \times \boldsymbol{B} \qquad \textbf{Equation 2.14}$$

Hence the change in $\boldsymbol{\mu}$ acts perpendicular to both $\boldsymbol{\mu}$ and $\boldsymbol{B}$ and therefore the magnetic field causes the direction of the magnetic moment to precess around $\boldsymbol{B}$.

2.3.3 The Biot-Savart Law

Following on from Maxwell's Equations 2.5 and 2.7, the magnetic field generated from a small current element, as a given point in free space can be described by the Biot Savart Law (Equation 2.15) [9]

$$\delta\boldsymbol{B} = -\frac{\mu_0}{4\pi} I \frac{r \times \delta l}{r^3} \qquad \textbf{Equation 2.15}$$

where *dl* is the current element length and *r* is the position vector from the current element to a given point in space

2.3.4 The B and H Fields

By integrating Equation 2.11 the magnetic field created by a number of electric currents can be calculated [1]. Therefore one can essentially envisage a magnetic solid as being composed of millions of infinitesimal current loops. When we consider magnetism relating to a magnetic solid we essentially "zoom out" and look at the overall magnetism of this system of current loops, and not the individual atomic magnetic moments. In such cases the magnetisation, ***M***, is defined as the magnetic moment per unit volume of the material. In free space (vacuum) where there is no magnetisation, the magnetic field can be described in terms of the vector fields ***B*** and ***H***, which are linearly related according to Equation 2.16 [2].

$$\boldsymbol{B} = \mu_0 \boldsymbol{H} \qquad \textbf{Equation 2.16}$$

From Equation 2.5 we know that the magnetic field does not diverge and therefore cannot exist as a point charge or monopole. By expressing Equation 2.5 in its integral form as opposed to the differential form and utilising the divergence theorem it can be concluded that the magnetic flux, ***B***, which enters a region or area, *dA*, must be equal to the flux leaving that same region (Figure 2.3) [1]. This gives rise to Gauss' Law.

$$\int_S \boldsymbol{B} \cdot dA = 0 \qquad \textbf{Equation 2.17}$$

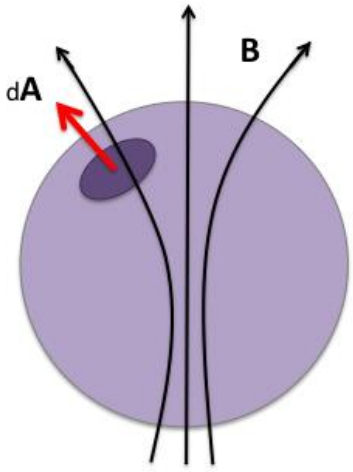

Figure 2.3: Schematic showing the divergenceless nature of the **B**-field

The element of magnetic flux flowing out of the surface, *s*, can be described by:

$$d\boldsymbol{\Phi} = \boldsymbol{B} \,.\, d\boldsymbol{A} \qquad \textbf{Equation 2.18}$$

This lets us conclude that:

$$\boldsymbol{B} = \frac{d\boldsymbol{\Phi}}{d\boldsymbol{A}} \qquad \textbf{Equation 2.19}$$

This is the reason why the B-field is sometimes referred to as the "magnetic flux density" or "magnetic induction". Considering only magneto-statics, that is, a system where magnetic fields are generated by steady currents, we can describe the relationship between the magnetic flux density, ***B***, and the current density, *j*, by the following form of Maxwell's equation (Equation 2.7).

$$\nabla \times \boldsymbol{B} = \mu_0 \boldsymbol{j} \qquad \textbf{Equation 2.20}$$

Expressing this in integral form gives the much more recognisable Ampère's law [8]:

$$\oint \boldsymbol{B} \cdot dl = \mu_0 I \qquad \textbf{Equation 2.21}$$

where *I* is the algebraic sum of the currents comprising a path of length *dl*.

This equation can be used to calculate the **B**-field resulting from highly symmetric current distributions, such as those produced from the current flowing through a long straight wire. In this case the **B**-field encircles the wire and is constant in magnitude at a distance, *r*, from the axis. Integrating Equation 2.17 around a circle of radius *r* results in:

$$B_{(r)} = \frac{\mu_0 I}{2\pi r} \qquad \textbf{Equation 2.22}$$

The **H**-field, known as the magnetic field strength or magnetising force, becomes important when we consider magnetic fields in a material medium. In these systems, when a magnetic field is applied the atomic magnetic moments in the material will be influenced by the field. If we consider Ampère's law in its differential form (Equation 2.21) we see the **B** field is related to the total current density. In a non-vacuum medium, this can be broken down into two parts according to:

$$\boldsymbol{j} = \boldsymbol{j_c} + \boldsymbol{j_m} \qquad \textbf{Equation 2.23}$$

where $\boldsymbol{j_c}$ is the conduction current in electrical circuits and $\boldsymbol{j_m}$ is the Ampèrian magnetisation current associated with the magnetised medium.

A problem arises in that there is no known experimental method to measure $\boldsymbol{j_m}$, and as such the **H** field was devised. Although it is not possible to measure the current circuits within matter, we know that they are related to the overall magnetisation of the material according to:

$$\boldsymbol{j_m} = \boldsymbol{\nabla} \times \boldsymbol{M} \qquad \textbf{Equation 2.24}$$

The **H**-field can then be introduced to retain Ampère's Law in a physically practical form where:

$$\boldsymbol{H} = \frac{\boldsymbol{B}}{\mu_0}\boldsymbol{M} \qquad \textbf{Equation 2.25}$$

This is normally represented in literature using the form shown in Equation 2.26.

$$\boldsymbol{B} = \mu_0(\boldsymbol{H} + \boldsymbol{M}) \qquad \textbf{Equation 2.26}$$

We can therefore think of ***B*** as the sum of the magnetic field in a vacuum, ***H***, and the magnetic polarisation of the material, ***M***. As a result ***H*** is sometimes referred to as the external magnetic field, ***M*** as the internal magnetic field and ***B*** as the total magnetic field i.e. the magnetic flux. ***B***, ***M*** and ***H*** are illustrated in Figure 2.4 for a uniformly magnetised block of material and the relationship between them is illustrated at point, *P*.

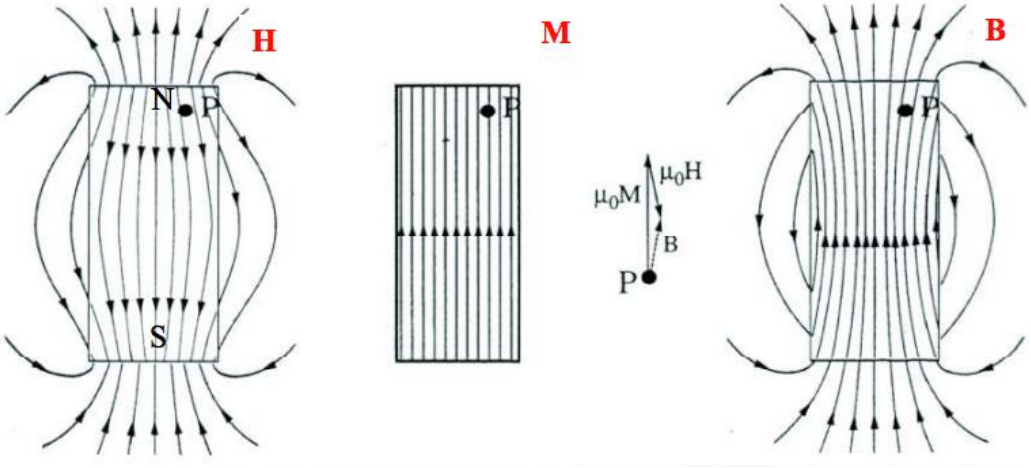

Figure 2.4: Schematic showing the **B**, **H** and **M** fields for a uniformly magnetised block of material

2.3.5 Quantum Mechanics and Magnetism

Although classical theory is sufficient for describing electromagnetism, quantum theory must be considered to fully understand the different forms of magnetic ordering. The two basic approaches adopted to interpret magnetism in the quantum mechanical sense are wave mechanics and matrix mechanics. As mentioned previously, the magnetic moments in solids are associated with electron motion. In 1924 Louis de Broglie proposed that wave-particle duality extended to matter as well as light and that the wavelength of an electron was related to its momentum by the following equation [10]:

$$p = \frac{h}{\lambda_e} \qquad \textbf{Equation 2.27}$$

If we consider an electron to be both a particle and a wave, the electron can be represented using wave mechanics by the complex wave function, $\Psi_{(r)}$, and the probability of finding an electron in a given volume, δ_r^3 , at a position $\underline{\boldsymbol{r}}$ is given by [1]:

$$\Psi^*_{(\boldsymbol{r})}\Psi_{(\boldsymbol{r})}\,\delta_r^3 \qquad \textbf{Equation 2.28}$$

The basis for this is the Schrödinger equation [11]:

$$H\Psi = \varepsilon\Psi \qquad \textbf{Equation 2.29}$$

where H is the Hamiltonian operator and ε is the energy.

The solutions are the eigenstates or stationary states of the system, $\Psi_{i(r)}$, and the eigenvalues are the energy levels. One of the limitations of the Schrödinger equation is that it only yields an exact solution for the specific case of the hydrogen atom. In the matrix formulation, known as the Heisenberg formulation, an n x n matrix representation is used for the Hamiltonian and the physical observables are represented by matrix operators. The eigenstates are n x 1 column vectors and the eigenvalues are real numbers. Diagonalization of the matrix is often employed to solve for the eigenvalues [12].

2.3.6 Spin Moment

In addition to the electron's orbit around the nucleus, there is a second inherent electron motion, which also contributes to an atoms magnetic moment. There is an intrinsic angular momentum associated with this electron motion, which is referred to as "spin", as it was originally thought that electrons rotated on their axis. As electrons are fermions and therefore fundamental particles this is technically not quite the case, but as electron spin is so counterintuitive the concept is still widely used. The angular momentum associated with the electrons orbital motion is referred to as orbital angular momentum and has a quantum number of $s = \frac{1}{2}$. Associated with this angular momentum is an intrinsic magnetic moment which can adopt one of two discreet orientations relative to the applied magnetic field (either parallel, 'up',

or anti-parallel, 'down') [13]. The spin magnetic quantum number is therefore given by $m_s = \pm\frac{1}{2}$ and can be calculated using Equation 2.30.

$$\mu_s = g\frac{q}{2m}s \qquad \textbf{Equation 2.30}$$

where g is the gyromagnetic ratio and is dependent on the internal structure of the fermion.

Quantum electrodynamics (QED) calculations to the first order determined that the gyromagnetic ratio of an electron is 2 and hence Equation 2.30 can be written as [14]:

$$\mu_e = -\frac{e}{2m_e} \qquad \textbf{Equation 2.31}$$

Hence, spin angular momentum is twice as effective at creating a magnetic moment as orbital angular momentum.

2.3.7 The Bohr Magneton

A useful unit in magnetism, and one that will be used throughout this thesis is the Bohr magneton. This is used to describe the size of atomic magnetic moments. Consider a hydrogen atom where a single electron with charge $-e$ and mass m_e precesses about the hydrogen nucleus (proton) [2]. This motion generates a current defined by:

$$I = \frac{-ev}{2\pi r} \qquad \textbf{Equation 2.32}$$

where v is the velocity of the electron and r is the radius of the electrons orbit. In its ground state the angular momentum of the electron is equal to the reduced Planck constant, $\hbar$.

Therefore we can say:

$$m_e v r = \hbar \qquad \textbf{Equation 2.33}$$

Substituting in Equation 2.32 and 2.31 for this particular case we can say:

$$\mu = \pi r^2 I \qquad \textbf{Equation 2.34}$$

By substituting the definition of the electrons angular momentum this relation can be rewritten as:

$$\mu = \frac{-e\hbar}{2m_e} \qquad \textbf{Equation 2.35}$$

This is known as the Bohr magneton, μ_b, and has a value of 9.274×10^{-24} Am^2.

2.3.8 Magnetic Ordering in Solids

Magnetic materials consist of millions of atoms, which may possess a magnetic moment. The density of atomic magnetic moments within a given material is given by its overall magnetisation. We can describe the magnetic response exhibited by a material by the following equation:

$$\boldsymbol{M} = \chi \boldsymbol{H} \qquad \textbf{Equation 2.36}$$

where χ represents the susceptibility of the material.

The susceptibility of a material is a measurement of the magnetic moment induced by a magnetic field, $\boldsymbol{H}$, that is to say, how susceptible a material is to changes in the external magnetic field. This can be used to distinguish materials into different forms of magnetic ordering.

Diamagnetism, paramagnetism, ferromagnetism, anti-ferromagnetism, ferrimagnetism and superconductivity are detailed in the following section.

2.3.8.1. Diamagnetism

Diamagnetism is a relatively weak magnetic property which is present in all materials. As it is weaker than other magnetic properties, diamagnetism is dominated by any other forms of magnetic ordering which may be present in the material. A purely diamagnetic material consists of atoms with all constituent electrons contained in closed orbitals. The electron spins therefore cancel and the material has no overall atomic magnetic moment. On application of an external field a force is applied to the individual electrons orbital magnetic moments. This generates a torque which causes the electrons to precess as described in section 2.2.2, resulting in induced magnetic moment within the atom. This force acts in the opposite direction of the applied field in accordance with Lenz's law, which states that the direction of an induced field is always such as to oppose the field that produces it, meaning a diamagnetic material exhibits a negative magnetic response (see Figure 2.5). This can be observed by the negative susceptibility exhibited by diamagnetic materials. In research carried out by Pierre Curie it was shown that the negative susceptibility exhibited by diamagnetic materials is temperature independent (see Figure 2.5). As diamagnetism is a relatively weak effect, a diamagnetic material will return to its original state of no net magnetisation, on the removal of the applied field.

Some examples of diamagnetic materials include silver, copper and bismuth.

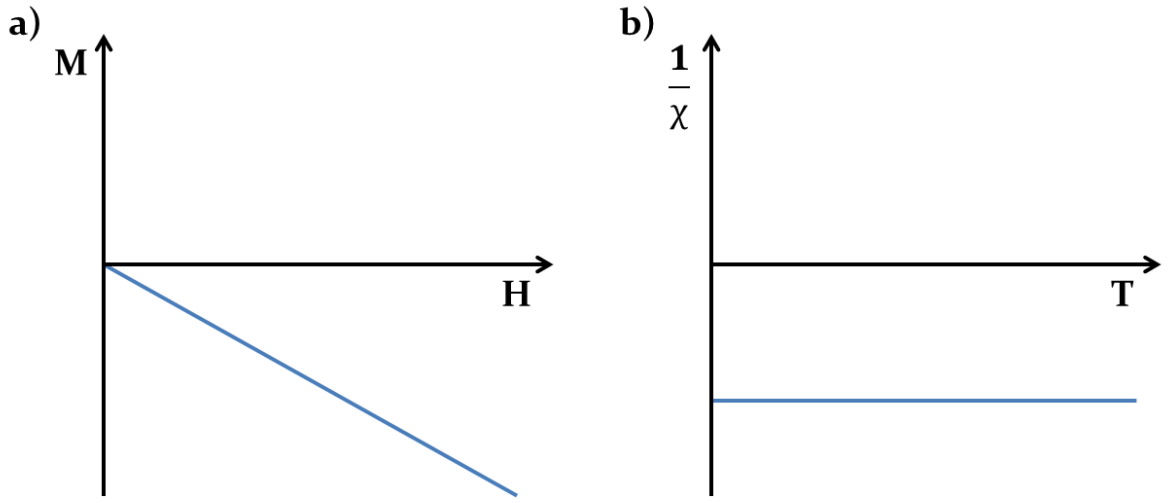

Figure 2.5: (a) Plot of the typical **M** versus **H** behaviour exhibited by a diamagnetic material (***b)*** Plot of the effects of temperature on the susceptibility of a typical diamagnetic material

2.3.8.2. Paramagnetism

Paramagnetism is a magnetic property present in materials comprised of atoms with a non-zero magnetic moment, due to unpaired electrons in partially filled electron orbitals. Only extremely weak interactions exist between neighbouring atoms in paramagnetic materials and they are therefore assumed to act independently of one another. As such the atomic magnetic moments of these materials are randomly aligned in the absence of an applied field, resulting in a zero net magnetisation of the material.

On application of an applied field the atomic moments start to align parallel to the magnetic field. Unlike diamagnetic materials, as the electrons in paramagnetic materials exist in partially filled orbitals they are not constrained in their orbitals and are therefore free to move in response to the applied field. The extent at which the magnetic moments align with the applied field is dependent on the magnetic field strength as shown in Figure 2.6.

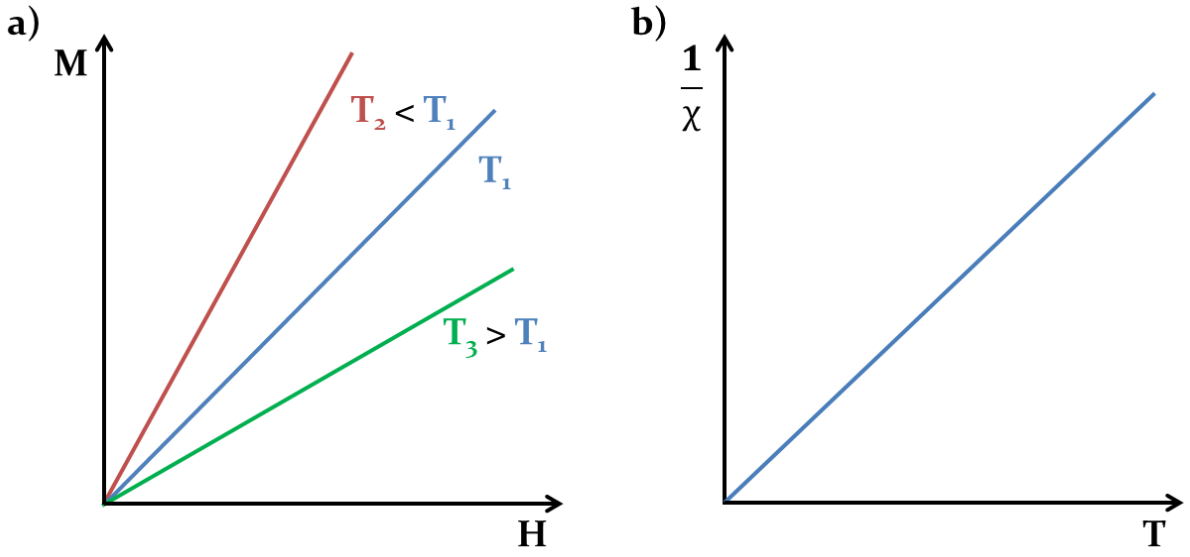

Figure 2.6: (a) Plot of the typical **M** versus **H** behaviour exhibited by a paramagnetic material at a range of different temperatures (***b)*** Plot of the effects of temperature on the susceptibility of a typical paramagnetic material

In the absence of other forces all the atomic moments in the material would align along the applied field to produce a very large net magnetic response. However thermal energy in the system causes some of the magnetic moments to flip randomly, resulting in only partial alignment of the atomic moments parallel to the applied field. This results in the material exhibiting a much smaller positive magnetic response. The randomisation of the magnetic

moments is directly proportional to the thermal energy in the system, meaning the magnetic response of the material is dependent on temperature as shown in Figure 2.6.

Although paramagnetism dominates over diamagnetism it is still a relatively weak effect and the atomic magnetic moments return to their original state of random orientation on removal of the applied field.

Some examples of paramagnetic materials include sodium, oxygen and aluminium.

2.3.8.3. Ferromagnetism

Ferromagnetic materials are akin to paramagnetic materials in that they are composed of atoms with a net magnetic moment, due to unpaired electrons in partially filled electron orbitals. However unlike paramagnetic materials, neighbouring atoms in a ferromagnetic material exhibit a very strong interaction, known as the exchange interaction (see section 2.2.9). This interaction couples neighbouring atomic magnetic moments and aligns them parallel to one another, resulting in a large net positive magnetisation. The long range ordering present in ferromagnetic materials, as a result of this exchange interaction, means that they exhibit a spontaneous magnetisation even in the absence of an applied field. This spontaneous magnetisation gives rise to the characteristic hysteretic behaviour of ferromagnetic materials.

Hysteresis loops are commonly used to characterise ferromagnetic materials, as they are specific to the material being investigated.

Figure 2.7 shows a typical M versus H curve for a sample ferromagnetic material. At point 0, the material has no net magnetisation and is said to be in a non-magnetised state. On application of an applied field the magnetisation of the sample gradually increases until it hits a maximum value at point a. The magnetisation of the sample at this point is referred to as the saturation magnetisation (M_s) of the sample and corresponds to a material specific applied field (y). Increasing the applied field beyond the point will have no impact on the magnetisation of the material. On decreasing the applied field the magnetisation of the sample decreases according to the curve ab. At point c where the applied field reaches zero, the material retains a remnant magnetisation (M_r). On application of an applied field in the opposite direction the magnetisation of the sample follows the same continuous curve until it reaches a maximum magnetisation in the opposite direction (point d). This negative saturation magnetisation will have the same magnitude as the one corresponding to the positively applied field. As the negative field is applied the magnetisation of the sample will be reduced to zero at a particular

applied field (point c). The applied field necessary to reduce the magnetisation of the sample to zero is referred to as the coercivity (H_c). Reducing the applied field back to zero and reapplying the field in the opposite direction will cause the magnetisation to change in accordance with the curve defa, completing the hysteresis loop characteristic of ferromagnetic materials.

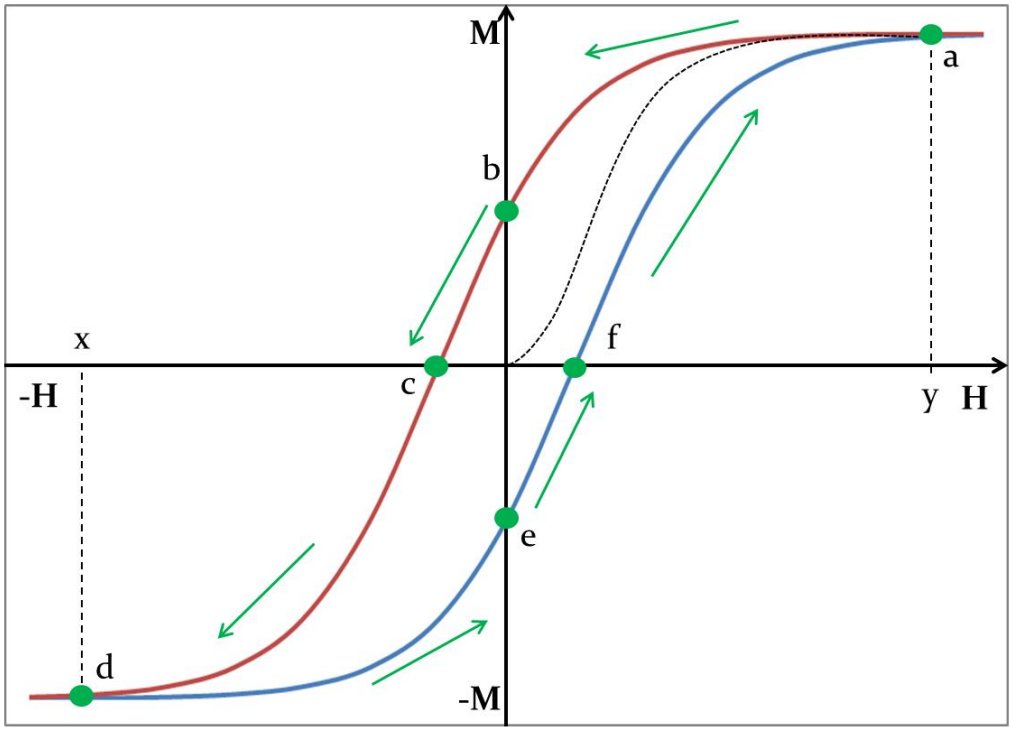

Figure 2.7: Plot of the typical **M** versus **H** behaviour exhibited by a ferromagnetic material

The hysteresis loops of ferromagnetic materials can be explained by the behaviour of domains, small regions in which the magnetic moments of the atoms are grouped together and aligned, (see section 2.3.12) in bulk ferromagnetic materials [15]. At point zero the domains of the material are spontaneously magnetised in such a way that they cancel one another and the material therefore exhibits a zero net magnetisation. On application of an applied field, the domains, which are aligned in the same direction as the applied field, begin to grow at the expense of the domains which are aligned anti parallel to the applied field. On increasing the applied field strength a point will be reached where it is more energetically favourable for the domains, which are not aligned with the applied field, to switch from their easy axis of magnetisation and align along the crystallographic axis that is nearest to the field direction. At this point the domain will rotate. At the point of saturation magnetisation all of the domains will

have rotated to a direction aligned with the magnetic field irrespective of the anisotropy of the material.

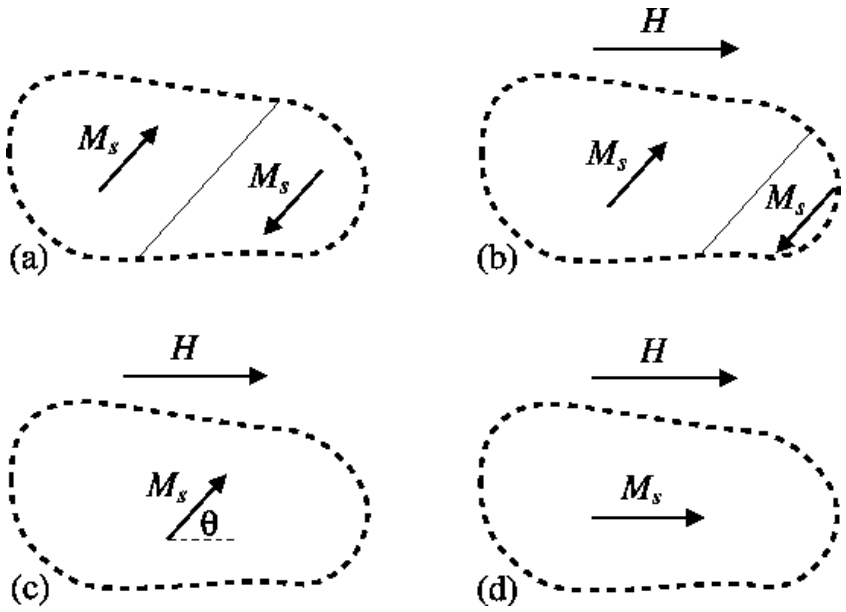

Figure 2.8: Schematic showing the domain wall motion and domain rotation in a ferromagnetic material in the presence of an applied field (**H**). In ***(a)*** M=0 Oe, in ***(b)*** M > 0 Oe and the upper domain grows at the expense of the lower one by downward motion of the domain wall, in ***(c)*** M = M_s cosθ the domain wall moves out of the region considered and in ***(d)*** M = M_s and the magnetisation rotates into parallelism with the applied field and the material is saturated.

Like paramagnetism, ferromagnetism is temperature dependent. At a material specific temperature, known as the Curie temperature, T_c, the thermal energy of the system causes the spontaneous magnetisation of the material due to collective alignment of atomic moments to decrease to zero. Above this temperature the material acts paramagnetically. Some examples of ferromagnetic materials include iron, nickel and cobalt.

2.3.8.4. Antiferromagnetism

Materials that exhibit antiferromagnet behaviour are very similar to ferromagnetic materials in that their magnetic behaviour is governed by exchange interactions between neighbouring atoms. In contrast to ferromagnetic materials however, the exchange interaction is negative and acts to align the magnetic moments of neighbouring atoms anti parallel to one another. Antiferromagnetic materials are composed of at least two sublattices, ferromagnetically coupled

together. On one sublattice the moments are all aligned up, whereas on the other they are aligned down. The arrangement of the sublattices is such that neighbouring atoms exist on different lattices and are therefore aligned anti parallel to one another [1] (see Figure 2.9)

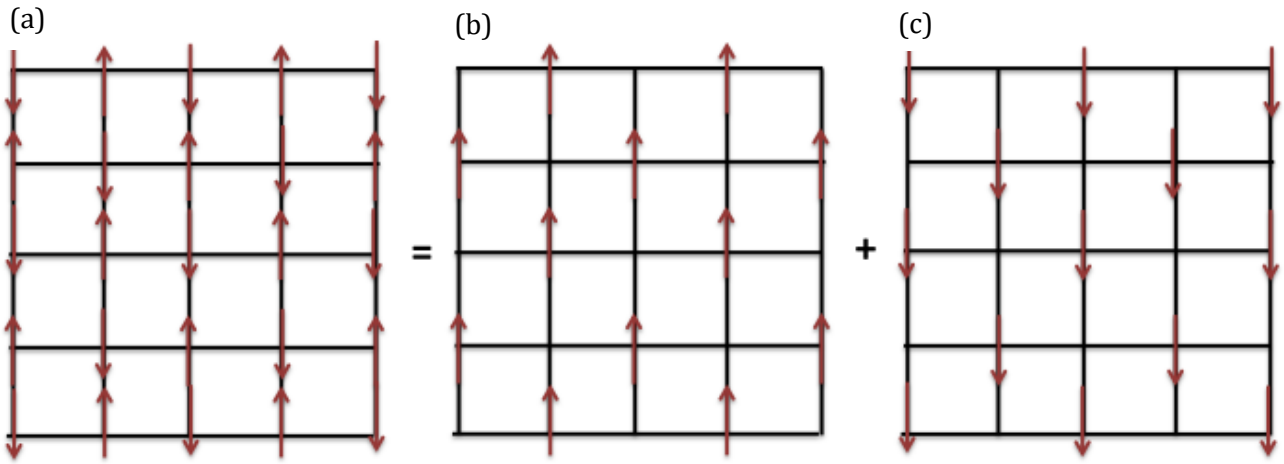

Figure 2.9: Schematic of an antiferromagnet and the two interpenetrating sublattices which can be said to compose it, where ***(a)*** shows the resultant magnetic lattice, ***(b)*** shows the sublattice where all moments are aligned up and ***(c)*** shows the sublattice where all moments are aligned down

As with ferromagnetic and paramagnetic materials, antiferromagnetism is temperature dependent, and above a certain temperature, known as the Néel temperature, the material will behave paramagnetically. The Néel temperature is analogous to the Curie temperature in ferromagnetic materials. Some examples of antiferromagnetic materials include hematite, nickel oxide and chromium.

2.3.8.5. Ferrimagnetism

Like antiferromagnetic materials, ferrimagnetic materials consist of at least two sublattices. However unlike antiferromagnetic materials, these sublattices are not equivalent. If the coupling between the sublattices is ferromagnetic then the material simply exhibits ferromagnetic behaviour. However if the sublattices interact antiferromagnetically then ferrimagnetism is observed. As the magnetic moments and on occasions the number of atoms on each sublattice are different, a net magnetisation is observed. Ferrimagnetic materials are temperature dependent, however this tends to be a lot more complex than that of the other magnetic materials as each sublattice has a different molecular field and therefore experiences a

different temperature dependence. A couple of examples of ferrimagnetic materials include yttrium iron garnet (YIG) and magnetite (Fe_3O_4).

2.3.8.6. Superparamagnetism

Superparamagnetism is a type of magnetism observable in magnetic nanoparticles of a particular size. Below a critical size, which is dependent of material properties such as the magnetic anisotropy (see section 2.3.13) and saturation magnetisation, the spontaneous magnetisation of the particle becomes unstable due to thermal energy and the orientation of the magnetisation will flip randomly [16]. Under the application of a magnetic field the net magnetic moment will align with the direction of the applied field. On removal of this applied field the magnetisation will slowly relax over this energy barrier. The time taken for the magnetisation to flip from one orientation to the other is referred to as the Néel relaxation time and is directly related to temperature as described by the following equation [17].

$$\tau_N = \tau_0 \exp(\frac{KV}{k_B T}) \qquad \textbf{Equation 2.37}$$

where τ_N is the Néel relaxation time, K is the anisotropy energy density of the complex and V its volume, k_B is the Boltzmann constant, T is temperature and τ_0 is a length of time characteristic of the complex.

Superparamagnetic materials can be described as going through a transition from the superparamagnetic state to a blocked state when the temperature is such that the Néel relaxation time is larger than the time taken to carry out a measurement of the magnetic moment of the molecule. This is referred to as the blocking temperature [1].

2.3.8.7. Superconductivity

In 1911 H. Kammerlingh Onnes made the first observation of superconductivity when he cooled mercury in liquid helium [18]. Superconductive materials are characterised by an absence of electrical resistance below a critical temperature. Additionally below this critical temperature they actively expel magnetic fields, a phenomenon known as the Meissner effect. This effect has earned superconductors the name of a "perfect diamagnet". In 1972 Bardeen, Cooper and

Schriffer suggested the BCS theory of superconduction, which earned them the 1972 Nobel prize in Physics [19]. This theory suggests that electrons in a superconductor exist in pairs known as Cooper pairs, which are bound together by means of a phonon interaction. It was theorised that the motion of an electron through a crystal lattice at extremely low temperatures results in "bending" of the positive lattice towards the electron. This effect causes the formation of a region of positive charge that is sufficient to attract a neighbouring electron and result in the formation of a Cooper pair. Single electrons are fermions and must therefore obey the Pauli exclusion principle, which states that multiple electrons in the same spin state cannot exist in the same quantum sate simultaneously. In a Cooper pair however, electrons with opposite spins add to give an overall spin of zero, and they can therefore be considered as bosons. Bosons are not restricted by the Pauli exclusion principle and can condense into the same energy level. The electron pairs have a slightly lower energy and leave an energy gap above them that inhibits the kind of collision interactions that lead to ordinary resistivity. For temperatures such that the thermal energy is less that this energy gap, the material will act as a superconductor and will exhibit zero resistivity.

2.3.9 Molecular Field Theory

Pierre Weiss proposed the molecular field theory model in 1907, in an attempt to explain the long range ordering exhibited by ferromagnetic and antiferromagnetic materials [20]. Pierre Weiss postulated the existence of an internal magnetic field in ferromagnetic materials, which acted in addition to the externally applied field. In the absence of an applied field Pierre theorised that this internal field would be sufficiently strong to cause some alignment of magnetic moments in the material, resulting in some extent of spontaneous magnetisation. This relationship is described by the following equation:

$$\boldsymbol{H^{\iota} = n_w M + H} \qquad \textbf{Equation 2.38}$$

where n_w is the Weiss coefficient.

This theory was called into question due to the large value of n_w necessary to account for some of the very large T_c's found in nature. However many years later Heisenberg was able to explain this large internal field as being the result of exchange interactions involving very large Coulomb energies [1].

2.3.10 Exchange Interaction

The exchange interaction is a direct result of the Pauli exclusion principle, which dictates that electrons can only exist simultaneously in the same quantum state if their spins are aligned antiparallel. Exchange interactions can be thought of as electrostatic interactions, arising because charges of the same sign cost energy when they are close together and save energy when they are apart. These interactions can occur directly, where atoms are positioned closely enough together that their electron clouds overlap, or indirectly through an intermediary. Direct exchange coupling is very strong but short ranged whereas indirect coupling occurs over much larger distances. Indirect coupling between non-neighbouring metallic ions, which is mediated by a non-metallic ion, is known as super exchange (see Figure 2.10).

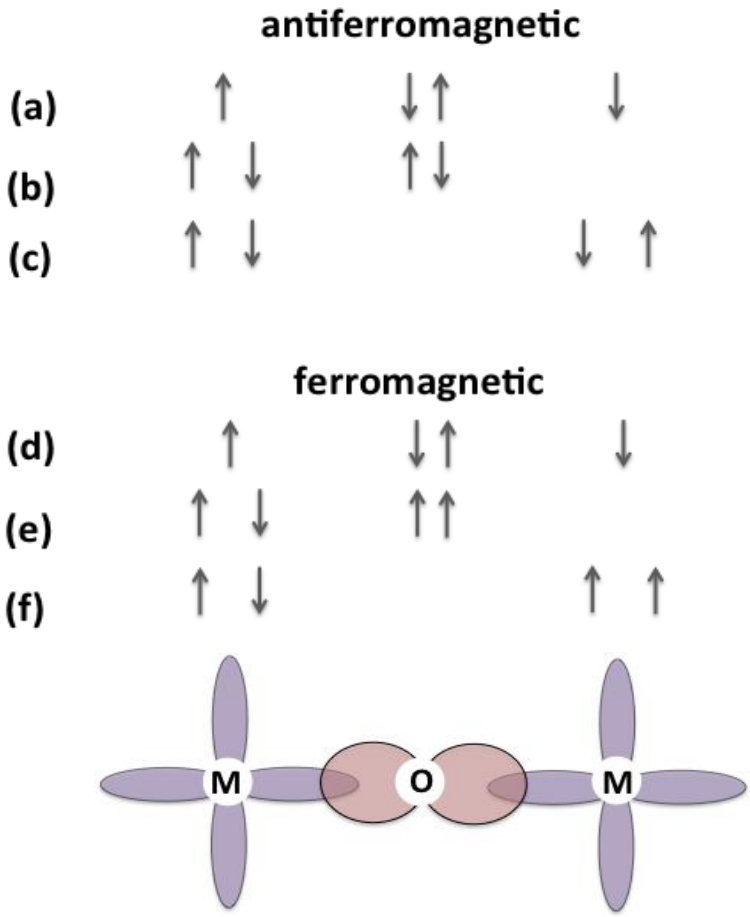

Figure 2.10: Schematic of the superexchange mechanism in a magnetic oxide. The arrows represent the spins of the electrons and their distribution over the metal ion and oxygen atom. Taken from reference 2.

Super exchange occurs because it is energetically favourable for the magnetic moments in such a system to align antiferromagnetically. Consider two transition metal ions, each with a single unpaired electron, separated by an oxygen ion. The single unpaired electrons in the metallic ions exist in a *d* orbital, and the oxygen ion has two electrons present in the *p* orbital in its outermost states. If the magnetic moments couple antiferromagnetically as shown in Figure 2.10, the ground state as shown in (a), can mix with the excited configurations shown in (b) and (c). The electrons can therefore be delocalised across the whole unit and the kinetic energy of the system is lowered. However if the magnetic moments couple ferromagnetically, the ground state (d) cannot mix with the excited states (e) and (f) due to the Pauli exclusion principle. The antiferromagnetic configuration is therefore more energetically favourable. An extension of super exchange is the double exchange mechanism, which takes place in systems where the magnetic ion shows mixed valency and can exist in more than one oxidation state. Common examples are systems that contain the Mn ion, which can exist as either Mn^{3+} or Mn^{4+}. Consider the Mn^{3+} - O - Mn^{4+} bonding system shown in Figure 2.11.

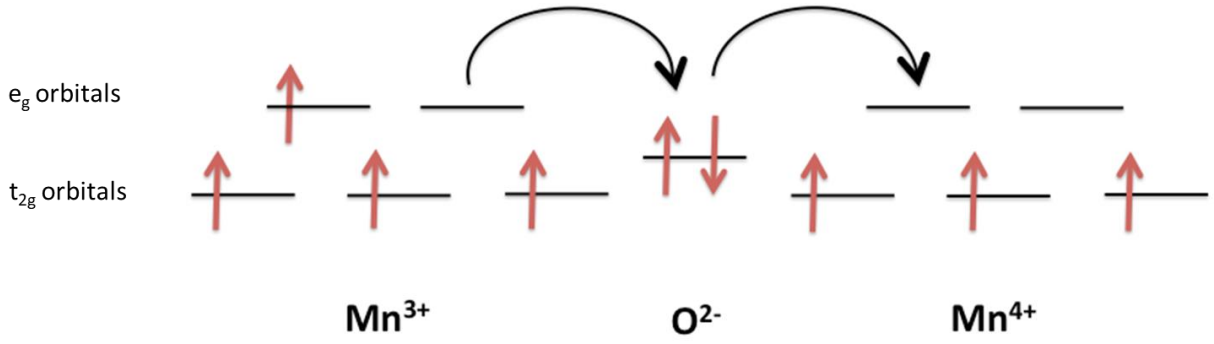

Figure 2.11: Schematic of the double exchange mechanism between Mn^{3+} and Mn^{4+} ions.

The outer electrons in manganese ions are held in *d* orbitals. Due to the octahedral structure of the manganese ions, there is a splitting of the energy levels of these *d* orbitals. The d_{xy}, d_{yz} and d_{xz} orbitals exist at a lower energy level (t_{2g}) than the $d_{x^2-y^2}$ and d_{z^2} orbitals (e_g) as displayed in Figure 2.11.

In the double exchange mechanism the e_g electron from the Mn^{3+} ion is transferred to the O^{2-} ion at the same time as an electron is transferred from the O^{2-} ion to the Mn^{4+} ion. Due to the strong exchange interaction between the e_g electron and the three electrons in the t_{2g} level of the Mn ion, this process is only energetically favourable when the electron moves to another system

where the t_{2g} electron are aligned parallel. Hence ferromagnetic alignment of neighbouring atoms is energetically favourable.

2.3.11 Zeeman Splitting and Spin Orbit Coupling

In addition to the exchange interaction, a weaker interaction due to coupling of electron spin and orbital momentum can take place within an atom. This effect is observable in the splitting of energy levels in the emission spectra of a hydrogen atom.

As described previously an electron possesses both spin and orbital angular momentum, each of which has an associated magnetic moment. Consider the hydrogen atom, but instead of taking the frame of reference from the nucleus take it from the electron, such that the electron is a stationary entity with the nucleus orbiting around it as shown in Figure 2.12 [2].

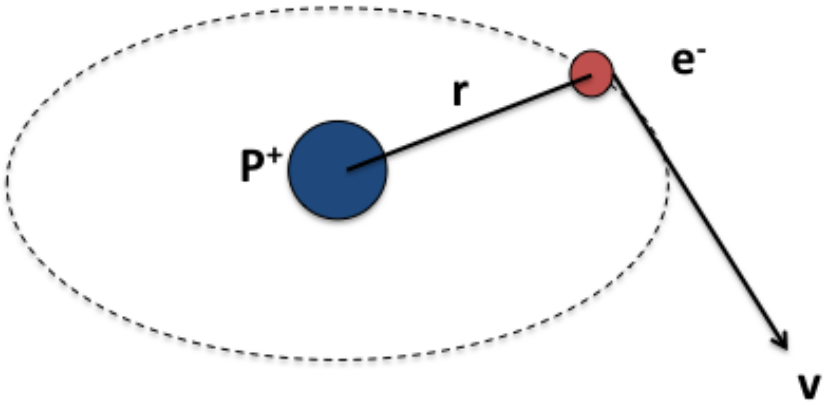

Figure 2.12: Schematic of an electrons motion in an atom from the reference frame of the nucleus, where p+ is the nucleus, e- is the electron, r is the radius of the electrons orbit around the nucleus and v is the velocity associated with the electrons motion.

The orbital motion of the nucleus creates a positive electro current loop which generates a **B**-field given by:

$$\mathbf{B} = \frac{\mu_0 I}{2r} \qquad \textbf{Equation 2.39}$$

The spin angular momentum of the electron induces a spin magnetic dipole moment, which sits well within the **B**-field generated by the orbiting nucleus. This **B**-field induces a torque on the

magnetic dipole that tends to orientate the dipole moment along the same direction of the **B**-field lines. This in turn results in a change of energy in accordance with the following equation:

$$\Delta E = -\overrightarrow{\mu_s} \cdot \vec{B} \qquad \textbf{Equation 2.40}$$

As **B** is related to the orbital angular momentum according to the following equation:

$$\mathbf{B} = \frac{\mu_0 Ze\vec{L}}{4\pi m_e r^3} \qquad \textbf{Equation 2.41}$$

And the spin magnetic dipole moment, $\overrightarrow{\mu_s}$, is related to the spin angular momentum we can say

$$\Delta E \propto \vec{S}.\vec{L} \qquad \textbf{Equation 2.42}$$

This interaction between *L* and *S* is the spin orbit interaction.

2.3.12 Domains

In nature it is demonstrated that ferromagnetic materials can exist in a non-magnetised state. This calls into question Pierre Weiss's molecular field theory, that ferromagnets exhibit spontaneous magnetisation through exchange forces [20]. In order to account for this Weiss postulated the existence of domains. Domains are small regions, typically around 10-100μm in size, in which the magnetic moments of the atoms are grouped together and aligned as a result of a materials physical properties such as crystal structure and anisotropy (see section 2.3.13). Neighbouring domains are separated from one another by domain walls, which allow for adjacent domains to exhibit different magnetisation states. In the absence of an applied field the domains of a ferromagnetic material can be spontaneously magnetised in such a way that they cancel one another and the material therefore exhibits a zero net magnetisation (see Figure 2.13).

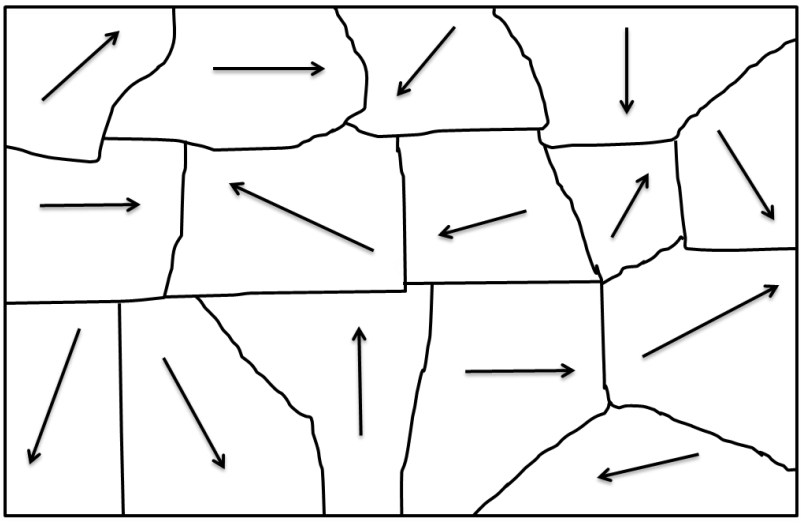

Figure 2.13: Schematic demonstrating the random magnetic orientation of domains in the absence of an applied field

The existence of domains can also explain how saturation magnetisation of some ferromagnetic materials can be observed on application of a very weak magnetic field (as low as 10^{-6} T) [2]. As the individual atomic magnetic moments are already macroscopically ordered in domains in ferromagnetic materials only the domains need to be ordered to achieve saturation magnetisation. This alignment can be achieved by motion of the domain walls.

Domain walls are characterised by the angle between the two magnetisation states of the neighbouring domains the wall separates. A 180° wall is referred to as a Bloch wall and separates domains of opposite magnetisation states. A 90° wall is known as a Néel wall and separates domains of perpendicular magnetisation states. Bloch and Néel domain walls in ferromagnetic materials undergo different motion on application of an applied field. In Bloch walls the magnetisation rotates in a plane parallel to the plane of the wall whereas in Néel walls the magnetisation rotates in a plane perpendicular to the plane of the wall (see Figure 2.14). If no other forces where acting in the material domain walls would continue to unwind indefinitely, growing in size throughout the whole system. This is because it is energetically costly for magnetic moments to exist twisted with respect to neighbouring moments. In the absence of other forces the magnetic moments in the system would therefore realign, however this does not happen in practice due to the presence of magnetocrystalline anisotropy in the system.

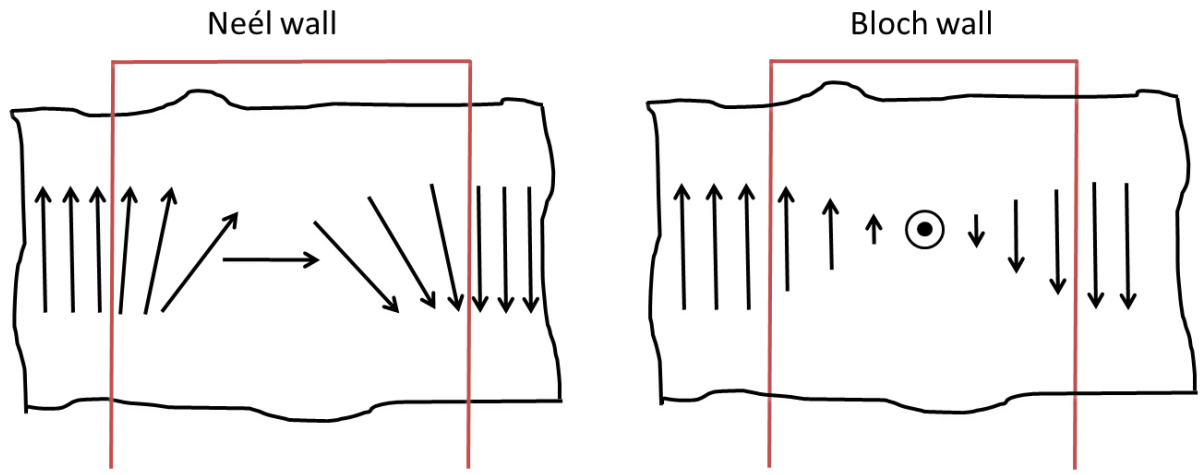

Figure 2.14: Schematic demonstrating domain wall motion in Bloch and Néel domain walls.

2.3.13 Magnetic Anisotropy

The magnetic anisotropy of a material tends to constrain the direction of magnetisation along one or more easy axes (crystallographic direction along which it is easiest to magnetise the crystal). The tendency of the magnetisation of a material to align along this easy axis can be described by the following equation,

$$E_a = K_u \sin^2\theta \qquad \textbf{Equation 2.43}$$

where θ is the angle between the direction of **M** and the easy axis, E_a is the anisotropy energy and K_u is the anisotropy constant.

There are three main sources of anisotropy related to the samples shape, crystal structure and atomic or micro-scale texture.

Shape anisotropy arises due to the internal demagnetising field generated inside ferromagnetic materials when an external field is applied. This demagnetising field is proportional to the field that created it and can be described by the following equation,

$$H_d = -N_d M \qquad \textbf{Equation 2.44}$$

N_d is known as the demagnetisation factor and is dependent on the shape of the material. It is at a minimum along the most elongated axis of the material. As such it is easier to overcome the demagnetising field and magnetise the sample along this easy axis.

In magnetocrystalline anisotropy the easy axis of magnetisation is dictated by the crystal structure of the material. Consider the three ferromagnetic transition metals Fe, Ni and Co. Each of these elements has a different crystallographic structure as shown in Figure 2.15. As can be seen from their corresponding magnetisation curves, each material shows a different approach to the saturation magnetisation depending on the crystallographic axis that the field is applied along. The axis that requires the lowest field to reach saturation magnetisation is referred to as the easy axis, whereas the axis that requires the largest field to reach saturation magnetisation is called the hard axis.

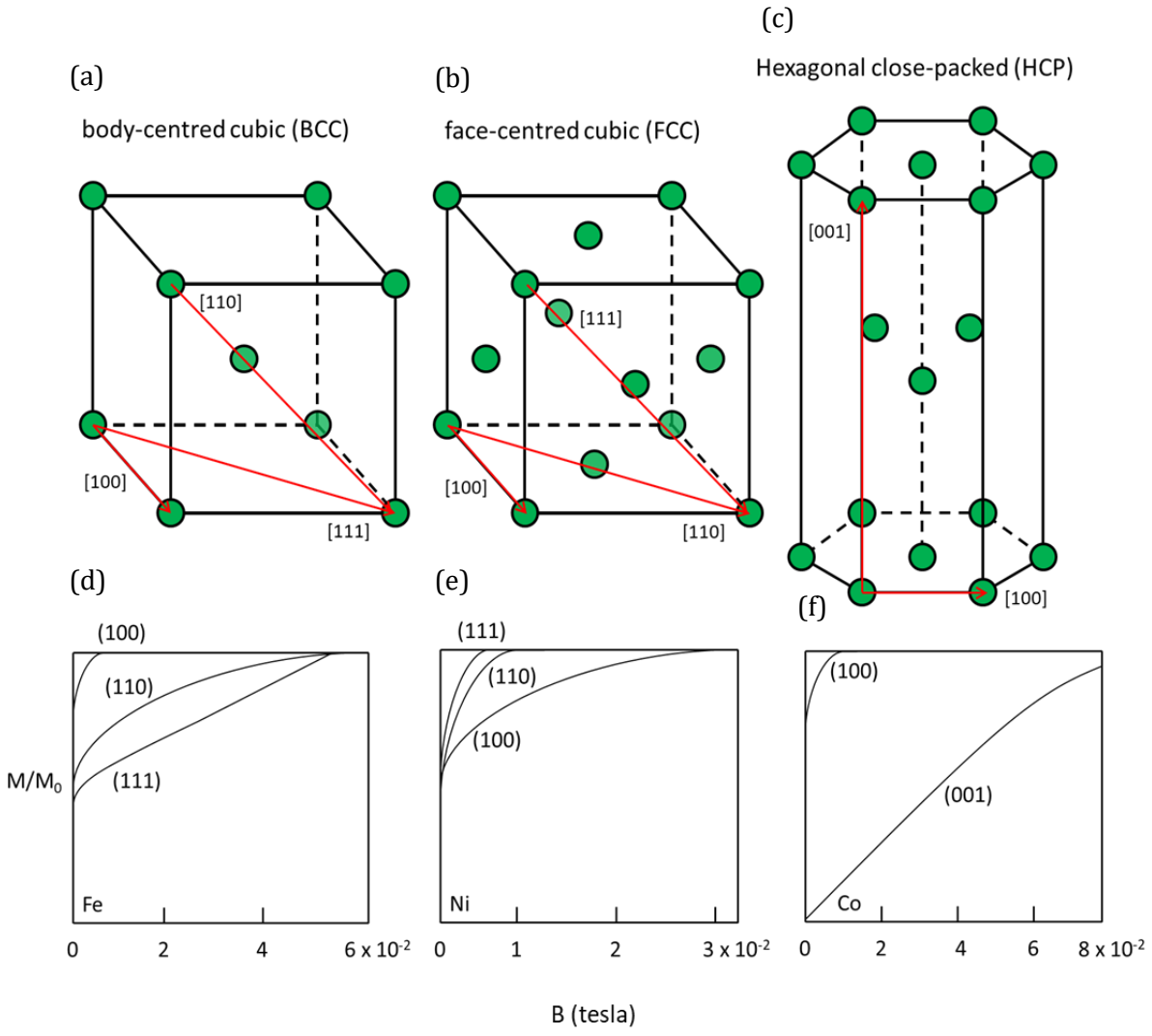

Figure 2.15: Crystallographic structures of ***(a)*** Fe (BCC), ***(b)*** Ni (FCC), and ***(c)*** Co (HCP) and their corresponding magnetisation curves along their different crystal planes, ***(d)*** Fe, ***(e)*** Ni and ***(f)*** Co.

From Figure 2.15 it can be seen that the easy axis for BCC iron is <100>, for FCC Ni is <111> and for HCP Co is the <100> axis. Magnetocrystalline anisotropy arises as a direct result of spin orbit coupling. On application of an applied field the electron spin attempts to align along the direction of the applied field. Hence, as a result of the spin-orbit coupling, the orbital momentum of the electron also attempts to align along the applied field. The orbital momentum is however strongly coupled to the lattice and tries to resist the reorientation of the spin. The energy required to overcome these is referred to as the magnetocrystalline anisotropy.

In induced anisotropy an easy direction of magnetisation is manually created through means such as applied stress or atomic scale texturing of the material [1].

2.3.14 Jahn-Teller Effect

We have shown how crystal structure can impact the magnetic behaviour of a material; however it is also possible that the magnetic properties of a material can have an impact on its crystal structure. The distortion of the crystal structure of a material in order to minimize the total energy of the system is known as the Jahn-Teller effect [2]. A common example of Jahn-Teller distortion is that observed for Mn^{3+} ions in an octahedral environment (see Figure 2.16).

In this case the octahedral complex distorts as depicted in Figure 2.16, causing splitting of the e_g and t_{2g} energy levels. The e_g level is lowered in energy, which results in an overall reduction in the total energy of the system. The d_{xz} and d_{yz} levels are also lowered in energy and the d_{xy} energy level is raised. The saving in energy from lowering the d_{xz} and d_{yz} levels is exactly balanced by the energy taken to raise the d_{xy} energy level.

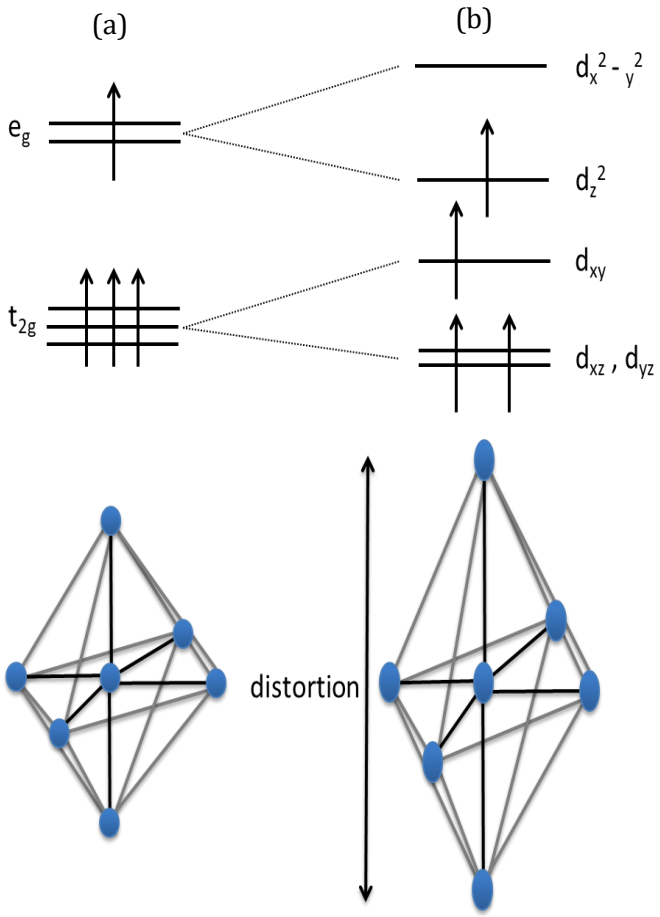

Figure 2.16: Schematic showing the distortion of octahedral crystal symmetry as a result of the Jahn-Teller effect for Mn^{3+} ($3d^4$) and corresponding shift in energy levels. An octahedral complex (a) can distort (b), thus splitting the t_{2g} and e_g levels. This distortion lowers the energy because the singly occupied e_g level is lowered in energy. The saving in energy from lowering of the d_{xz} and d_{yz} levels is exactly balanced by the raising of the d_{xy} level.

2.4 Magnetic Nanoparticles

In Chapter 4 we investigate the use of lanthanum manganese oxide magnetic nanoparticles as potential mediators in mild hyperthermia treatment. Mild hyperthermia cancer therapy is a medical treatment that involves exposing cancerous tissue to temperatures slightly above that of normal body temperature (41-46 °C) to damage or kill the cancerous cells or to enable anti-cancer drugs to work more efficiently [21]. The advantage of restricting the heating to this range is that it reduces the risk of overheating occurring and there being damage to neighbouring healthy tissue [22]. In this temperature range it is unlikely that all of the cancerous tissue will die directly as a result of the heating and hence mild hyperthermia is typically used in addition to conventional chemo- or radio therapies, helping them to work more effectively.

Many different approaches have been used to apply hyperthermia treatment to tumour regions including techniques involving lasers, ionizing radiation and microwaves. One common issue with such techniques is the harmful secondary effects due to a lack of selectivity that they can have on neighbouring tissue. In order to eradicate this issue and achieve more localised heating of the cancerous tissue the magnetocaloric effect (MCE) experienced by magnetic nanoparticles (MNPs) is commonly exploited. The MCE is a magneto-thermodynamic phenomenon in which a temperature change of a suitable material is caused by exposing the material to a changing magnetic field [23]. This temperature change can be either positive (enhanced MCE) or in some cases negative (reduced MCE) depending on the material used. For magnetic hyperthermia treatment, only materials that exhibit a positive MCE and enhanced magnetic heating are of interest.

The MCE is caused due to the varying magnetic entropy of a magnetic material in a varying magnetic field. Entropy is defined as the degree of randomness of a system and can be described by the sum of the different entropies which make up the system,

$$S_{tot} = S_c + S_T + S_e + S_m + S_d \qquad \textbf{Equation 2.45}$$

where S_{tot} is the total entropy of the system, S_c is the configuration entropy, S_T is the thermal entropy, S_e is the electronic entropy, S_m is the magnetic entropy and S_d is the dielectric entropy.

In a system which is comprised of only thermal and magnetic entropy, the total entropy of the system will be the sum of these two components.

Consider the effect of applying a magnetic field to a simple ferromagnetic material, close to the Curie temperature. On application of a DC magnetic field the electron spins within the material are forced into alignment with the applied field. This alignment means that the magnetic randomness of the system is reduced and hence there is a decrease in the magnetic entropy of the system. In order to satisfy the first law of thermodynamics, that the total energy of an isolated system is constant, the thermal entropy of the system (due to vibration of the lattice) must increase to compensate for the decrease in magnetic entropy. This can be observed by an increase in temperature. On removal of the applied field the electron spins will return to the original random alignment and the magnetic entropy will increase. In order to compensate for the increase in magnetic entropy, the thermal entropy of the system will decrease and the system will undergo a decrease in temperature. By introducing an AC magnetic field to the

system, this reordering of magnetic spins is continually enacted and the thermal entropy of the system is continually compensating for the reduction of magnetic entropy to maintain the total entropy of the system. The result of this continuous reordering of magnetic orientation is therefore an increase in temperature dependent upon the magnetic moment of the material and the frequency of the applied field.

In hyperthermia treatment the MNPs can be administered to the patient in a number of different ways, and typically directed to the target tissue using significantly strong magnetic forces. A radio-frequency alternating magnetic field is then applied close to the area containing the MNPs, initiating the MCE and localised heating in the desired area, see Figure 2.17.

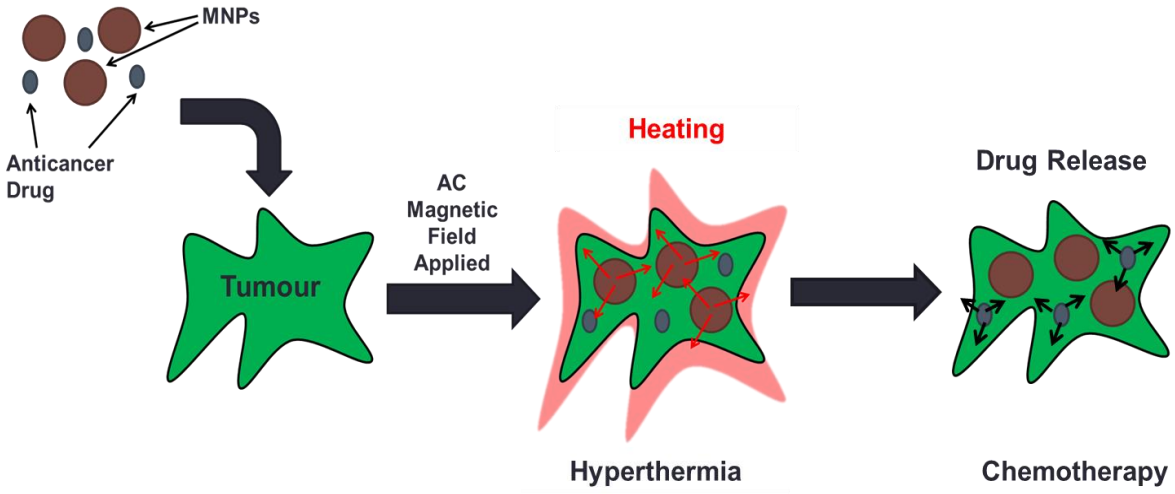

Figure 2.17: Schematic showing the use of MNPs in hyperthermia therapy. An alternating magnetic field is applied causing localised heating of cancer cells allowing anticancer drugs to act more effectively.

For MNPs to be considered for mild hyperthermia they must be biocompatible, have a low Curie temperature (T_c) and have a high specific absorption rate (SAR) [23]. The SAR is a measure of the rate of energy absorption by a material, when exposed to an electromagnetic field; therefore it can be seen as a direct reflection of the extent of MCE exhibited by a material. Another important consideration is the size of the MNP as this can also affect the extent of the MCE exhibited by the material [24]. Additionally if the MNPs are created too large and they will start to retain remnant magnetisation on the removal of the magnetic field, which is in general an undesirable property in biomedical applications. The presence of remnant magnetisation in the MNP's can lead to magnetic dipolar interactions between particles causing aggregation and clots in the bloodstream. The advantage of the MNP's having a low T_c is that once this temperature

has been reached the material will make a transition from ferromagnetic to paramagnetic essentially switching off the heating effect; this is known as self-regulating hyperthermia. This helps to prevent any overheating of the tissue from taking place.

Until very recently the vast majority of MNPs investigated for hyperthermia treatment were iron-based as these are both biocompatible and have high SARs. However iron based MNPs also tend to have very high T_c's, ranging from 280°C to 956°C, which can lead to overheating of the local tissue [25-26]. As a result there has been an increased interest in the use of perovskites in this field, as it is possible to alter their composition and as a result their magnetic properties without significantly changing the perovskite phase [27-28].

The ideal metal oxide perovskite structure is of the type ABO_3 with cubic geometry. The perovskites have a face centred cubic (FCC) lattice with the A sites located on the corners and the B sites in the centre, see Figure 2.18.

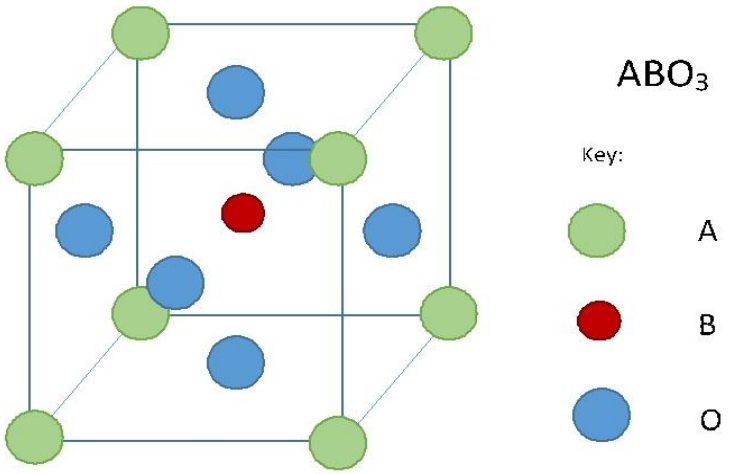

Figure 2.18: Schematic demonstrating the ABO_3 perovskite structure for potential applications in mild hyperthermia treatment

This structure can be altered by the substitution of ions with different atomic radii or valances onto the A or B sites in a process known as doping. By controlling the doping cation and dopant concentration it is possible to tune the magnetic behaviour of the perovskites to the desired properties for magnetic hyperthermia [29-30]. Tuning of the magnetic properties can also be achieved by altering the synthesis process [31]. This is investigated in Chapter 4.

2.5 Ionic Liquids

In Chapter 5 a family of lanthanide ionic liquids are synthesised and characterisation of their magnetic properties is conducted. Ionic liquids are defined as a salt with a melting point below the boiling point of water. Most ionic liquids are composed of an organic cation and inorganic anions. In order to be in liquid state at room temperature the cation needs to be bulky and unsymmetrical, i.e. the alkyl groups should be different [32].

Ionic liquids are showing increasing promise in the field of chemical synthesis. In Chapter 6, three magnetic crystals are synthesised using the ionic liquid [C_{2MIm}], 1-Ethyl-3-methyl-imidazolium acetate. In contrast to conventional solvents ionic liquids do not have significant vapour pressure and are non-volatile [33]. In terms of crystal engineering however, the most exciting thing about ionic liquids is the possibility to alter certain properties, such as polarity and hydrophilicity or hydrophobicity, by altering the combination of these anions and cations [34]. As a result ionic liquids are commonly called designer solvents as they can be altered to suit different reaction conditions. The tunability of the physical and chemical properties of the ionic liquids renders them attractive not only for their use as a reaction medium for organic reactions but also in inorganic synthesis. One of the issues which hampers the application of ionic liquids in the field of synthetic chemistry, is the difficulty to separate the ionic liquid from the reaction product. As a result of their low volatility ionic liquids cannot be removed by evaporation. Furthermore often there is an issue with the low solubility of inorganic salts in certain ionic liquids. This issue is often addressed by using task specific ionic liquids, which are ionic liquids with a functional group covalently tethered to the cationic or anionic part. A functional group that has the ability to coordinate to the metal ion (i.e. a ligand) facilitates the dissolution of metal oxides or metal salts in an ionic liquid [35].

2.6 Single Molecule Magnetism

2.6.1 Introduction to Molecular Magnetism

In Chapter 6, we investigate a trio of molecular magnets that were synthesised using ionic liquids in place of more conventional solvents. Molecular magnetism deals with the magnetic properties of isolated molecules and assemblies of molecules and as such can be described as a multidisciplinary area of research, where quantum chemists, solid state physicists and material scientists come together to design, synthesise, characterise and utilise molecular systems with new and ideally predictable magnetic properties [36].

Traditionally magnetic materials have been prepared from substances that are essentially the products of inorganic chemistry. However in the late 1970s the discovery of organic matter exhibiting metal like conducting properties led to increased interest in the utilization of organic molecules [2]. Unlike inorganic matter, the rich carbon structure of organic molecules makes them reasonably tuneable. It is possible to make small adjustments to each molecule making it theoretically conceivable that such molecular compounds could be 'tailor made' to exhibit desired magnetic properties. Although it is possible to achieve fully organic magnets [37], i.e. magnetic molecules composed of purely organic elements, there is a limited selection of the organic free radicals required to attain a metallic moment on an organic compound which are stable enough to be assembled into crystalline structures. Additionally in general these magnets exhibit a transition temperature of less than 2K, which ultimately limits any practical applications [38-39].

In an attempt to resolve this issue, molecular magnets were proposed, were a transition metal ion would be used to provide the localised magnetic moment in place of an organic free radical. Organic molecules would be employed to act as exchange pathways, linking these metallic ions together and forming organic/inorganic molecular clusters exhibiting interesting metallic properties. It was stemming from this basic principle that the first single molecule magnet (SMM) was fabricated in 1993 [40]. In comparison to conventional molecular magnets, which display either ferromagnetic or ferrimagnetic behaviour below a specific critical temperature, SMMs are essentially superparamagnetic, i.e. below a time, or frequency dependent blocking temperature, the linear magnetic response freezes and the magnetization shows hysteresis [41]. Contrary to traditional molecule-based magnets, SMMs exhibit magnetic hysteresis of purely molecular origin and collective long-range ordering of magnetic moments is not necessary. This proves to be an attractive quality for potential applications in the storage and processing of digital information [42]. In recent years the constant desire for device miniaturization coupled with increased digital information storage has resulted in a high demand for the production of smaller and smaller identical magnets. As traditional approaches of nano-scaling bulk magnetic material rapidly approach the superparamagnetic limit [43], SMMs, which are essentially molecular analogues of traditional bulk magnets, pose a promising alternative solution. Unfortunately, thus far, SMMs generally exhibit blocking temperatures in the 2-5K range meaning their potential in this field can only be realised using liquid helium cooling [44]. As a result either the operation temperature of the molecules must increase or applications so novel arise that temperature ceases to be an issue. Hence, currently, the main drive in SMM research is the design and fabrication of molecules which can operate at room temperature. Other potential applications of SMMs include use in molecule based spintronic devices [45] and the

exciting new field of quantum computing [46]. Perhaps even more importantly however, as the first materials to provide unambiguous evidence of quantum size magnetic effects in metals [47], SMMs can be exploited as a means of furthering our understanding of the complexities of magnetism at a quantum level. Furthermore they may provide us with the knowledge to postulate why specific behaviour is exhibited in more complex magnetic structures.

2.6.2 Single Molecule Magnets

SMMs can be defined as paramagnetic molecules, which below a blocking temperature will exhibit magnetic behaviour of intrinsically molecular origin in the absence of a magnetic order [48]. Unlike bulk magnetic materials, where the magnetic response comes from domains where the spins on a large number of metallic sites are correlated, in SMMs the magnetic response stems directly from intrinsic properties of the electronic structure of the molecule itself [49].

In general SMMs are composed of paramagnetic transition metal ions connected by intervening ligand donor atoms [50]. These metallic ions are coupled to one another via superexchange interactions. The overall magnetic properties of the cluster are described by the sum of all the individual spins of the composite metal ions – referred to as the total spin quantum number of the ground state (S). A requirement for SMM behaviour is the presence of $S \geq 1$, in order for the molecule to exhibit zero-field splitting (ZFS) of the ground state [51]. ZFS, removes the degeneracy of the M_s levels of the ground state in the absence of a magnetic field (first order Zeeman effect). It arises as a result of coupling of the ground state with the excited states via spin-orbit coupling. ZFS is a vital requirement in SMMs as it causes a single-ion anisotropy, which ultimately results in magnetic bistability, i.e. the magnetic moment has two stable orientations antiparallel to one another, separated by an energy barrier [52]. This gives rise to superparamagnetic behaviour analogues to that of singular domain nano magnets [53].

The following Hamiltonian mathematically describes the effect of zero field splitting parameters D and E of the magnetic behaviour of an SMM [54],

$$\hat{\mathrm{H}} = DS_z^2 + E\,(S_x^2 - S_y^2) \qquad \textbf{Equation 2.46}$$

where D represents the axial zero field splitting parameter and E represents the rhombic zero field splitting parameter.

In SMMs the sign of D is a determining factor as it describes the essential type of magnetic anisotropy associated with the S state required for SMM behaviour [55]. A positive sign implies that the $M_s = 0$ level will be of the lowest energy in the system. As a result there is no energy cost in losing direction of spin, i.e. moving from spin S=10 to S=0, and the magnetic relaxation of the system would be incredibly fast. A negative sign however implies the $M_s = \pm S$ state with the largest component of the spin vector along the quantization axis will be most stable – hence there will be a slow magnetic relaxation. This is an essential requirement for SMM behaviour.

Consider the specific situation where S=10 (see Figure 2.19) [56].

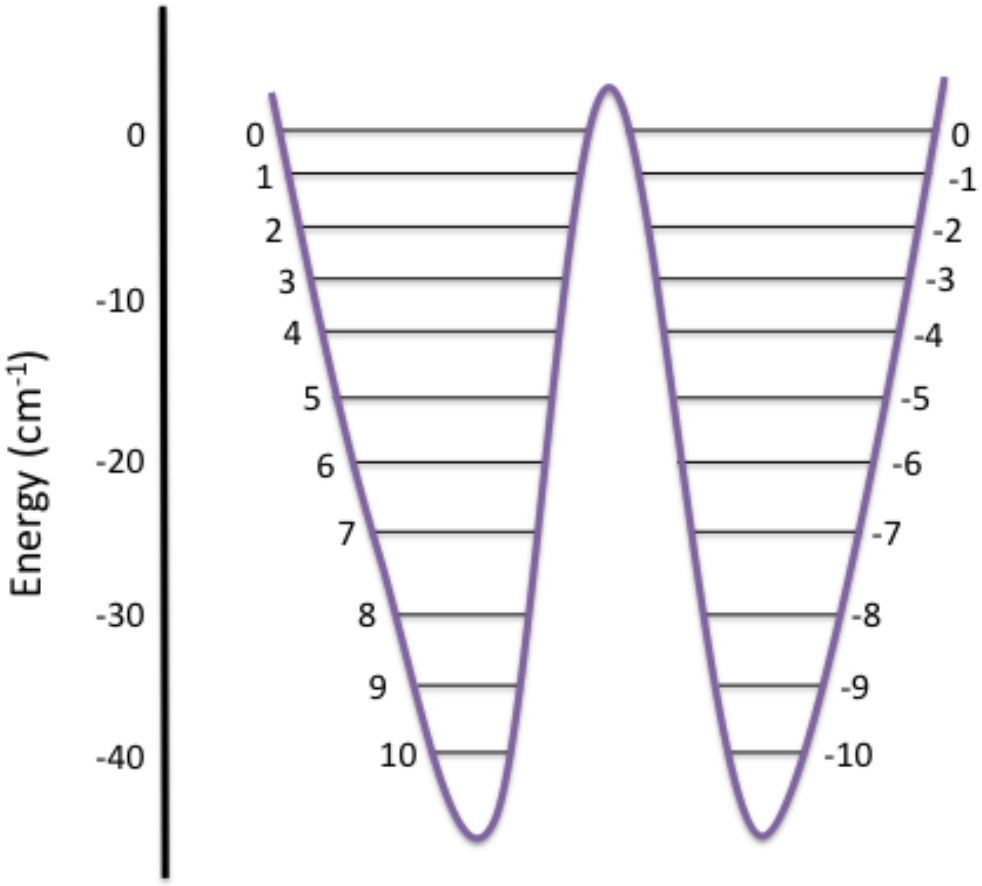

Figure 2.19: Energy of a classical S=10 magnetic moment as a function of the angle between the moment and the main anisotropy axis. The horizontal lines represent the spin microstates belonging to the S=10 multiplet.

The negative axial zero field splitting together with the selection rule of $\Delta M_s = \pm 1$ for allowed transitions, results in an energy barrier, ΔE, separating the two lowest energy levels of $M_s = \pm 10$. In general the ΔE is proportional to S^2D (for integer spin) or $(S^2 - ¼)D$ (for half integer spin) [57]. On application of a magnetic field either the positive or negative M_s levels will be stabilised

and thereby selectively populated due to the Zeeman energy. If the magnetisation of the system reaches its saturation value, then only the $M_s = \pm S$ level will be populated. On reversal of the field the system will return to thermal equilibrium in a series of steps, such as those depicted in Figure 2.19, hence, theoretically the larger the intrinsic energy barrier the larger the relaxation time of the magnetisation. This fact coupled with the desire for a room temperature blocking temperature drives current SMM research resulting in the desire to create complexes exhibiting high spin ground states with a large negative zero field splitting [56].

2.6.3 Quantum Effects in SMMs

In terms of the development of scientific understanding, one of the most important results obtained from SMM research was the experimental observation of theoretically predicted macroscopic quantum tunnelling (MQT) between the different states of magnetization in the molecule. From this the relaxation dynamics of magnetic moments in SMM systems could be derived. The MQT effect was first observed in the molecule $[Mn_{12}O_{12}(O_2CCH_3)_{16}(H_2O)_4].4H_2O_2CH_3CO_2H]$ (Mn_{12}-acetate), in 1993 [58]. As can be observed in Figure 2.20, the hysteresis loop of this molecule is not smooth and instead shows stepping at regular intervals along the magnetisation against applied field plot. The observed steps in the hysteresis loop correspond to an increase in the rate of change of magnetization occurring and have since been attributed to thermally assisted quantum tunnelling of the magnetisation.

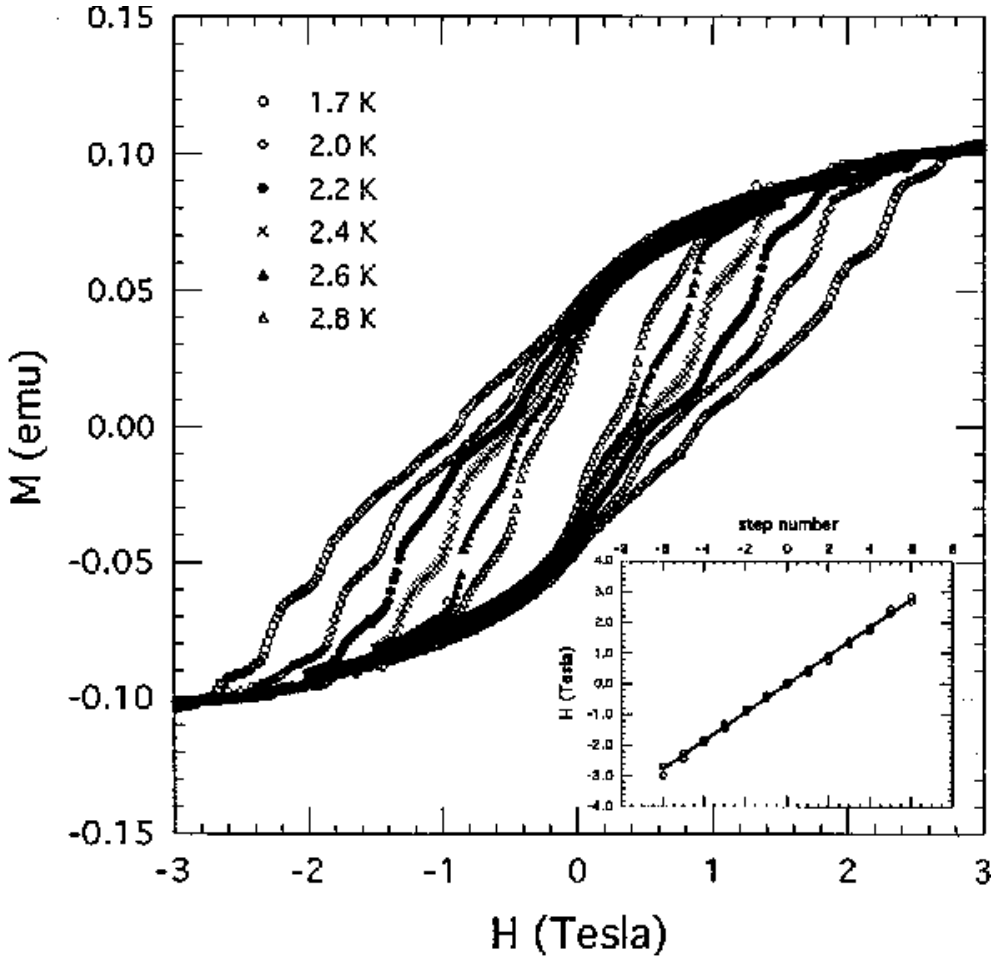

Figure 2.20: Magnetisation of Mn_{12} as a function of magnetic field at six different temperatures. The inset shows the field at which steps occur versus step number. Taken from reference 58.

The magnetic bistability of SMMs means that they can theoretically be modelled as two potential wells, separated by a potential barrier. Consider an electron existing in one of the two wells. The wavefunction associated with this electron can extend over both wells, in which case the probability of observing it in both wells at the same time is non-zero. As such the position of the electron must be described by a superposition of both states, as it is possible for the particle to be in both the right and left hand well. Provided there is some form of admixing of the wavefunctions associated with the two energy states in question the electron can pass from one to the other without climbing the potential barrier; it can quantum tunnel between the two states [57].

Again consider the example where S = ±10, see Figure 2.19 [56]. In order for quantum tunnelling to occur in SMMs it is a requirement that two or more of the M_s levels in neighbouring wells are in resonant alignment, in order for admixing of the states. For an applied field of H=0, as shown

in Figure 2.19, each of the positive M_s levels is in perfect alignment with its corresponding negative M_s level, and as such the resonance condition is fulfilled and quantum tunnelling can be observed. As previously described, on the application of an applied field either the positive or negative M_s levels will be favoured depending on the direction of the field. As the strength of the field is increased the energy levels will shift, with one side of the well shifting up and the opposite shifting down, until the potential energy barrier disappears. At regular intervals during this process, corresponding to the number of M_s levels in the systems, the resonance condition for quantum tunnelling will be satisfied, i.e. S = +10 will align with S = -9, then S = -8 and so on. At these points quantum tunnelling between states can take place and an increased rate of change of magnetisation can be observed. As such hysteresis loops can be used to map the number of M_s energy levels of the ground state.

Quantum tunnelling is not always observed between all pairs of adjacent energy levels in a system; in particular it is less common to see the effect between the lower, more stable levels [42]. As the value of M_s increases the overlap of the wavefunctions of the two states becomes less and as a result so too does the tunnelling rate. This effect can be observed in the hysteresis loop of Mn_{12}-acetate, Figure 2.20, where there is no direct evidence of tunnelling between the $M_s = \pm 10$, at H = 0, whilst tunnelling between higher-energy M_s states is observed by steps in the hysteresis loop at increasing applied field [58]. As a result, much of the loss of magnetisation in this particular complex is as a result of thermally assisted tunnelling. The first evidence of quantum tunnelling between the lowest energy M_s states of a system did not actually come until 7 years after initial observation of QMT, when it was shown to occur in the Fe_8 complex by D. Gatteschi et al [59].

References

[1] Coey, J. M. D., "Magnetism and Magnetic Materials", (2010), *Cambridge University Press*

[2] Blundell, S., "Magnetism in Condensed Matter", (2001), *Oxford Master Series in Condensed Matter Physics, Oxford University Press*

[3] Moskowitz, B. M., "Fundamental Physical Constants and Conversion Factors", (1970), *American Geophysical Union*, 5-8

[4] Oersted, H. C., "Experiment on the effect of a Current of Electricity on the Magnetic Needle", (1820), *Annals of Philosophy*, Vol **16**, 273-276

[5] Hall, G., "Maxwell's electromagnetic theory and special relativity", (2008), Philosophical *Transactions of the Royal Society A*, Vol **366**, 1849-1860

[6] Niven, W. D., "The scientific papers of James Clerk Maxwell", (1965), *New York, NY: Dover Publications, Inc*

[7] Faraday, M., "Experimental researches in electricity", (1839), *London, R. and J. E. Taylor*, Vol **1**

[8] Maxwell, J. C., "A treatise on electricity and magnetism", (1873), *Oxford: Clarendon Press*, Vol **1**

[9] Erlichson, H., "The experiments of Biot and Savart concerning the force exerted by a current on a magnetic needle", (1998), *American Journal of Physics*, Vol **66**, 385

[10] Weinberger, P., "Revisiting Louis de Broglie's famous 1924 paper in the Philosophical Magazine", (2006), *Philosophical Magazine Letters*, Vol **86**, 7, 405-410

[11] Schrödinger, E., "An Undulatory Theory of the Mechanics of Atoms and Molecules", (2008), *Physical Review*, Vol **28**, 6, 1049-1070

[12] Styer, D. F., Balkin, M. S., Becker, K. M., Burns, M. R., Dudley, C. E., Forth, S. T., Gaumer, J. S., Kramer, M. A., Oertel, D. C., Park, L. H., Rinkoski, M. T., Smith, C. T., and Wotherspoon, T. D., "Nine formulations of quantum mechanics", (2002), *American Journal of Physics*, Vol **70**, 3

[13] Dirac, P. A. M., "The Quantum Theory of the Electron", (1928), *Proceedings of the Royal Society A*, Vol **117**, 778, 610-624

[14] Aoyama, T., Hayakawa, M., Kinoshita, T., and Makiko, N., "Tenth-Order QED Contribution to the Electron g-2 and an Improved Value of the Fine Structure Constant", (2012), *Physical Review Letters*, Vol **109**, 1118078

[15] Cullity, B., and Graham, C., "Introduction to Magnetic Materials", (2009), *IEEE Press*

[16] Vonsovkii, S. V., "Physical Encyclopedia: Superparamagnetism", (1966), *Nauka, Moscow*, Vol **5**

[17] Kurti, N., "Selected Works of Louis Néel", (1988), *Gordon and Breach Science Publishers,* 407-427

[18] Delft, D., and Kes, P., "The discovery of superconductivity", (2010), *American Institute of Physics*

[19] Bardeen, J., Cooper, L. N., and Schrieffer, J. R., "Theory of Superconductivity", (1957), *Physical Review*, Vol **108**, 5

[20] Weiss, P., "L'hypthèse du chemp moléculaire et la propriété ferromagnétique", (1907), *Jounal de Physique*, Vol **6**, 1, 661-690

[21] Storm, F. K., Harrison, W., Elliott, R. S., Kaiser, L. R., Silberman, A. W., and Morton, D. L., "Clinical Radiofrequency Hyperthermai by Magnet-Loop Induction", (1981), *Journal of Microwave Power*, Vol **16**, 179-184.

[22] Landeghem, F. K. H., Maier-Hauff, K., Jordan, A., Hoffmann, K., Gneveckow, U., Scholz, R., Theisen, B., Brück, W., and Deimling, A., "Post-mortem studies in glioblastoma patients treated with thermotherapy using magnetic nanoparticles", (2009), *Biomaterials*, **30**, 52-56

[23] Kuznetsov, O. A., Sorokina, O. N., Leontiev, V. G., Shlyakhtin, O. A., Kovarski, A. L., and Kuznetsov, A. A., "ESR study of thermal demagnetization processes in ferromagnetic nanoparticles with Curie temperatures (T_c) 40-60^{o}C", (2007), *Journal of Magnetisation and Magnetic Materials*, Vol **311**, 204-207

[24] Mathew, S. P., and Kaul, S. N., "Tuning magnetocaloric effect with nanocrystalline size", (2011), *Applied Physics Letters*, Vol **98**, 172505

[25] Teja, A. S., and Koh, P., "Synthesis, properties, and application of magnetic iron oxide nanoparticles", (2009), *Progress in Crystal Growth and Characterization of Materials*, Vol **55**, 1-2, 22-45

[26] Apostolova, L., and Wesselinowa, J. M., (2009), "Possible low-T_c nanoparticles for use in magnetic hyperthermia treatments", *Solid State Communications*, Vol **149**, 986-990

[27] Prasad, N. K., Hardel, L., Dubuet, E., and Bahadur, D., "Magnetic hyperthermia with biphasic gel of $La_{1-x}Sr_xMnO_3$ and maghemite", (2009), *Journal of Magnetisation and Magnetic Materials*, Vol **321**, 1490-1492

[28] Pollert, E., Veverka, P., Veverka, M., Kaman, O., Záveta, K., Vasseur, S., Epherre, R., Goglio, G., and Duguet, E., "Search of new core materials for magnetic fluid hyperthermia: Preliminary chemical physical issues", (2009), *Progress in Solid State Chemistry*, Vol **37**, 1, 1-14

[29] Epherre, R., Pepin, C., Penin, N., Duguet, E., Mornet, S., Pollert, E., and Goglio, G., "Evidence of non-stoichiometry effects in nanometric manganite perovskites: influence on the magnetic ordering temperature", (2011), *Journal of materials Chemistry*, Vol **21**, 14990-14998

[30] Natividad, E., Castro, M., Goglio, G., Andreu, I., Epherre, R., Duguet, E., and Mediano, A., "New insights into the heating mechanism and self-regulating abilities of manganite perovskite nanoparticles suitable for magnetic fluid hyperthermia", (2012), *Nanoscale*, Vol **4**, 3954-3962

[31] Gaur, A., and Varma G. D., "Sintering temperature effect on electrical transport and magnetoresistance of nanophasic La0.7Sr0.3MnO3", (2006), *Journal of Physics: Condensed Matter,* Vol **18**, 39

[32] Wasserscheid, P., Keim, W., "Ionic Liquids – New "Solutions" for Transition Metal Catalysis", (2000), *Angewandte Chemie International Edition*, Vol **39**, 21

[33] Olivier-Bourbigou, H., Magna, L., and Morvan, D., "Ionic liquids and catalysis: Recent progress from knowledge to applications", (2010), *Applied Catalysis A: General*, Vol **373**, 1-2

[34] Taubert, A., "CuCl nanoplatelets from an ionic liquid-crystal precursor", (2004), *Angewandte Chemie International Edition,* Vol **43**, 5380-5382

[35] Caibo, Y., Dong, F., Lin, L., and Ting-Feng, Y., "Synthesis and application of task-specific ionic liquids used as catalysts and/or solvents in organic unit reactions", (2011), *Journal of Molecular Liquids*, Vol **163**, 3, 99-121

[36] Kahn, O., "Molecular Magnetism", (1993), *Wiley-Blackwell*

[37] Brook, D, J, R., "Magnetic Properties of Organic Materials", (1999), *Journal of the American Chemical Society*, Vol **122**, 14, 3566

[38] Chairelli, R., Novak, M, A., Rassat, A., and Tholence, J. L., "A ferromagneric transition at 1.48K in an organic nitroxide", (1993), *Nature*, Vol **363**, 147-149

[39]Veciana, J., Cirujeda, J., Rovira, C., and Vidal-Gancedo, J., "Ferromagnetic interactions in organic/molecular materials", (1995), *Advanced Materials*, Vol **7**, 2, 221-225

[40] Sessoli, R., Gatteschi, D., Canschi, A., and Novak, M, A., "Magnetic bistability in a metal-ion cluster", (1993), *Nature*, Vol **365**, 141-143

[41] Oshio, H., Hoshino, N., and Ito, T., "Superparamagnetic behaviour in an alkoxo-bridges iron (11) cube", (2000), *Journal of the American Chemical Society,* Vol **122**, 12602-12603

[42] Christou, G., Gatteschi, D., Hendrickson, N., and Sessoli, R., "Single Molecule Magnets", (2000), *MRS Bulletin*, Vol **25**, 11, 66-71

[43] Affronte, M., "Molecular nanomagnets for information technologies", (2009), *Journal of materials chemistry*, Vol **19**, 1731-1737

[44] Murrie, M., "Cobalt (11) single-molecule magnets", (2010), *Chemical society reviews*, Vol **39**, 1986-1995

[45] Bogani, L., and Wernsdorfer, W., "Molecular spintronics using single-molecule magnets", (2002), *Nature*, Vol **416**, 406-409

[46] Wernsdorfer, W., Aliaga-Alcalde, N., Hendrickson, D., and Christou, G., "Exchange-biased quantum tunnelling in a supramolecular dimer of single-molecule magnets", (2002) *Nature*, Vol **416**, 406-409

[47] Thomas, L., Lionti, F., Ballou, R., Gatteschi, D., Sessoli, R., and Barbara, B., "Macroscopic quantum tunnelling of magnetisation in a single crystal of nanomagnets", (1996), *Nature*, Vol **383**, 145-147

[48] Pedersen, K. S., Bendix, J., and Clerac, R., "Single-molecule magnet engineering: building-block approaches", (2014), *Chemical Communications*, Vol **50**, 4396-4415

[49] Dunbar, K., "Quantum molecular magnets", (2012), *Inorganic Chemistry*, Vol **21**, 12055-12058

[50] Que, L., "Physical methods in bioinorganic chemistry: spectroscopy and magnetism", (2000), *University science books*, 345-348

[51] Collison, D., Organesvan, V., Piligkos, S., Thomson, A., Winpenny, R., and McInnes, E., "Optical determination of the single-ion zero-field splitting in large spin clusters", (2003), *Journal of the American Chemical Society,* Vol **125**, 5, 1168-1169

[52] Barbara, B., Imry, Y., Sawatzky, G., and Stamp, P., "Quantum magnetism", (2008), *Springer*, 126

[53] Kittel, C., "Theory of the structure of ferromagnetic domains in films and small particles", (1946), *Physical Reviews*, Vol **70**, 965

[54] Nakamura, H., "Dynamics of molecules and chemical reactions", (1996), *Marcel Dekker, New York*

[55] Bagai, R., and Christou, G., "The Drosophila of single-molecule magnetism $[Mn_{12}O_{12}(O_2CR)_{16}(H_2O)_4]$", (2008), *Chemical Society Reviews*, Vol **38**, 1011-1026

[56] Yang, P., "Chemistry of Nanostructured Materials", (2003), *World Scientific Publishing*, Hong Kong

[57] Gatteschi, D., and Sessoli, R., "Quantum tunnelling of magnetisation and related phenomena in molecular materials", (2003), *Angewandte Chemie International Edition,* Vol **42**, 3

[58] Friedman, R., and Sarachik, "Macroscopic measurement of resonant magnetisation tunnelling in high-spin molecules", (1996), *Physical Review Letters*, Vol **79**, 6031

[59] Gatteschi, D., Sessoli, R., and Cornia, A., "Single-molecule magnets based on iron(111) oxo clusters", (2000), *Chemical communications*, **0**, 725-732

Chapter 3

Experimental Techniques

3.1. Outline

In this chapter the experimental techniques adopted for the magnetic analysis conducted throughout this thesis are outlined. Due to the fundamental role of SQUID magnetometry in this study, the instrument is briefly introduced at the start of this chapter. The basic fundamental principles of the instrument are covered along with some of the different types of measurements, which can be conducted using the instrument. Some of the experimental considerations, which must be taken into account when conducting magnetic analysis using SQUID magnetometry, are also discussed in this chapter. These include the physical considerations, which must be considered when choosing an appropriate sample holder and also the appropriate application of magnetic corrections for both background signals and sample specific diamagnetic responses. Finally the two magnetic fitting programs, PHI and ANISOFIT 2.0, which were used in this thesis, are also briefly discussed.

3.2 SQUID Techniques

3.2.1. Introduction to the SQUID

This thesis is concerned with the magnetic behaviour of a variety of different materials, on a bulk, molecular and atomic scale. As such, care had to be taken when choosing a suitable magnetic sensor to gather data. There are numerous experimental instruments commercially available which typically gather data through the detection of either magnetic fields or magnetic flux [1]. Each device is generally specialised to detect a specific magnetic property and as such the instrument used in a given experiment is dependent on the information we want to learn about a particular sample. Table 3.1 outlines some key magnetic properties and the corresponding experimental instruments which can be employed to measure these properties.

Magnetic Property	Description	Measurement Method
Intrinsic Coercivity	Measure of a magnet's resistance to de-magnetization	Hysteresisgraph, Vibrating sample magnetometer (VSM) and Super conducting quantum interference device (SQUID) magnetometer
Magnetic Flux	Measure of magnetic output; related to magnetic moment	Helmholtz or Search Coil and Fluxmeter
Magnetic Field Strength, flux density	Measure of the magnetic (flux) output per unit area	Gaussmeter (Hall element or Nuclear magnetic resonance (NMR))
Reversible Temperature Coefficients	Indicate how the magnetic characteristics change with temperature	Hysteresisgraph, VSM or SQUID magnetometer
Field Distribution	Measure of the distribution of the flux	Magnetic Field Scanners; Gauss probe and meter and x-y-z and/or rotational stage

Table 3.1: Key magnetic properties and corresponding methods of measurement. Taken from reference 2.

In each section of this thesis the samples response to changes in temperature is of particular interest. As such the three most appropriate instruments for magnetic measurement were the Hysteresisgraph, VSM and SQUID magnetometer.

A Hysteresisgraph is an automatic system for characterization of hard magnetic materials where a magnetic field is applied to a test sample in a closed magnetic circuit. The sample is positioned alongside a sensory pickup coil, inside an electromagnet air gap, which is used to generate the applied field. When the sample is introduced into the air gap the poles of the electromagnet are adjusted to close the gap and form a closed magnetic circuit. The pick up coil measures the flux from the sample whilst two outer coils in series opposition measure the applied field surrounding the sample. This information is fed into a feedback loop which processes these signals to determine the total flux generated by the sample [3]. Measurements in a Hysteresisgraph can generally be performed at temperatures ranging from ambient up to 220 °C under applied fields of up to 3.2T [3-4]. There is a lower limit on the coerecivity detectable by a Hysteresisgraph of around 25-50Oe, meaning these instruments are not suitable for measuring soft magnetic materials [2].

Similarly to a Hysteresisgraph, a VSM detects changes in the magnetic flux of the sample material. The sample is mounted onto a rod which is attached to an oscillator in a region of space between two poles of a large electromagnet. A magnetic field is applied to the sample by means of the electromagnet and a magnetic flux is generated in the sample. The sample is then vibrated at a set frequency and an electromotive force (EMF) is induced in pick up coils which are located on the poles of the electromagnet. This signal is finally processed to determine the magnetic response of the sample [5]. A typical VSM operates in the temperature range 4.2K – 1,273K, however cryogenic VSM's also exist which can operate at temperatures as low as 1.6K [6-7]. The electromagnets used in VSM's can typically generate fields up to around 3.5T and commercially available instruments have the ability of achieving resolutions of around 10^{-7} T [6]. Unlike a Hysteresisgraph, VSM measurements are not conducted in a closed circuit and a correction for the self-demagnetising stress internal to the magnet must be applied, introducing an additional variable and potential source of error.

The sensor primarily used in this thesis was a SQUID magnetometer, which is the most sensitive instrument commercially available for measuring magnetic flux with the ability of achieving resolutions of 10^{-17} T or better [8-9]. As with both the VSM and Hysteresisgraph, the SQUID magnetometer uses a pick up coil to detect changes in magnetic flux in the sample upon application of an applied field. However in addition SQUID magnetometry exploits the quantum mechanical effects in Josephson junctions to detect very small changes in the magnetic flux of

the sample. The measurement process of the SQUID magnetometer is described in detail in the following section (section 3.2.1.). A typical SQUID magnetometer can operate in the temperature range 1.8-330K and apply a field of up to 7T [9]. However sample ovens can be added to the equipment which can allow for temperatures up to 700K to be achieved [10]. The main disadvantage of using a SQUID magnetometer is the running cost of the instrument. Typically a single temperature or field strength scan can take up to several hours, which results in the consumption of a large amount of liquid helium, an expensive commodity.

For the purpose of this thesis the SQUID magnetometer was deemed the most appropriate piece of experimental equipment for a number of reasons. The majority of the samples measured, in particular the paramagnetic ionic liquids in Chapter 5, had a relatively low magnetic signal ($x10^{-5}$ emu) which would not have been detected by either a Hysteresisgraph or a VSM. Additionally for the magnetic crystal samples investigated in Chapter 6, the magnetic response at low temperatures and high applied fields was of particular interest, neither of which could be achieved using a Hysteresisgraph. Although low temperatures could be achieved using a VSM, the maximum applied field (around 3.5T) was insufficient for these purposes. Finally the chemical composition of the samples measured in this thesis made them unsuitable for VSM measurement. The hydrophilic nature of the magnetic crystal samples, the liquid state of the ionic liquids and the powdered composition of the magnetic nanoparticles necessitated the use of an isolation vessel (peek capsule) which is not compatible with the VSM.

3.2.2. Squid Theory

Contrary to its name, the Super Conducting Quantum Interference Device (SQUID) magnetometer does not directly measure the magnetic moment of the sample and is in fact an extraction magnetometer [11]. In order to allow for the application of large magnetic fields and a wide range of temperatures, a very sophisticated system of superconducting pick up coils and wires is adopted to transfer a current signal from the sample to the SQUID detector (see Figure 3.2). The magnetized specimen is moved up and down through superconducting pick up coils; known as flux transformers, which are located outside of the sample chamber [12]. The change in magnetic flux generated by the sample motion induces a current to flow within the pick up coils. The current is then carried along superconducting wires to the SQUID input coil [13]. As the pick up coils, superconducting wires and SQUID input coil are all part of a closed system, the current received at the SQUID is directly proportional to the change in magnetic flux generated by the sample. The SQUID sensor itself is located in a protected environment, generally a niobium shield immersed in liquid helium, away from the sample chamber [12]. The beauty of having the

sample chamber isolated from the superconducting network is that the conditions within the sample chamber can be changed as desired without the limitations inflicted by superconducting materials. For example the sample chamber can be heated to temperatures well above the critical temperature of the superconducting components (9.3K) and large fields of the same magnitude as the critical field of the superconducting wires (24.5T) can be applied [14].

The SQUID input coil couples the current carried from the flux transformer into a superconducting ring such as the one shown in Figure 3.1. This superconducting ring will contain one or more 'weak links'; very thin resistive regions called Josephson Junctions, depending on whether the SQUID utilizes direct current (two junctions) or alternating current (one junction) [15].

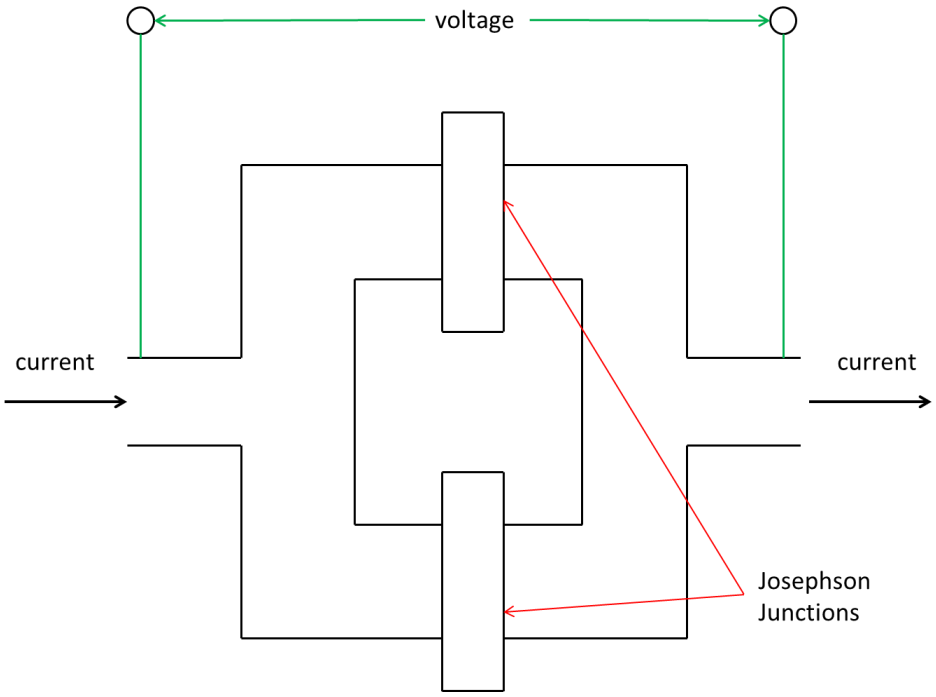

Figure 3.1: Superconducting quantum interference device (SQUID) as a simple magnetometer.

As detailed earlier in section 2.1, current travels through a superconductor in the form of Cooper pairs [16]. If you consider a current travelling along the superconducting ring detailed in Figure 3.1, one might expect the wave function of the Cooper pairs to quickly decay across the 'weak links' preventing the flow of any further current. However in 1962 Josephson predicted the possibility of electrons tunnelling through such a barrier, travelling from one

superconducting region to another [17]. In fact it was proven that when the 'weak link' is smaller in thickness than the coherence length of the superconducting material and the current flowing is less than a particular critical current I_c characteristic of the weak link, cooper pairs can tunnel across a resistive barrier and the superconducting current can penetrate the resistive barrier without a detectable drop in voltage [18]. This phenomenon is exploited in SQUID magnetometry.

Again consider the superconducting ring shown in Figure 3.1. If the material is initially in an applied field and then the temperature is lowered below the critical temperature, the magnetic field will be expelled from the superconducting loop, however it will still be present in the hole at the center of the loop. When the applied field is removed the field trapped at the center of the loop will remain and be maintained by a current (I_s) flowing along the inner surface of the loop. It can be proven that this circulating current (I_s), and hence the magnetic flux contained at the center of the loop is quantized as outlined below [19].

Consider the momentum (p) of a cooper pair, expressed quantum mechanically, as it moves around the superconducting ring. It can be expressed by the following equation,

$$p = \hbar(\nabla\theta) = e^{*}\Lambda J + e^{*}A \qquad \textbf{Equation 3.1}$$

where $e^{*}$is the charge of the Cooper pair, m is the mass of the Cooper pair, J is the Cooper pair current density, ħ is Planck's constant A is the vector potential of the magnetic field generated and $\Lambda = \frac{m_e}{n_s e^2}$, where m_e is the electron mass, e is the electron charge and n_s is the number of electrons per cm^3.

Integration along a complete superconducting loop gives,

$$\hbar \oint \nabla\theta \; . \; dl = e^{*} \oint (\Lambda J + A) \cdot dl \qquad \textbf{Equation 3.2}$$

As the phase must be coherent around the loop, then we can conclude $\oint \nabla\theta \cdot dl = 2\pi n$, where n = 1, 2, 3…. Deep inside the superconductor J ≈ 0, therefore at this position we can rearrange the right side of the equation using Stokes' theorem to give,

$$\oint_c A \cdot dl = \int_s (\nabla x A) \cdot ds = \int_s B \cdot ds = \Phi \qquad \textbf{Equation 3.3}$$

Equating the right and left hand side of the equation gives,

$$2\pi n\hbar = e^*\Phi \rightarrow \Phi = n\Phi_o \qquad \textbf{Equation 3.4}$$

with $\Phi_o = \frac{h}{e^*}$

showing that the magnetic flux is quantized.

This phenomenon was experimentally confirmed by R. Turton through the investigation of a superconducting ring with a circumference of several meters [20].

AC and DC SQUID magnetometers operate slightly differently, as outlined below. The SQUID sensor in a DC SQUID magnetometer is comprised of a superconducting ring with two Josephson junctions such as the one depicted in Figure 3.1. As mentioned earlier these junctions will have a critical current, I_c, which is much smaller in magnitude than the critical current of the ring as a whole [21]. Accordingly there is a very low current density within the ring and the cooper pairs possess a small momentum and consequentially a large wavelength. This results in there being little difference in the phase of the cooper pairs throughout the superconducting ring. If a magnetic field is applied perpendicular to the plane of the ring then a phase difference will be introduced at the 'weak links' [22]. As the SQUID sensor in a DC SQUID contains two Josephson Junctions a phase difference will be introduced at both of these points in the superconducting loop. When the magnetic flux through the loop is equal to 0, Φ_o, $2\Phi_o$ etc, then the phase difference introduced at each junction will be the same and result in constructive interference. Alternatively when the magnetic flux is $\frac{\Phi_o}{2}$, $\frac{3\Phi_o}{2}$ and so on, then an opposite phase difference will be introduced at each of the junctions and destructive interference will occur [23]. In order to satisfy the condition that the magnetic flux that passes through the superconducting loop is always a multiple of Φ_o, as outlined earlier, the superconducting current within the ring will vary accordingly to compensate [24]. As such it is possible to measure extremely weak magnetic fields through the detection of changes in quantums of flux via monitoring the current flowing in the superconducting loop. In DC SQUID magnetometry this is monitored by measuring the change in voltage across the junction as a function of the total current flowing through the device. This is then modulated and fitted to in order to derive a magnetic moment [25]. In an AC

SQUID magnetometer the SQUID sensor is comprised of a superconducting ring, which has only one Josephson junction [26-28]. An oscillating external flux is applied to the superconducting loop, which is inductively coupled to an LC tank circuit driven by an RF current. The magnetic flux from the specimen being measured is carried to a coil, which is positioned at the center of the ring. When the flux carried from the sample is significantly less than $n\Phi_o$, then the AC applied flux can be chosen to be such that there is no transition from one flux state to another, however if the flux from the sample is much larger than $\left(n + \frac{1}{2}\right)\Phi_o$ then the AC flux will enough that the SQUID will make internal flux state transition [24]. These transitions trace out a loop of energy, which is drawn from the tank circuit and a drop in the RF voltage amplitude can be observed. This signal can be interpreted using a negative feedback loop, to give the magnetic signal generated by the sample [9].

Although ultimately both AC and DC SQUID magnetometers detect changes in the magnetic flux of the sample, the main discrepancy in the two devices arises from the fact that magnetic materials respond differently to DC and AC fields. Static magnetic responses can be investigated using a DC SQUID magnetometer whereas dynamic responses can be investigated using an AC SQUID magnetometer. AC SQUID magnetometers are particularly useful when investigating the magnetic relaxation of a material, from one magnetization state to another.

3.2.3. Sample Mounting

In this thesis a MMPS Quantum Design SQUID magnetometer is used. As with many commercial SQUIDs, this particular SQUID magnetometer uses a second order gradiometer coil set up, whereby each of the detection coils has an equal number of turns in each direction (see Figure 3.2) [29].

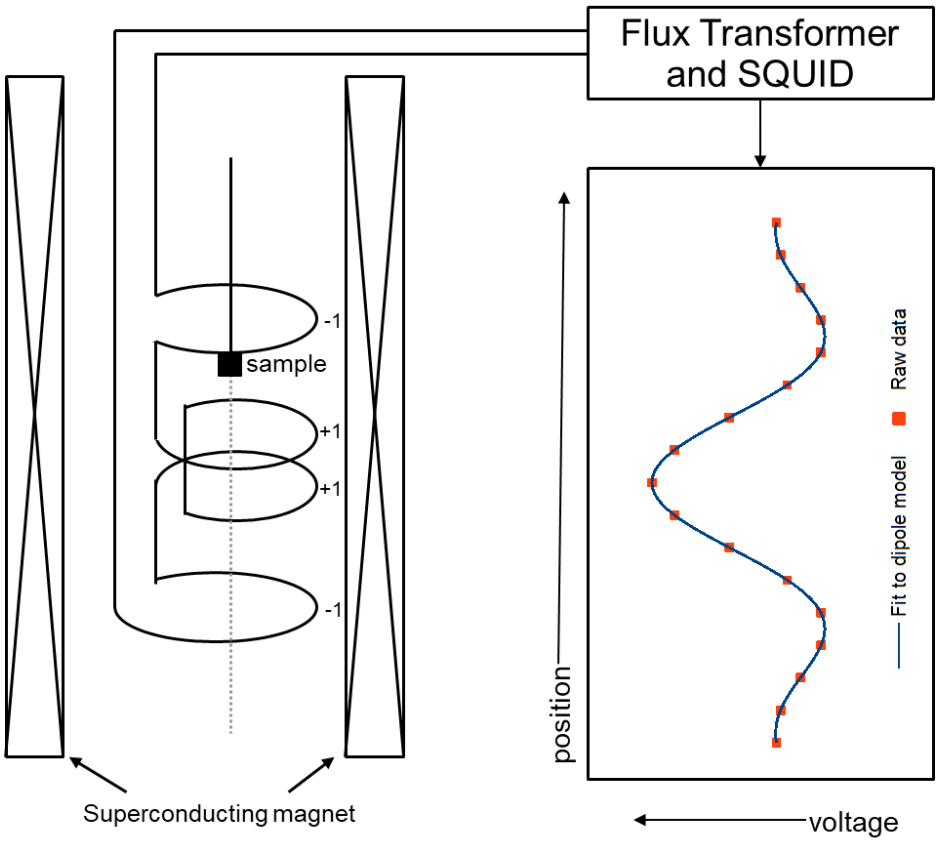

Figure 3.2: Pick-up-coil geometry and theoretical response signal of ideal dipole vs scan length in a MPMS SQUID magnetometer.

This set up is advantageous in that the pick up assembly is far less sensitive to distant moments than to those inside the volume of the gradiometer. Additionally as long as the object is magnetically homogenous, the magnetic signal from a vertical source larger than the size of the gradiometer will cancel out (around 4.5cm) [13]. Quantum Design suggests that a length of 15-20cm is sufficient to satisfy this condition. It is still however advised to use a sample holder with as low a magnetic signal as possible. MPMS XL recommends the use of transparent drinking straws, which have a very small diamagnetic signal below the order of 10^{-7} emu. This is the method adopted in this thesis [30-31]. On placing the sample and sample holder into the device a centering scan is completed in order to position the sample at the optimum measurement position inside the gradiometer. A sample is perfectly centered when the raw magnetic response from the sample aligns with the fit to the dipole model generated by the instrument (shown in Figure 3.2).

Throughout this work, the samples produced where in either a powdered solid or liquid form, and as such great care had to be taken to adequately contain the samples as they posed a special contamination threat. MPMS XL suggest the use of gelatin capsules to contain such samples, as they have a relatively small magnetic susceptibility of 10 emu g^{-1} Oe^{-1}, with a typical capsule

having a mass of around 50mg [31]. MPMS XL also suggest that for powdered samples, if the material is highly magnetic, embedding it in a low susceptibility epoxy matrix like Duco cement is advantageous as this can prevent the sample from shifting within the capsule during the measurement. This method was not adopted during this thesis as a lot of the samples measured had only a relatively small magnetic signal. Instead the gelatin capsules where closed the 'wrong way around', in that the cap was inserted inverted and inserted inside the sample holder (see Figure 3.3).

Figure 3.3: Gelatin capsule sample holder used to contain MNPs samples in Chapter 4, where cap top is inverted to compress powder

In this way the sample was forced to the bottom of the holder and held firmly in place by the cap. Although the gelatin capsules proved to be suitable sample holders for both the ionic liquid samples and the majority of the powdered magnetic nanoparticles samples, they do have some limitations which made them unsuitable for a number of the measurements required in this thesis. Namely, due to a melting temperature of around 320K, they were not suitable for the final set of measurements carried out on the magnetic nanoparticles, which required heating the samples to 350K. Additionally gelatin capsules are hygroscopic (easily absorb water from the atmosphere) and hence have a particularly large water content. The magnetic crystals measured in Chapter 6 all had varying degrees of hygroscopic behaviour and would degrade to a different compound on contact with moisture. In face when initially placed into the gelatin capsule for measurement, the samples drew all the water from the capsules causing them to dry out, as shown in Figure 3.4(b). As such it was necessary to devise an alternate way to contain these samples.

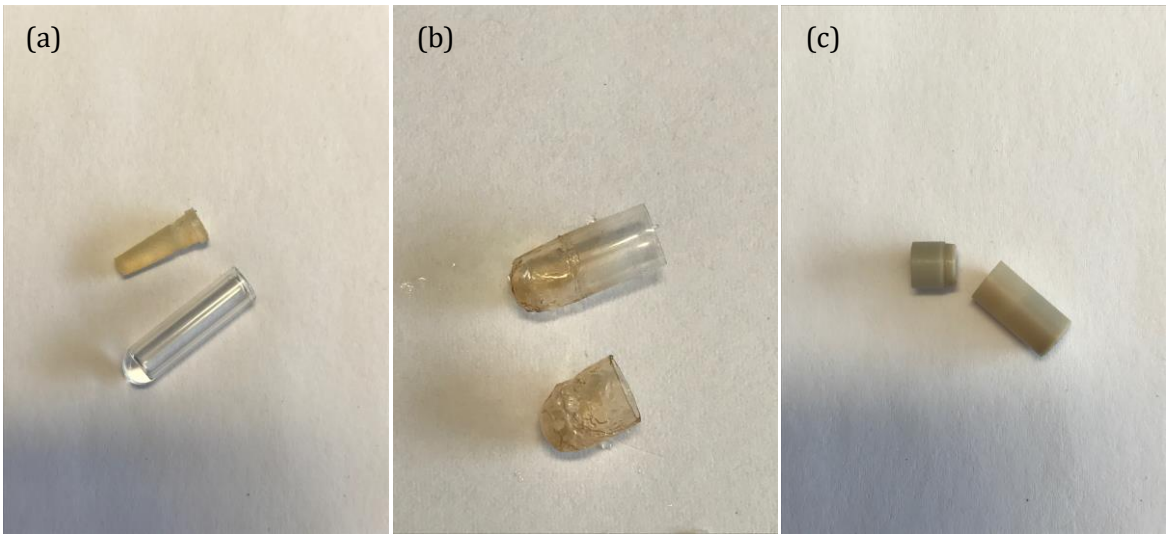

Figure 3.4: (a) Glass capsule manufactured to contain hygroscopic samples. ***(b)*** Example of capsule 'drying' out, cause by hygroscopic samples drawing water from gelatin capsule. ***(c)*** Peek capsule used to contain magnetic crystal samples in Chapter 6

Specialised glass capsules, with thin capillary like walls, were manually blown and measurements attempted using these Figure 3.4(a). However unfortunately the walls could not be made thin enough to prevent the creation of a temperature gradient from the outer atmosphere of the capsules to the inside, were the sample was contained. As such the temperature reading, given by the SQUID magnetometer, corresponding to a particular magnetisation value, was not in fact the temperature of the sample at that time. Finally, specialised Peek capsules were manufactured to contain the samples Figure 3.4(c). These could be made significantly thinner than the glass capsules ensuring accurate heating and cooling of the samples.

If possible the best way to affix samples for measurement inside the sample holders is simply to place them between the two walls of the straw. This method was adopted in this thesis when gelatin capsules where used to contain the samples. The capsules where of ideal size, in that when positioned inside the straw they did not move during the measurement. Movement of the sample during measurement can cause the sample to move off center resulting in a characteristic dip in the measured magnetic signal. Confirmation that a sample has moved during measurement can be achieved by carrying out a centering scan on completion of the experiment. If the sample has moved the raw data points of the characteristic dipole vs scan length curve will not be aligned with the dipole model curve generated by the instrument (see

Figure 3.2). The peek capsules used in Chapters 4 and 5 however where slightly too small to adopt this method and some modifications had to be made. In order to limit the movement of samples during measurements and avoid any loss of centering, small incisions where made in the straw both above and below the peek capsule, and the straw folded in. This created a container for the capsule within the straw. Unfortunately the process of folding in the straw does create an additional diamagnetic signal due to an accumulation of the material, which had to be accounted for. Failure to account for diamagnetic contributions in a magnetic measurement will return a diminished response than that which would be expected, due to the characteristic negative magnetic response of diamagnetism. As the peek capsule also possessed a diamagnetic signal, a temperature dependent scan was carried out to determine the magnetic response of the capsule and straw, however as the signal from the capsule was so small it wasn't possible to accurately center the sample for measurement. As such the magnetic signal of the peek capsule and straw was calculated by firstly obtaining the magnetic susceptibility of a very small nickel wire sample contained within the peek capsule, under an applied field of 500Oe in the temperature range 10K-300K. This measurement was then repeated for just the nickel wire, which was pierced through the straw at the desired measurement position. The difference of the two measurements, which corresponds to the magnetic susceptibility of the peek capsule and straw, was then calculated and is displayed in Figure 3.5.

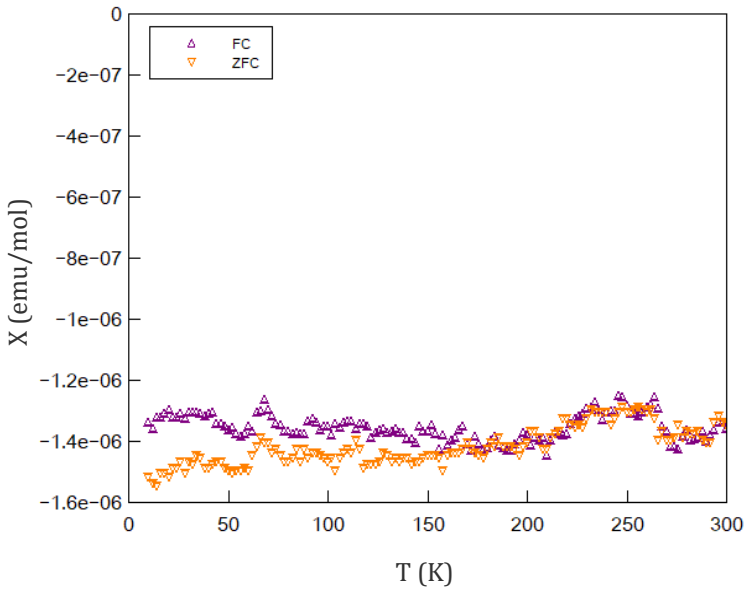

Figure 3.5: Susceptibility data collected for the peek capsule in the temperature range 10-300K. The purple triangles represent the data collected under field cooled conditions and the orange inverted triangles represent the data collected under zero-field cooled conditions

As can be seen from this plot the magnetic susceptibility remains fairly constant throughout the measured temperature range and an averaged value of -1.39 x 10^{-6} was taken to be the diamagnetic contribution due to the capsule and straw.

In addition the diamagnetic signal resulting from the sample holder, there will be a further diamagnetic signal originating from the atoms and bonding present in the samples being measured, as diamagnetism is present in all materials [35]. This underlying diamagnetism must be accounted for in order to get a true representation of the magnetic behaviour exhibited by the samples. Typically this is achieved by applying a correction using tabulated values. These correction factors were first described by Pascal in 1910 and are now commonly referred to as Pascal's constants [32-34]. As these values and the method of analysis have been altered many times since their origin in 1910, it is often problematic to find consistent figures in the literature. On this occasion the values quoted in the paper by Bain and Berry have been employed, as this work pulls from a wide cross section of the literature [35].

3.3. SQUID Measurements

3.3.1. Magnetic Susceptibility Measurements

Magnetic susceptibility is a dimensionless quantity used to describe the degree magnetization exhibited by a material in response to an applied magnetic field, as described by the following equation [11].

$$\chi = M/H \qquad \textbf{Equation 3.5}$$

where χ denotes the magnetic susceptibility, M the magnetization of the material and H the applied magnetic field.

Magnetic susceptibility measurements as a function of temperature can be particularly useful when investigating materials which do not order magnetically. As outlined in section 2, a paramagnet will exhibit a magnetic response in the direction of an applied field and will therefore possess a positive magnetic susceptibility, whereas a diamagnet will exhibit a magnetic response in the opposite direction to the applied field and will therefore have a

negative magnetic susceptibility [36]. For the majority of diamagnetic materials their susceptibility is independent on temperature, however in the case of paramagnets the susceptibility is typically inversely proportional to the temperature in accordance with the Curie Law, Equation 3.6 [37].

$$\chi = C/T \qquad \textbf{Equation 3.6}$$

where C is the Curie constant.

Typically the magnetic susceptibility data collected for a Curie type paramagnet is displayed as a plot of $1/\chi$ against temperature, in which case the gradient is equal to the Curie constant of the material. The Curie constant is described by the following equation,

$$C = b\, p_{eff}^2\, N \qquad \textbf{Equation 3.7}$$

where p_{eff} denotes the effective magnetic moment, b is a universal constant and N is the concentration of magnetic atoms contained in the sample.

Where the molar susceptibility is known (the susceptibility per mole of sample), the effective magnetic moment of the sample can be determined using the following equation [38],

$$p_{eff} = \left(\frac{3\, k\, C_m}{N}\right)^{\frac{1}{2}} \qquad \textbf{Equation 3.8}$$

where C_m is the molar susceptibility in units of emu.K/mol, k is Boltzmann's constant in units of erg/K ($1.38\ x\ 10^{-16}$), N is Avogadro's number ($6.02\ x\ 10^{23}$) and p_{eff} is the effective magnetic moment in units of erg/Oe.

In the majority of the literature, and throughout this thesis, the effective magnetic unit is given in units of Bohr magnetons (μ_B). Erg/Oe can be converted to μ_B by dividing through by the conversion factor, $0.927\ x\ 10^{-20}$ [39].

Ferromagnetic, ferrimagnetic and antiferromagnetic materials all exhibit a positive susceptibility. As described in section 2, below the Curie temperature the individual magnetic moments of the atoms for these materials all order magnetically. In this region the magnetic susceptibility of the material is both history and field dependent and hence cannot be used to deduce a constant magnetic moment as described above for a paramagnet [11]. It should be noted however that above the Curie temperature these materials all begin to act paramagnetically as described in Chapter 2. In these cases their magnetic susceptibility will typically follow a Curie-Weiss relationship as described by Equation 3.9 [40].

$$\chi_{CW} = \frac{C}{T-\theta} \qquad \textbf{Equation 3.9}$$

where θ is the Curie-Weiss temperature.

In comparison to a typical paramagnet where the only force acting is the interaction between the magnetic moment and the applied field, there is the additional force of the interaction between magnetic moments on neighbouring atoms (exchange interaction) in these materials, hence the additional temperature term, θ. The Curie-Weiss term is directly proportional to the strength of the exchange interaction between neighbouring atoms and is dependent on whether this interaction helps to align the moment in the same, or opposite directions. A ferromagnet will have a positive Curie-Weiss temperature whereas an antiferromagnet will have a negative Curie-Weiss temperature [41]. As is the case for a paramagnet, the magnetic susceptibility data for these materials is typically plotted as $1/\chi$ against temperature. The graph will intersect the x-axis at a value greater or smaller than 0, depending on the sign of the Curie-Weiss temperature as shown in Figure 3.6.

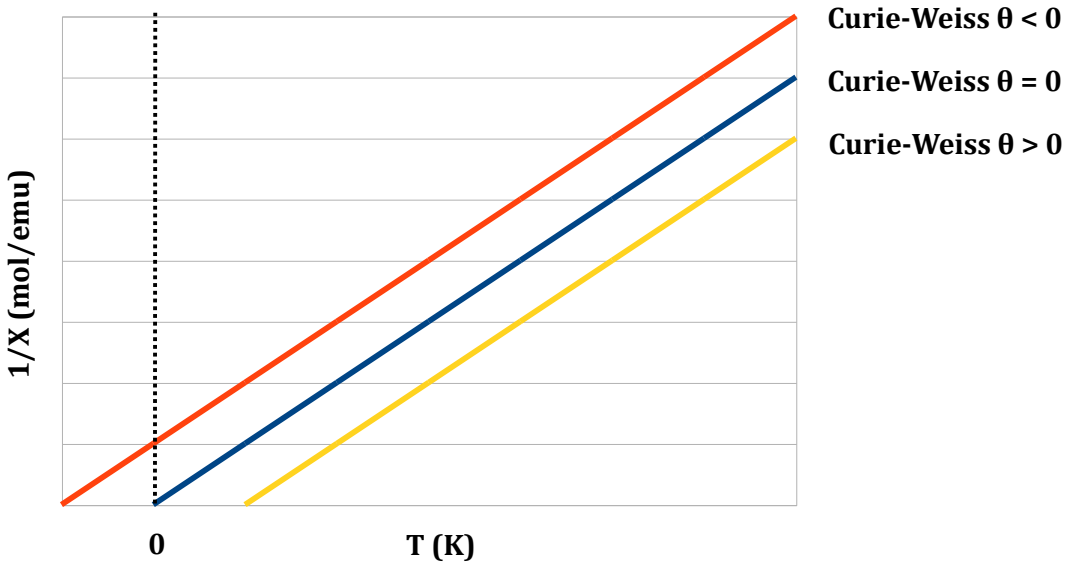

Figure 3.6: Plot of the inverse of χ against T for systems exhibiting Curie and Curie-Weiss behavior. When $\theta > 0$, yellow line, neighbouring moments align parallel to one another, when $\theta < 0$, red line, neighbouring moments align antiparallel. When $\theta = 0$, blue line, neighbouring moments act independently.

As described in Chapter 2, ferromagnets possess remnant magnetization on the removal of an applied field and their hysteresis loops therefore exhibit irreversibility [11, 39]. Magnetic hysteresis can be measured using SQUID magnetometry by incrementally varying the applied magnetic field at a constant temperature, however another quick and effective way of determining whether or not irreversibility exists and the point of magnetic transition in a material, is to carry out field-cooled (FC), zero field-cooled (ZFC) plots, at small applied fields.

As described in section 2, the anisotropy of a ferromagnetic material is responsible for the observed irreversibility in the magnetization. As temperature is decreased the anisotropy becomes stronger and the remnant magnetization exhibited by the material becomes larger [3][30]. Above the Curie temperature a ferromagnetic material behaves paramagnetically and the magnetic spins in the material are randomly orientated. On application of an applied field these spins will move to align along the direction of the applied field. On cooling a ferromagnetic sample down in an applied field some of the magnetic moments are frozen in the direction of the applied field. Therefore when measuring the sample on heating, the FC branch will show a larger magnetization than the ZFC branch, as some of the magnetic moments in the sample will already be orientated in the correct orientation. Hence bifurcation of the FC/ZFC branches is observable until above the Curie temperature, where the material becomes paramagnetic and the history of the sample no longer affects the magnetization, as shown in Figure 3.7 [42].

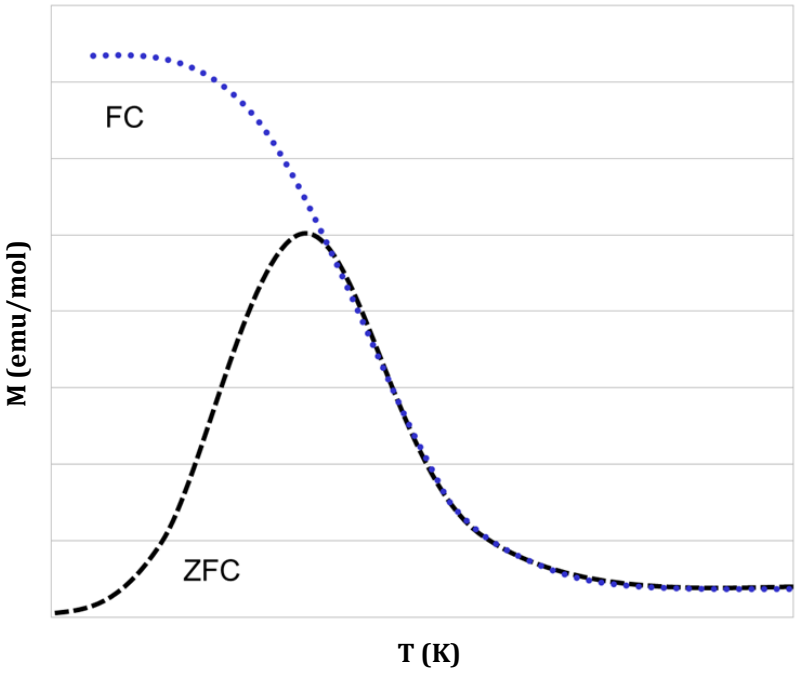

Figure 3.7: Plot of the magnetisation (M) against temperature for a ferromagnetic material where the sample is first cooled in H=0, a small field applied and then data collected on warming, black dashed line, (ZFC) and, when data are collected as the sample in cooled in the same field, blue dotted line (FC).

Extreme care must be taken to apply a small enough field that the magnetization of the sample is not saturated during the experiment as this would result in the FC/ZFC measurements being the same.

The process of carrying out a FC/ZFC scan using a SQUID magnetometer is as follows [13];

1. The SQUID magnetometer is brought up to room temperature and the sample inserted into the sample space chamber. The applied magnetic field is then set to 0Oe using the no overshoot approach; this is the most accurate method of setting a magnetic field using this device.
2. The system is then brought up to the maximum temperature in the desired measurement range, in order to completely demagnetize the sample. For the majority of experiments in this thesis this step was not necessary as the maximum temperature in the measurement range was generally at, or below room temperature.
3. The sample is then brought down to the lowest temperature in the desired measurement range with the 0Oe applied field.

4. Once the SQUID magnetometer has stabilized at this temperature a small magnetic field is applied. The size of the applied field necessary for this measurement is dependent on the magnitude of the magnetic signal exhibited by the sample. The aim is to align enough of the magnetic spins that a decent signal can be obtained, without fully saturating the sample as this would result in the FC/ZFC branches of the measurement being the same. In the case of this thesis the smallest field that allowed for a magnetic signal large enough to accurately center the sample was chosen.
5. The sample is then slowly brought up to the highest desired temperature in the measurement range and the magnetization measured at regular intervals. This is the ZFC part of the measurement.
6. Steps 3-5 are then repeated, but this time the small magnetic field remains on when cooling the sample down, to obtain the FC part of the measurement. It should be noted that the FC measurements can be collected on cooling the sample in the applied field, however most cryogenic systems tend to operate more effectively on heating and hence the data collected on heating tends to be more accurate.

3.3.2. AC Susceptibility Measurements

Another useful susceptibility measurement is the measurement of AC susceptibility, which is vastly used in the literature to confirm complexes behave as SMMs [43]. In practice the sample is cooled to a set temperature of around 1.7K and a weak field which switches direction at a fixed frequency applied across the sample [44]. The temperature is then slowly incremented to around 10K and the out-of-phase component of the susceptibility recorded; this is the portion of the magnetic susceptibility which cannot keep up with the switching field. In SMMs the relaxation rate of the magnetisation is dependent on temperature in accordance with the following equation,

$$\tau = \tau_0 exp^{(\frac{U_{eff}}{k_B T})} \qquad \textbf{Equation 3.10}$$

where τ is the relaxation time of the magnetisation, τ_0 is the relaxation attempt frequency, U_{eff} is the effective potential energy barrier of the molecule, k_B is the Boltzmann constant and T is the temperature [44].

At a specific temperature the relaxation rate $1/\tau$, will be in agreement with the frequency of the switching field, resulting in a resonance condition and a subsequent peak in the out of phase susceptibility of the molecule. By repeating the measurements for a range of AC frequencies, a plot of ln τ against $1/T$ can be obtained and from this values of both the effective potential energy barrier and the relaxation attempt frequency of the complex calculated, see Equation 3.6 [45-47]. These parameters are quite often used to support the success of a particular SMM as they ultimately reflect the length of time such a complex could retain magnetic information below the blocking temperature.

Whilst AC susceptibility measurements are indeed a good indication of SMM behaviour it is not definitive evidence and should ideally be coupled with the existence of a temperature or field dependent hysteresis loops [48, 49].

3.3.3. Reduced Magnetisation Experiments

Quite often when the use of an AC frequency enabled SQUID is not freely available, reduced magnetisation plots will be provided to support the theory that a particular compounds acts as a single molecule magnet [50]. To obtain these data a DC applied field of set magnitude is applied across the complex and its resulting magnetisation as a function of increasing temperature measured. This process is then repeated for a selection of different magnetic field strengths, and the magnetisation per molecule is plotted as a function of the applied field strength over the temperature range. In a paramagnetic material, at temperatures where only the ground state is populated, it is expected that such a plot would follow the Brillouin function [51],

$$B_J(y) = \frac{2J+1}{2J}\coth\left(\frac{2J+1}{2J}y\right) - \frac{1}{2J}\coth\frac{y}{2J} \qquad \textbf{Equation 5.11}$$

where J represents the total angular momentum quantum number and

$$y = g\mu_B JB/k_B T \qquad \textbf{Equation 5.12}$$

Here g represents the Landé g factor, μ_B the Bohr magneton, B the magnetic flux density, k_B the Boltzmann constant and T, temperature [51].

The subsequent magnetisation is described as

$$M = ng\mu_B J B_J \qquad \textbf{Equation 5.13}$$

where n is the number of atoms per unit volume [51].

However whenever ZFS of the ground state occurs this relationship does not hold and as a result there is a lack of superposition of the curves taken at different applied fields, see Figure 3.8 [52]. As such reduced magnetisation plots can be used to show a lack of paramagnetic behaviour in a molecular complex, indicating ZFS and as a result, SMM behaviour. Additionally fitting to such curves using appropriate spin Hamiltonians, can be exploited to return estimates for the values of the S, D and E parameters [53].

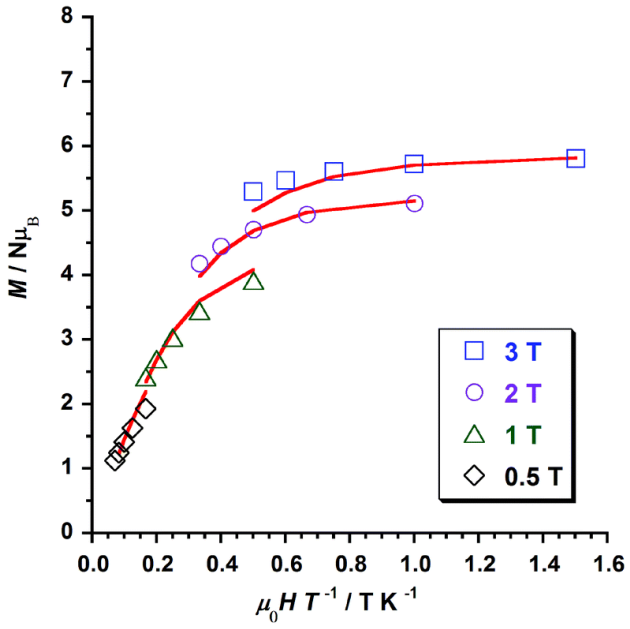

Figure 3.8: Plot of the reduced magnetisation of complex $[Mn_6(\mu_3\text{-}O)_2(H_2N\text{-}sao)_6(py)_6(EtOH)_2](ClO_4)_2 \cdot 4EtOH$, in the 0-2K temperature range, for applied magnetic fields of 0.5, 1, 2 and 3T. Taken from reference 43.

3.3.4. Uncertainty in SQUID Measurements

As mentioned previously, SQUID magnetometers are the most sensitive instruments commercially available for measuring magnetic flux. With respect to the SQUID magnetometer used throughout this thesis the direct device-related uncertainty in the magnetic moment is well below practical consideration, with accuracy of $\Delta m_{dev} \sim 10^{-8}\ emu$ documented for fields of $\mu_0 H \leq 0.25\text{T}$ [12]. This marginal error arises from the measurement of the potential difference. In this thesis the smallest magnetic moments measured where of magnitude $10^{-6}\ emu$. Quantum design states that the uncertainty associated with the application of a large applied field ($\mu_0 H = 7\text{T}$) is $\frac{\Delta H}{H} = 5\%$, and the temperature sensitivity well below $\Delta T \leq 1K$ [30].

3.4. Magnetic Fitting Programs

A portion of the work in this thesis necessitated the use of fitting software to return magnetic parameters from a measured signal (Chapter 4). While there are commercially available solutions i.e. MAGPACK [54-55], the PHI [56] and ANISOFIT 2.0 [57-58] fitting software were leveraged, in part due to their open source nature making them easily accessible, but more importantly as they have an extensive history of being employed in relevant literature. This section details the workings of these programs.

3.4.1. Phi

In order to fit to the magnetic susceptibility data obtained in Chapter 4 of this thesis the PHI computer package developed by The Chilton Group was employed [56]. PHI was designed specifically for the calculation and interpretation of the magnetic properties of systems containing orbitally degenerate and strongly anisotropic ions, through the inclusion of Spin-Orbit (SO) coupling and Crystal-Field (CF) effects. PHI utilizes an optimization algorithm to calculate phenomenological Hamiltonians, which give the best fit to a given set of experimental data.

The Hamiltonian adopted by PHI is comprised of four separate operators as outlined below.

$$\hat{H} = \hat{H}_{SO} + \hat{H}_{EX} + \hat{H}_{CF} + \hat{H}_{ZEE} \qquad \textbf{Equation 3.14}$$

where $\widehat{H}_{SO}$ is the spin orbit coupling operator, $\widehat{H}_{EX}$ is the exchange coupling operator and $\widehat{H}_{CF}$ is the crystal field interaction operator and $\widehat{H}_{ZEE}$ is the Zeeman effect coupling operator.

PHI fits to experimental data by iterating through values of contributing variables (i.e. Landé g factor) to the above operators, within certain user-defined restrictions. This is of assistance when some parameters are known in advance and also aids in preventing fits by over parameterization, that is to say providing so many degrees of freedom that a physical fit is inevitable. In contrast to other similar fitting programs, PHI is extensively parallelized resulting in a much-reduced processing time.

3.4.2. ANISOFIT 2.0

In order to fit to the reduced magnetization data in Chapter 4, the ANISOFIT 2.0 computer program developed by Shores et al, was used [57-58]. ANISOFIT 2.0 was developed specifically for the estimation of the zero field splitting parameters in high-spin magnetic clusters. Similarly to PHI, ANISOFIT 2.0 adopts an optimization algorithm to calculate a spin Hamiltonian, which best fits a set of experimental data. The Hamiltonian adopted is of the following form.

$$\widehat{H} = D\widehat{S_z^2} + E\left(\widehat{S_z^2} + \widehat{S_z^2}\right) + g_{iso}\mu_B \boldsymbol{S} \cdot \boldsymbol{B} \qquad \textbf{Equation 3.15}$$

where μ_B is the Bohr magneton, D is the axial zero-field splitting parameter, E is the rhombic zero-field splitting parameter, S is the spin field vector, B is the magnetic field vector and g_{iso} is the isotropic Landé g factor.

Unlike the PHI fitting program, ANISOFIT 2.0 assumes that the Landé g factor is isotropic to prevent overparameterization. The program also assumes that only the spin ground state of the molecule is significantly populated. As such for molecules where, for example, superexchange or direct exchange is involved, care must be taken to model magnetization data only at temperatures where this condition is satisfied. Additionally the program makes no provision for intermolecular spin coupling, so this must be borne in mind when dealing with experimental data collected at very low temperatures.

References

[1] Lenz, J.E, "A review of magnetic sensors", (1990), *Proceedings of the IEEE*, Vol **78**, 6, 973-989

[2] Allcock, R. and Constantinides, S., "Magnetic Measuring Techniques for Both Magnets and Assemblies", http://arnoldmagnetics.com/WorkArea/DownloadAsset.aspx?id= 5936, (accessed 21/10/2018)

[3] Lake Shore Cryotronics, Inc. "User's Manual, 7800 Series Hysteresisgraph System", (2001), Rev. 1.2, 119-650

[4] Laboratorio Electtrofisico, "AMH-500-Hysteresisgraph Hard Magnetic Materials", (2015) 1-14

[5] Froner, S., "Versatile and sensitive vibrating-sample magnetometer", Review of Scientific Instruments, (1959), Vol **30**, 7, 548-557

[6] Lake Shore Cyrotronics, Inc., "7400-S Series VSM Specifications" (2018), https://www.lakeshore.com/products/Vibrating-Sample-Magnetometer/7400-S-Series-VSM/pages/Specifications.aspx, (accessed 21/10/2018)

[7] Cryogenic Limited, "Vibrating sample magnetometer (VSM)", (2012), http://www.cryogenic.co.uk/products/vibrating-sample-magnetometer-vsm (accessed 21/10/2018)

[8] Martínez-Pérez, M. J. and Koelle, D., "NanoSQUIDs: Basics & recent advances", (2017),

[9] Fagaly, R.L, "Superconducting quantum interference device instruments and applications", (2006), *Review of Scientific Instruments*, Vol **77**, 10, 101101

[10] Bendanta, S., Petracic, O., Aderholz, M. and Kleemann, W., "A sample holder design for high temperature measurements in superconducting quantum interference device magnetometers", (2005), *Review of Scientific Instruments*, Vol **76**, 083910

[11] Coey, J. M. D, "Magnetism and magnetic materials", (2010) Cambridge UK; Cambridge University Press, 1st ed.

[12] Sawicki, M, Stefanowicz, W and Ney, A, "Sensitive SQUID magnetometry for studying nanomagnetism", (2011), *Semiconductor Science and Technology*, Vol **26**, 064010

[13] McElfresh, M, “Fundamentals of Magnetism and Magnetic Measurements Featuring Quantum Design’s Magnetic Property Measurement System”,(1994), San Diego CA, Quantum Design Inc, Purdue University.

[14] Rohlf, J. W., “Modern Physics from a to Z0”, (1994), Wiley

[15] Maguire-Boyle, S, Barron, A. R, “Theory of a Superconducting Quantum Interference Device (SQUID)”, OpenStax-CNX module: m22750, (2009), Version 1.3

[16] Bardeen, J, Cooper, L.N, and Schrieffer, J.R, “Theory of Superconductivity”, (1957), *Physical Review*, Vol. **108**, 1175

[17] Josephson, B.D, “Possible new effects in superconductive tunneling”, (1962), *Physics Letters*, Vol. **7**, 251-253

[18] Anderson, P.W, and Rowell, J.M, “Probable Observation of the Josephson Superconducting Tunneling Effect”, (1963), *Physics Review Letters*, Vol **10**, 230-232

[19] Nturambirwe, J. F. I., “Superconducting Quantum Interference Device (SQUID) Magnetometers: Principles, Fabrication and Applications”, (2010), Thesis Submission, African Institute for Mathematical Sciences (AIMS)

[20] Turton, R, “The physics of solids”, (2002), Oxford University press, 2nd ed, no. 0 19 850352

[21] Tinkham, M, “Introduction to Superconductivity”, (1996), New York: McGraw-Hill, 2nd ed. 198

[22] Rose-Innes, A. C, “Introduction to Superconductivity”, (1978), Pergamon Press plc, 2nd ed. 173

[23] Hahlbohm, H.D, and Lubbig, H, “SQUID ’85, Superconducting Quantum Interference Devices and their Applications”, (1985), Walter de Gruyter, Berlin, New York, 589

[24] Gallop, J.C, and Petley, B.W, “SQUIDs and their applications”, (1976), *Journal of Physics E: Scientific Instruments*, Vol **9**, 6, 417-429

[25] Clarke, J, and Braginski, A.I, “Fundamentals and technology of SQUIDs and SQUID Systems”, The SQUID Handbook, (2004), Wiley, New York, Vol. 1

[26] Silver, A.H., Zimmerman, J.E, “Quantum states and transitions in weakly connected superconducting rings”, (1964), *Physical Review Letters*, Vol **12**, 159-160.

[27] Mercereau, J.E., "Superconducting magnetometers", (1970), *Revue de Physique Appliquée*, Vol **5**, 21

[28] Nisenoff, M., "Superconducting magnetometers with sensitivities approaching 10-10 gauss" (1970), *Revue de Physique Appliquée*, Vol **5**, 21

[29] Bendanta, S., "A sample holder design for high temperature measurements in superconducting quantum interference device magnetometers", (2005), *Review of Scientific Instruments*, Vol **76**, 083910

[30] Quantum Design, Magnetic Property Measurement System, (1999) MPMS MultiVu Application User's Manual, 2nd Ed

[31] Quantum Design, (2000) MPMS Application Note, 1014-201, 11/01/2000

[32] Pascal, P., "Magnetochemical Researches", (1910), *Annales de Chimie et de Physique*, Vol **19**, 5.

[33] Pascal, P., "Magnetochemical research. 2" (1912), *Annales de Chimie et de Physique*, Vol **25**, 289.

[34] Pascal, P., "Magnetochemical Investigations 11", (1913), *Annales de Chimie et de Physique*, Vol **28**, 218.

[35] Bain, G.A. and Berry, J.F., "Diamagnetic Corrections and Pascal's Constants", (2008), *Journal of Chemical Education*, Vol. **85**, 4

[36] Petrovsky, E. and Kapicka, A., "On determination of the Curie point from thermomagetic curves", (2006), *Journal of Geophysical Research*, Vol. **11**, B12S27

[37] Curie, P., "On symmetry in Physical Penomena, Symmetry of an Electric Field and of a Magnetic Field", (1894), *Journal de Phsique,* Vol **3**, 401.

[38] Hoppe, J.I., "Effective magnetic moment", (1972), *Journal Chemical Education*, Vol **49**, 7, 505

[39] Blundell, S. "Appendix A, Magnetism in Condensed Matter", (2001) Oxford University Press

[40] Kittel, C., "Introduction to solid state physics" (1996), New York, Wiley, 7th ed.

[41] Aharoni, A., "Introduction to the theory of ferromagnetism", (2000), Oxford University Press

[42] Joy, P.A., Anil Kumar P.S. and Date, S.K., "The relationship between field-cooled and zero-field cooled susceptibilities of some ordered magnetic systems", (1998) *Journal of Physics: Condensed Matter*, Vol **10**, 48

[43] Sun, Z., Grant, C., Castro, S., Hendrickson, D., and Christou, G., "Single-molecule magnets: out of phase ac susceptibility signals from tetranuclear vanadium (111) complexes with an S=3 ground state", (1998), *Chemical Communications*, Vol **6**, 721-722

[44] Long, J., "Molecular cluster magnets", (2003) In chemistry of nanostructured materials, World Scientific Publishing: Hong Kong, 291 – 307

[45] Andres, H., Winpenny, R. et al, "Studies of a nickel-based single-molecule magnet", (2002), *Chemistry European Journal*, Vol **8**, 21, 4867 – 4876

[46] Milios, C., and Brechin, E., et al. "A record anisotropy barrier for a single-molecule magnet", (2007), *Journal of the American Chemical Society*, Vol **129**, 10, 2754 – 2755

[47] Costes J., Dahan, F., and Wernsdorfer, W., "Heterodinuclear Cu-Tb single-molecule magnet", (2006), *Inorganic Chemistry*, Vol **45**, 1, 5-7

[48] Rinehart, J., Fang, M., Evans, W., and Long, J., "Strong exchange and magnetic blocking in N_2^{3-} - radical-bridged lanthanide complexes", (2011), *Nature Chemistry*, Vol **3**, 538 – 542

[49] Li, Y., Liu, R., Liu, H., and Pang, Y., "Equal interval splitting of of quantum tunnelling in single molecule magnets with identical exchange coupling", (2014), *Physical Review B*, Vol **89**, 184401

[50] Inglis, R., Dalgarno, S., and Brechin, E., "A new family of Mn6 SMMs using phosphinate ligands", (2010), *Dalton Transcriptions*, Vol **39**, 4826 – 4831

[51] Blundell, S., "Magnetism in Condensed Matter", (2001), Oxford University Press, 27-29

[52] Martinez-Lillo, J., Dolan, N., Brechin, E.K., "A family of cationic oxime-based hexametallic manganese(III) single-molecule magnets", (2014), *Dalton Press*, Vol **43**, 4408 – 4414

[53] Soler, M., Christou, G., et al., "Single molecule magnets: two electron reduced version of an Mn12 complex and environmental influences on the magnetization relaxation of (PPh4)2[Mn12O12(O2CCHCI2)16 (H2O)4" (2003), *Journal of the American Chemical Society*, Vol. **125**, 12, 3576 – 3588.

[54] Borrás-Almenar, J. J., Clemente-Juan, J.M., Coronado, E., and Tsukerblat, B. S., "High-nuclearity magnetic clusters: generalized spin hamiltonian and its use for the calculation of the

energy levels, bulk magnetic properties, and inelastic neutron scattering spectra", (1999), *Inorganic Chemistry*, Vol **38**, 6081

[55] Borrás-Almenar, J. J., Clemente-Juan, J.M., Coronado, E., and Tsukerblat, B. S., "MAGPACK1 A package to calculate the energy levels, bulk magnetic properties, and inelastic neutron scattering spectra of high nuclearity spin clusters", (2001), *Journal Computational Chemistry*, Vol **22**, 985

[56] Chilton, N.F., Anderson, R. P., Turner, L.D., Soncini, A., and Murray, K.S., "PHI: A Powerful New Program for the Analysis of Anistropic Monomeric and Exchange-Coupled Polynuclear d- and f- block Complexes", (2013) *Journal Computational Chemistry*, Vol **34**, 1164-1175.

[57] Banci, L., Bertini, I., Bren, K.L., Cremonini, M.A., Gray, H.B., Luchinat, C., Turano, P., "The use of pseudocontact shifts to refine solution structures of paramagnetic metalloproteins, Met8oAla cyano-cytochrome c as an example", (1996), *Journal Biological Inorganic Chemistry*, Vol **1**, 2, 117-126

[58] Banci, L., Bertini, I., Huber, J. G., Luchinat, C., Rosato, A., "Partial Orientation of Oxidized and Reduced Cytochrome b5 at High Magnetic Fields: Magnetic Susceptibility Anisotropy Contributions and Consequences for Protein Solution Structure Determination", (1998), *Journal of the American Chemical Society*, Vol **120**, 49, 12903-12909

Chapter 4

Optimisation of doped LMO MNPs for potential use as mediators in hyperthermia treatment

4.1. Outline

In this chapter the use of doped lanthanum manganate magnetic nanoparticles (MNPs) as possible mediators for hyperthermia treatment was investigated. The effect of varying the synthesis process, dopant material and dopant concentration on the crystallographic structure and magnetic properties of the material was studied with the aim of tuning the magnetic properties to fall within the desired ranges for hyperthermia treatment. Structural characterisation was carried out using scanning electron microscopy (SEM), X-ray powder diffraction (XRD) and infra-red (IR) spectroscopy. The magnetic properties were characterised using SQUID magnetometry and the magnetic heating of the MNPs was assessed using induction heating experiments. The material synthesis, structural characterisation and magnetic heating experiments detailed in this chapter were completed by Katherine McBride, who the author

gratefully acknowledges. The results have been included to support the magnetic characterisation analysis conducted by the author. The experimental results from this chapter are detailed in the following three publications:

1. "Evaluation of $La_{1-x}Sr_xMnO_3$ ($0 \leq x < 0.4$) synthesised via a modified sol-gel method as mediators for magnetic fluid hyperthermia". McBride, K., Cook, J., Gray, S., Felton, S., Stella, L., and Poulidi, D., (2016), *CrystEngComm*, **18**, 3, 407-416
2. "Synthesis, characterisation and study of magnetocaloric effects (enhanced and reduced) in manganate perovskites", McBride, K., Partridge, N., Bennington-Gray, S., Felton, S., Stella, L., and Poulidi, D., (2017), *Materials Research Bulletin*, **88**, 69-77
3. "Improving the crystallinity and magnetocaloric effect of the perovskite La0.65Sr0.35MnO3 using microwave irradiation" , McBride, K., Bennington-Gray, Cook, J., Stella, L., S., Felton, S., and Poulidi, D., (2017), *CrystEngComm*, **19**, 3776-3791

4.2. Introduction

As described in Chapter 2, the requirements for a suitable mediator for mild hyperthermia treatment are that the material is biocompatible, has a low Curie temperature (T_c) and a high specific absorption rate (SAR) [1]. In recent years perovskites have garnered increased interest in this field due to the ability to alter their composition and magnetic properties without significantly changing the perovskite phase. The ideal metal oxide perovskite structure is of the type ABO_3 with cubic geometry as shown in Figure 2.18.

In this study we have chosen to investigate doped manganates of the parent compound lanthanum manganate (LMO) as possible candidates for hyperthermia treatment, as it has previously been reported as being a potentially promising material [2]. In LMO the La^{3+} ions are found on the A-sites, the smaller Mn^{3+} or Mn^{4+} ions are found on the B-sites and the oxide ions are located on the faces. In this study LMO was found to exist in two crystal phases, with the prominent phase being rhombohedral with the space group R-3c and the other phase present being orthorhombic with the space group Pnma [3]. The lattice parameters and atomic coordinates for each phase are detailed below [12].

Atom	Wycoff Position	X	y	Z
A	4c	0.55	0.3	0
B	4a	0	0	0
O(1)	4c	-0.011	0.3	-0.1
O(2)	8d	0.309	0	0.2

Table 4.1: Orthorhombic (Pnma) atomic coordinates for LMO. Lattice cell parameters (Å): a = 5.5743, b = 7.695 and c = 5.537. α = β = γ = 90°

Atom	Wycoff Position	X	y	Z
A	6a	0	0	0.3
B	6b	0	0	0
O	18e	0.55	0	0.3

Table 4.2: Rhombohedral (R-3c) atomic coordinates for LMO. Lattice cell parameters (Å): a = b = 5.5212 and c = 13.3791. α = β = 90° and γ = 120°

Magnetic properties in the manganates arise through the double exchange mechanism (see *section 2.3.10*) [5]. The extent of magnetic exchange via this mechanism is dependent on both the oxidation state of the manganese ions, the length of the Mn-O bond and the bond angle formed by the two manganese ions with the oxygen ion between them [6]. Hence the effect of varying the dopant material and the dopant concentration, on the magnetic properties of the material, are investigated in this chapter.

In addition to changes in composition altering the physical properties of certain perovskites it has also been shown that the actual method of synthesis employed will have an effect on these properties [6-7]. Throughout the literature it can be seen that different synthesis methods to make the same perovskite (LMO) have resulted in particles of varying size and morphology which can in part lead to observed differences in the physical properties exhibited by these materials [8-10]. In the final part of this chapter the effect of using microwave heating during the synthesis process of the MNPs is investigated.

4.3. Effect of varying A-site dopant cation

In the first part of this study the effect of substituting the A-site cation with smaller (Ca^{2+}) or larger (Sr^{2+} or Ba^{2+}) cations is investigated. The cationic radii of these ions are displayed in the following table for comparison. These values have been taken from reference 11.

Cation	Cationic Radii (Å)
La^{3+}	1.36
Ca^{2+}	1.34
Sr^{2+}	1.44
Ba^{2+}	1.61

Table 4.3: Lattice cell parameters for Rhombohedral (R-3c) and Orthorhombic (Pnma) LSMO40, LCMO40 and LBMO40

By altering the size of the A-site cation a distortion will occur in the crystal lattice causing a change in the bond lengths and bond angles, see Figure 4.1 (taken from reference 13).

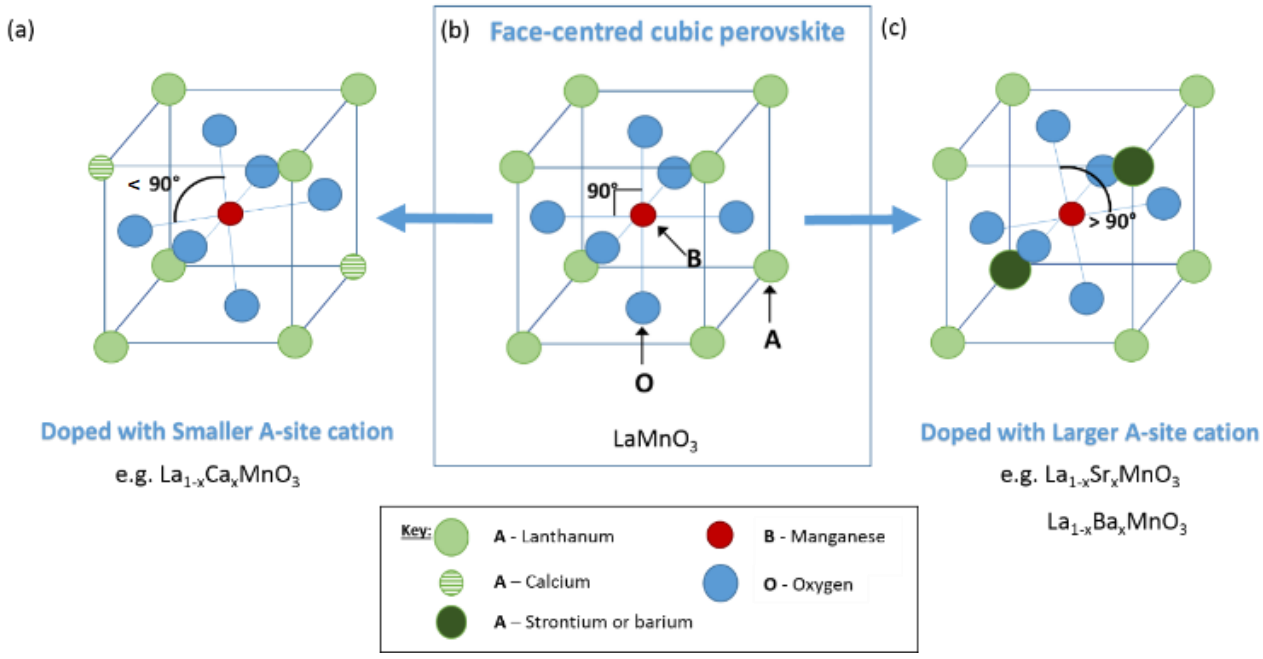

Figure 4.1: The effect of doping with smaller ***(a)*** and larger ***(c)*** A-site cations on the crystal structure of the parent LMO perovskite ***(b)***. [13]

This will affect the extent of the double exchange mechanism and therefore alter the magnetic properties of the material [4].

If we were just to consider the effect of substituting the La^{3+} ions with an ion with a smaller ionic radius we would expect to see a decrease in the angle γ. Conversely, we would expect an increase in the angle γ from 90° to around 120°, and corresponding increase in the rhombohedral crystal phase present, when the La^{3+} ions are substituted with an ion with a larger ionic radius. It is important to note however that by substituting the La^{3+} ions with ions with valency 2+, there is a simultaneously substitution of Jahn-Teller active Mn^{3+} for non Jahn-Teller active Mn^{4+}. The Jahn-Teller active ions in LMO cause a distortion of the crystal lattice, as discussed in section 2.3.14, and result in the predominant rhombohedral crystal phase observed. A decrease in the Jahn-Teller active ions will decrease this distortion and there is an overall decrease in the rhombohedral crystal phase observed when LMO is doped with alkaline earth metals.

Details of the expected lattice parameters for each complex in each crystal phase are detailed below [13].

Orthorhombic (Pnma) lattice parameters						
Complex	**a (Å)**	**b (Å)**	**c (Å)**	**α (°)**	**β (°)**	**γ (°)**
LSMO40	5.574	7.695	5.537	90	90	90
LBMO40	5.574	7.695	5.537	90	90	90
LCMO40	5.452	7.678	5.437	90	90	90
Rhombohedral (R-3c) lattice parameters						
LSMO40	5.521	5.521	13.379	90	90	120
LBMO40	5.477	5.477	13.310	90	90	120
LCMO40	5.477	5.477	13.310	90	90	120

Table 4.4: Lattice cell parameters for Rhombohedral (R-3c) and Orthorhombic (Pnma) LSMO40, LCMO40 and LBMO40

In this section we are interested in the effect of dopant cationic radii on the crystal structure and magnetic properties of the resulting complex, rather than the Mn^{3+}/Mn^{4+} ratio. As such we compare the structural modifications to the perovskite structure along with the subsequent effects on the magnetic properties of the three doped complexes rather than compare them with

the parent compound. The effect of Mn^{3+}/Mn^{4+} ratio is investigated in the second section of this chapter.

4.3.1. Experimental

4.3.1.1. Material Synthesis

The doped perovskites $La_{1-x}Sr_xMnO_3$ (LSMO40), $La_{1-x}Ca_xMnO_3$ (LCMO40) and $La_{1-x}Ba_xMnO_3$ (LBMO40) with x=0.4, were prepared using a modified peroxide sol-gel synthesis. x=0.4 was chosen as at this dopant level all materials showed either an enhanced or reduced MCE.

The aqueous modified sol-gel method used was based on a method developed by Liu et al [14] and Chen *et al.* [15]. The following powder precursors were used in the synthesis of LBMO40, LCMO40 and LSMO40: barium carbonate ($BaCO_3$), 99% purity; calcium carbonate($CaCO_3$), 99% purity; strontium carbonate ($SrCO_3$), ≥ 99.9% trace metal basis; lanthanum (III) oxide, > 99.9% (La_2O_3); and manganese (II) carbonate, ≥ 99.9% trace metal basis. The powder precursors were added to 150ml of deionised H_2O in appropriate proportions in order to obtain the desired stoichiometric ratio. Whilst stirring the powder precursors into the H_2O, 100mL of hydrogen peroxide was added, to oxidise the manganese and act as a complexation agent, followed by 3mL of ammonium hydroxide, to peptize the solution into a stable solution. The mixture was the stirred at 70°C for 2 hours before being dried at 90°C. Finally calcination at 1100°C for 16 hours was used to remove the residual carbon. The resulting crystalline xerogel was then ground into a powder.

4.3.1.2. Characterisation

The morphology of the samples was studied using scanning electron microscopy (SEM) (eSEM – FEI Quanta FEG – Environmental SEM Oxford Ex – Act) and the stoichiometry was confirmed on the same instrument using energy-dispersive X-ray spectroscopy (EDX) with the Aztec based XACT system. In both cases an accelerating voltage of 20kV was used. Atomic percentage was determined using the relative ratio of La to dopant elements in each sample.

Structural determination was carried out using X-ray diffraction (XRD) (Panalytical X'Pert PRO) with a $CuK_{\alpha 1}$ radiation source of wavelength 1.540598 Å, and X'Pert High Score Plus was used to conduct the Rietveld analysis. The input parameters and atomic coordinates for the individual crystal structures from the literature which best matched the diffraction patterns for these

particular samples, where identified and used in the quantification of the whole pattern [16-17]. The background was not subtracted and refinement of the atomic coordinates was undertaken before refining the instrumental parameters. Fourier Transform Infrared Spectroscopy (FTIR Perkin Elmer Spectrum 2) was used to elucidate the degree of strain in the Mn-O bond in order to infer the extent of the MCE.

The magnetic characterisation of the samples was carried out using a super conducting quantum interference device (SQUID) magnetometer (Quantum Design MPMS DC XL, 7T and 1.8-400K). Magnetic susceptibility measurements were collected under an applied field of 100Oe in both field cooled (FC) and zero field cooled (ZFC) conditions, in the temperature regime of 100-380K. Field dependent magnetisation measurements were conducted in the range of -5000Oe to +5000Oe, at 100K and 150K. Gelatine capsules were used to contain the ground samples in order for the magnetic data to be collected. Diamagnetic corrections for the samples were calculated from Pascal's constants and applied to all the magnetic data. The mass of the measured samples, number of moles of each sample and diamagnetic contributions are displayed in Table 4.5.

Sample	**Mass (g) x10^{-4}**	**Moles of sample (mol) x10^{-6}**	**Diamagnetic correction applied (emu/mol) x10^{-5}**
LSMO40	7.10 ± 0.05	3.208 ± 0.023	-6.460 ± 0.097
LCMO40	9.10 ± 0.05	4.498 ± 0.025	-6.116 ± 0.092
LBMO40	8.70 ± 0.05	3.608 ± 0.021	-6.760 ± 0.101

Table 4.5: Table displaying the sample mass, number of moles of each sample and the material specific diamagnetic correction applied to the magnetic measurements

A diamagnetic background contribution of 5 x 10^{-9} emu/Oe due to the straw and gelatine capsules containing the samples was also calculated and accounted for.

The non-adiabatic heating experiments were conducted using a radio frequency (RF) magnetic field generator (Easyheat 0112) coupled with a water-cooled induction coil (6-turn 12cm length coil). A set current of 219A was used which generated a magnetic field with frequency 175kHz and a magnetic field strength of 137.6Oe. The temperature measurements were recorded using an IR temperature probe (Optocon AG) FOTEMP 1 coupled to a (Optocon AG) TS2/2 sensor. A schematic showing the experimental set up of the induction rig is shown in Figure 4.2.

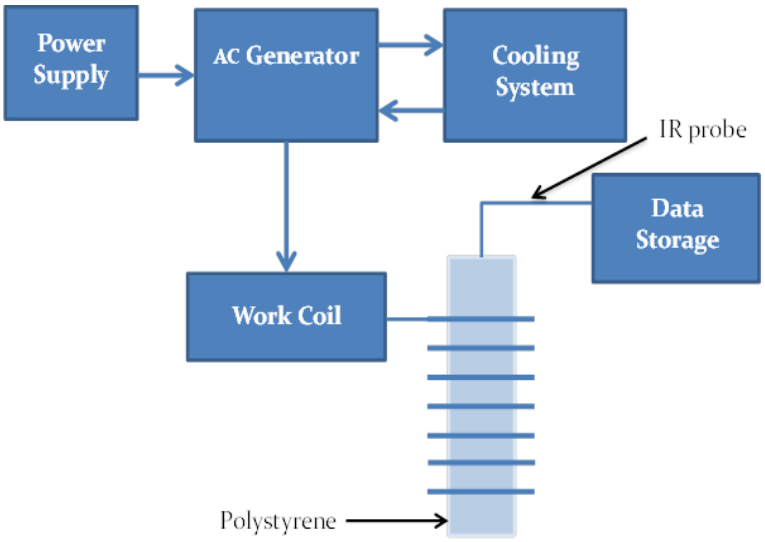

Figure 4.2: Schematic of the equipment used in the induction heating experiments

Aqueous suspensions of the powders of suspension concentration 5mgmL^{-1} were prepared. The heating curves from these experiments are presented in terms of temperature difference rather than measured temperature to reduce systematic errors. Using these data the specific absorption rate (SAR) was calculated for each material using the following corrected slope method equation (Equation 4.1) following Wildeboer *et al.'s* method [18].

$$SAR_{corrected\ slope} = \frac{C_w \frac{\Delta T_w}{\Delta t} + L\Delta T_w}{m_{MNP}} \qquad \textbf{Equation 4.1}$$

where C_w is the specific heat capacity (Jg$_{-1}$K$_{-1}$) of water, m_{MNP} is the weight fraction of the magnetically active element, $^{\Delta T_w}/_{\Delta t}$ is the change in temperature against time, and L is the thermal losses of the system [18].

Due to electrical resistance in the induction coil there is some conventional heating reported in the literature in such experiments, which causes a reported temperature increase of 3°C in a 10-minute period [18]. As a control, the temperature increase of 1mL of water (the blank) was measured under the same conditions as the other samples to serve as a standard to define either an enhanced (greater than the blank) or reduced (less than the blank) magnetic heating effect. In this study, in agreement with the literature, the temperature in the blank was found to reproducible increase by 3°C in a 10-minute period when the initial temperature was 25°C. In order to keep the experimental data consistent with the literature for easy comparison, the magnetic heating curves presented in this study have not been corrected for the blank heating profile in keeping with the conventional presentation of such data. The heating profile of the blank is however included in the plots of the heating curves of the samples to deduce whether an enhanced or reduced magnetic heating is in fact taking place. The blank is taken into consideration when calculating the SAR for each sample. The SAR of the blank was calculated and used as a comparison for the range of materials investigated in this work.

4.3.2. Results and discussion

4.3.2.1. Crystalline structure and configuration analysis

SEM and EDX analysis was carried out for each of the complexes in this study. Details of these experiments and the SEM images and EDX maps for each complex can be found in the main paper or supplementary information of reference 13. The SEM images showed that the particles synthesised in this study formed agglomerates and made identification of individual particle size unachievable.

The stoichiometry of the synthesised samples verified using EDX is presented in Table 4.6.

Sample	Sample Name	EDX stoichiometry
$La_{0.6}Sr_{0.4}MnO_3$	LSMO40	$La_{0.62}Sr_{0.38}MnO_3$
$La_{0.6}Ca_{0.4}MnO_3$	LCMO40	$La_{0.66}Ca_{0.34}MnO_3$
$La_{0.6}Ba_{0.4}MnO_3$	LBMO40	$La_{0.62}Ba_{0.38}MnO_3$

Table 4.6: Details of the samples prepared and investigated during this study including the stoichiometry of each sample as determined by EDX analysis.

EDX analysis carried out on the synthesised particles showed all samples displayed stoichiometry in range of the desired ratios for this investigation (i.e. x=0.4). The overall analytical accuracy in the EDX measurements in this study is around ± 2%, owing to uncertainties in the compositions of the standards used in the quantification and the various corrections applied to the raw data.

XRD, and subsequent Rietveld analysis on the parent LMO compound, which was synthesised using the same modified peroxide sol-gel process as the samples in the study, confirmed the presence of both rhombohedral (R-3c) and orthorhombic geometries (Pnma), with the predominant geometry to be rhombohedral (R-3c) (96% relative weight percentage), in agreement with what is reported in the literature [3]. Details of the XRD and Rietveld analysis and the XRD patterns for each complex can be found in the main paper and supplementary information of reference 13.

The Rietveld analysis of the Ca, Sr and Ba-doped lanthanum manganates showed the presence of both the rhombohedral (R-3c) and orthorhombic (Pnma) geometries present in the LMO compound, in all three complexes. The relative weight percentage of the orthorhombic (Pnma) with respect to the rhombohedral (R-3c) geometry, was however significantly greater for the doped lanthanum manganates than for the LMO parent compound. This is supported by the work of Slobodin et al. who found a reduction of the orthorhombic phase in doped lanthanum manganates, caused by increasing Mn^{4+} content and La^{3+} substitution with larger sized cations [19]. This is due to a reduction in the Jahn-Teller active Mn^{3+} ions as a direct result of substitution of La^{3+} with ions of valency 2+. This causes a decrease in the distortion of the crystal lattice due to the Jahn-Teller effect.

The crystallite size and relevant weight percentages of each crystal phase and their corresponding lattice parameters, derived from the Rietveld analysis, for each of the doped lanthanum manganates synthesised in this study, are displayed in the following table.

Sample	Cryst. Dia. (nm)	Space Group	a / Å	b / Å	c / Å	α / °	β / °	γ / °	V / Å³	Wt. Perc. / %
LBMO40	54.9	Pnma	5.940	8.367	5.126	90	90	90	254.8	20.7
		R-3c	5.511	5.511	13.354	90	90	120	357.8	79.3
LCMO40	45.0	Pnma	5.423	7.692	5.435	90	90	90	226.7	42.0
		R-3c	5.470	5.470	13.356	90	90	120	346.1	58.0
LSMO40	61.9	Pnma	5.448	7.750	5.456	90	90	90	230.4	31.2
		R-3c	5.511	5.511	13.354	90	90	120	351.2	68.8

Table 4.7: Structural information for the LBMO40, LCMO40 and LSMO40 complexes derived from Rietveld analysis

From Table 4.7 we can see a reduction of the orthorhombic phase with increasing dopant radii. The increase in average A-site cationic radii from LCMO40 (Ca^{2+} cationic radius = 1.34Å) to LSMO40 (Sr^{2+} cationic radius = 1.44Å) and LBMO40 (Ba^{2+} cationic radius = 1.61Å) is seen to correspond to an increase in the rhombohedral R-3c crystal structure. The relative weight percentage of this phase increases from 58% for LCMO40 to 68.8% for LSMO40 and 79.3% for LBMO40. Additionally an increase in the cell volume with the increasing size of the average A-site cationic radii is also observed when comparing the doped lanthanum manganates, as would be expected.

The FTIR analysis for the prepared manganate samples is displayed in Figure 4.3.

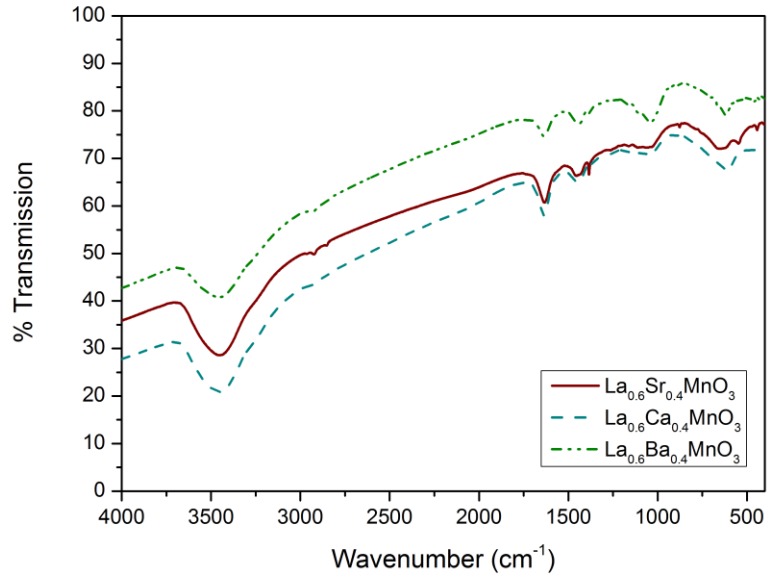

Figure 4.3: FTIR spectra for LBMO40, LCMO40 and LSMO40

The presence of octahedral MnO_6 is revealed by absorption in the low-frequency region at approximately 600cm^{-1} by the Mn-O bond. This absorption can be seen in all three cases. Figure 4.3 shows that the wavenumber for the Mn-O absorbance is greatest for LSMO40 (~645cm^{-1}) followed by LBMO40 (~625cm^{-1}) and then LCMO40 (~610cm^{-1}). The relationship between wavenumber and bond order can be interpreted using Equation 4.2, which has been derived using Hooke's Law.

$$\tilde{\nu} = \frac{1}{2\pi c}\sqrt{\frac{k}{\mu}} \qquad \textbf{Equation 4.2}$$

where $\tilde{\nu} = {}^{1}/_{\lambda}$, k is the force constant and μ is the reduced mass of the system where $\mu = \frac{m_1 m_2}{m_1 + m_2}$.

The reduced mass for the absorption wavenumber of the Mn-O bond remains constant between each of the doped lanthanum manganates, therefore the observed variance in the vibrational frequency must be attributed to variance in the force constant for each sample (a larger force constant results in an increased vibrational frequency). This is not surprising given that the force constant is a measure of the bond order and therefore is impacted by the extent of the double exchange mechanism present in the Mn-O bond. With different changes in the crystal structure occurring for each dopant cation, varying changes in bonds lengths and bond angles are expected. This will give rise to different degrees of orbital overlap and hence the extent of the double exchange mechanism will vary for each of the doped lanthanum manganates. The greater the extent of the double exchange mechanism the greater we would expect the extent of the observed properties (i.e. the MCE) to be [4]. Although this is a narrow study where we are only looking at three different ions, there does not appear to be a direct correlation between the average A-site cationic radii and the characteristic wavelength of the Mn-O bond.

4.3.2.2. Magnetic heating experiments

The heating curves obtained for 5mgmL^{-1} aqueous suspensions of the materials with dopant x=0.4 are shown in Figure 4.4.

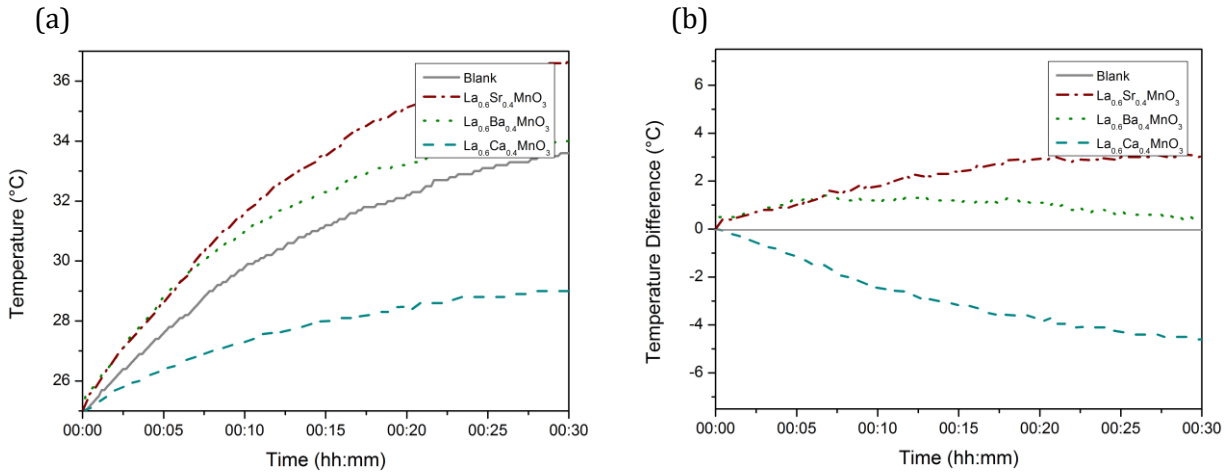

Figure 4.4: (a) Induced heating curves collected for LBMO40, LCMO40 and LSMO40 samples, of aqueous solutions of 5mgmL^{-1}. ***(b)*** Heating curves normalised to the curve obtained from the blank control to show the enhanced heating observed for the LSMO40 and LBMO40 samples, and reduced magnetic heating observed for the LCMO40 sample, relative to the blank.

Although not included in these figures, the heating profile of the LMO parent compound was also determined and found to be indistinguishable from that of the blank control capsule. We can therefore conclude that any variance in the heating curves of the samples from the blank control heating curve can be attributed as being a direct consequence of the dopant cation.

It can be seen from Figure 4.4 (a) that the extent of magnetic heating exhibited by each of the samples seems to be related to the wavelength of the IR absorptions for the Mn-O bond. The higher the wavelength of the absorption, the greater the extent of heating observed, with LCMO40 showing the shallowest curve with the smallest saturation value, followed by LBMO40 and then LSMO40. The saturation value shown by all three samples at this concentration is smaller than that required for mild hyperthermia treatment, 41-46°C with the LSMO40 sample showing heating closest to this value (36.5°C). Figure 4.4 (b) shows the temperature difference between each of the samples and the blank as a function of heating time. It can be observed from the plot that LSMO40 and LBMO40 both show an enhanced magnetic heating effect whereas LCMO40 shows a reduced magnetic heating effect, or relative magnetic cooling. It

should be noted that both LSMO40 and LBMO40 were doped with A-site cations of larger radii than the La^{3+} ion of the LMO parent compound, whereas LCMO40 was doped with an A-site cation of smaller radii. This would suggest that the crystal structure changes in LMO caused by doping with a smaller A-site cations may result in a reduced MCE whereas doping with cation of larger cationic radii may lead to an increased MCE.

The calculated SAR of each of the doped lanthanum manganates samples is plotted as a function of the characteristic wavenumber of absorption of the Mn-O bond in Figure 4.5. In general the SAR is seen to increase with increasing wavenumber, excluding LCMO40 which shows an SAR significantly lower than that of the blank in agreement with the reduced magnetic heating observed for this sample. This is as would be expected as the wavenumber essentially describes the extent of the bond order, of the Mn-O bond, on this occasion as the reduced mass remains constant between each sample. Therefore as the wavenumber increases the greater we expect the extent of the double exchange mechanism to be. This would result in an increase in the observed magnetic behaviour meaning the material must possess an increased ability to absorb energy when exposed to electromagnetic radiation (SAR).

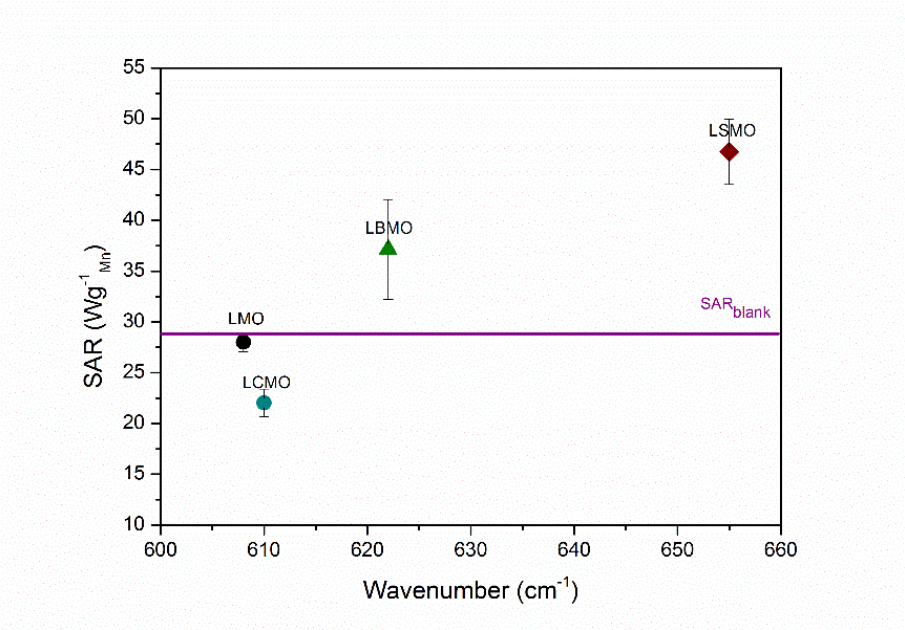

Figure 4.5: Relationship between the wavenumber of the Mn-O bond and the SAR for LSMO40, LBMO40 and LCMO40 and the undoped parent compound LMO

4.3.2.3. Magnetic measurements

Figure 4.6 shows the magnetic susceptibility of the doped lanthanum manganate samples with respect to temperature.

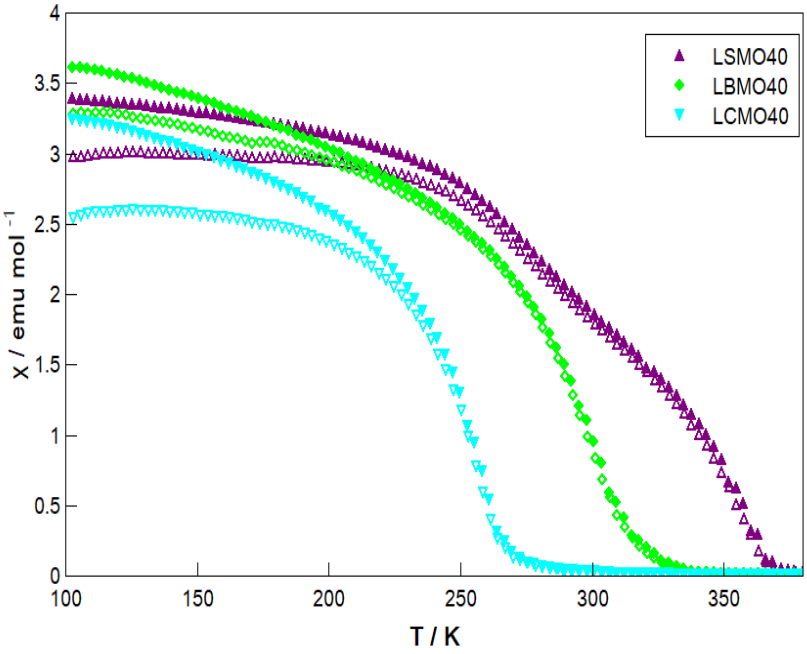

Figure 4.6: Magnetic susceptibility of LBMO40, LCMO40 and LSMO40 samples in the temperature range 100-380K. Filled symbols represent the field cooled (FC) measurement and unfilled symbols represent the zero-field cooled measurement (ZFC).

As mentioned in section 3.3.4, SQUID magnetometers are the most sensitive instruments commercially available for measuring magnetic flux. The direct device-related uncertainty for the instrument used in this study is negligible, with accuracy of $\Delta m_{dev} \sim 10^{-8}\ emu$ documented for fields of $\mu_0 H \leq 0.25T$. The smallest raw moment measured in this chapter is of magnitude 10^{-5} *emu*. The temperature sensitivity of the instrument is well below $\Delta T \leq 1K$ and the uncertainty in the applied field is around 0.5Oe, which equates to around 0.1% for the small fields applied in the susceptibility measurements. Experimental uncertainty in the measurement of the sample mass is the biggest contributor to the overall uncertainty in the magnetic measurements. The measurement device related uncertainty for the sample mass is 5 x 10^{-7} g which equates to an overall uncertainty of 0.7% in the final susceptibility measurement. As the uncertainties associated with the magnetic measurements are so small, error bars have been omitted from the plots for clarity, which is congruence with convention in the literature.

All three samples exhibit a ferromagnetic to paramagnetic transition and show different degrees of variance between the FC and ZFC curves in the low temperature regime, indicating a degree of remnant magnetisation present. As described in section 2.4, the presence of remnant magnetisation in potential mediators for hyperthermia treatment is an undesirable property as it can lead to aggregation of the MNPs and clotting in the bloodstream[13]. The presence of this remnant magnetisation would suggest that the MNPs synthesised using this process are either too large to be single domain and show superparamagnetic behaviour, or there is some form of interaction taking place between neighbouring MNPs due to the conglomeration of the particles into agglomerates. Depending on what is giving rise to this remanence it may be possible to resolve the issue by either reducing the MNP size (however this would in turn reduce the MCE exhibited) or by separating the MNP agglomerates into individual particles. This is an area of future study. In addition further insight into the magnetic mechanisms at play in these particles could be gained by studying the state of domains and domain wall motion in this system.

The ferromagnetic to paramagnetic transition region for LSMO40 shows two slight inflections. This would suggest the presence of two different ferromagnetic phases each with a different T_c, arising from the presence of two different stoichiometries. The presence of only one stoichiometry was identified by both EDX analysis and trialling different model stoichiometries used for the model structures in the Rietveld analysis carried out on the samples. LCMO40 and LBMO40 show much steeper ferromagnetic to paramagnetic transitions with no indication of multiplicity. This suggests that only one ferromagnetic phase due to a single stoichiometry is present in these two samples.

The T_c's of each sample were calculated from the magnetic susceptibility data (Figure 4.7) and are displayed in Table 4.8 [20].

Sample	M_s @ 100K (emu/mol)	M_r @ 100K (emu/mol)	T_c (K)
LSMO40	3500 ± 22	175 ± 2.5	352 ± 6
LBMO40	3800 ± 22	162 ± 2.5	312 ± 5
LCMO40	4800 ± 24	342 ± 3.1	262 ± 2

Table 4.8: Parameters derived from the magnetisation measurements for LSMO40, LCMO40 and LBMO40 (T_c – Curie temperature, Ms – saturation magnetisation and Mr – remnant magnetisation)

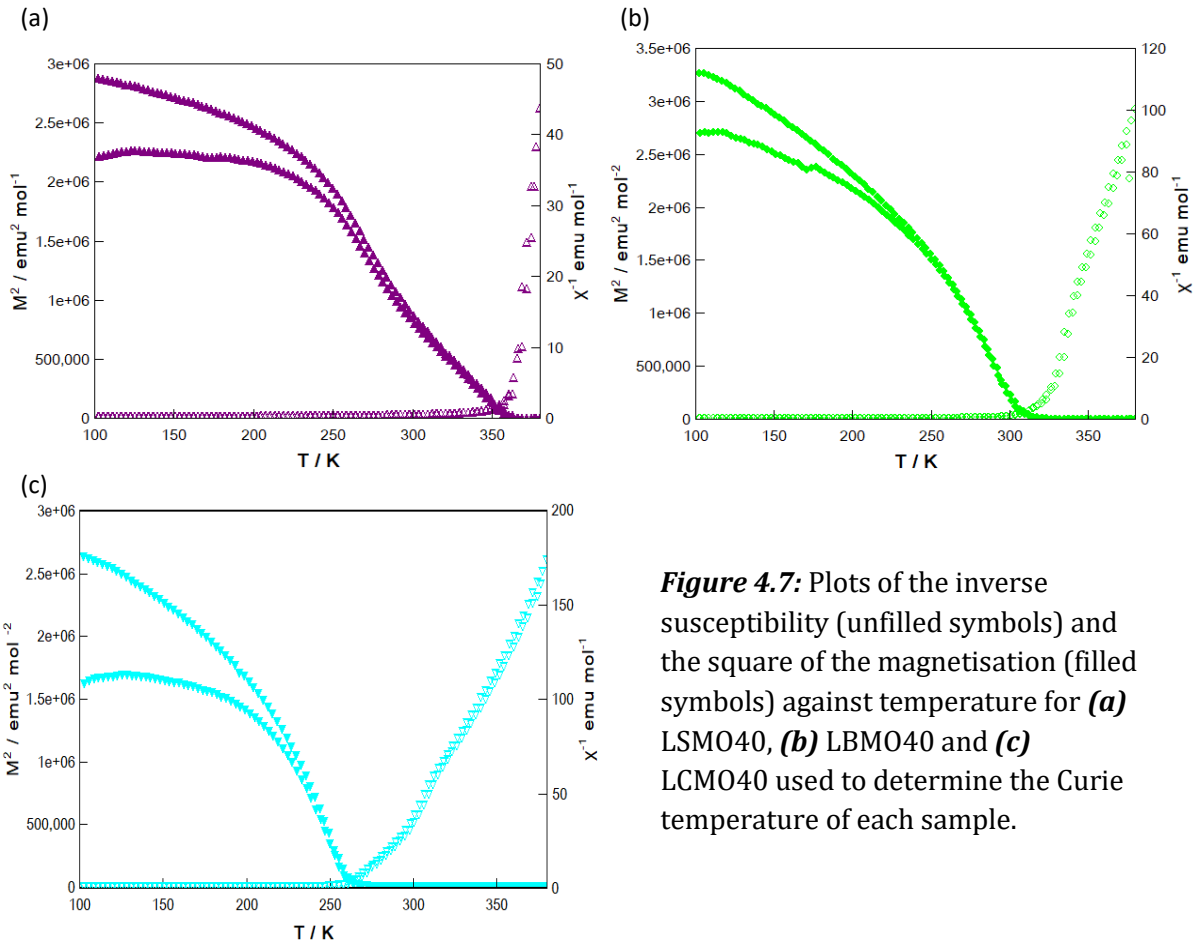

Figure 4.7: Plots of the inverse susceptibility (unfilled symbols) and the square of the magnetisation (filled symbols) against temperature for ***(a)*** LSMO40, ***(b)*** LBMO40 and ***(c)*** LCMO40 used to determine the Curie temperature of each sample.

Usually T_c is estimated through the temperature derivative of the magnetisation in the transition region, but the multiplicity in the magnetic susceptibility exhibited by the LSMO40 sample makes it difficult to obtain a single T_c in this manner as a result of a skewed magnetisation derivative. Therefore on this occasion the T_c was calculated by determining the point at which the plots of the inverse susceptibility against temperature and magnetisation squared against temperature intersect, see Figure 4.7. The T_c obtained for the LSMO40 sample will be an average of the two different T_c's of the ferromagnetic stoichiometries present.

As can be seen from Table 4.8 the T_c obtained for LCMO40 is significantly below room temperature, the T_c obtained for LBMO40 is just above room temperature and the T_c obtained for LSMO40 is significantly larger than room temperature. The low T_c's identified for LSMO40 and LBMO40 (262K and 312K respectively) are in keeping with the literature and would suggest that neither material would exhibit a significant MCE at room temperature [21][5]. This is supported by the magnetic heating data, which show both the LCMO40 and LBMO40 heating curves to display only a relatively small variance to that of the blank, in comparison to the LSMO40 sample. A normal or enhanced magnetic heating is generally found to take place when the MNPs exhibit ferromagnetic behaviour as described in section 2 in detail [22-23].

When a magnetic field is applied to a ferromagnetic MNP three types of dissipative magnetic response may take place: Neél rotations, Brownian rotations or hysteresis, as the electron spins align along the applied field. All three responses lower the magnetic entropy of the system resulting in a localised increase in temperature to conserve the overall entropy of the system. When a material has a low T_c, it will only be able to undergo a limited amount of heating before a transition from the ferromagnetic to paramagnetic state is initiated. When the material transitions to the paramagnetic state there is no longer the same magnetic ordering with applied field and resultant lowering of magnetic entropy. A change in thermal entropy is therefore no longer necessary to conserve the total entropy of the system, and magnetic heating halts. In hyperthermia treatment there is a trade-off between wanting a material with a low T_c to prevent overheating of neighbouring tissues, and wanting a material with a high enough T_c to reach the mild hyperthermia treatment range of 41-46°C.

As both LSMO40 and LBMO40 are ferromagnetic at room temperature it is unsurprising that they both exhibit some degree of magnetic heating. As mentioned previously further insight into the origin of the ferromagnetic behaviour at play in these particles could be gained by studying the state of domains and domain wall motion in this system. This will be addressed in the conclusions and future work section.

In comparison to LSMO40 and LBMO40, LCMO40 is paramagnetic at room temperature and actually shows a small degree of magnetic cooling. It is possible that LCMO40 undergoes some form of crystal transformation as a result of the application of the magnetic field, akin to that reported by Urushibara et al. [24-25].

If we consider the heat capacity of the system we can explain what may be happening to the LCMO40 sample during the heating experiments. Heat capacity is a measure of the change in internal energy, comprised of magnetic, electronic and lattice contributions, with observed temperature change. Where there is a considerable change in the internal energy, such as in the region of a magnetic phase transition we would expect to see anomalous behaviour in the heat capacity of the material. As LCMO40 is in the paramagnetic regime at room temperature, and the T_c of the sample is significantly lower than room temperature, the effect of magnetic contributions to the heat capacity is likely to only be very minimal. It is therefore likely that a change in the lattice heat capacity caused by a crystal structure transformation is responsible for the magnetic cooling shown by this sample. Latent heat resulting from conventional heating in the induction coils may well be sufficient to initiate this change in crystal structure. In order to maintain the entropy of the system the sample uses the latent heat energy to facilitate this transition and as a result it is not dissipated. Hence the observed relative reduction in magnetic heating compared with the blank observed from the induction heating experiment.

DC field dependant measurements were taken for each sample at 100 and 150K, to investigate the remnant magnetisation and saturation magnetisation of each sample at these temperatures, Figure 4.8.

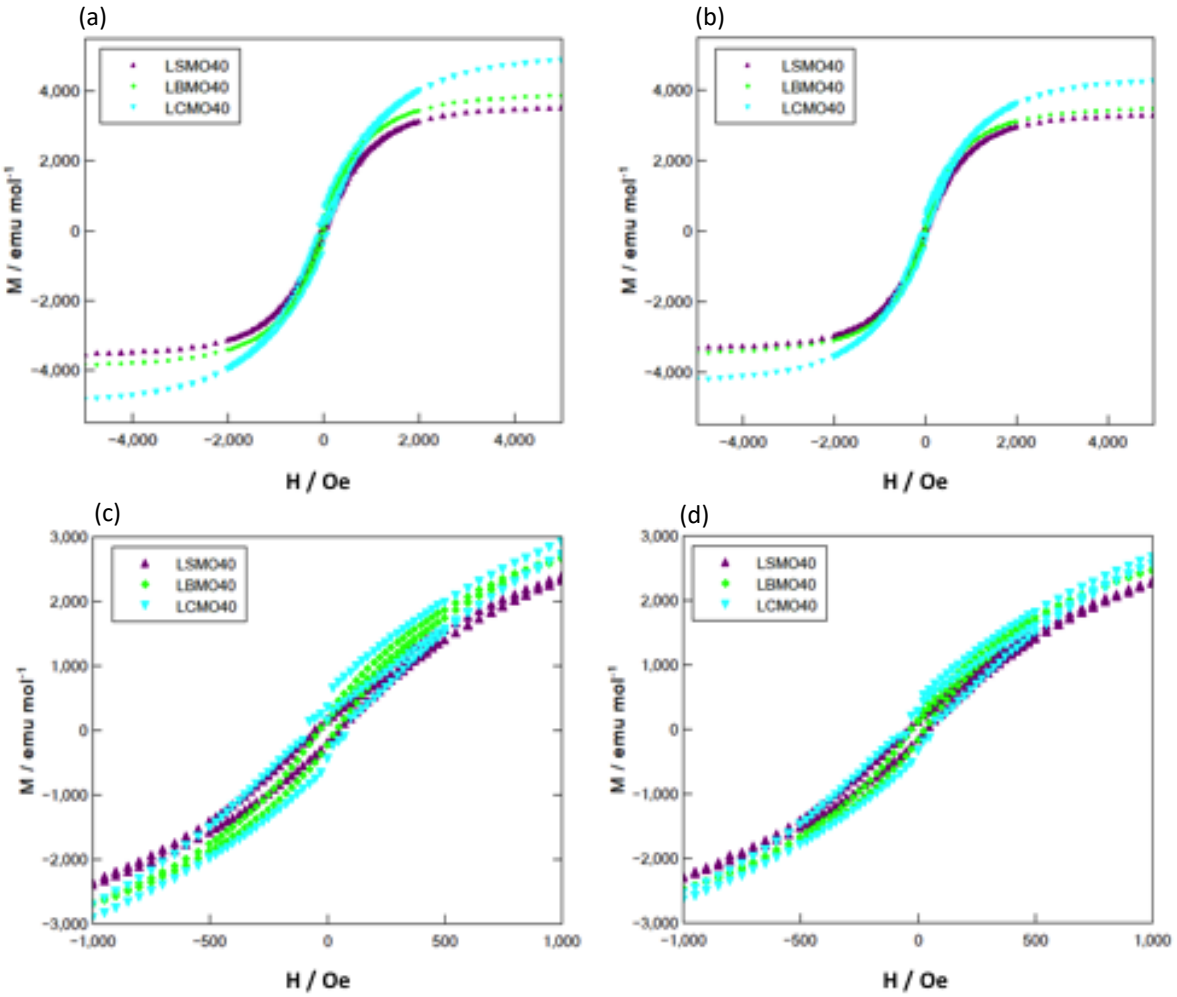

Figure 4.8: Field dependent magnetisation data collected for LSMO40, LCMO40 and LBMO40 with a maximum applied field of 5000Oe, collected at 100K (***(a)***and ***(c)***) and 150K (***(b)***and ***(d)***).

At both temperatures it can be seen that LCMO40 shows the highest magnetisation saturation (M_s) value, followed by LBMO40 and then LSMO40. At both 100K and 150K all three samples are in the ferromagnetic state. Typically materials with a larger M_s will show a more efficient magnetic heating as if the applied field is large enough it will give rise to a larger magnetic response. However we see the largest magnetic heating from LSMO40 followed by LBMO40 and then LCMO40, which shows reduced magnetic heating. This is as a direct result of the T_c's of these three materials. Although LCMO40 has the highest M_s of the three materials at 100K and 150K, it is in fact paramagnetic at room temperature and therefore shows no enhanced magnetic heating in the high temperature regime. The next highest M_s was shown by LBMO40, which is ferromagnetic at room temperature. The T_c for LBMO40 was found to be 312K which is very close to the saturation heating value of 307K found for the 5mgmL^{-1} aqueous suspension of the material. It is likely that the ferromagnetic to paramagnetic transition of the material was

starting to occur during the heating experiments, essentially switching off the magnetic heating of the sample and preventing a larger magnetic heating from taking place. Although LSMO40 showed the smallest M_s, it showed the highest extent of magnetic heating of the three samples. The T_c obtained for LSMO40 was 352K and therefore significantly larger than both room temperature and the temperature reached by the sample due to magnetic heating in the AC applied field (309K). Therefore no ferromagnetic to paramagnetic transition of the material occurred during the induction heating experiments and a maximum final saturation of magnetic heating was achieved.

The remnant magnetisation of each sample at both 100K and 150K was obtained from the hysteresis loops and is displayed in Table 4.8. It is important to note that all three samples showed some remanence at these temperatures, with LCMO40 to the greatest extent, followed by LSMO40 and then LBMO40. Therefore the MNP's are either too large to be single domain and show superparamagnetic behaviour or there is some form of intra-particle interaction occurring which is giving rise to this behaviour. Further work is currently ongoing to both explain and address this issue. As these magnetisation measurements where collected using a DC field rather than an AC field as in the magnetic heating experiments, it is not possible to draw any further comparisons or conclusions from the two data sets. AC susceptibility data will be collected in future work.

4.3.3. Conclusions

$La_{1-x}Ca_xMnO_3$, $La_{1-x}Ba_xMnO_3$ and $La_{1-x}Sr_xMnO_3$ were synthesised using a modified peroxide sol-gel synthesis, where x=0.4, which hasn't previously been reported for either LCMO or LBMO. We were able conclude that using an A-site dopant of larger cationic radii than La^{3+}, Sr^{2+} and Ba^{2+}, led to an enhanced magnetic heating effect whereas doping using an A-site cation of smaller radii than La^{3+}, Ca^{2+}, led to a reduced magnetic heating. None of the three samples exhibited magnetic heating in the mild hyperthermia range (41°C – 46°C), but LSMO40 proved to be the most promising candidate of the three, exhibiting both the largest magnetic heating (36.5°C) and highest SAR ($46 Wg^{-1}_{Mn}$). The trend of diminishing SAR with dopant cationic radii, from LSMO40 to LBMO40 and then LCMO40, was identified from the heating curves and was consistent with the trend visible for the characteristic absorbance of the Mn-O bond in each of the materials. As mentioned earlier a low T_c is an attractive property for MNPs for use in hyperthermia treatment as this helps to prevent overheating of neighbouring healthy tissue. However this study has outlined the issues that can arise when the T_c of the material is too low (i.e. below or too close to room temperature).

As mentioned at the start of this section, we were particularly interested in the effect of the dopant cationic radii on the crystal structure and magnetic properties of the resulting complex. However by substituting the La^{3+} ions with ions with valency 2+, there is a simultaneously substitution of Jahn-Teller active Mn^{3+} for non Jahn-Teller active Mn^{4+}. This results in a decrease in the Jahn-Teller distortion of the crystal complex and an overall decrease in the rhombohedral crystal phase observed when LMO is doped with alkaline earth metals. As such we choose to compare the structural modifications to the perovskite structure along with the subsequent effects on the magnetic properties of the three doped complexes rather than compare them with the parent compound. We go on to investigate the effect of Mn^{3+}/Mn^{4+} ratio and resulting change in Jahn-Teller distortion in doped complexes in the second section of this chapter.

4.4. Effect of varying A-site dopant concentration

In the second part of this study, the effect of dopant concentration on the magnetic properties (magnetic susceptibility, SAR and T_c) of lanthanum strontium manganates ($La_{1-x}Sr_xMnO_3$) prepared using a modified sol-gel method, was investigated. As with the previous section, the aim was to enhance the SAR of the MNPs whilst reducing the T_c, to optimise the material for potential use in hyperthermia treatment. As shown in the previous section the substitution of larger Sr^{2+} ions for the smaller La^{3+} ions results in a distortion of the local crystal lattice away from the rhombohedral geometry of the parent compound, causing a change in the Mn-O bond length and Mn^{3+}-O^{2-}-Mn^{4+} bond angle. In addition to this, the substitution of Sr^{2+} results in the substitution of Jahn-Teller active Mn^{3+} for non Jahn-Teller active Mn^{4+} ions. Both of these consequences of Sr^{2+} substitution have different effects on the extent of the double exchange mechanism leading to a change in the magnetic properties of the material, as outlined in section 2.4. As with the previous study in this chapter, the structural modifications to the perovskite structure along with the subsequent effects on the magnetic properties of the material are investigated in this study.

4.4.1. Experimental

4.4.1.1. Material Synthesis

The $La_{1-x}Sr_xMnO_3$ MNP's were synthesised using the same modified peroxide sol-gel synthesis described in section 4.3.1.1. The desired stoichiometric ratios (x=0.2, 0.25, 0.3, 0.35, and 0.4) for the different Sr-doping levels were achieved by carefully controlling the proportions of lanthanum (II) oxide (La_2O_3), manganese (II) carbonate and strontium carbonate precursors used in the synthesis process. Table 4.10 shows all the synthesised samples with their corresponding Sr dopant levels and their designated sample names.

4.4.1.2. Characterisation

The synthesised samples underwent the same analysis as outlined in section 4.3.1.2. SEM, EDX, XRD and subsequent Rietveld analysis, FTIR and SQUID magnetometry were all carried out using the same instruments and conditions as described previously.

The mass of the measured samples, number of moles of each sample and diamagnetic contributions applied to the magnetic measurements conducted in the SQUID magnetometer are displayed in Table 4.9.

Sample	**Mass (g) x10^{-4}**	**Moles of sample (mol) x10^{-6}**	**Diamagnetic correction applied (emu/mol) x10^{-5}**
LSMO25	6.30 ± 0.05	2.751 ± 0.022	-6.475 ± 0.097
LSMO35	7.10 ± 0.05	3.171 ± 0.022	-6.465 ± 0.097
LSMO40	7.10 ± 0.05	3.208 ± 0.023	-6.460 ± 0.097
LSMO45	6.90 ± 0.05	3.154 ± 0.023	-6.455 ± 0.097

Table 4.9: Table displaying the sample mass, number of moles of each sample and the material specific diamagnetic correction applied to the magnetic measurements

As in the previous section, an additional diamagnetic background contribution of 5 x10^{-9} emu/Oe due to the straw and gelatine capsules containing the samples was also calculated and accounted for.

Non-adiabatic heating experiments were conducted using the same experimental set up as before (Figure 4.2) but in addition to an aqueous solution of the MNP's of 5mgmL^{-1} being prepared and investigated, suspensions at 10mgmL^{-1} and 15mgmL^{-1} were also studied. In practice, in hyperthermia treatment, the suspension of MNPs administered to the patient can be tailored to bring the overall heating of the particles into the mild hyperthermia range. In this study the aim was to achieve heating within this desired temperature range. Suspensions of the MNPs are only investigated in the magnetic heating experiments; powdered samples are used in the rest of the experiments. The results obtained from the induction heating measurements were used to calculate the SAR of each sample using Equation 4.1. In addition to the analysis methods outlined in section 4.3.1.2., the experimental heating curves were modelled using a simple two temperature model, by L. Stella. This model is based on the balance between energy absorbed and released by the MNP and heat lost to the environment. This can be expressed by the following two differential equations

$$f_m C_p^{(m)} \frac{dT_m}{dt} = f_m K_{rf} - f_m g\,(T_m - T_s), \qquad \textbf{Equation 4.3}$$

$$C_p^{(s)} \frac{dT_s}{dt} f_m g\,(T_m - T_s) - K_{out}\,(T_s - T_{room}), \qquad \textbf{Equation 4.4}$$

where T_m is the temperature of the MNP, T_s is the temperature of the solvent, T_{room} is the temperature of the environment, $C_p^{(m)}$ is the specific heat capacity at constant pressure of the MNP, $C_p^{(s)}$ is the specific heat capacity at constant pressure of the solvent, f_m is the sample concentration of MNP's in water, g is the specific heat transfer coefficient, K_{rf} is the specific absorption rate of the MNP's (and not per g_{Mn} as is the SAR), and K_{out} is the specific loss rate of the solvent to the environment. To simplify the calculations, it was assumed that all parameters in the equations are temperature independent. In particular, $C_p^{(m)}$ was set = 1.44706 x 10^3 J kg^{-1} K^{-1} and $C_p^{(s)}$ = 42 x 10^3 J kg^{-1} K^{-1} (for water). The sample concentration has been set to f = 10 mg g^{-1} = 0.01.

Following Rietveld refinement of the diffraction patterns, the Scherrer equation using full-width half maximum was used to determine the size of the crystallites. The most intense reflection was used, which in all cases occurred at approximately 32 degrees 2ϑ from the XRD patterns [26]. Using the calculated crystallite size and the saturation magnetisation determined from the SQUID magnetometry measurements, it was possible to calculate a magnetically dead layer for

each sample. This considers each nanoparticle as a core-shell nano-object where the crystalline core is embedded in this magnetically dead layer. The thickness of this layer was determined according to the following equation [27].

$$th_{MDL} = \left(\frac{S_{cryst}}{2}\right)\{1 - \left[\frac{M_S^{nano}}{M_S^{bulk}}\right]^{\frac{1}{3}}\} \qquad \textbf{Equation 4.5}$$

where M_S^{nano} is the saturation magnetisation for the nanometric material, M_S^{bulk} is the saturation magnetisation for the bulk homogeneous material and S_{cryst} is the average crystallite size for the sample.

The saturation magnetisation values for each sample were taken from the field dependant measurements carried out at 100K. The M_S^{bulk} value was taken for the bulk sample measured in the work by L. Balcells et al [28]. As the saturation magnetisation value for this sample was obtained at 10K it was necessary to scale it to the value we would expect when T=100K, using Bloch's law. This gave a M_S^{bulk} of 20943 emu/mol.

4.4.2. Results and discussion

4.4.2.1. Crystalline structure and configuration analysis

As in the previous section, SEM and EDX analysis was carried out for each of the complexes in this study. Details of these experiments and the SEM images and EDX maps for each complex can be found in the main paper or supplementary information of reference 26. Similarly to the MNPs synthesised in the previous section, the SEM images showed that the particles synthesised in this study formed agglomerates and made identification of individual particle size unachievable.

Table 4.10 shows the stoichiometry of the synthesised samples, as verified by EDX, to be in keeping with the desired ratios.

Sample	Sample Name	EDX stoichiometry
$LaMnO_3$	LMO	-
$La_{0.8}Sr_{0.2}MnO_3$	LSMO20	$La_{0.82}Sr_{0.18}MnO_3$
$La_{0.75}Sr_{0.25}MnO_3$	LSMO25	$La_{0.76}Sr_{0.24}MnO_3$
$La_{0.7}Sr_{0.3}MnO_3$	LSMO30	$La_{0.72}Sr_{0.28}MnO_3$
$La_{0.65}Sr_{0.35}MnO_3$	LSMO35	$La_{0.66}Sr_{0.34}MnO_3$
$La_{0.6}Sr_{0.4}MnO_3$	LSMO40	$La_{0.62}Sr_{0.38}MnO_3$

Table 4.10: Details of the samples prepared and investigated during this study including the stoichiometry of each sample as determined by EDX analysis.

As in the previous section, the overall analytical accuracy in the EDX measurements in this study is around ± 2%, owing to uncertainties in the compositions of the standards used in the quantification and the various corrections applied to the raw data.

XRD and subsequent Rietveld analysis of the LSMO samples and parent LMO compound, which had been synthesised using the same modified peroxide sol-gel process, confirmed the predominant geometry present to be rhombohedral (R-3c) with a small amount of orthorhombic (Pnma) geometry also evident in all samples. It was observed that with increasing strontium dopant, the relative weight percentage of the orthorhombic (Pnma) crystalline phase increased with respect to the rhombohedral (R-3c) crystalline phase (see Figure 4.9). This behaviour was also reported by Dokiya et al. who documented the structural transition of LSMO from rhombohedral (R3c) to higher orthorhombic and rhombohedral symmetries with increasing Sr dopant or decreasing oxygen content [29]. Details of the XRD and Rietveld analysis and the XRD patterns for each complex can be found in the main paper and supplementary information of reference 26.

The crystallite size and relevant weight percentages of each crystal phase and their corresponding lattice parameters, derived from the Rietveld analysis, for each of the doped lanthanum manganates synthesised in this study, are displayed in the following table.

Sample	Cryst. Dia. (nm)	Space Group	a / Å	b / Å	c / Å	α / °	β / °	γ / °	V / Å^3	Wt. Perc. / %
LMO	164.9	Pnma	7.431	8.416	5.714	90	90	90	357.4	4.5
		R-3c	5.522	5.522	13.369	90	90	120	353.1	95.5
LSMO25	82.4	Pnma	5.437	7.798	5.433	90	90	90	230.4	8.2
		R-3c	5.515	5.515	13.355	90	90	120	351.7	91.8
LSMO35	82.4	Pnma	5.448	7.743	5.468	90	90	90	230.4	19.7
		R-3c	5.512	5.512	13.354	90	90	120	351.4	80.3
LSMO40	61.9	Pnma	5.448	7.750	5.456	90	90	90	230.4	31.2
		R-3c	5.511	5.511	13.354	90	90	120	351.2	68.8

Table 4.11: Structural information for the LMO, LSMO25, LSMO35 and LSMO40 complexes derived from Rietveld analysis

From the Rietveld analysis an overall decrease in the cell volume was observed with increased strontium dopant, Table 4.11. This may seem counterintuitive as lanthanum (cationic radius of 1.36Å [12]) ions are being substituted with larger strontium ions with cationic radii 1.44Å [12], but can actually be attributed to the decrease in the B-site cationic radii which arises as a direct result of this substitution. As the LMO parent compound is doped with Sr ions there is a substitution of the B-site cation Mn^{3+} with radius 0.645Å [12] with the smaller Mn^{4+} ion of cationic radius 0.53Å [12]. As the difference in the cationic radii between Mn^{3+} and Mn^{4+} (0.115Å) is larger than the difference in cationic radii between La^{3+} and Sr^{2+} (0.08Å), an overall decrease in the cell volume is observed with increasing Sr dopant concentration [30].

Figure 4.9 shows the relative weight percentage of each crystalline phase present in the doped manganate samples, and the corresponding cell volumes, derived from Rietveld analysis of powdered samples of the MNPs.

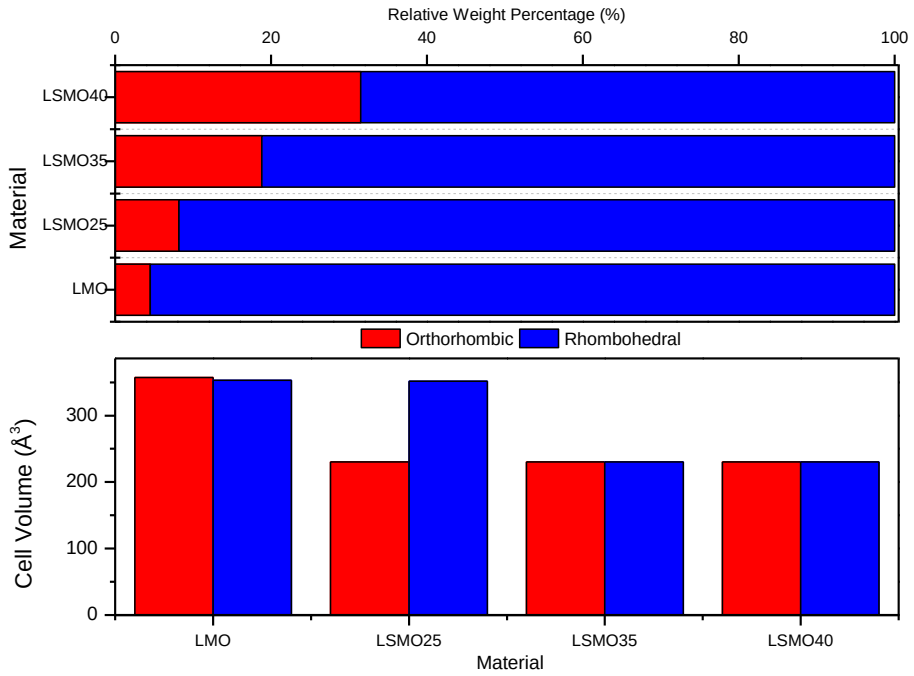

Figure 4.9: Crystal structure comparison of orthorhombic and rhombohedral phases for relative weight percentages and unit cell volumes for LMO, LSMO25, LSMO35 and LSMO40.

From Figure 4.9 it appears that there is minimal difference in the cell volume between the orthorhombic and rhombohedral crystalline phases in the LMO, LSMO35 and LSMO40 samples. For LSMO25 however, there is a 52% increase in the cell volume of the rhombohedral structure than the cell volume of the orthorhombic structure. From Sr dopant concentration of x=0 to x=0.25 there is only a 3.7% increase in the relative weight percentage of the orthorhombic phase observed however the increase in the relative weight percentage of the orthorhombic phase is 11.5% when the Sr dopant level changes from x=0.25 to x=0.35 and also from x=0.35 to x=0.4. It is possible that these two traits in the crystalline structure may be related. For both the rhombohedral and orthorhombic crystal phases there is a reduction in cell volume of approximately 35% between x=0 and x=0.35. This decrease in cell volume would result in shorter bond lengths and greater bonding orbital overlap meaning the double exchange mechanism will be more effective. Hence we would expect to see enhancement of the magnetic properties between x=0 and x=0.35. In addition, the change in crystal structure from rhombohedral to orthorhombic geometry causes a reduction in γ from 120° – 90°. This means that a greater proportion of Mn^{3+}-O^{2-}-Mn^{4+} bonds should come close to 180°, which is optimal for the double exchange mechanism [4]. It is therefore expected that LSMO35 and LSMO40 should be able to participate more effectively in the double exchange mechanism. We would

therefore expect these complexes to exhibit a more enhanced MCE as they will exhibit a larger change in magnetic entropy on application of an applied field, due to their enhanced magnetic behaviour, and therefore greater magnetic heating is required to conserve the entropy of the system.

Figure 4.10 shows the FTIR analysis for the prepared manganate samples.

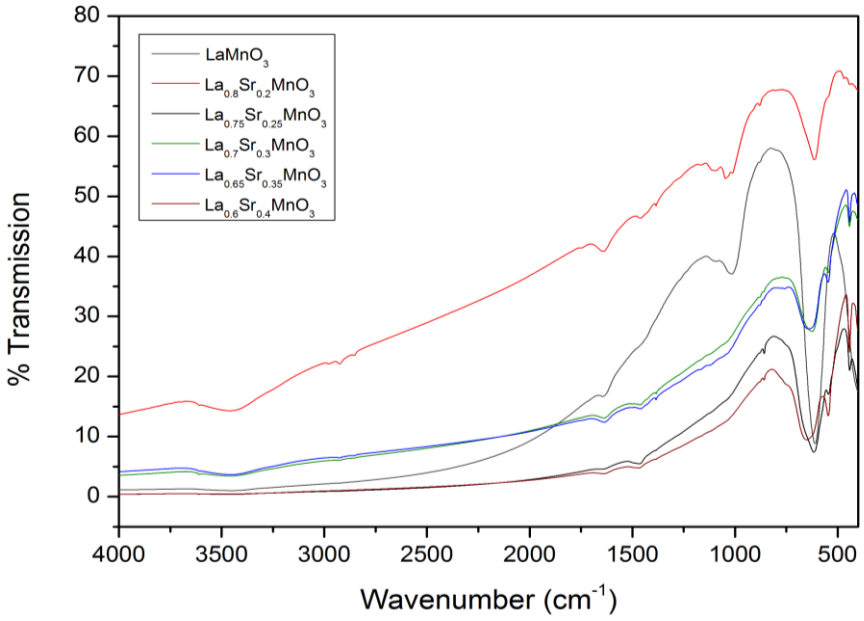

Figure 4.10: FTIR spectra for LSMO20, LSMO25, LSMO30, LSMO35 and LSMO40 compared with LMO

In all six cases the Mn-O bond can be identified by the absorption at 600cm^{-1}, indicating the presence of octahedral MnO_6. The wavenumber of this absorption is observed to increase with increased doping of Sr ions which is evidence of the increasing energy required to manipulate the Mn-O bond in the more distorted orthorhombic crystal structure than the rhombohedral crystal structure. In the previous section it was reported that an increase in wavenumber corresponded to an increase in the extent of the double-exchange mechanism present in the Mn-O bond and hence the extent of the predicted magnetic properties such as the MCE. As a result you may expect that the MCE exhibited by each sample would simply increase with increased dopant concentration. However it is important to note that that optimal MCE is often observed in regions of magnetic and crystal phase transitions (see section 2.4). As it is around x=0.35 (LSMO35) where we begin to see significant changes in the relative weight percentages of the orthorhombic and rhombohedral geometries and a sizable reduction in the cell volumes of both these crystal phases, we may expect the maximum caloric effect for the LSMO35 sample. Additionally as there is no difference in the cell volume of the orthorhombic and rhombohedral

crystal structures between x=0.35 and x=4, it is possible that there will be no shortening of the Mn-O bond length in this region and hence no enhancement of the double exchange mechanism as a direct result of this. Further investigation of this will be discussed in the conclusions and future work section.

4.4.2.2. Magnetic heating experiments

Figure 4.11 shows the heating curves for doped LSMO samples where 0.2 < x < 0.4 for a sample concentration of 10mgmL^{-1}.

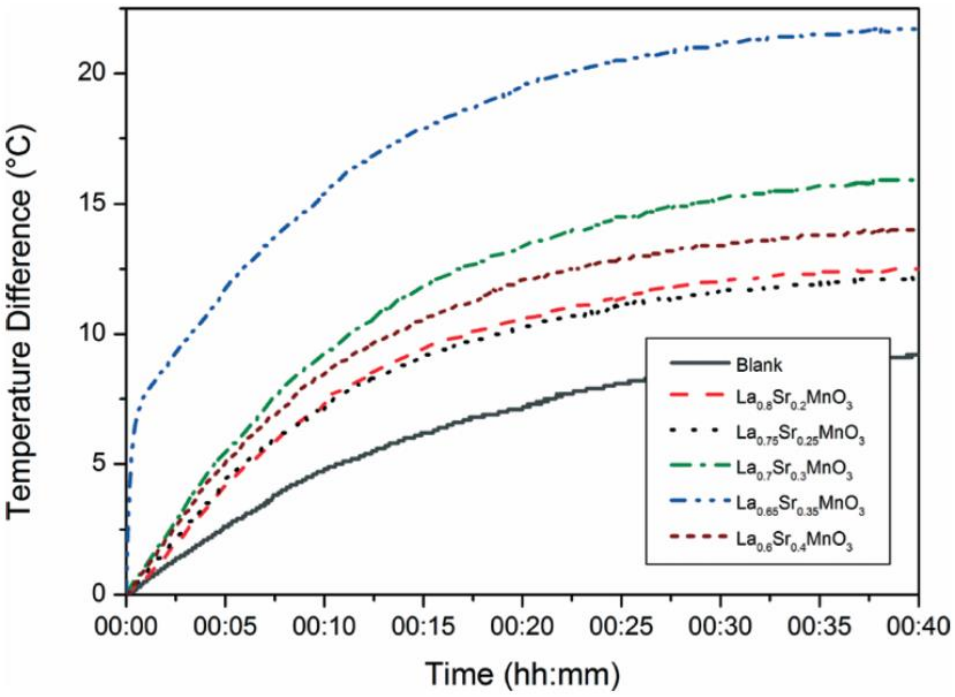

Figure 4.11: Heating curves of the range of doped LSMO materials using aqueous suspension of 10 mg mL $^{-1}$ and 1mL volume.

A different saturation temperature will be achieved for each concentration of the MNPs however the heating profile will follow the same profile. It can be seen that in general between 0.2 < x < 0.35 as the Sr dopant increases so does the maximum temperature reached by each heating profile. LSMO40 however does not follow this trend and the maximum temperature reached by the heating profile for this sample lies between that reached by the LSMO20 and LSMO30. It is also observed that the heating profiles obtained for LSMO20 and LSMO25 are very

similar. We observed during the XRD and Rietveld analysis that only a small relative weight percentage change was observed in the orthorhombic crystal structure from x=0 to x=0.25 (+3.7%). In addition, although there is a reduction in the cell volume of the orthorhombic crystal phase, there was no reduction observed for the rhombohedral crystal phase between x=0 and x=0.25. We would therefore expect that LSMO20 and LSMO25 would show less magnetic heating than for the samples were x > 0.25 where there is a much more significant change in the relative weight percentage of the orthorhombic crystal phase and a 35% reduction in the cell volumes of both the rhombohedral and orthorhombic crystal phases. In addition, the change in crystal structure from rhombohedral to orthorhombic geometry causes a reduction in γ from 120° – 90°. This means that a greater proportion of Mn^{3+}-O^{2-}-Mn^{4+} bonds should come close to 180°. As detailed in section 4.4.2.1, we expect that as the orthorhombic geometry increases and more Mn^{3+}-O^{2-}-Mn^{4+} bonds should come close to 180°, there will be an enhancement of the double exchange mechanism [4]. This combined with the shorter bond lengths which accompany the reduction in cell volume observed for this change in geometry result in enhancement of the magnetic properties of these materials. We would therefore expect these complexes to exhibit a more enhanced MCE as they will exhibit a larger change in magnetic entropy on application of an applied field, due to their enhanced magnetic behaviour, and therefore greater magnetic heating is required to conserve the entropy of the system.

The reason for the reduction in the magnetic heating exhibited by the LSMO40 sample in comparison to the LSMO35 sample is probably as a result of the increased substitution of Jahn-Teller active Mn^{3+} for non Jahn-Teller active Mn^{4+}. The decrease in Jahn-Teller active ions means there is a reduction in the Jahn-Teller distortion of the Mn^{3+}-O^{2-}-Mn^{4+} bond toward 180° and as a result a decrease in the extent of the double exchange mechanism [4]. It is possible that below x=0.4 the effect of reduced Jahn-Teller distortion with increased Sr dopant is not having an overall impact on the magnetic heating exhibited as the enhancement of the double exchange mechanism due to the crystal structure change from rhombohedral to orthorhombic is larger than the reduction caused by decreased Jahn-Teller distortion. Therefore there would be an overall enhancement of the double exchange mechanism and an overall increase of magnetic heating is observed. However if above x=0.35 there is a reduction in the change of crystal structure the reduction in Jahn-Teller distortion may become the dominant effect causing an overall reduction in the extent of the double exchange mechanism and the magnetic heating exhibited to start to decrease. Although the change in relative weight percentage of the orthorhombic crystal phase is large between x=0.35 and x=0.4, we do notice that there is no change in the cell volume of these two phases at these dopant levels. Therefore there will be no

further enhancement of the double exchange mechanism as a result of shortening of the Mn-O bond length.

Figure 4.12 (a) shows the saturation temperatures achieved by all the LSMO samples at the three different concentrations investigated (5mgmL^{-1}, 10mgmL^{-1} and 15mgmL^{-1}). Samples of 1mL in volume where measured.

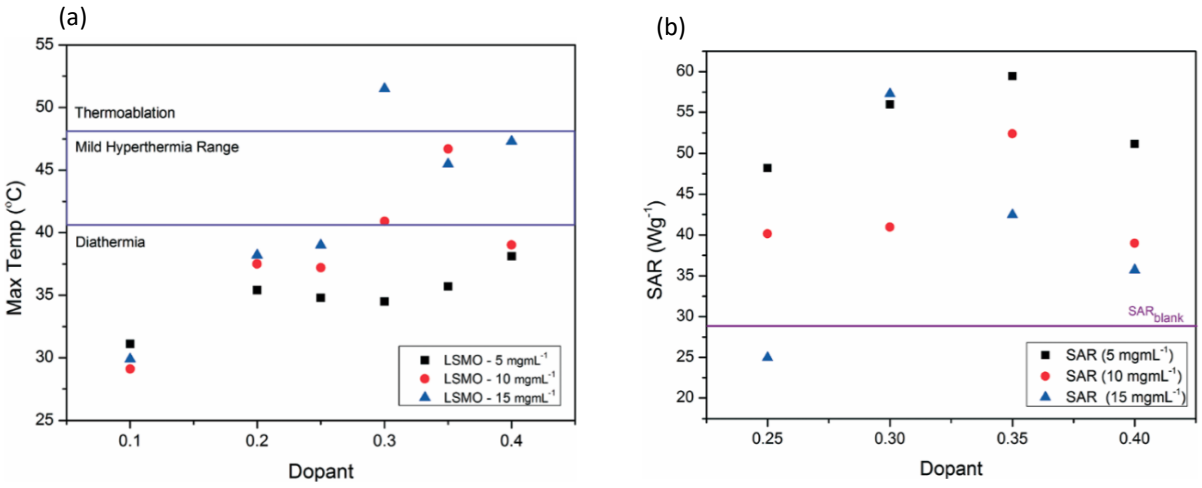

Figure 4.12: (a) Maximum temperatures reached by the range of d0ped LSMO materials at various suspension concentrations. ***(b)*** Specific absorption rates reached by the range of doped LSMO materials.

In general increasing the suspension concentration increases the maximum temperature achieved. For example; where x=0.3, the maximum temperature reached increases from 34.5°C at 5mgmL^{-1}, to 40.9°C at 10mgmL^{-1} and to 51.5°C at 15mgmL^{-1}. The dopant concentration for obtaining the optimal maximum temperature is also a function of the suspension concentration dropping from x=0.4 for 5mgmL^{-1} (38.1°C) to x=0.35 for 10mgmL^{-1} (46.7°C) and then to x=0.3 for 15mgmL^{-1}. The results obtained from the induction heating experiments were used to calculate the SAR for each sample, which are displayed for each suspension concentration in Figure 4.12 (b) as a function of dopant concentration. The optimal SAR's at concentrations of 5, 10 and 15mgmL^{-1} are found for samples were $0.3 < x < 0.35$. The greatest optimal SAR of 59.43 Wg_{Mn}^{-1} was obtained at a concentration of 5mgmL^{-1} where x=0.35. However the maximum heating temperature achieved by this sample at this suspension concentration was only 35.7°C. As outlined earlier the heat generated by MNP's in hyperthermia treatment should be in the range of 41°C – 46°C. It is also important that these MNP's have a high SAR. The MNP's in this study which best satisfy these two conditions are LSMO with x=0.35 at a suspension

concentration of 10mgmL^{-1}, which have a maximum heating temperature of 46.7°C and an SAR of 52.5 Wg_{Mn}^{-1}.

Equations 4.3 and 4.4 were both solved numerically for suspension concentration 10mg/mL, and the result for $T_s(t)$ was fitted to the experimental heating data, using a standard least square regression. The calculated parameters (as discussed previously) as a function of the doping, x, are shown in Table 4.12. These are in very good agreement with the SAR's calculated using Wildeboer et al's method, shown in Figure 4.12 [18].

Sample	**SAR W g_{MN}^{-1}**	**T_{MAX} (°C)**
LSMO20	53.67	35.60
LSMO25	47.97	35.12
LSMO30	53.12	34.61
LSMO40	53.83	35.91

Table 4.12: Calculated modelling parameters using Equations 4.3 and 4.4.

4.4.2.3. Magnetic measurements

Figure 4.13 shows the magnetic susceptibility of a selection of the doped lanthanum manganate samples ($0.25 < x < 0.45$) with respect to temperature. As detailed 4.3.2.3 the direct device-related uncertainty for the instrument used in this study is negligible due to the size of magnetic responses being investigated. Experimental uncertainty in the measurement of the sample mass is the biggest contributor to the overall uncertainty in the magnetic measurements which amounts to 0.7% uncertainty in the final susceptibility measurement. As the uncertainties associated with the magnetic measurements are so small, error bars have been omitted from the plots for clarity, which is congruence with convention in the literature.

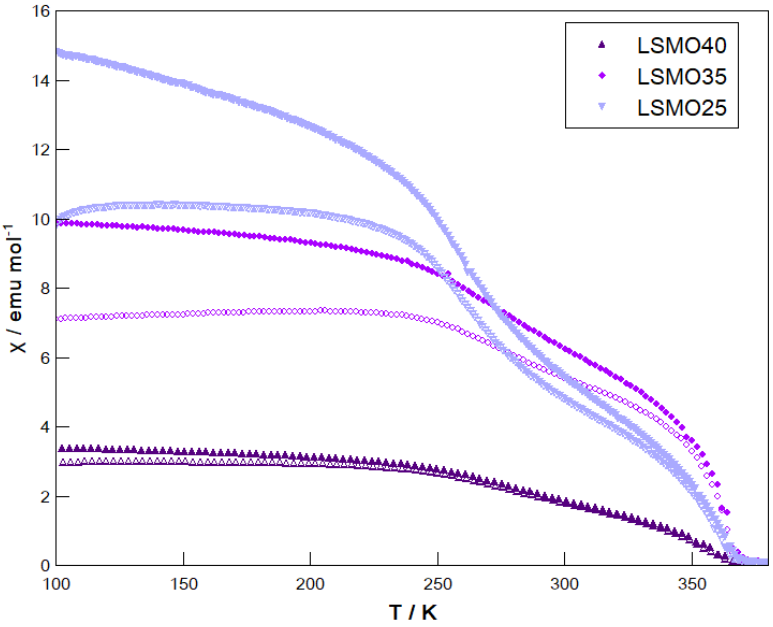

Figure 4.13: Magnetic susceptibility of LSMO25, LSMO35 and LSMO40 samples in the temperature range 100-380K. Filled symbols represent the field cooled (FC) measurement and unfilled symbols represent the zero-field cooled measurement (ZFC)

All three samples show a ferromagnetic to paramagnetic transition, with some degree of variance between the FC and ZFC curves in the low temperature regime. As described in section 4.3.2.3. this indicates the presence of remanence behaviour in the MNP's, which is an undesirable property for mediators in hyperthermia treatment. As stated previously work is being done both to determine the origin of the remanence behaviour and to attempt to address the issue.

The susceptibilities of the LSMO materials decrease with increase dopant. All three samples exhibit a shallow magnetic transition region from ferromagnetic to paramagnetic which contains two slight inflections. This indicates the presence of more than one ferromagnetic phase, each with a different T_c, arising from the presence of two different stoichiometries. Only one stoichiometry is observed for each sample in the EDX, XDR and subsequent Rietveld analysis, which is detailed in reference 26.

The T_c's of each sample were calculated from the magnetic susceptibility data (Figure 4.14) as in section 4.3.2.3, and are displayed in Table 4.13 [20]

Sample	M_s @ 100K (emu/mol)	M_r@ 100K (emu/mol)	T_c (K)	MDL (nm)
LSMO25	12800 ± 30	339 ± 5.7	346 ± 3	6.24 ± 0.13
LSMO35	13000 ± 36	408 ± 6.5	362 ± 4	6.05 ± 0.12
LSMO40	3500 ± 22	175 ± 2.5	352 ± 6	13.90 ± 0.31

Table 4.13: Parameters derived from the magnetisation measurements for LSMO25, LSMO30 and LSMO40 (T_c – Curie temperature, Ms – saturation magnetisation, Mr – remnant magnetisation and MDL – magnetically dead layer)

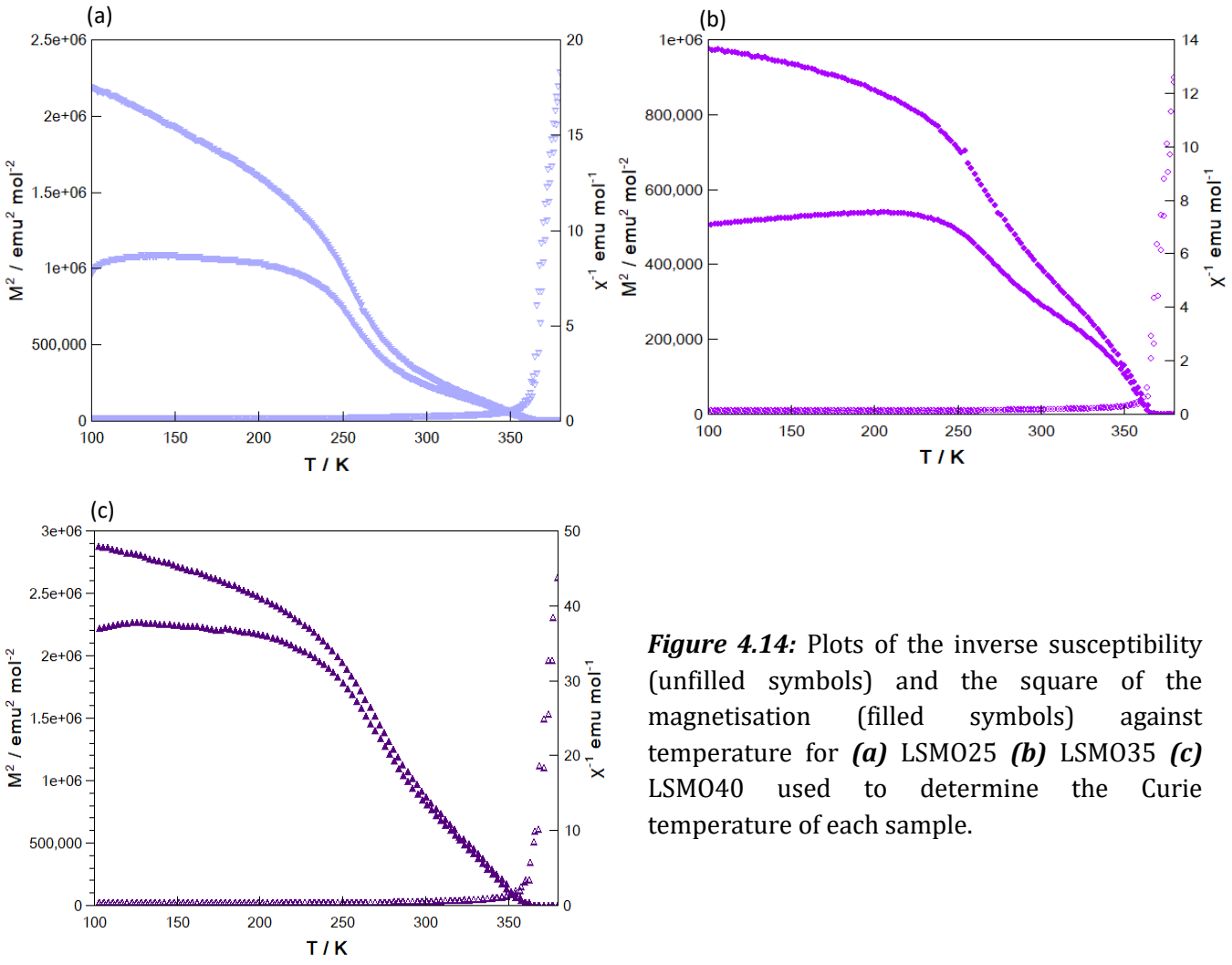

Figure 4.14: Plots of the inverse susceptibility (unfilled symbols) and the square of the magnetisation (filled symbols) against temperature for ***(a)*** LSMO25 ***(b)*** LSMO35 ***(c)*** LSMO40 used to determine the Curie temperature of each sample.

As before, this method was chosen as it is a more accurate way of determining the T_c when more than one ferromagnetic phase is present, than the traditional method of estimating the T_c through the temperature derivative of the magnetisation in the transition region. The T_c's obtained from these three samples will be an average of the two different T_c's of the ferromagnetic stoichiometries present in each sample. Increasing from x=0.25 to 0.35 for LSMO, we see that the T_c increases, and then decreases again for x=0.40. This is the same pattern exhibited by the magnetic heating profiles of the samples in Figure 4.11.

The sample where x=0.40 has a higher T_c than the phase diagram would suggest [31], however all calculated T_c's are in keeping with the experimental trends reported by Urushibara et al [32]. As can be seen in Table 4.13 the T_c's for each of the doped lanthanum manganates is significantly above room temperature, hence all the samples are ferromagnetic at room temperature. A normal or enhanced magnetic heating is normally exhibited by ferromagnetic MNP's, see section 2.4, which is supported by the fact that all the doped LSMO samples exhibited enhanced magnetic heating in this study. It was outlined in section 4.2 the importance of a low T_c in the MNP's used as mediators in hyperthermia treatment as this helps to prevent overheating of localised healthy neighbouring tissues. A T_c of around 320K would be ideal, as this would prevent any magnetic heating above this temperature [1]. All the T_c's obtained for the samples in this study are significantly larger than this and work is currently being carried out to reduce this into the therapeutic range without significantly changing the magnetic heating exhibited.

DC field dependant measurements were taken for each of the materials at x=0.25, x=0.35 and x=0.40, at constant temperatures of 100K and 150K, to investigate the remnant magnetisation and the saturation magnetisation of each sample, at these temperatures, Figure 4.15. The quantitative analysis from these experiments is displayed in Table 4.13, along with the magnetically dead layer calculated from Equation 4.5

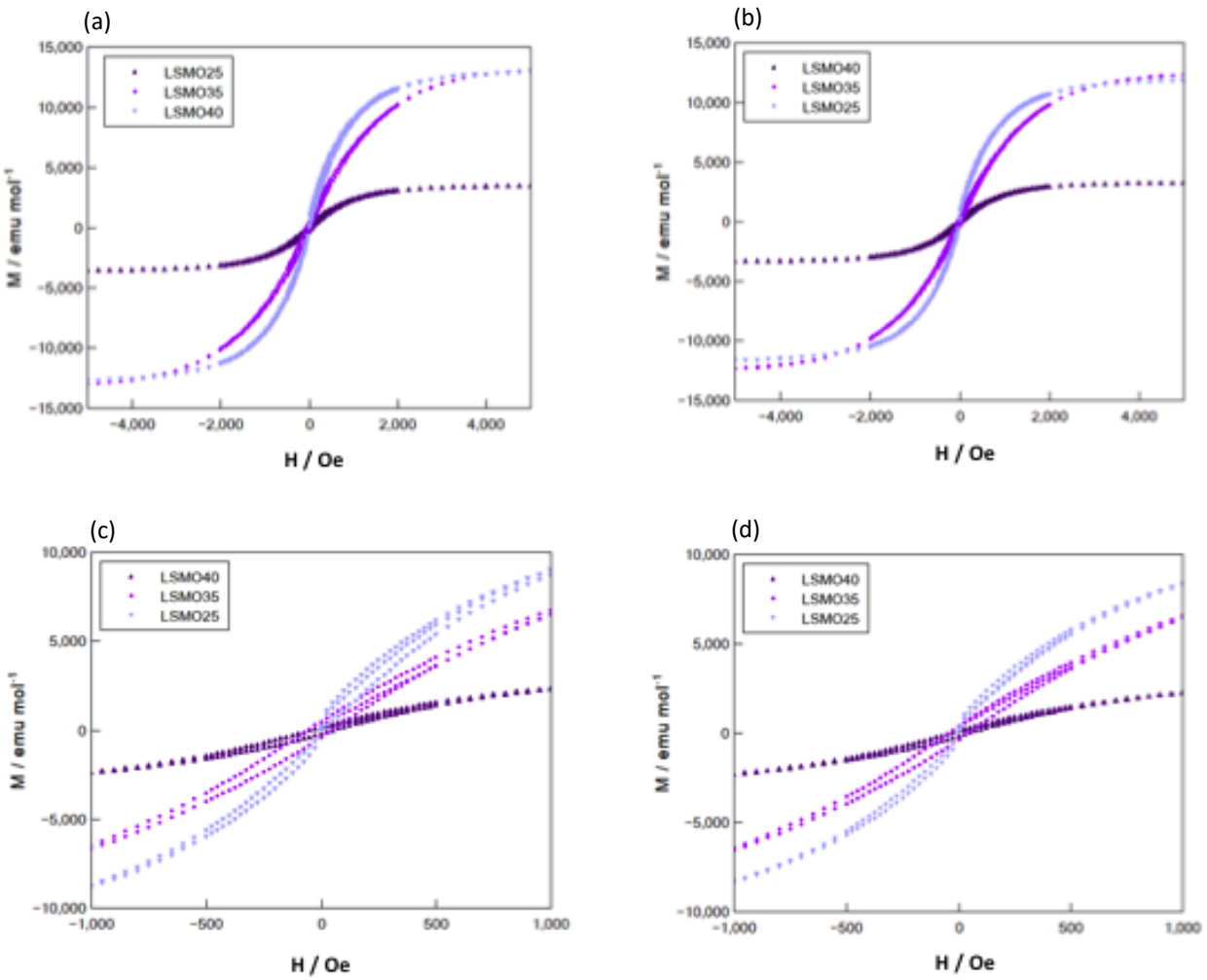

Figure 4.15, Field dependent magnetisation data collected for LSMO25, LSMO35 and LSMO40 with a maximum applied field of 50000e, collected at 100K (***(a)*** and ***(c)***) and 150K (***(b)*** and ***(d)***).

At both temperatures, LSMO35 exhibits the highest saturation magnetisation (M_s), 13000 ± 36 emu/mol, which is in keeping with the fact it shows the greatest magnetic heating of the three samples. LSMO25 shows the second largest M_s, 12800 ± 30 emu/mol, and LSMO40 shows a much smaller M_s than the other two samples of 3500 ± 22 emu/mol. The M_s obtained for LSMO25 is larger than we would have expected and the M_s obtained for LSMO40 is significantly smaller than expected as the LSMO40 sample showed a greater extent of magnetic heating than the LSMO25 sample.

Following Rietveld analysis, the average crystallite size of each sample was calculated using the Scherrer equation, Table 4.11. These values along with the saturation magnetisation values determined using SQUID magnetometry measurements were then used to calculate the magnetically dead layer for each sample, Table 4.13 [27]. LSMO35 was found to have the smallest

magnetically dead layer (MDL), 6.05 ± 0.12 nm, meaning it had the largest ferromagnetic core to MDL ratio, of the three samples. This is unsurprising given the fact that it exhibits both the largest saturation magnetisation and shows the largest extent of magnetic heating. LSMO25 was found to have a slightly larger MDL than LSMO35, 6.24nm ± 0.13 nm, which is in keeping with the fact that it exhibits a smaller amount of magnetic heating than LSMO35. The MDL for LSMO40 was found to be significantly larger than that of both LSMO25 and LSMO35, 13.90nm ± 0.31, as a result of the reduced saturation magnetisation and magnetic susceptibility shown by LSMO40. This does not account for the magnetic heating exhibited by LSMO40 which although less than LSMO35, is greater than that shown by LSMO25. It must be stressed however that the two measurements are not directly comparable as the MDL was calculated using saturation magnetisation values obtained under a static field whilst the induction heating experiments were carried out using an alternating field.

The remnant magnetisation (M_r) for each sample at 100K and 150K is displayed in Table 4.13. The remanence magnetisation is seen to follow the same pattern as the saturation magnetisation, with LSMO35 exhibiting the largest M_r, 408 ± 4 emu/mol, followed by LSMO25, 339 ± 3 emu/mol and then LSMO40, 155 ± 6 emu/mol. As mentioned earlier, remanence is not a desirable property for MNP's in hyperthermia treatment and work is on-going to address this issue in the MNP's presented in this study. The remanence is observed to decrease with increasing dopant concentration, from x=0.25 to x=0.40. This decrease in remanence with increasing dopant could possibly be attributed to the increasing substitution of Jahn-Teller active Mn^{3+} for non Jahn-Teller active Mn^{4+}. The decrease in Jahn-Teller active ions causes a decrease in the extent of Jahn-Teller distortion within the samples and as a direct result the extent of the double exchange mechanism is reduced. As mentioned previously, as these results were collected under a DC field, no direct comparison can be made with the magnetic heating data, which was collected using an AC field. AC susceptibility data will be collected in future work.

4.3.3. Conclusions

A family of $La_{1-x}Sr_xMnO_3$ MNP clusters where $0.25 < x < 0.40$ where synthesised using a modified peroxide sol-gel synthesis. The polycrystalline structure of the MNP's were evaluated and linked with the magnetic properties of the materials with the aim to make predictions with respect to the best LSMO composition for use as a mediator in mild hyperthermia treatment. We were able to conclude that as the dopant concentration increases, so does the maximum temperature reached by each heating profile, and therefore the MCE, until an optimum is reached at x=0.35,

after which this maximum temperature of saturation decreases again. Taking into account the target temperature range and requirement for a low MNP dosage for therapeutic application it was found that $La_{0.65}Sr_{0.35}MnO_3$ appeared to be the most suitable material, with a high SAR of 56 Wg_{Mn}^{-1} and maximum magnetic heating of 46.7°C. A transition in crystalline structure of the perovskite crystal between rhombohedral and orthorhombic was observed with increasing dopant in agreement with that observed by Slobodin et al. [18]. This transition in crystalline structure was seen to correspond to an increase in the magnetic properties exhibited by LSMO, and the MCE as a direct result.

4.5. Effect of using microwave irradiation during the synthesis process

In the final study in this area, the effect of using microwave (MW) irradiation to assist the modified peroxide sol-gel synthesis of $La_{1-x}Sr_xMnO_3$ (LSMO), where x=0.25, 0.35 and 0.40, was investigated.

MW irradiation has shown promise as an alternative heating mechanism to conventional heating showing many advantages over such methods, such as faster reaction times of the precursors and the synthesis of smaller more consistently sized particles [33]. In MW heating, electrical dipole moments, found in polar materials, align along the applied electromagnetic MW field. The application of an alternating MW field causes the polar molecules to rotate with the electromagnetic field, which results in heat dissipation as a consequence of friction and collisions between molecules and their surroundings [34-35]. As this heat dissipation occurs within the core of the reactant mixture, a more regular heating is achieved than via conventional means [36-37].

It is reported in the literature that MW-heating in established synthesis has been advantageous in producing materials which have a purer monocrystalline phase, in addition to allowing reasonable control over the crystalline growth and crystal structure depending on the reaction conditions [38-39]. The link between the degree of crystallinity with variation in the extent of magnetic contribution is investigated by Zhang et al [27]. In Zhang's model, it is proposed that the MNPs are composed of a ferromagnetic core surrounded by an antiferromagnetic shell. It was postulated that the ratio of this ferromagnetic core to antiferromagnetic shell was directly impacted by the crystallinity of the complex, and as a direct result improved crystallinity was related to enhanced magnetic behaviour.

Thus far there is very limited information regarding the direct impact of MW irradiation during the synthesis process on the magnetic properties of perovskite material. However, Yu et al,

identified enhanced dielectric properties of the perovskite $CaCu_3Ti_4O_{12}$ when synthesised using MW heating [40]. It has been reported in the literature that there is a great deal of similarity in the origin of dielectric and magnetic properties, and therefore we expect that the use of MW irradiation in the modified peroxide sol-gel synthesis of LSMO will result in improved crystallinity of the synthesised samples and enhancement of the magnetic properties [41-42]. To our knowledge this is the first time that MW irradiation has been applied to a peroxide sol-gel synthesis.

The focus of the study was to investigate how altering the synthesis conditions of LSMO MNPs would impact the materials magnetic behaviour. As with the previous two studies, the overarching aim was to produce a suitable material for use in mild hyperthermia treatment. The MW settings (time and power) were varied and the subsequent effects on the synthesised samples investigated. It is predicted that enhancement of the magnetic properties will be observed with improved crystallinity.

4.5.1. Experimental

4.5.1.1. Material Synthesis

Two sample batches of $La_{1-x}Sr_xMnO_3$ MNP's, with x=0.35, were synthesised. One sample batch was synthesised using conventional heating and the other sample batch was synthesised using microwave irradiation. The $La_{1-x}Sr_xMnO_3$ MNP's synthesised using conventional heating were synthesised using the same modified peroxide sol-gel synthesis described in section 4.3.1.1. The powder precursors (lanthanum (II) oxide, manganese (II) carbonate and strontium carbonate) were mixed in appropriate proportions to obtain the desired stoichiometric ratios. For the MW synthesis process, adjustments to the reactant mixture used for the conventional heating synthesis were necessary to make it suitable for MW heating. In contrast to the conventional heating synthesis process, the powder precursors where not dissolved in water before the addition of hydrogen peroxide and ammonium hydroxide. Instead smaller amounts of hydrogen peroxide (1.25mL) and ammonium hydroxide (~ 120μL) were added directly to the powder precursors. After the addition of hydrogen peroxide and ammonium hydroxide, the mixture was transferred to a closed, 10mL microwave tube and placed in a microwave holder. The microwave (CEM Discover 2.45GHz) was set to 50W, 100W or 200W, and the mixture stirred for 10min, 30min or 2 hours at 70°C. The resulting solution was then dried at 110°C. This process was repeated 30 times for each sample and the powder samples combined is order to obtain enough material for investigation. Calcination at 1100°C for 16 hours was then used to obtain a

crystalline product. The samples were all manually ground in an agate mortar and pestle before characterisation and testing. As the samples synthesised using conventional heating and microwave heating were prepared using slightly different methods, a sample, LSMO35-RedVol, was prepared using the same synthesis process as for the microwave samples but under conventional heating, i.e. reduced amounts of hydrogen peroxide and ammonium hydroxide were added directly to the powder precursors without the addition of water. This allows for direct comparison of these samples to separate the contribution of MW irradiation, to the physical properties.

4.5.1.2. Characterisation

The synthesised samples underwent the same analysis as outlined in section 4.3.1.2. XRD and subsequent Rietveld analysis, SEM, EDX, FTIR and SQUID magnetometry were all carried out using the same equipment and conditions as described previously.

The mass of the measured samples, number of moles of each sample and diamagnetic contributions applied to the magnetic measurements conducted in the SQUID magnetometer are displayed in Table 4.14.

Sample	**Mass (g) x10^{-4}**	**Moles of sample (mol) x10^{-6}**	**Diamagnetic correction applied (emu/mol) x10^{-5}**
LSMO35-Con	13.00 ± 0.05	5.807 ± 0.022	-6.465 ± 0.097
LSMO35-50W	11.00 ± 0.05	4.913 ± 0.022	-6.465 ± 0.097
LSMO35-100W	11.00 ± 0.05	4.913 ± 0.022	-6.465 ± 0.097
LSMO35-200W	9.00 ± 0.05	4.020 ± 0.022	-6.465 ± 0.097

Table 4.14: Table displaying the sample mass, number of moles of each sample and the material specific diamagnetic correction applied to the magnetic measurements

It should be noted that in the SQUID magnetometry measurements, peek capsules were used to contain the samples instead of gelatine capsules which were used in the previous two studies (sections 4.3. and 4.4.). The gelatine capsules used previously were from the same sample batch and showed no deformation in the temperature range studied. In contrast, initial experiments in this section were conducted using gelatine capsules from a different sample batch. These

capsules melted during the magnetic susceptibility measurements at around 325K. As a consequence of the gelatine capsules melting, we choose to contain the samples in peek capsules in this study. Diamagnetic corrections were applied for the sample holder and the results obtained using LSMO35con in gelatine capsules were shown to be reproducible when the peek capsules were used, so comparison can be reliably made between the conventional synthesis used in previous work and the MW-irradiated synthesis used here.

Non-adiabatic heating experiments were conducted using the same experimental set up as before (Figure 4.2) but analysis was carried out solely on aqueous solutions of the MNP's of $10 mgmL^{-1}$.

4.5.2. Results and discussion

4.5.2.1. Crystalline structure and configuration analysis

LSMO35 synthesised using both MW (LSMO35-MW) and conventional heating (LSMO35-Con) is investigated in this section. The LSMO35 sample synthesised using MW heating was heated for the same length of time (2 hours) as the sample synthesised using conventional heating, and at a MW power of 100W.

XRD and Rietveld analysis was conducted on each of the synthesised complexes. Details of this analysis and the XRD patterns for each complex can be found in the main paper and supplementary information of reference 43. The crystallite size and relevant weight percentages of each crystal phase and their corresponding lattice parameters, derived from the Rietveld analysis for the LSMO35-Con and LSMO35-MW sample, are displayed in Table 4.15.

On direct comparison of the diffraction patterns of the LSMO35-MW sample with the diffraction pattern for LSMO35-Con sample, see reference 43, it was observed that the diffraction pattern of the LSMO35-MW sample had a straighter background with less noise. This would suggest that MW irradiation may result in MNP's with an improved degree of crystallinity over those produced using conventional heating. Increased crystallinity according to Zhang et al's model may also lead to an increased ferromagnetic to MDL ratio, meaning an enhancement of the magnetic properties of the samples would be observed [27]. As with the two previous studies orthorhombic (Pnma) and rhombohedral (R-3c) were observed in both samples with rhombohedral (R-3c) being the dominant geometry. The relative weight percentages of the two phases were observed as being relatively constant between the two samples, see Table 4.15.

Sample	Space Group	a / Å	b / Å	c / Å	α / °	β / °	γ / °	V / Å³	Wt. Perc. / %
LMO35-Con	Pnma	5.448	7.743	5.468	90	90	90	230.4	19.7
	R-3c	5.512	5.512	13.355	90	90	120	351.4	80.3
LSMO35-MW	Pnma	5.095	9.178	6.999	90	90	90	327.3	19.0
	R-3c	5.494	5.494	13.348	90	90	120	348.9	81.0

Table 4.15: Structural information for the LSMO35-Con and LSMO35-MW complexes derived from Rietveld analysis

The stoichiometries of the three samples made by MW-assisted synthesis were confirmed using EDX as in the previous two sections. This information along with the EDX maps can be found in main paper and supplementary information of reference 43. Figure 4.16 shows the SEM images obtained for the LSMO35-Con and LSMO35-MW samples. Details of these experiments can also be found in reference 43.

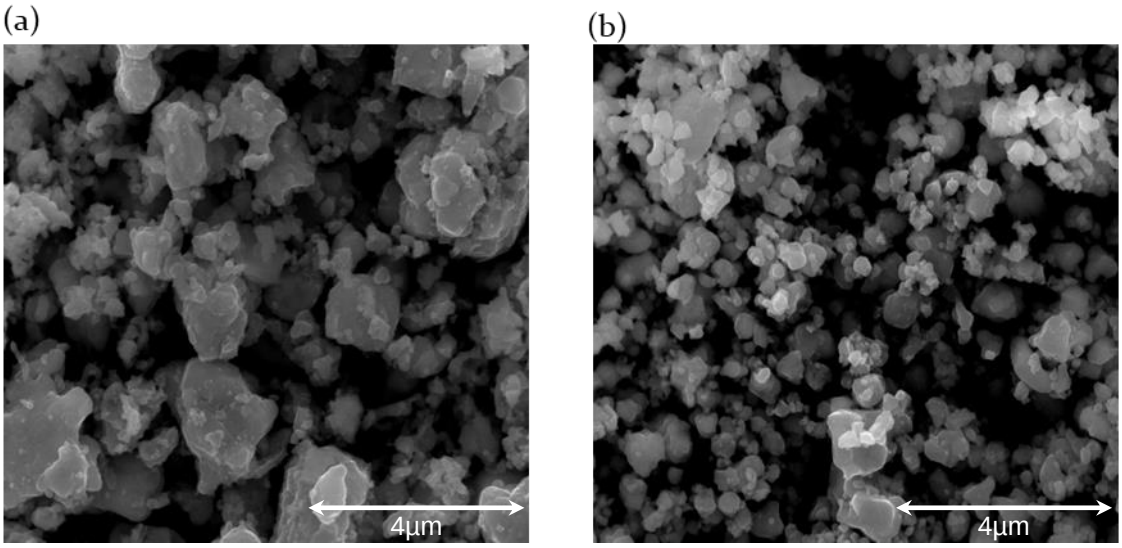

Figure 4.16: Scanning Electron Micrographs of ***(a)*** LSMO35-Con and ***(b)*** LSMO35-MW

From Figure 4.16, the MNP's obtained using the MW assisted synthesis appear to be of a more crystalline material and appear to be a lot more uniform in terms of both size and shape than those synthesised using conventional heating, were a wide range of agglomerate particle size and shapes are apparent. As with the previous two sections the fact that the particles synthesised in this study formed agglomerates made identification of individual particle size difficult. However for the purpose of this section the mean particle size was estimated to allow comparison between the LSMO35-MW and LSMO35-Con samples. Details of particle size and the distribution of sizes observed in the SEM experiments are detailed in reference 43.

Although the MNP's synthesised using MW heating appear smaller than those synthesised using conventional heating, the particle size seemed to remain consistent between the two samples, with an estimated mean particle length of approximately 300nm ± 50nm in each case. The observed difference in size is due to a decreased agglomeration of the MNP's synthesised by MW heating compared with those synthesised by conventional heating. The difference in crystallinity between the two samples may be as a result of an increased rate of synthesis, due to the MW heating, which is commonly observed in the literature.

In addition to identifying the crystal structure compositions and the degree of crystallinity for the various LSMO samples, the Mn-O bond lengths of the LSMO samples were also investigated, in order to better relate their structures with their observed magnetic behaviour. It is possible to calculate the bond lengths following Rietveld refinement of the powder diffraction patterns. It is important to note the goodness of fit for the Rietveld analysis was significantly better for the LSMO35-Con samples than for the LSMO35-MW samples. Therefore the subsequent bond lengths calculated will also be more accurate for the samples synthesised using conventional heating.

Figure 4.17 shows the model Mn-O octahedrons present in LSMO and the calculated bond lengths, for the LSMO35-Con and LSMO35-MW samples.

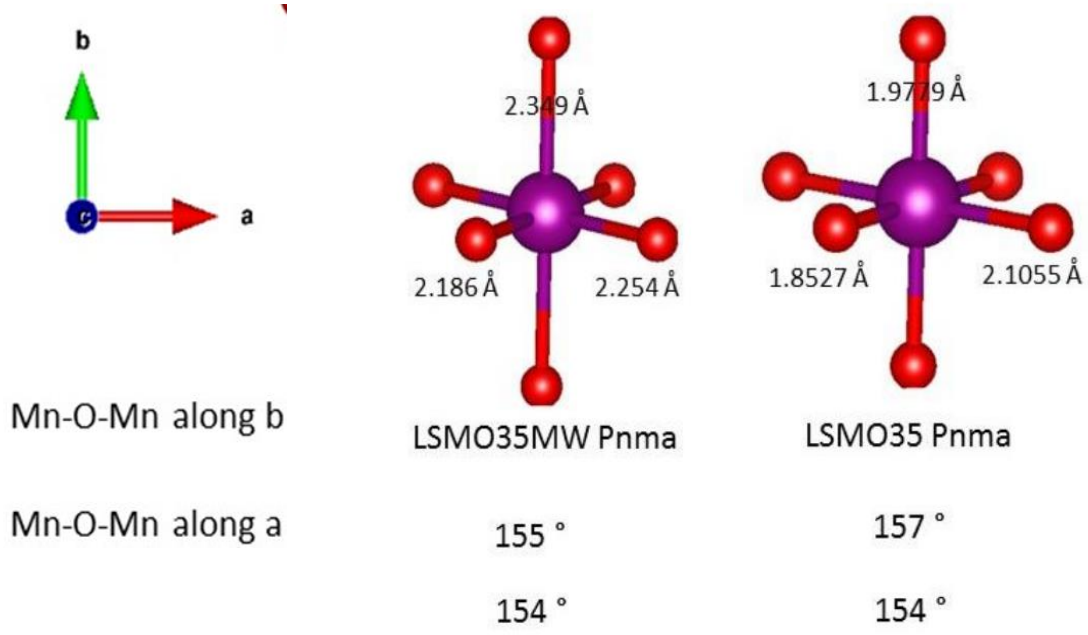

Figure 4.17: Mn-O polyhedron for the LSMO35Con and LSMO35MW samples highlighting the bond lengths and Mn^{3+}-O–Mn^{4+} bond angles.

These were isolated using the VESTA software following Rietveld analysis of the powder diffraction patterns [44]. A substantial increase in the average Mn-O bond length was observed for LSMO35-MW in comparison to LSMO35-Con along with a sizable reduction (35%) in the variation of bond lengths. If this is due to a decrease in Jahn-Teller distortion, this, coupled with the larger Mn-O bond lengths exhibited by LSMO35-MW, would suggest a reduction in the extent of the double exchange mechanism. This generally means a reduction in magnetic properties would be observed. The increase in Mn-O bond lengths, and reduction in the variation of the bond lengths for LSMO35-MW results in the existence of a much larger unit cell (327.3 Å). This results in the formation of aggregates of much smaller crystal size. The smaller aggregates in LSMO35-MW may better participate in Brownian and Néel relaxations and thus aggregate crystal size may be a more influential parameter than Mn-O bond lengths in determining the magnetic properties of the material.

4.5.2.2. Magnetic heating experiments

Figure 4.18 shows the heating curves for 10mgmL^{-1} aqueous suspensions of LSMO35-MW for different MW time settings and different MW power settings.

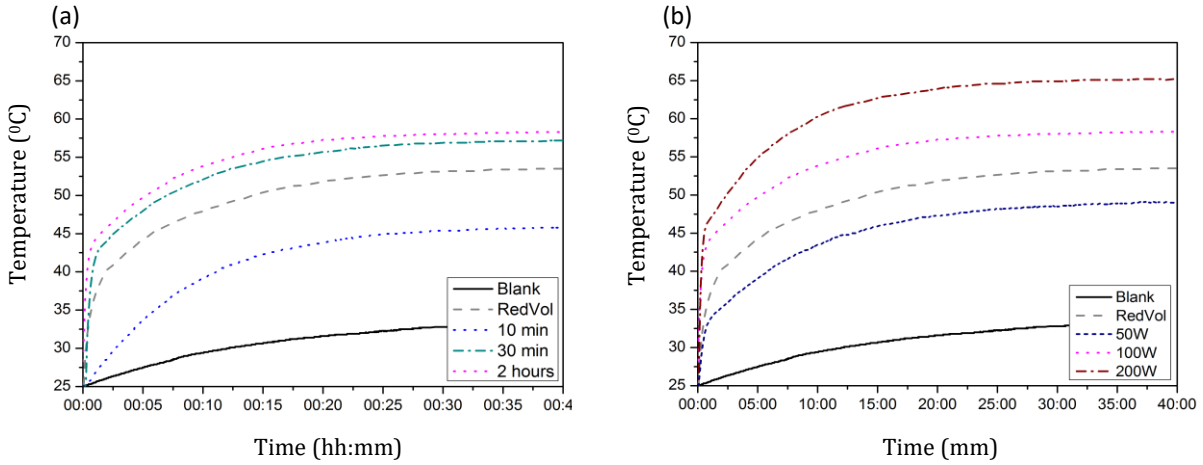

Figure 4.18: Induction heating data for LSMO35 samples synthesised for ***(a)*** different time intervals and ***(b)*** LSMO35 samples synthesised using various MW power settings

In order to make direct comparisons between the impact of conventional and MW-assisted synthesis on the magnetic heating of the samples it was necessary to include the LSMO35-RedVol samples which was synthesised using the same method as the MW samples but using conventional heating. In Figure 4.18 (a) we can see that the samples synthesised using MW heating for 30 minutes (LSMO35-30min) and 2 hours (LSMO35-2hr) have a similar heating profile to the one obtained for the LSMO35-RedVol sample where conventional heating is used in the synthesis. For all three samples an initial rapid increase in temperature is observed followed by saturation at a particular maximum temperature. The same initial rapid increase in temperature is not observed for the LSMO35-10min sample, which can possibly be attributed to incomplete synthesis due to the reduced heating time. This sample also exhibited a smaller extent of magnetic heating compared with the sample synthesised using conventional heating, which would support this argument. It can be seen from Figure 4.18 (a) that the maximum heating reached by LSMO35-30mins (57.0°C) and LSMO35-2hr (58.3°C) is greater than that reached by LSMO35-RedVol (52°C). These two samples show longer heating in the linear regime before settling at a higher saturation temperature. It can be concluded from these measurements that MW heating not only reduces reaction time needed for the synthesis of LSMO35, over conventional heating, but also leads to materials, which exhibit increased magnetic heating.

Figure 4.18 (b) shows the effect of changing the power settings used for the MW heating on the magnetic heating exhibited by the synthesised samples. The MW samples in this sample batch were heated using the MW for the same length of time that is used in the conventional heating synthesis (2 hours), using microwave power settings of 50W, 100W and 200W. The samples synthesised at MW power settings of 100W and 200W both showed greater magnetic heating than the LSMO35-RedVol sample, whereas the LSMO35-50W sample showed a reduction in the extent of magnetic heating. The extent of magnetic heating looks to be directly related to the MW power setting with the saturation temperature reached, increasing with increased MW power setting. LSMO35-50W reaches a saturation temperature of 49.1°C, LSMO35-100W reaches a temperature of 58.3°C and LSMO35-200W reaches a temperature of 65.1°C. The difference in the extent of magnetic heating exhibited by these samples may be as a result of the different rates at which the water produced by the decomposition of hydrogen peroxide is evaporated at the different MW power settings. For example this takes 30 minutes using 50W, whereas it only takes 15 minutes when 200W is used.

The SAR's of the LSMO35-MW samples synthesised at the different time and power settings were calculated and are plotted in Figure 4.19.

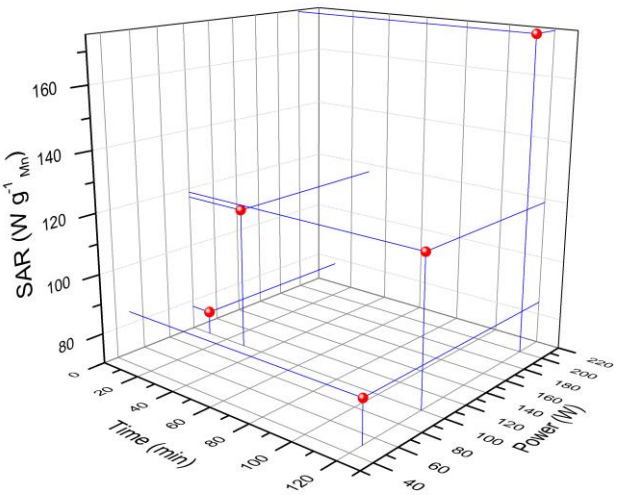

Figure 4.19: SARs of LSMO35 samples synthesised for different time intervals (10 minutes, 30 minutes and 2 hours) and various MW power settings (50, 100 and 200W)

This shows that increasing MW power settings and longer heating times correlate to a greater SAR. It appears that the MW power setting is more influential than the heating time.

4.5.2.3. Magnetic measurements

Figure 4.20 shows the magnetic susceptibility for the LSMO35-MW samples synthesised using different MW power settings, (50W, 100W and 200W). In keeping with the previous two sections experimental uncertainty in the measurement of the sample mass is the biggest contributor to the overall uncertainty in the magnetic measurements which amounts to 0.7% uncertainty in the final susceptibility measurement. In keeping with the literature, error bars have been omitted from the plots for clarity.

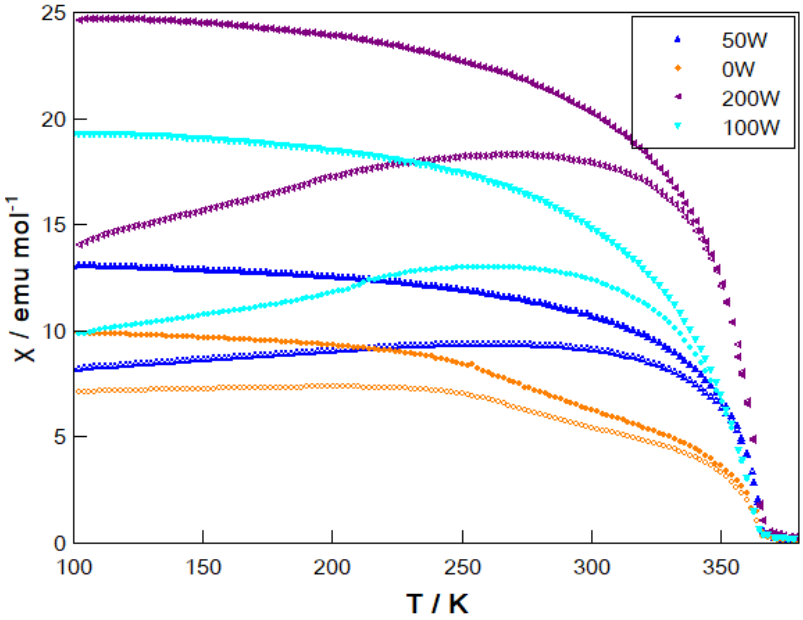

Figure 4.20: Magnetic susceptibility of the LSMO35 family synthesised using MW power settings of 50W, 100W and 200W, in the temperature range 100-380K. Filled symbols represent the field cooled (FC) measurement and unfilled symbols represent the zero-field cooled measurement (ZFC)

LSMO35-Con is included in the magnetic measurements to directly compare the magnetic properties of the samples synthesised using MW heating with those synthesised using conventional heating. As can be seen from Figure 4.20, the magnetic susceptibilities of the LSMO35-MW samples were greater than the LSMO35-Con sample (orange downward triangles).

It can also be seen that the magnetic susceptibilities seem to increase with the increasing MW power setting, used to synthesise the MW samples. This can be attributed in part to the higher MW power settings causing an increased rate of evaporation of water from the sol-gel mixture, resulting in better crystallised nanoparticles. This will result in a thinner non-magnetic surface layer (the magnetically dead layer), meaning the ferromagnetic core to MDL ratio is increased resulting in the observed increase in magnetic susceptibility [27]. A similar observation was made by Hong et al. who identified an increase in magnetic susceptibility when MW heating was used in the synthesis Fe_3O_4 MNPs compared with MNPs synthesised using conventional heating [45]. Hong et al. attributed the observed enhancement in magnetic susceptibility to the improved crystallisation of the MNP's synthesised using MW heating as they observed little difference in the average crystallite size (8-9nm) of the MNP's in their study, unlike in this case where there is significant difference in the average crystallite size, decreasing from 24.8nm for LSMO35-Con to 8.8nm for LSMO35-MW.

Figure 4.20 shows that all samples undergo a transition from ferromagnetic to paramagnetic. This transition appears to be much steeper for the samples synthesised using MW irradiation in comparison to the samples synthesised using conventional heating. The ferromagnetic to paramagnetic transition gradient of LSMO35-Con is -0.2 $emumol^{-1}K^{-1}$ compared with -0.6 $emumol^{-1}K^{-1}$ for LSMO35-50W and LSMO35-100W, and -0.8 $emumol^{-1}K^{-1}$ for LSMO35-200W. The steeper transition gradients exhibited by the LSMO35-MW samples mean they will have ferromagnetic character for longer with increasing temperature until its T_c where there is a sudden drop in the magnetic susceptibility. In contrast, LSMO35-Con has a weak transition gradient meaning that its ferromagnetic character weakens further in advance of its T_c. The improved magnetic heating and SAR observed for the MW samples compared to the conventionally synthesised sample may be in part due to the increased magnetic susceptibility and this sharper ferromagnetic to paramagnetic transition. These attributes mean faster, more efficient switching of the magnetic dipoles within the LSMO35-MW samples with an alternating magnetic field, which will generate more heat in the process via Néel and Brownian rotations. As a result an increased magnetic heating would be observed.

The T_c for each sample was calculated using the same method as for the previous two sections (Figure 4.21), and is displayed in Table 4.16.

Sample	M_s @ 100K (emu/mol)	T_c (K)
LSMO35-Con	13,000 ± 38	360 ± 3
LBMO35-50W	16,000 ± 42	362 ± 4
LSMO35-100W	16,500 ± 44	362 ± 4
LSMO35-200W	19,000 ± 49	362 ± 4

Table 4.16: Parameters derived from the magnetisation measurements for LSMO35-Con, LSMO35-50W, LSMO35-100W and LSMO-200W samples (T_c – Curie temperature, Ms – saturation magnetisation, Mr – remnant magnetisation and MDL – magnetically dead layer)

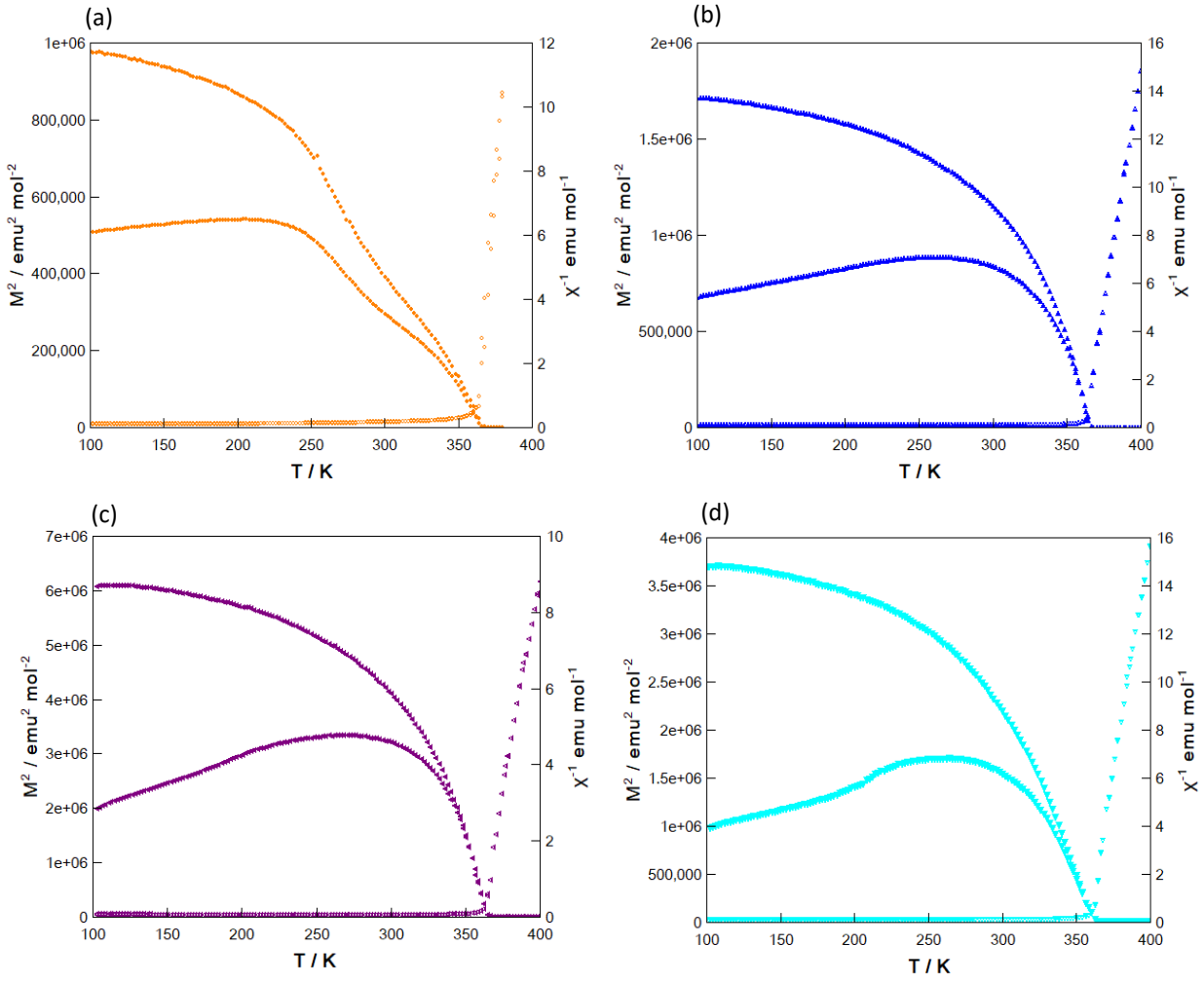

Figure 4.21: Plots of the inverse susceptibility (unfilled symbols) and the square of the magnetisation (filled symbols) against temperature for ***(a)*** LSMO35-Con ***(b)*** LSMO35-50W ***(c)*** LSMO35-100W and ***(d)*** LSMO35-200W used to determine the Curie temperature of each sample.

The T_c found for each sample is ≈362K (the T_c for LSMO35-Con was found to be marginally lower (360K)). As T_c is a material constant it is expected that this would be the same for each of the LSMO35 samples, as the dopant concentration remains constant.

It can be seen that there are two slight inflections in the ferromagnetic to paramagnetic transition observed for the LSMO35-Con sample, that are not present in the LSMO35-MW samples. The inflections are indicative of the presence of more than one ferromagnetic phase, with different stoichiometries, each with its own T_c. Hence the T_c calculated for LSMO35-Con is actually an average of the T_c's of these two phases. This might explain why it is 2K higher than the T_c obtained for the LSMO35-MW samples. As with the previous two sections in this investigation, this additional phase was not identifiable using Rietveld analysis of the powder diffraction pattern, or EDX.

It is possible that it is in fact the surface layer; the magnetically dead layer (MDL), which is causing the inflections in the ferromagnetic to paramagnetic transition, as according the Zhang's model this will have a different transition temperature than the core material [27]. The fact that no inflections are observed in the ferromagnetic to paramagnetic transitions in the LSMO35-MW samples, suggests the presence of only one crystal phase. This suggests MW-irradiation makes purer samples than those synthesised using conventional heating. If it is in fact the MDL that is responsible for the inflection observed for the LSMO35-Con sample, it is possible that this layer is significantly thinner in the MW samples and therefore is unobservable in the magnetic susceptibility measurements. This is investigated further in the following DC field dependent experiments.

DC field dependent measurements were carried out at constant temperatures of 100K and 150K on the LSMO samples synthesised using conventional heating and microwave irradiation and are displayed in Figure 4.22.

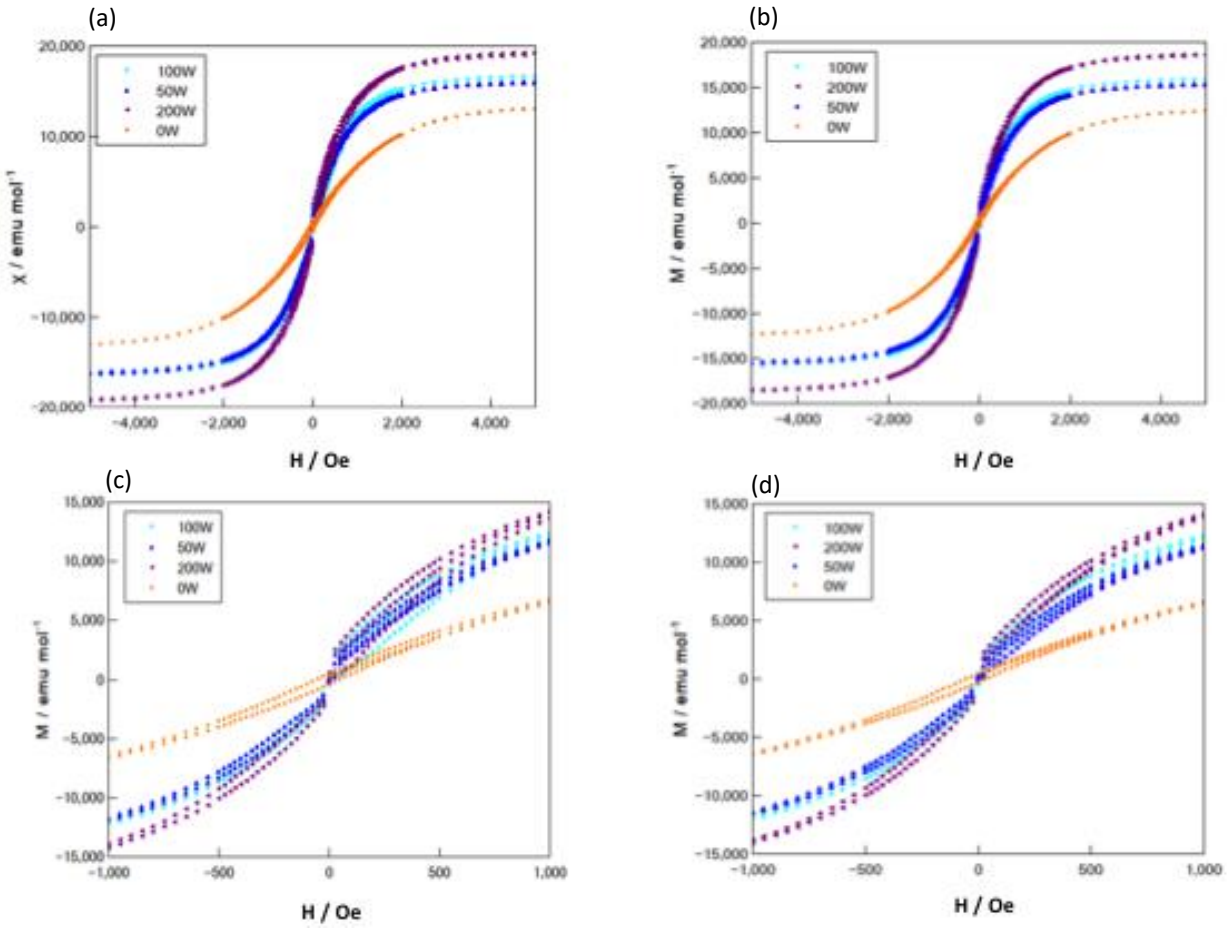

Figure 4.22: Field dependent magnetisation data collected for LSMO35-Con, LSMO35-50W, LSMO35-100W and LSMO35-200W samples with a maximum applied field of 5000Oe, collected at 100K (***(a)*** and ***(c)***) and 150K (***(b)*** and ***(d)***).

As can be seen from Figure 4.22 the saturation magnetisation seems to increase with the MW power setting used in the synthesis process. As M_s is material dependent we would expect it to be the same for all the samples in this section. In determining the M_s of a sample using SQUID magnetometry, it is necessary to divide through by the number of moles in the sample. This is calculated using the measured mass of the sample. Where the sample is not 100% pure, the measured mass will be greater than the exact mass of the desired material present. This will result in a smaller M_s than expected being returned. We can therefore conclude that the LSMO samples which return the largest M_s are the purest, and therefore it can be concluded that increasing the MW power setting used in the MW-assisted synthesis increases the purity of the synthesised sample. Directly comparing the LSMO35-MW samples with the LSMO35-Con sample we can see there is a significant increase in the M_s of all three LSMO35-MW samples. Hence it can be concluded that MW heating produces better crystallised samples than those synthesised using conventional heating. We would also expect the MDL layer for these samples

to be reduced as a direct result of the improved crystallinity. We can prove this by calculating the MDL layer of the LSMO35-Con and LSMO35-100W samples, using Equation 4.5. This is found to be 6.05 ± 0.12 nm and 2.36 ± 0.05 nm respectively (for respective crystallite sizes of 82.4nm and 61.8nm). The reduction in the MDL layer means there is an increase in the ferromagnetic core to MDL ratio and helps to explain the enhancement in magnetic behaviour seen for the LSMO35-MW samples (observed both in the SQUID measurements and magnetic heating measurements). As we saw earlier there is a reduction in cluster formation between the LSMO35-Con and LSMO35-100W samples (Figure 4.16). This can also be a cause of the enhanced magnetic properties observed. Epherre et al. proposed that reduced proportions of magnetic clusters can lead to fewer local distortions within the particle cores which in turn increases the saturation magnetisation and magnetic susceptibility, as we have seen in this work [46].

4.3.3. Conclusions

The use of MW irradiation was shown to improve the crystallinity of LSMO synthesised using a modified peroxide sol-gel synthesis. Despite the improved crystallinity observed there was no significant change observed in the proportions of orthorhombic to rhombohedral crystal geometries present. MW irradiation was however shown to reduce the MDL present in the MNP's in comparison to those synthesised using conventional heating, causing an increase in the ferromagnetic core to MDL ratio. This explains why an enhancement was observed in the magnetic properties (magnetic susceptibility and magnetic heating) of the MW samples. Through work to optimise the magnetic properties of LSMO35-MW, a linear relationship between the MW power setting used (50, 100 and 200W) and the magnetocaloric effect (producing SAR's of 37.7, 56.6 and 57.5 Wg^{-1} respectively) was identified. As the LSMO35-MW particles show enhanced magnetic properties and are more discrete and crystalline than those synthesised using conventional heating, they will be more effective mediators for mild hyperthermia treatments.

References

[1] Kuznetsov, O. A., Sorokina, O. N., Leontiev, V. G., Shlyakhtin, O. A., Kovarski, A. L.,and Kuznetsov, A. A., "ESR study of thermal demagnetization processes in ferromagnetic nanoparticles with Curie Temperatures (Tc) 40 to 60^{o}C", (2007), *Journal of Magnetism and Magnetic Materials*, Vol **311**, 204-207

[2] Pollert, E., Veverka, P., Veverka, M., Kaman, O., Záveta, K., Vasseur, S., Epherre, R., Goglio, G., Duguet, E., "Search of new core materials for magnetic fluid hyperthermia: preliminary chemical and physical issues", (2009), *Progress in Solid State*, Vol **37,** 1-14

[3] Huang, Q., Santoro, A., Lynn, L., Erwin, R., Borchers, J., Peng, J. and Green, R., "Structure and magnetic order in undoped lanthanum manganite", (1997), *Physical Review B*, Vol **55**, 14987

[4] Persson, K., "Materials Data on $LaMnO_3$ (SG:62) by Materials Project", (2015), https://materialsproject.org/materials/mp-601181/, accessed 28/10/2018

[5] Zener, C., "Interaction between the d-shells in the transition metals. 11. Ferromagnetic compounds of manganese with perovskite structure" (1951), *Physical Review*, Vol **82**, 403

[6] Guar, A., and Varma, G. D., "Sintering temperature effect on electrical transport and magnetoresistance of nanophasic $La_{0.7}Sr_{0.3}MnO_3$", (2006), *Journal of Physics: Condensed Matter*, Vol **18**, 8837

[7] Conceição, L., Silva, C. R. B., Ribeiro, N, F, P., and Souza, M, M, V, M., "Influence of the synthesis method on the porosity microstructure and electrical properties of $La_{0.7}Sr_{0.3}MnO_3$ cathode materials", (2009), *Materials Characterization*, Vol **60**, 12, 1417-1423

[8] Kaman, O., Veverka, P., Jirák, Z, Maryško, M., Knižek, K,. Veverka, M., Kašpar, P., Burian, M., Šepelák, V., and Pollert, E., "The magnetic and hyperthermia studies of bara and silica-coated $La_{0.75}Sr_{0.25}MnO_3$ nanoparticles", (2011), *Journal of Nanoparticle Research*, Vol **13**, 1237-1252

[9] Pollert, E., Knižek, K., Maryško, M., Kašpar, P., Vasseur, S., and Duguet, E., "New T_c-tuned magnetic nanoparticle for self controlled hyperthermia", (2007), *Journal of Magnetism and Magnetic Materials*, Vol **316**, 122-125

[10] Guo, R.S., Wei, Q, T., Li, H. L., and Wang, F. H., "Synthesis and properties of $La_{0.7}Sr_{0.3}MnO_3$ cathode by gel combustion", (2006)., *Materials Letters*, Vol **60**, 2, 261-265

[11] Shannon, R.D., "Revised Effective Ionic Radii and Systematic Studies of Interatomic Distances in Halides and Chalcogenides", (1976), *Acta Crystallographica A*, Vol **32**, 751-767

[12] Zhang, Q., Nakagawa, T., and Saito, F., "Mechanochemical synthesis of $La_{0.7}Sr_{0.3}MnO_3$ by grinding constituent oxides", (2000), *Journal of alloys and compounds*, Vol **308**, 121-125

[13] McBride, K., Partridge, N., Bennington-Gray, S., Felton, S., Stella, L. and Poulidi, D., "Synthesis, characterisation and study of magnetocaloric effects (enhanced and reduced) in managnate perovskites", (2017), *Materials Research Bulletin*, Vol **88**, 69-77

[14] Liu, S., Tan, X., Li, K., and Hughes, R., "Synthesis of Strontium Cerates-Bases Perovskite Ceramics via Water-Soluble Complex Precursor Routes", (2002), *Ceramics International*, Vol **28**, 3, 327-335

[15] Chen, C. H., Kruidhof, H., Bouwmeester, J. M., and Burggraaf, J., "Preparation of gas-tight strontium-doped lanthanum cobaltate by an aqueous sol-gel process", (1996), *Material Science Engineering B*, Vol **39**, 129-132

[16] Islam, M. A., Rondinelli, J. M., and Spanier, J. E., "Normal mode determination of perovskite crystal structures with octahedral rotations: theory and applications", (2013), *Journal of Physics: Condensed Matter*, Vol **25**, 17

[17] Green, D., Neumann, K., "Green's functions for Neumann boundary conditions", (2012), *arXiv preprint arXiv*, **1105**, 2700

[18] Wildeboer, R. R., Southern, P., and Pankhurst, Q. A., "On the reliable measurement of specific absorption rates and intrinsic loss parameters in magnetic hyperthermia materials", (2014), *Journal of Physics D: Applied Physics*, Vol **47**, 49

[19] Slobodin, B, V., Vladimirova, E, V., Petukhov, S. L., Surat, L. L., and Leonidov, I. A., "Synthesis and structure of (Ca, Sr)- substituted lanthanum manganite", (2005), *Inorganic Materials*, Vol **41**, 8, 869-875

[20] Arrott, A., "Criterion for ferromagnetism from observations of magnetic isotherms", (1957), *Physical review journals archive*, Vol **108**, 1394

[21] Zhang, X. X., and Tejada, J., "Magnetocaloric effect in $La_{0.67}Sr_{0.33}MnO_{\delta}$ and $La_{0.6o}Y_{0.07}Ca_{0.33}MnO_{\delta}$ bulk materials", (1996), *Applied Physics Letters*, Vol **69**, 3596

[22] Krenke, T., Duman, E., Acet, M., Wassermann, E. F., Moya, X., Mañosa, L., and Planes, A., "Inverse magnetocaloric effect in ferromagnetic Ni-Mn-Sn alloys", (2005), *Nature Materials*, Vol **4**, 450-454

[23] Ranke, P. J., Oliveira, N. A., Alho, B. P., Plaza, E, J, R., Sousa, V. S. R., Caron, L., and Reis, M, S., "Understanding the inverse magnetocaloric effect in antiferro- and ferromagnetic arrangements", (2009), *Journal of Physics: Condensed Matter*, Vol **21**, 5

[24] Asamitsu, A., Moritomo, Y., Tomioka, Y., Arima, T., and Tokura, Y., "A structureal phase transition induced by an external magnetic field", (1995) *Nature*, Vol **373**, 407-409

[25] Urushibara, A., Moritomo, Y., Arima, T., Asamitsu, A., Kido, G., and Tokura, Y., "Insulator-metal transition and giant magnetoresistance in $La_{1-x}Sr_xMnO_3$", (1995), *Physical Review B*, Vol **51**, 14103-14109

[26] McBride, K., Cook, J., Gray, S., Felton, S., Stella, L., and Poulidi, D., "Evaluation of $La_{1-x}Sr_xMnO_3$ ($0 \leq x < 0.4$) synthesised via a modified sol-gel method as mediators for magnetic fluid hyperthermia" (2016), *CrystEngComm*, Vol **18**, 3, 407-416

[27] Zhang, N., Yang, W., Ding, W., Xing, D., and Du, Y., "Grain size-dependent magnetism in fine particle perovskit, $La_{1-x}Sr_xMnO_z$", (1999), *Solid state communications,* Vol **109**, 8, 537-542

[28] Valencia, S., Konstantinov, Z., Gaupp, A., Schmitz, D., and Balcells, L. I., et al., "Interfacial effects in $La_{2/3}Sr_{1/3}MnO_3$ thin films with different complex oxide capping layers", (2011), *Journal of Applied Physics*, Vol **109**, O7D718

[29] Dokiya, M., (1995), *Proceedings of the Fourth International Symposium on Solid Oxide Fuel Cells (SOFC-IV),* The Electrochemical Society.

[30] Shannon, R. D., "Revised effective ionic radii and systematic studies of interatomic distances in halides and chalcogenides", (1976), *Acta Crystallographica Section A*, Vol **A32,** 751-767

[31] Markovich, M., Wisniewski, A., and Szymczak, H., "Handbook of magnetic materials", (2014), *Elsevier*, ed. Nonymous, Vol **22**, 1-201

[32] Urushibara, A., Moritomo, Y., Arima, T., Asamitsu, A., Kido, G., and Tokura, Y., "Insulator-metal transition and giant magnetoresistance in $La_{1-x}Sr_xMnO_3$", (1995), *Physical Review B*, Vol **51**, 14103

[33] Zhu, X., "Peroskite Nanopowders: Synthesis, Characterization, Properties and Applications", (2011), *ChemInform*, Vol **42**, 31

[34] Von Hippel, A. R., "Dielectric Materials and Applications", (1995), Artech House Publishers

[35] Kao, K. C., "Dielectric phenomena in solids", (2004), Elsevier Academic press, Amsterdam

[36] Kappe, C. O., Pieber, B., Dallinger, D., "Microwave effects in organic synthesis: myth or reality", (2013), *Angewandte Chemie International Edition*, Vol **52**, 4, 1088-1094

[37] Herrero, M. A., Kremsner, J. M., Kappe, C. O., "Nonthermal microwave effects revisited: on the importance of internal temperature monitoring and agitation in microwave chemistry", (2008), *The Journal of Organic Chemistry*, Vol **73**, 1, 36-47

[38] Farhadi, S., Momeni, Z., and Taherimehr, M., "Rapid synthesis of perovskite-type $LaFeO_3$ nanoparticles by microwave-assisted decomposition of bimetallic La [Fe (CN) $_6$]. $5H_2O$ compound", (2009), *Journal of Alloys and Compounds*, Vol **471**, L5-L8

[39] Hutagalung, S. D., Ikhwan, M., Ibrahim, M., and Ahmad, Z, A., "Microwave assisted sintering of $CaCu_3Ti_4O_{12}$", (2008), *Ceramics International*, Vol **34**, 4, 939-942

[40] Yu, H., Liu, H., Luo, D., and Cao, M., "Microwave synthesis of high dielectric constant Ca $Cu_3Ti_4O_{12}$", (2008), *Journal of Materials Processing Technology*, Vol **208(1-3),** 145-148

[41] Von Hippel, A. R., "Dielectric materials and applications", (1954), *Artech House on Demand*

[42] Kao, K. C., "Dielectric materials and applications", (2004), *Elsevier Academic press*, Amsterdam

[43] McBride, K., Bennington-Gray, Cook, J., Stella, L., S., Felton, S., and Poulidi, D., "Improving the crystallinity and magnetocaloric effect of the perovskite La0.65Sr0.35MnO3 using microwave irradiation", (2017), *CrystEngComm*, **19**, 3776-3791

[44] Momma, K., and Izumi, F., "VESTA 3 for three-dimensional visualization of crystal, volumetric and morphology data", (2011), *Journal of Applied Crystallography*, Vol **44**, 1272-1276

[45] Hong, R., Pan, T., and Li, H., "Microwave synthesis of magnetic Fe_3O_4 nanoparticles used as a precursor of nanocomposites and ferrofluids", (2006), *Journal of Magnetism and Magnetic Materials,* Vol **303**, 60-68

[46] Epherre, R., Pepin, C., Penin, N., Duguet, E., Mornet, S., Pollert, E., and Goglio, G., "Evidence of non-stoichiometry effects in nanometric manganite perovskites: influence on the magnetic ordering temperature", (2011), *Journal of Materials Chemistry*, Vol **21**, 38, 14990-14998

Chapter 5

Magnetic characterisation, using SQUID magnetometry, of monomeric ionic liquids

5.1. Outline

Magnetic analysis was conducted, by means of SQUID magnetometry, on a family of monomeric ionic liquids. The magnetic moment associated with each sample was deduced and compared with those reported in the literature. Dimeric Dy and Nd ionic liquids were synthesised and magnetic analysis was again conducted via SQUID magnetometry. The data were compared with that obtained for the respective monomeric counterparts and other similar complexes reported in the literature. The material synthesis and crystal analysis outlined in this chapter was conducted by Peter Nockemann *et al*. The work in this chapter is published in the following paper:

"Easily Accessible Rare-Earth-Containing Phosphonium Room-Temperature Ionic Liquids: EXAFS, Luminescence and Magnetic Properties", Alvarez Vicente, J., Dandil, S., Banerfee, D., Gunaratne, H. Q. N., Gray, S., Felton, S., Srinivasan, G., Kaczmarek, A. M., Van Deun, R., and Nockemann, P., (2016), Journal of Physical Chemistry B, **120**, 23, p.5301-5311

5.2. Monomeric Lanthanide Ionic Liquids

A family of monomeric lanthanide ionic liquids, with the chemical formula $[P_{66614}]_3[LnCl_6]$ were synthesised by means of a simple metathesis reaction process, where Ln = La, Ce, Pr, Tm, Yb, Lu, Nd, Sm, Eu, Gd, Tb, Dy, Ho and Er. The complete family of compounds was synthesised for completeness. This is the first documented case of the incorporation of highly charged metals, the lanthanides, into an ionic liquid, forming low-melting metal-containing ionic liquids (ILs) [1].

Metal-containing ionic liquids show promise in numerous applications, particularly in the field of organic synthesis were they can be employed in cyclization and isomerization, alkylation, carboxylation and metathesis. Other potential applications include biomass refining, CO_2 capture and fuel desulfurization and denitrogenation [2]. The incorporation of highly charged metals into ionic liquids results in compounds with unique physicochemical properties including high magnetic moments, enhanced hydrophobicity and the ability to solvate a wide range of molecules. The tunability of magnetic ionic liquids (MILs) enables magnet based technologies which can be incorporated into organic synthesis, complement needed extraction requirements or target specific analytes [3].

The metal-containing ILs synthesized in this chapter consist of 1-hexyl-3- methylimidazolium ($C_{6\,MIm}$) cations and heptathiocyanato lanthanate (III) anions with the general formula $[C_{6\,MIm}]_{5-x}[Ln(SCN)_{8-x}(H_2O)_x]$ ($x = 0 - 2$, $[C_{6\,MIm}]$ = 1-hexyl-3-methylimidazolium) (Ln = lanthanide). Extended X-ray absorption fine structure (EXAFS) and single crystal X-ray diffraction were used in order to determine the crystal structure of the complexes and the magnetic properties of the series where studied by means of SQUID magnetometry.

5.2.1. Experimental

5.2.1.1. Material Synthesis

The family of lanthanide ionic liquids (shown Figure 5.1) were synthesised using a simple metathesis reaction. The lanthanide ionic liquids can be achieved using the one of the two synthetic pathways displayed below depending on whether the rare earth chloride salt used is hydrated or anhydrous;

A. $$3[P_{66614}]Cl + RECl_3.6H_2O \rightarrow [P_{66614}]_3[RECl_6] + 6H_2O$$

B. $$3[P_{66614}]Cl + RECl_3 \rightarrow [P_{66614}]_3[RECl_6]$$

where RE = La, Ce, Pr, Nd, Sm, Eu, Gd, Tb, Dy, Ho, Er, Tm, Yb and Lu.

The process for synthetic pathway A was to react three parts phosphonium salt with one part anhydrous lanthanide chloride salt. The phosphonium salt $[P_{66614}]Cl$ was well dried and added to the RE chlorides under a nitrogen atmosphere in a glove box. The sealed mixture was then heated and stirred continuously at around 80°C, resulting in the formation of the desired ionic liquids. Attempts were made to synthesise the complete series using anhydrous salts as hydrated lanthanide chlorides are known to form undesired by-products. However the pathway was found to be unsuitable for the Eu, La, Ce and Tm samples. In this case synthetic pathway B had to be employed. The phosphonium chloride and hydrated lanthanide chloride salt were independently dissolved in ethanol and the resulting two mixtures mixed together for 1 to 2 hours at room temperature. The ethanol was then removed using a rotary evaporator set to 80°C. Finally the resulting compounds were dried overnight in a high vacuum environment at 130°C. Fabrication of a selection of samples using both synthetic pathway A and B proved that the samples synthesised by pathway A were identical to well dried samples synthesised using pathway B.

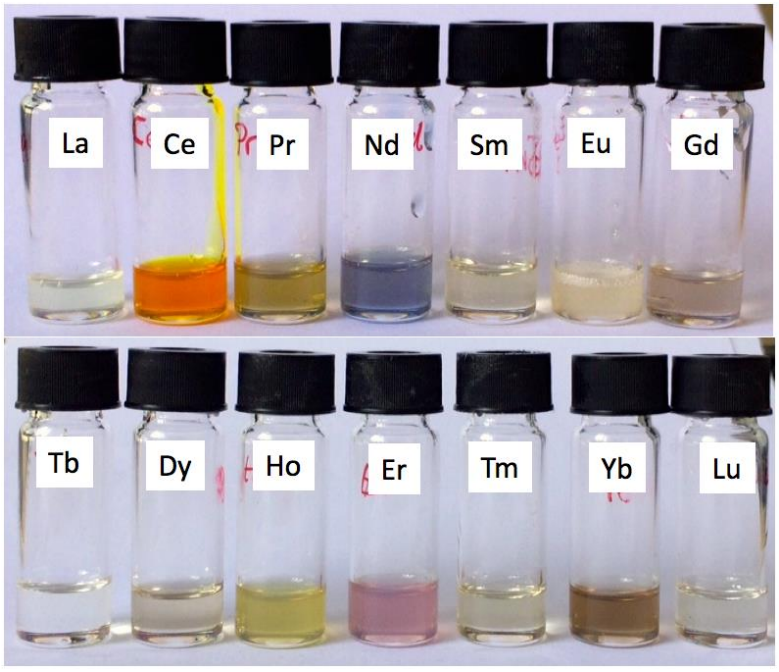

Figure 5.1: Samples of the room-temperature liquid lanthanide series with formula $[P_{66614}]_3[LnCl_6]$ where Ln = La, Ce, Pr, Nd, Sm, Eu, Gd, Tb, Dy, Ho, Er, Tm, Yb and Lu.

5.2.1.2. Characterisation

Extended X-ray absorption fine structure (EXAFS) spectra of the Eu, Nd and Dy ionic liquids at room temperature was collected at the Dutch-Belgian Beamline (DUBBLE) at the European Synchrotron Radiation Facility (ESRF). Single crystal X-ray diffraction was carried out on an analogous crystalline Eu sample, where the $[P_{66614}]$ cation was replaced by the shorter alkyl-chain cation analogue, $[P_{4444}]^+$, using the Kappa APEX 11 (Bruker AXS) diffractometer.

DC magnetic susceptibility measurements were performed using a Quantum Design MPMS DC XL SQUID magnetometer. The samples were contained in gelatine capsules, which were prepared in a glovebox under an argon atmosphere and sealed with vacuum grease. The capsule was then positioned into a drinking straw for measurement. The magnetisation of the samples was measured as a function of temperature in the range 180-380K with an applied field of 500Oe. Measurements where taken both on heating and cooling the samples and were found to be identical. Diamagnetic corrections due to the atoms and bonding present in the complexes were calculated from Pascal's constants and applied to the data. These are displayed in Table 5.1, along with the number of moles of each sample measured.

Sample	**Mass (g) x10^{-2}**	**Moles of sample (mol) x10^{-5}**	**Diamagnetic correction applied (emu/mol) x10^{-3}**
$[P_{4444}]_3[NdCl_6]$	8.47 ± 0.005	4.6833 ± 0.0028	-1.47 ± 0.022
$[P_{4444}]_3[DyCl_6]$	10.80 ± 0.005	5.9120 ± 0.0274	-1.50 ± 0.023
$[P_{4444}]_3[TbCl_6]$	9.63 ± 0.005	5.2818 ± 0.0027	-1.91 ± 0.029
$[P_{4444}]_3[ErCl_6]$	9.04 ± 0.005	4.9357 ± 0.0027	-1.46 ± 0.022
$[P_{4444}]_3[HoCl_6]$	5.20 ± 0.005	2.8427 ± 0.0273	-1.58 ± 0.024
$[P_{4444}]_3[GdCl_6]$	5.77 ± 0.005	3.1676 ± 0.0027	-1.52 ± 0.023
$[P_{4444}]_3[EuCl_6]$	4.82 ± 0.005	2.6538 ± 0.0027	-1.41 ± 0.021

Table 5.1: Table displaying the sample mass and number of moles of the measured ionic liquids samples and the sample specific diamagnetic correction applied to each sample.

An additional background diamagnetic response, of 5 x 10^{-9} emu/Oe from both the straw and gelatine capsules used to contain the samples was also accounted for [2].

5.2.2. Results and discussion

5.2.2.1. Crystalline structure and configuration analysis

Attempts were made to synthesise suitable crystals of each of the ionic liquid compounds for crystal structure analysis. As none of the compounds with the $[P_{66614}]^+$ cation crystallise, crystallised samples were synthesised using the heavier symmetric $[P_{4444}]^+$ cation. Only the $[P_{4444}]_3[EuCl_6]$ sample was of adequate quality to carry out single crystal X-ray diffraction analysis on. The crystal analysis revealed each $[EuCl_6]^{3-}$ anion to be surrounded by three crystallographically independent $[P_{4444}]^+$ cations as displayed in Figure 5.2. It is expected that the other ionic liquids in the family exhibit the same crystal structure.

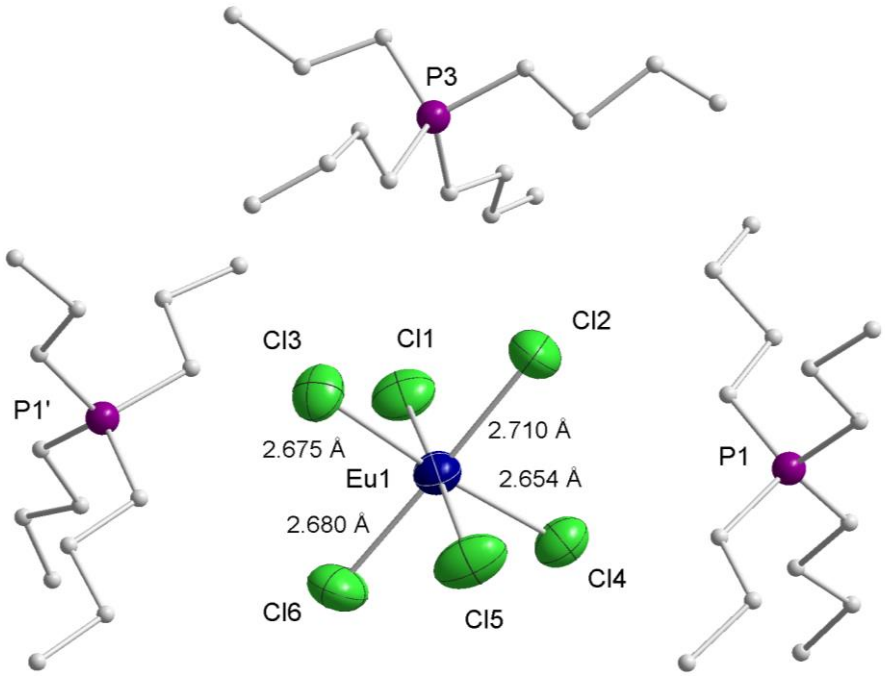

Figure 5.2: Packing in the unit cell of $[P_{4444}]_3[EuCl_6]$

EXAFS was carried out on the Nd, Eu and Dy ionic liquid samples. These measurements confirmed the hexa-coordination of the lanthanide ions by six chloride ligands in the liquid state. Additionally, they confirmed the Ln-Cl distances in each complex as summarised in Table 5.2.

Sample	R (Å)
$[P_{4444}]_3[NdCl_6]$	2.696(3)
$[P_{4444}]_3[EuCl_6]$	2.664(2)
$[P_{4444}]_3[DyCl_6]$	2.647(2)

Table 5.2: Table displaying the Ln-Cl distances in the Nd, Eu and Dy dimeric ionic liquids as confirmed by EXAFS.

As expected the Ln-Cl distance decreases with decreasing lanthanide ionic radius. As the lanthanide radius decreases, the associated charge density increases. As a direct result the attraction between the lanthanide ion and the chloride ligands becomes stronger, and the Ln-Cl distance is reduced.

5.2.2.2. Magnetic Susceptibility Data

The magnetic susceptibility data collected for the ionic liquid family where Ln = Gd, Ho, Er, Tb, Dy and Nd, is displayed in Figure 5.3.

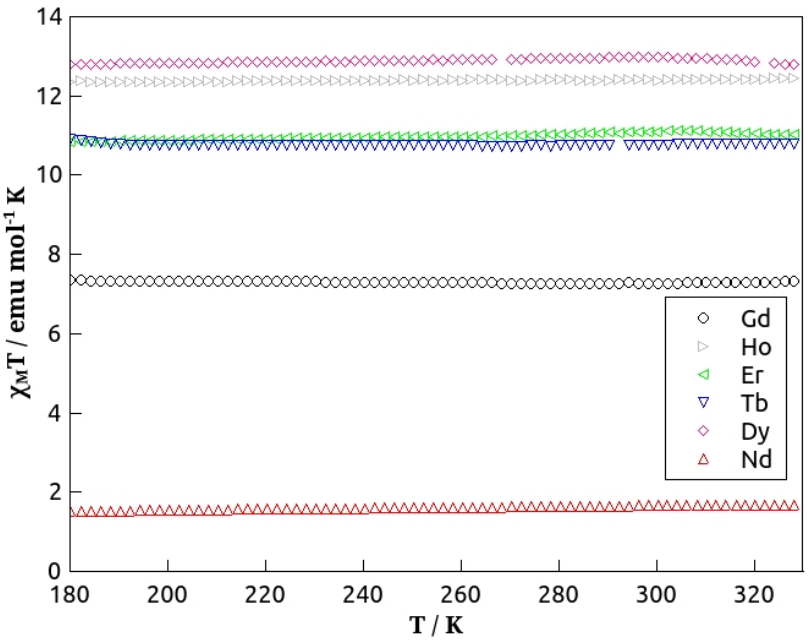

Figure 5.3: $\chi_M T$ against T for $[P_{66614}]_3[RECl_6]$ (RE = Gd, Ho, Er, Tb, Dy, Nd) between 180-330K collected upon heating with an applied field of 500Oe.

Figure 5.3, shows that all of the samples measured in this study returned constant $\chi_M T$ values over the measured temperature range and therefore display simple paramagnetic behaviour under these conditions. This was as predicted as the distance between two neighbouring metallic centres in the complex is two large to expect any interaction to take place. Hence the spin associated with each metallic centre acts independently to any others in the compound. On application of an applied field some of the unpaired spins associated with the metal centres in the complex will realign parallel to the field, however if the field is not sufficiently large enough to saturate the sample, some of the unpaired spins will remain randomly aligned. At the initial measurement temperature of 180K, a set number of unpaired spins for each sample will align parallel to the applied field. As the temperature is increased and more thermal energy is put into the system, the orientation of the aligned spins will start to randomise, due to increased thermal motion, in such a way that $\chi_M T$ remains constant. The magnetic susceptibility data for the lanthanide family were also plotted as inverse susceptibility against temperature in order to calculate the magnetic moment associated with each sample, see Figure 5.4 (a) and (b).

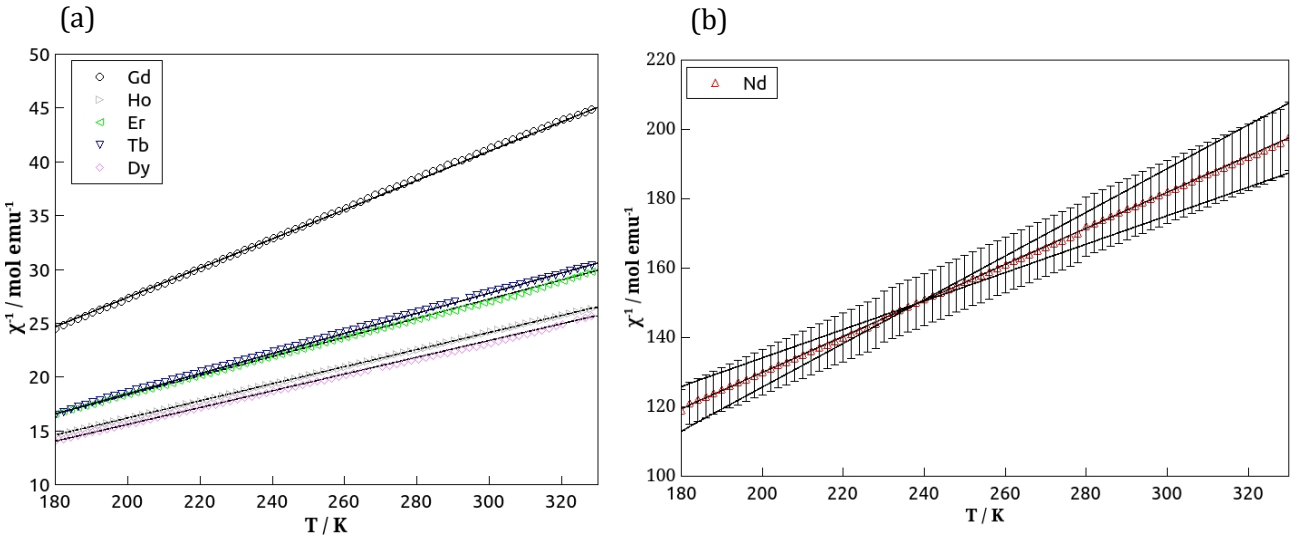

Figure 5.4: Magnetic susceptibility measurements for ***(a)*** Er, Dy, Tb, Ho, Gd and ***(b)*** Nd samples in the temperature range 180K-330K, collected on heating with an applied field of 500Oe. The symbols represent the experimental data and the lines show the Curie-Weiss fits used to determine the effective magnetic moments. The Nd data shows error bars associated with the uncertainty in the measurement and the maximum and minimum lines of best fit.

An averaged diamagnetic contribution of 5 x 10^{-9} emu/Oe, as a result of the gelatine capsules used to contain the samples was accounted for however it is important to note that this value

can vary by around ±2 x 10^{-10} emu/Oe emu depending on the capsule. Additionally some uncertainty can enter into the measurement as a result of heat contraction/expansion of the drinking straw moving the sample slightly off –centre during the measurement. Such uncertainties are normally negligible, as is the case for the measurements conducted in Chapters 4 and 5, due to the auto center control on the SQUID magnetometer and comparably small magnetic response of the gelatine capsule, however in the case of this experiment they did have a small impact on the data collected [3]. As the magnetic response of the samples was so small (around 10^{-5} emu), it was challenging to center the samples without the application of a very large field, as a result the auto-centering would not be 100% accurate throughout the measurement. Additionally, the diamagnetic response due to the gelatine capsule was found to be around 9% of the magnitude of the magnetic response from the samples and hence the uncertainty in this value could contribute an overall uncertainty of around 0.4% to the data collected. The largest area of uncertainty in the measurements however arises from the measurement of the mass of the samples, as this is used to calculate the number of moles of each sample. Although the actual measurement of the mass is relatively precise, it is possible that some unreacted reagents may still remain in the sample, contributing to the mass but not the observed magnetic behaviour. This is estimated to introduce an uncertainty or around 4.5% into the measurement and as a result it was concluded that the overall uncertainty associated with the measured magnetic moment of the samples was around 5%. The impact of this degree of uncertainty is displayed by the error bars included in the Nd data in Figure 5.4 (b).

The data in Figures 5.4 (a) and (b) were fitted using the Curie-Weiss law in order to calculate the magnetic moment associated with each sample, Equation 3.9.

The gradient of an inverse susceptibility against temperature plot for a paramagnet is equal to 1 over the curie constant. From this value the magnitude of the magnetic moment associated with each sample can be calculated using the following equation,

$$\mu_{eff} = 2.84\sqrt{C} \qquad \textbf{Equation 5.1}$$

The effective magnetic moment calculated for each sample is displayed in Table 5.3.

Lanthanide Ion	Curie Constant, C, (emu K mol^{-1} Oe^{-1})	Weiss Temperature, θ (K)	Calculated Effective Magnetic Moment, μ_B (B.M.)	Observed Magnetic Moment from Literature (B.M.)[4]	$\chi_M T$ (emu/mol K)
Dy	12.9±2.4	0±43.8	10.2±0.9	10.4-10.7	12.9±0.6
Nd	1.9±0.4	-49.5±63.8	3.9±0.4	3.5-3.6	1.6±0.08
Er	11.2±2.1	-6.2±44.7	9.5±0.9	9.4-9.6	11.0±0.6
Tb	10.7±1.8	2.7±38.6	9.3±0.8	9.5-9.8	10.8±0.5
Ho	12.6±2.4	-3.8±45.0	10.0±0.9	10.4-10.7	12.4±0.6
Gd	7.4±1.1	-1.5±42.8	7.7±0.7	7.9-8.0	7.3±0.4

Table 5.3: Effective magnetic moments, Curie constants, Weiss temperatures and $\chi_M T$ values for Er, Dy, Nd, Ho, Gd and Tb samples.

The uncertainties associated with these values were calculated by determining the magnetic moments corresponding to lines of maximum and minimum fits which fell within the error bars and determining the deviation of these results from our calculated moments. The calculated effective magnetic moments were found to be consistent with those in the literature for the observed values of the lanthanide ions, within the range of experimental uncertainty [4]. It should be noted that the Weiss temperatures are small enough that they can be taken to be zero within the experiment uncertainties. The Weiss temperature calculated for the Nd sample is significantly larger than that of the other samples, due to the increased uncertainty in accurately fitting to the data due to the much smaller magnetic response of the sample. The data for the Nd sample can however be convincingly fit with the Weiss temperature set equal to zero.

Although attempts were made to obtain magnetic measurements for the Sm sample within the desired temperature range, it was not possible to satisfactorily center the sample within the SQUID magnetometer. This was due to the small magnetic response of the sample, which from literature is observed to be in the range of 1.4-1.7 B.M [4]. Some difficulty was also encountered when centring the Eu sample, which is observed as having a magnetic response of 3.3-3.5 B.M. Although it was possible to obtain a data set for this sample a convincing fit could not be achieved due to the small magnetic response detected ($x10^{-5}\ emu$). As the diamagnetic response from the gelatine capsule is of magnitude $x10^{-6}\ emu$, the uncertainty in the Eu measurement would be too large to draw any quantitative conclusions. The measurement has however been included in Figures 5.5 (a) and (b), for completeness.

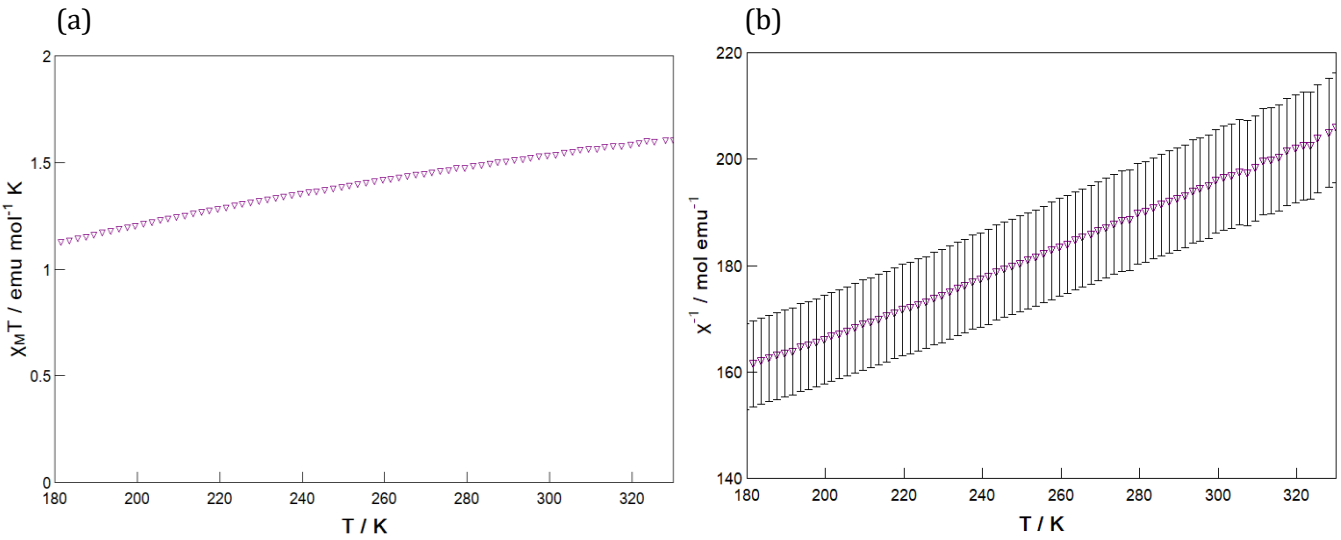

Figure 5.5: (a) $1/\chi_M$ against T and ***(b)*** $\chi_M T$ against T (right) for $[P_{66614}]_3[EuCl_6]$ collected on heating in the temperature range 180K-330K, with an applied field of 5000e.

The linear relationship displayed between the inverse susceptibility and temperature suggests that the Eu sample exhibits simple paramagnetic behaviour in keeping with the rest of the family. However, as can be seen from Figure 5.5 (b), a small decrease in the value of $\chi_M T$ from 1.6 emu.K.mol^{-1} at 330K to 1.2 emu.K.mol^{-1} at 180K was observed. Unlike the previous samples the Eu sample was measured on cooling and this slight decrease is likely observed due to the sample going slightly off centre during the measurement.

5.3. Dimeric Lanthanide Ionic Liquids

Following on from the work completed on the family of monomeric lanthanide ionic liquids, two dimeric liquid compounds with the chemical formulae $[P_{66614}]_2[Dy_2(C_7H_{15}COO)_8]$ and $[P_{66614}]_2[Nd_2(C_7H_{15}COO)_8]$ were synthesised. SQUID analysis was carried out on the compounds with the intention of comparing the effective magnetic moments of the dimeric samples to the moments calculated in section 5.2.2.2 for the monomeric counterparts. In theory discrepancies between the measured magnetic moments would indicate the presence of spin-spin interactions between the metal centres in the dimeric compounds. Due to experimental difficulties in obtaining a pure sample, a number of samples of each of the two compounds were produced and their magnetic response measured using SQUID magnetometry. Unfortunately for both compounds, the magnitudes of the values obtained were not consistent across the different

samples. This is most likely as a result of uncertainty in the mass of the measured samples. It is probable that some unreacted product is left following the synthesis process, which is not completely removed from the sample to be measured. Hence the measured mass of the sample, which we have assumed to be pure, is likely to include some unknown mass of reactants. This means that the number of moles of the desired product, which is calculated from the sample mass, is likely to be slightly skewed. As each sample will have a different amount of unreacted product present in it, it is not possible to achieve a consistent magnetic response across the different samples. Hence it is not feasible to carry out quantitative analysis on the data. A brief qualitative analysis is however outlined below.

5.3.1. Experimental

5.3.1.1 Characterisation

As for the monomeric samples, DC magnetic susceptibility measurements were performed using a Quantum Design MPMS DC XL SQUID magnetometer. The samples were contained in the same type of peek capsules used to contain the magnetic crystals in Chapter 2. The capsules were prepared in a glovebox under an argon atmosphere and sealed with vacuum grease to prevent cross contamination. Magnetisation data was collected as a function of temperature in the range 180-380K with an applied field of 500Oe. The measurements were collected on heating. On this occasion no diamagnetic corrections were applied to the data, as purely qualitative analysis was being conducted.

5.3.2. Results and discussion

5.3.2.1 Magnetic Susceptibility Data

The magnetic susceptibility data collected for the Nd and Dy dimeric ionic liquids are displayed in Figure 5.6.

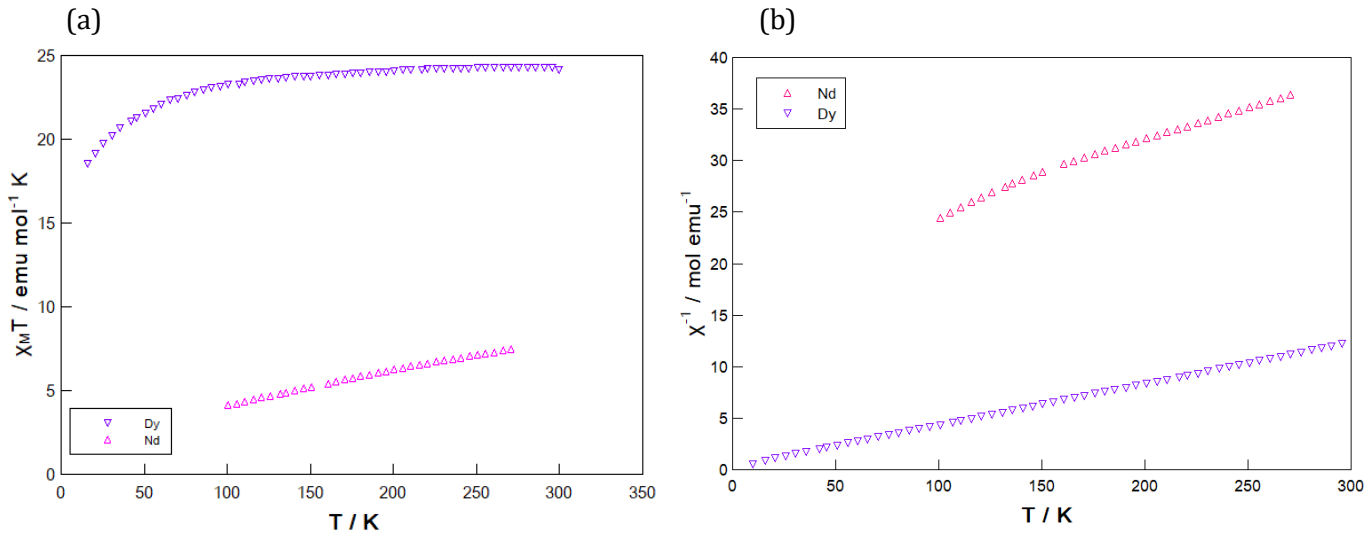

Figure 5.6: (a) $1/\chi_M$ against T for $[P_{66614}]_2[Dy_2(C_7H_{15}COO)_8]$ and $[P_{66614}]_2[Nd_2(C_7H_{15}COO)_8]$ collected upon heating with an applied field of 5000e. ***(b)*** $\chi_M T$ against T for $[P_{66614}]_2[Dy_2(C_7H_{15}COO)_8]$ and $[P_{66614}]_2[Nd_2(C_7H_{15}COO)_8]$ collected upon heating with an applied field of 5000e.

The $\chi_M T$ value for both samples remains relatively constant in the temperature range 100K – 300K. As it was not possible to carry out qualitative analysis on the data it is not possible to confirm exactly how the two metal ions within each individual $[P_{66614}]_2[Ln_2(C_7H_{15}COO)_8]$ complex interact in this temperature range. The constant $\chi_M T$ value however suggests that the neighbouring $[P_{66614}]_2[Ln_2(C_7H_{15}COO)_8]$ complexes behave paramagnetically in this region. Below 100K the $\chi_M T$ value is observed to decrease for both samples. Due to the large distances between neighbouring complexes in the ionic liquids we would not expect them to interact which each other [5]. Therefore the decrease in observed $\chi_M T$ is most likely due to an anti-ferromagnetic interaction between the lanthanide metal centres in the dimers. In order to estimate the distance between the metallic centres in the dimers, analogous crystal complexes with the chemical formula $[P_{66614}]_2[Ln_2(OAc)_8]$ were synthesised. X-ray analysis was carried out on these crystals and the bond distances between the metal centres for the Dy and Nd crystal structures were found to be 3.87 Å and 4.00 Å respectively. The supporting data for this work can be found in reference 5. Very similar behaviour was observed by Eliseeva *et al.* who synthesised a series of dimeric lanthanide(111) polycrystalline compounds with the chemical formula $[Ln(hfa)_3(4-cpyNO)]_2$ [6]. Both the Gd and Tb complexes were shown to exhibit weak antiferromagnetic interactions between the Ln metallic centres as exhibited in Figure 5.7 which shows the temperature dependence of $\chi_M T$ for the Gd complex. The constant value of $\chi_M T$ was

found to be consistent with that of two non-interacting Gd metal centres. Below 70K the reduction in the $\chi_M T$ value observed is evidence of the anti-ferromagnetic interactions present between the Gd ions. Single crystal X-ray diffraction analysis determined the distance between neighbouring metal ions for this dimeric ionic liquid family to range from 3.99 – 4.13 Å. As the Ln-Ln metal distances are comparable with the Dy-Dy and Nd-Nd centres for the sample synthesised in this study, it is conceivable that the two families would exhibit comparable magnetic behaviour.

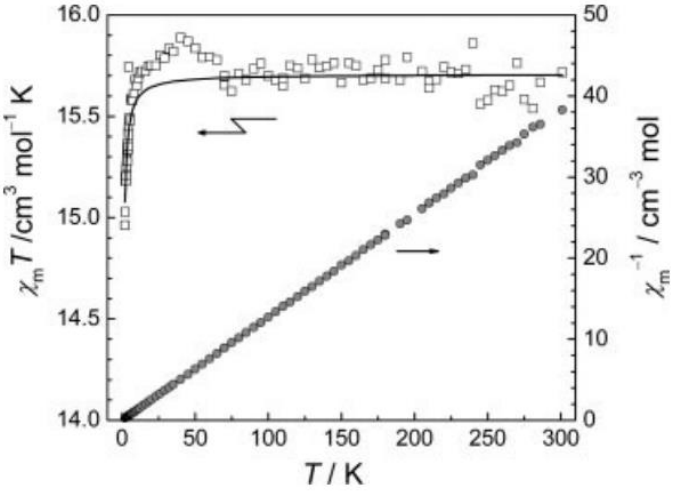

Figure 5.7: Temperature dependence of $1/\chi_M$ (filled circles) and $\chi_M T$ (open squares) for $[Gd(hfa)_3(4-cpyNO)]_2$; the solid line represents the best fit calculated values. Taken from reference 6.

5.4. Conclusions

A family of monomeric ionic liquids were synthesised and their magnetic behaviour was investigated by SQUID magnetometry. The ionic liquids were found to behave paramagnetically within the measured temperature range. By fitting to the Curie-Weis law, the magnetic moments associated with each sample were calculated and found to be comparable with those quoted in the literature. A Dy and Nd dimeric ionic liquid were synthesised and analysed in the same manner as the monomeric family. Unfortunately, due to difficulty completely removing the reactants from the finished sample it was not possible to obtain an accurate sample mass and hence only qualitative analysis was possible. Both samples appeared to show anti-ferromagnetic interactions between neighbouring metal centres below 100K. These results

appeared to be consistent with the magnetic behaviour observed for similar complexes in the literature.

References

[1] Nockemann, P., Thijis. B., Postelmans, K., Van Hecke, K., Van Meervelt, L., and Binnemans, K., "Anionic rare-earth thiocyanate complexes as building blocks for low-melting metal-containing ionic liquids", (2006), *Journal of the American Chemical Society*, Vol **128**, 13658-13659

[2] Zazybin, A., Rafikova, K., Yu, V., Zolotareva, D., Dembitsky, V. M., and Sasaki, T., "Metal-containing ionic liquids: current paradigm and applications", (2017), *Russian Chemical Reviews*,Vol **86**, 12

[3] Clark, K. D., Nacham, O., Purslow, J. A., Pierson, S. A., and Anderson, J. L., "Magnetic ionic liquids in analytical chemistry: A review", (2016), *Analytica Chemica Acta*, Vol **934**, 31, 9-21

[2] Quantum Design, (2000) *MPMS Application Note,* 1014-201, 11/01/2000

[3] Maguire-Boyle, S, Barron, A. R, "Theory of a Superconducting Quantum Interference Device (SQUID)", *OpenStax-CNX module: m22750*, (2009), Version 1.3

[4] Bain, G.A. and Berry, J.F., "Diamagnetic Corrections and Pascal's Constants", (2008), *Journal of Chemical Education*, Vol. **85**. 4

[5] Nockemann, P., Felton, S., Esien, K., McCourt, E., and Zhenyu, Li, "Designing Dimeric Lanthanide (111)-Containing Ionic Liquids", (2018), *Angewandte Chemie International Edition*

[6] Eliseeva, S.V., Ryazanov, M., Gumy, F., Troyanov, S.I., Lepnev, L.S., Bunzli, J.G., and Kuzmina, N.P., "Dimeric Complexes of Lanthanide(111) Hexafluoroacetylacetonates with 4-Cyanopyridine N-Oxide: Synthesis, Crystal Structure, Magnetic and Photoluminescent Properties", (2006), *European Journal of Inorganic Chemistry*, Vol. **23**, 4809-4820

Chapter 6

Magnetic characterisation, using SQUID magnetometry, of metallic crystal clusters fabricated using ionic liquids

6.1. Outline

The overarching aim of this study was to fabricate magnetic crystals, which exhibited interesting magnetic properties, in particular molecular magnetism, using a simple and 'green' synthesis process, which utilises ionic liquids. In this chapter nickel, manganese and cobalt acetate crystal clusters were synthesised using a simple one step synthesis process. The formation processes of these complexes were studied and revealed to be concentration and temperature dependent, showing this synthetic pathway to show promise in the fabrication of a variety of different magnetic crystals. The crystal structures of the complexes synthesised in this chapter were investigated using single crystal X-ray diffraction (XRD) and the magnetic properties were studied via SQUID magnetometry.

6.2. Introduction

The motivation for this chapter was to produce metallic crystals with interesting magnetic properties using a green synthesis process. The production of magnetic crystals generally involves very complex procedures often involving volatile solvents, which pose extreme environmental risks [1]. In the general field of crystal engineering and material chemistry, increased use of ionic liquids has allowed for a move away from conventional solvents aiding the ever growing desire to practise green or sustainable chemistry [2]. In comparison to conventional solvents, the by-products produced from ionic liquids are non-toxic and environmentally safe [3]. In this chapter we present three unique transition metal clusters which have been synthesised using the ionic liquids [C_{2MIm}], or 1-Ethyl-3-methyl-imidazolium acetate. Acetate bridged hexameric nickel (Ni^{2+}), trimeric cobalt (Co^{2+}) and polymeric manganese (Mn^{2+}) crystal clusters were synthesised using a simple one step ionothermal synthesis process whereby metal acetate salts were heated in 1-ethyl-3-methyl-imidazolium acetate and the resulting crystals isolated by means of manual drying. The synthesis method employed in the production of the three crystal complexes in this chapter is particularly novel in that it requires no additional ligands or solvothermal conditions using autoclaves. Of particular interest was the fact that the three crystals formed were chemically different even though the same synthesis process was adopted each time and the transition metals all had a +2 charge. It was in fact determined that the complexes formed were dependent on both the temperature they were heated to during synthesis, and the concentration of metal acetate solution used. This shows that this synthetic pathway has promise for the production of a wide range of chemically different cluster complexes. On investigating the magnetic properties of the crystal cluster it was concluded that at least one may potentially be a single molecule magnet. It is believed that this is the first time ionic liquids have been used in the synthesis of magnetic crystals which could potentially be SMMs.

6.3. Hexameric Ni(II) crystal complex

In the first part of this study a hexameric Ni(II) compound was synthesised by the dissolution of Ni(II) acetate in the ionic liquid, [C_2mim][OAc]. The crystal structure of the complex was studied via XRD and the magnetic properties studied in detail using SQUID magnetometry. Fitting of the magnetic susceptibility and reduced magnetisation data, by the programmes PHI [4] and ANISOFIT 2.0 [5-6] respectively, helped to determine the magnitude of a range of the magnetisation parameters of the complex.

6.3.1. Experimental

6.3.1.1. Material Synthesis

Single crystals of a hexameric wheel-like assembly, of the compound $[C_2mim]_4[Ni_6(OAc)_{13}(OH)_2(H_2O)_2][\ OAc]\cdot H_2O$ were formed on heating a nickel(II) acetate solution (> 20 mol%) in the ionic liquid, $[C_2mim][OAc]$ (where $[C_2mim]^+$ = 1-methyl-3-ethylimidazolium). The solution was heated for a few hours to 363 K, and the crystals grew on cooling.

6.3.1.2. Characterisation

Structural determination of the Ni complex was carried out using single crystal X-ray diffraction (XRD) (Panalytical X'Pert PRO) with a CuKα1 radiation source of wavelength 1.540598Å. Magnetic characterisation was performed using a Quantum Design MPMS DC XL SQUID magnetometer. The crystalline samples were ground into a powder before the SQUID magnetometry measurements were carried out, in order to eliminate any issues arising from preferential magnetisation down a particular crystal axis. DC magnetic susceptibility measurements were carried out under an applied field of 500Oe in the range 2–300K. The measurements were collected on heating the sample, after it had been cooled both with and without a field applied. Work was done to fit to susceptibility data using the PHI programme and employing the coupling regime shown in Figure 6.6. As outlined in section 3.4.1., PHI software utilizes many Hamiltonians describing contributions such as spin orbit coupling, exchange coupling, crystal field interaction and Zeeman effects to fit the experimental data and return values for the various parameters used [4]. Hence extreme care had to be taken not to over parameterize when fitting the experimental data (see section 3.4.1.). Reduced magnetisation data were also collected, in the temperature range 2-8K at set applied fields at increments of 1T, between 3 and 7T. Fitting of this data was achieved using the ANISOFIT2.0 software, which fits data using the following Hamiltonian [5-6]:

$$\hat{H} = D\hat{S}z_2 + E(\hat{S}x_2 + \hat{S}y_2) + g_{iso}\mu_B \boldsymbol{S} \cdot \boldsymbol{B} \qquad \textbf{Equation 6.1}$$

By means of this fit, values for the rhombic and axial zero field splitting parameters, an overall Landé g factor and a value for the spin ground state of the complex could be established (see section 3.4.2.). DC field dependent measurements were also carried out, at a range of different

temperatures in a variety of different field ranges, using SQUID magnetometry. The DC field dependent measurements taken at low temperatures (1.8-4K) were of particular interest as these would help to identify the presence of SMM behaviour.

Unfortunately contamination is an issue with the magnetic crystal complexes investigated in this chapter, due to their hygroscopic nature. The Ni compound is particularly sensitive, and was found to draw moisture from the atmosphere immediately after production, and undergo degradation to the paramagnetic nickel(II) acetate tetrahydrate ionic liquid. Measures were taken to limit the extent of this degradation as detailed in section 3.2.2. and the magnetic crystals were eventually measured using peek capsules (see Figure 3.4(b)).

6.3.2. Results and discussion

6.3.2.1. Crystalline structure and configuration analysis

The structure of the Ni(II) complex was identified using single crystal XRD (see Figure 6.1).

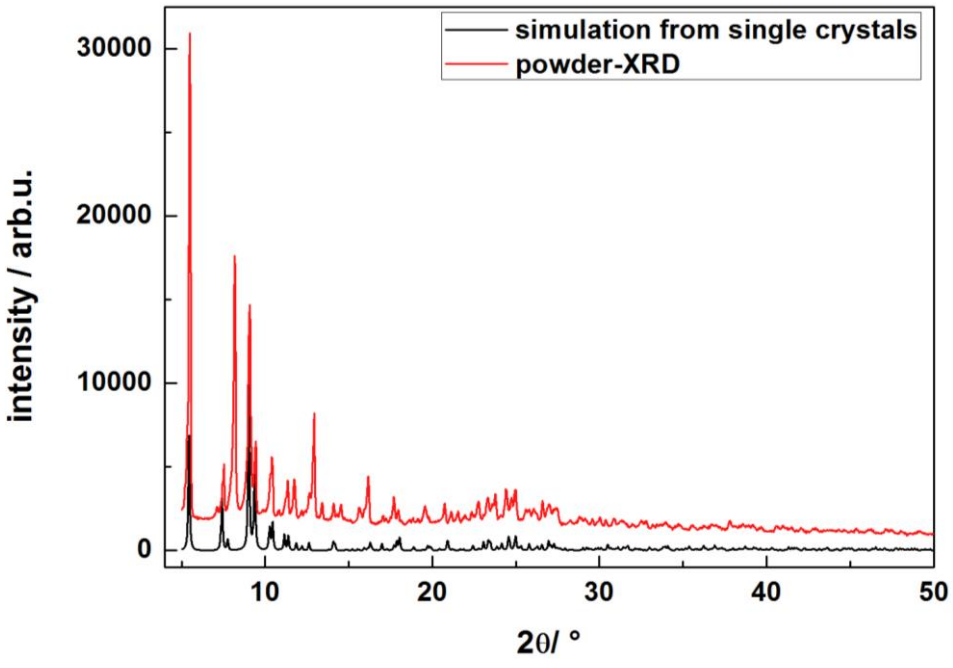

Figure 6.1: Powdered XRD of $[C_{2\ MIM}]_4\ [Ni_6(OAc)_{13}(OH)_2(H_2O)_2][OAc]\cdot H_2O^-$ measured from the Ni crystals (red) and simulated from the single crystal structure (black) using "Mercury 3.3"

The Ni(II) complex was found to consist of six distorted octahedral nickel centres arranged into a hexameric ellipsoidal ring which exhibits a two-fold axis of symmetry through the centre (see Figure 6.2).

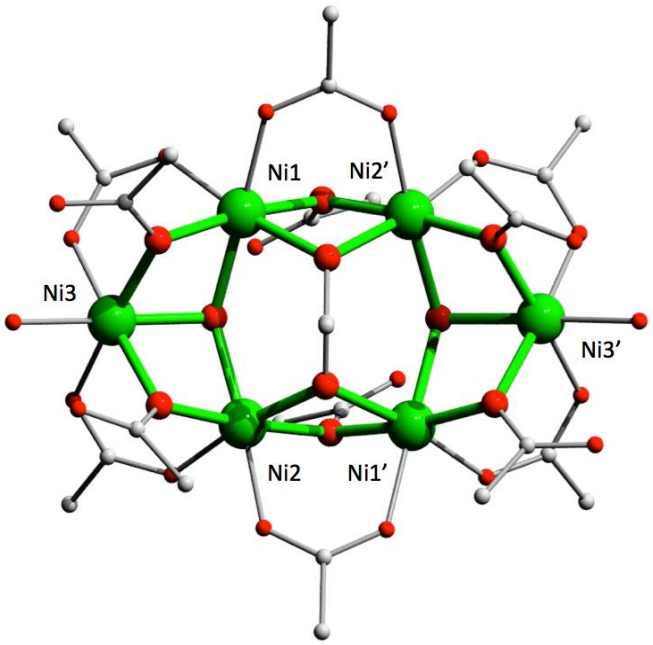

Figure 6.2: The hexameric Ni(11) unit, $[Ni_6\ (OAc)_{13}(OH)_2(H_2O)_2]^{3-}$ present in the Ni(II) complex. The hydrogen atoms are omitted for clarity.

The Ni(II) distances were found to range from 3.026(2) to 3.083(2)Å. Two μ_3-hydroxides connect each of three Ni(II) centres on both sides of the compound, essentially grouping the six Ni(II) centres into groups of three. The hexanuclear ring is surrounded by two $[C_{2\ MIM}]^+$ cations, which form hydrogen bonds originating from the imidazolium C2-H to the anionic cluster. Between each two adjacent Ni centres, two bridging acetates were identified, one in the $\mu - \eta^1 : \eta^1$ mode and one in the $\mu - \eta^2$ mode. In this notation μ represents the bridging ligand with a subscript number denoting the number of metals bound to the bridging ligand. Often μ_2 is simply denoted as μ. The hapticity, coordination of the ligand to the metal center via an uninterrupted series of atoms, is denoted by the symbol η. A superscript number is used to describe the number of atoms through which the ligand is coordinated. An additional, acetate situated on top of the hexameric cluster was found in a unique $\mu - \eta^2 : \eta^2$ binding mode, with the acetate bridging between four nickel centres (see Figure 6.3).

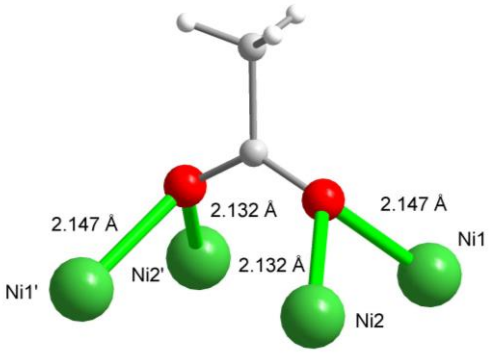

Figure 6.3: μ – η^2 : η^2 acetate binding mode found in Ni(II) crystal complex

To our knowledge this is the first time this binding mode has been reported for a crystal structure with carboxylate ligands. Although other hexanuclear nickel(II) complexes have been previously reported, the topology of the anionic hexamers presented here is unprecedented [7-9].

6.3.2.2. Magnetic measurements

As detailed in section 6.3.2.1 the hygroscopic nature of the Ni crystals and subsequent degradation to the paramagnetic nickel(II) acetate tetrahydrate ionic liquid results in contamination of the sample used for the magnetic measurements.

Although extreme care was taken to reduce to extent of this degradation, as detailed in section 3.2.2, it was not possible to prevent this happening altogether. Additionally due to the non-volatility of the ionic liquid used in the synthesis of the Ni complex, it was not possible to completely remove the ionic liquid from the resulting Ni crystals by drying ($3.4 \times 10^{-3} \pm 0.5 \times 10^{-4}$ g of nickel(II) acetate tetrahydrate ionic liquid was present in the final sample). As a result the overall mass of the final sample used in the magnetic measurements contained a combination of the desired Ni(II) crystal complex and undesired nickel(II) acetate tetrahydrate ionic liquid. As all the data collected on the SQUID magnetometer requires the number of moles of the magnetic sample present to be accurately known it was necessary to determine the mass of the contaminants present in the sample and subtract this from the measured mass. As nickel(II) acetate tetrahydrate is paramagnetic, it was possible to fit to the linear regions of magnetisation observed in the field dependent measurements taken in this study, to determine the mass of this contaminant present. The fits were achieved using the Brillouin function (Equation 6.2) [10]

$$B_J(x) = \frac{2J+1}{2J}\coth\left(\frac{2J+1}{2J}\,x\right) - \frac{1}{2J}\coth\left(\frac{1}{2J}\,x\right) \quad \textbf{Equation 6.2}$$

where J is the total angular momentum of the complex and *x* is given by the following equation (Equation 6.3);

$$x = \frac{g\mu_B JB}{k_B T} \quad \textbf{Equation 6.3}$$

where g is the landé g factor, μ_B is the Bohr magneton, k_B is the Boltzmann constant, T is the temperature and B is the applied field strength. On this occasion g was taken to equal 2.2 and J to equal 1, in accordance with the literature [11]. The final magnetisation, in emu per mole of nickel acetate tetrahydrate, could then be calculated using the following equation (Equation 6.4):

$$M = Ng\mu_B J \cdot B_J(x) \quad \textbf{Equation 6.4}$$

where N is the number of atoms per unit volume (Avogadro's number).

DC field dependent measurements were taken at 1.8, 3, 4, 6, and 7, in the field range -7 T to +7T. Detailed measurements showed ferromagnetic behaviour to be observed below 20K in the -1000 Oe to +1000 Oe that was attributed to interactions in the Ni crystal complex. As such the magnetic behaviour observed outside of this range was concluded to arise as a direct result of the paramagnetic nickel(II) acetate tetrahydrate. The data was plotted as magnetisation per mole of nickel(II) acetate tetrahydrate, using an estimated mass, and the corresponding Brillouin fit was then plotted on the same axis. The mass was then changed until the experimental data best agreed with that of the Brillouin fit. This was repeated for the magnetisation data taken at each temperature, and the single mass, which allowed for the best overall fit to each data set, was concluded as being roughly the mass of nickel(II) acetate tetrahydrate present in the sample, Figure 6.4.

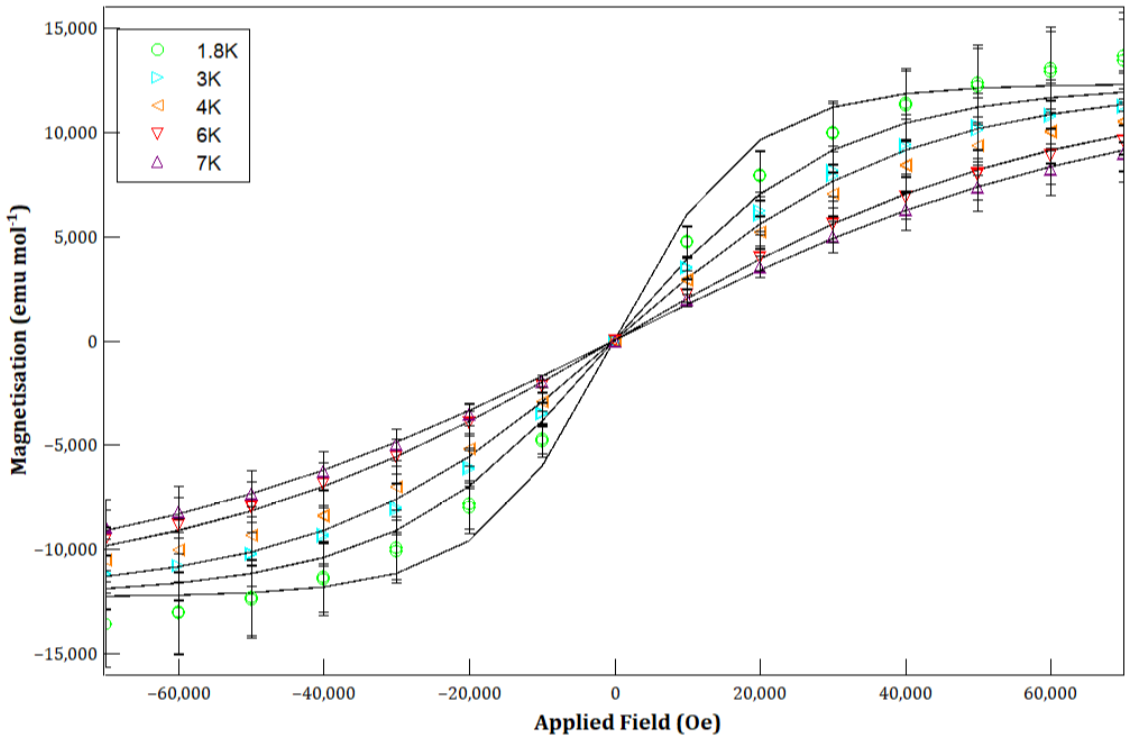

Figure 6.4: Plots of magnetisation against applied field for the Ni(II) complex, taken at temperature 1.8, 3, 4, 6, 7K, assuming a mass of 3.4 $x10^{-5}$ ± 0.5 $x10^{-5}$ g. The solid lines represent Brillouin fits to the data.

This was found to be around 3.4 $x10^{-5}$ ± 0.5 $x10^{-5}$ g. The paramagnetic response of the ionic liquid could then be calculated for each data set, and subtracted, and the mass of the measured sample corrected for this contaminant. The resulting mass of the nickel(II) complex was calculated as being 8.7 $x10^{-3}$ ± 0.5 $x10^{-3}$ g.

Diamagnetic corrections for the sample were also applied to the magnetic data. These were calculated from Pascal's constants and applied to all data [12]. The diamagnetic contributions due to each ion and each bond in the compound were found to amount to a value of -81.7 $x10^{-5}$ ± 1.2 $x10^{-5}$ g emu/mol. The diamagnetic background contribution, due to the straw and peek capsule used to contain the sample, were also accounted for as detailed in section 3.2.2. The average value was calculated to be -4.194 x 10^{-5} ± 0.062 $x10^{-5}$ emu/mol, for an applied field of 500e. On applying these corrections it was possible to achieve fits to both the magnetic susceptibility and reduced magnetisation data, leading us to believe that if any of the reactant ionic liquid was in fact present in the sample, it was present in a small enough quantity to be negligible.

6.3.2.3. Reduced Magnetisation Data

Figure 6.5 shows the reduced magnetisation data collected for the Ni complex after the diamagnetic and paramagnetic corrections outlined in section 6.3.1.2. had been applied.

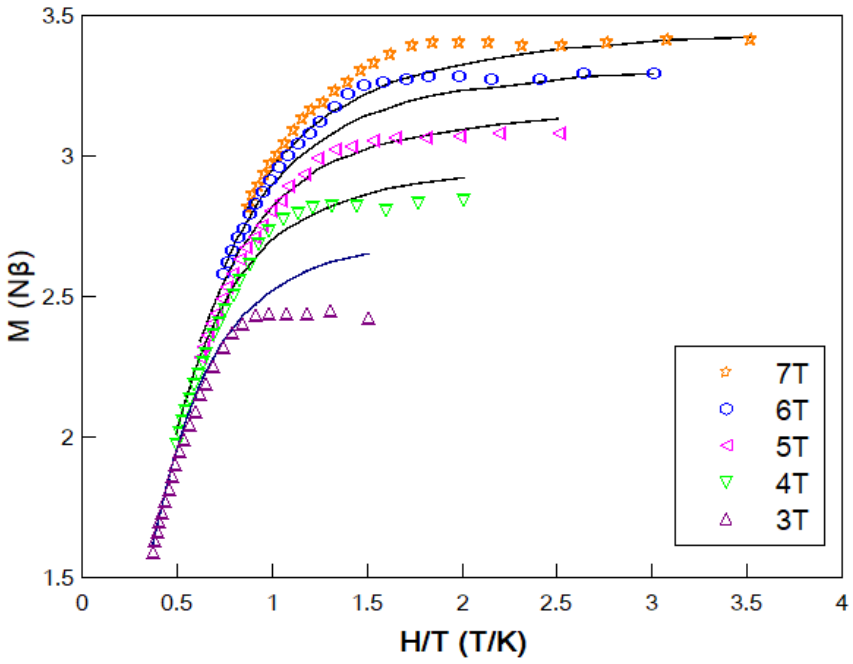

Figure 6.5: Reduced magnetisation data collected for the Ni(II) complex under applied fields of 3, 4, 5, 6 and 7T, in the temperature range 2-8K. The solid lines represent the best fit achieved using the ANISOFIT 2.0 [5-6] programme.

The paramagnetic response at each temperature point was calculated using the Brillouin function, in emu per mole of nickel (II) acetate tetrahydrate. This data were then converted into emu, by multiplying by the number of moles of nickel (II) acetate tetrahydrate present in the sample, and subtracted from the raw magnetic moments measured by the SQUID magnetometer. The resulting magnetic data was then converted into Bohr magnetons per mole of the Ni(II) crystal complex.

In contrast to the magnetic responses measured in Chapter 5, the raw magnetic moments in this chapter are relatively large, ranging in magnitude from 10^{-5} to 10^{-2} emu, depending on applied field. As a result there was no difficultly in centering the complexes in the SQUID sample chamber and the auto-centering device of the SQUID can be assumed to be completely

functional during the experimental measurements. This will correct for any movement of the sample off centre by thermal expansion/contraction of the sample holder during measurement.

As mentioned in section 3.3.4, the direct device-related accuracy for the SQUID magnetometer used in this thesis is $\Delta m_{dev} \sim 10^{-8}\, emu$ for fields of $\mu_0 H \leq 0.25T$. The device-related uncertainty is therefore negligible for the magnetic measurements conducted in this Chapter. As in Chapter four, experimental uncertainty in the measurement of the sample mass is the biggest contributor to the overall uncertainty in the magnetic measurements. This uncertainty is heightened in this section due to the contamination of the sample measured and subsequent corrections made, as detailed in section 6.3.2.2. Overall the uncertainty in the nickel mass is 5 $x10^{-5}$ g, which equates to an uncertainty of around 8% at the lower end of the temperature range, 2K, and 7% at the higher end of the temperature range, 8K, in the reduced magnetic measurements. Error bars have been omitted from the plots of the magnetic measurements due to the density of data points, in keeping with convention in the literature.

The reduced magnetisation is known to saturate at a value roughly equal to gS, however where there is sizable zero field splitting present this saturation value is hard to determine experimentally, as increased fields increase the saturation value observed, up to a point [13]. As can be seen from Figure 6.5, this seems to occur at roughly 3.5 Nβ for an applied field of 7T.

Figure 6.6 displays a schematic of the bonding present in the Ni(II) crystal complex. The complex is essentially made up of two inverted triangles of Ni centres, where Ni(1) is equivalent to Ni(1') and Ni(2) is equivalent to Ni(2') and so on. As a result we expect J1 = J1', J2 = J2', J3 = J3' and J4 = J4'. The different bonding orientations possible in the complex are displayed in Figure 6.6, suggesting that spin ground states of 0, 2 and 6 may be possible.

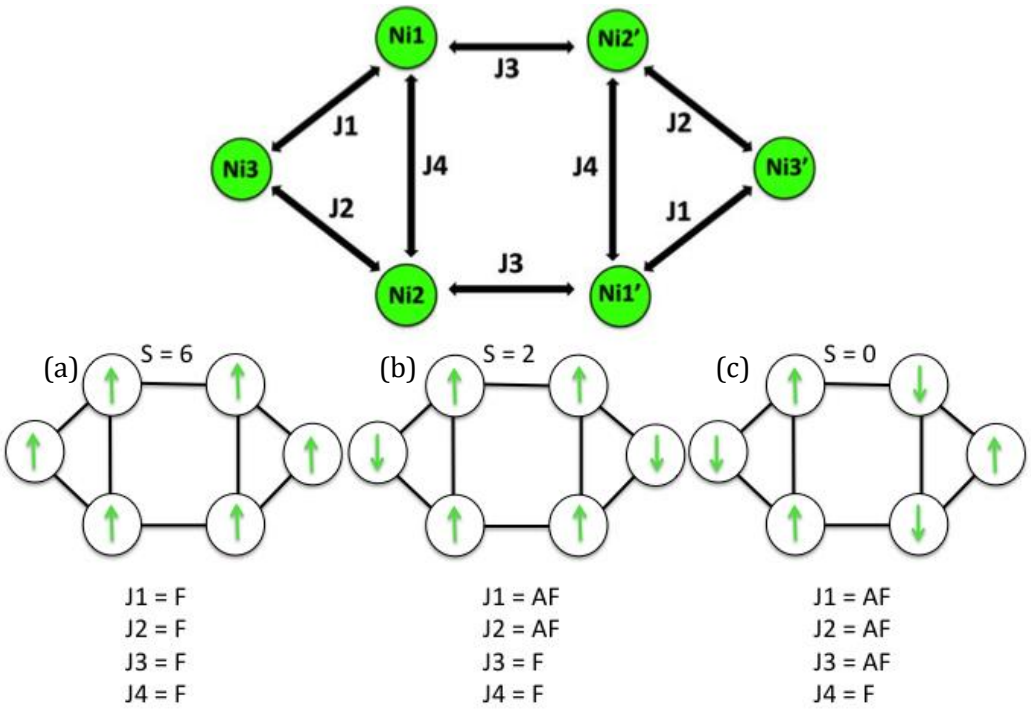

Figure 6.6: Schematic showing the atomic layout and exchange parameters present in the Ni(II) crystal complex, with allowable bonding configurations, ***(a)*** S=6, ***(b)*** S=2 and ***(c)*** S=0, where F corresponds to ferromagnetic coupling and AF to antiferromagnetic coupling between neighbouring ions

Considering the reduced magnetisation saturation value of 3.5 Nβ, a spin ground state of 0 is not feasible and it is likely that the spin ground state of the complex is 2. Fitting to the data was achieved using the ANISOFIT 2.0 software and the parameters are displayed in Table 6.1 [5-6].

Parameter	Value
Spin ground state (S)	2
Landé g factor (g)	1.92 cm^{-1}
Axial zero field splitting (D)	-2.34 cm^{-1}
Rhombic zero field splitting (E)	0.00 cm^{-1}
Goodness of fit (f)	0.37

Table 6.1: Parameters returned from the best fit achieved to the reduced magnetisation data for the Ni(II) crystal complex, using the ANISOFIT 2.0 [5-6] programme.

In agreement with the previous prediction a spin ground state equal to 2 is returned from the fit. This can be achieved by the bonding configuration shown in Figure 6.6.

An obvious non-superposition of the isofield lines is observed for the Ni (II) complex, which would suggest the presence of sizable zero-field splitting [13]. The presence of sizable zero-field splitting is confirmed by the value of the rhombic zero-field splitting parameter returned from fitting to the data. This is not surprising, as although Ni(II) does not possess first order angular momentum, as the spin ground state is greater than ½, ZFS of the ground state is possible through spin orbit coupling with the excited states [14]. It is also worthwhile noting that a negative value for the rhombic zero field splitting was returned. A negative D value is deemed crucial for a slow magnetic relaxation as the negative sign implies the $M_s = \pm S$ state with the largest component of the spin vector along the quantization axis will be most stable [15]. This coupled with a spin ground state of greater than ½ would suggest that this complex satisfies the conditions to act as an SMM. It is however important to note that although ANISOFIT 2.0 is deemed reasonably accurate at determining the magnitude of the ZFS parameters and spin ground state of a complex, extreme care has to be taken when assigning a direction to the ZFS parameters [5-6].

On occasions a positive D value may be initially returned were the value should in fact be negative. In an attempt to ensure accurate determination of the sign of the ZFS parameters different fits were attempted constraining the D value to be both positive and negative and using a different initial D value each time. A selection of these results are displayed in Table 6.2.

A negative D value was eventually decided on, as no reasonable optimization could be obtained, *i.e.* the condition $3|E| \leq |D|$ was not satisfied when the initial D factor was positive.

Parameter	D constrained positive, Initial Values, g=2, D=10, E=2	D constrained positive, Initial Values, g=2, D=30, E=0	D constrained negative, Initial Values, g=2, D=10, E=2	D constrained negative, Initial Values, g=2, D=10, E=2	D unconstrained, Initial Values, g=2, D=10, E=2
Spin ground state (S)	2	2	2	2	2
Landé g factor (g)	1.93	1.93	1.92	1.92	1.92
Axial zero field splitting (D)	1.16	1.16	-2.34	-2.34	-2.34
Rhombic zero field splitting (E)	-1.38	-1.38	-1.38	-1.38	-1.38
Goodness of fit (f)	0.49	0.49	0.37	0.37	0.37

Table 6.2: Parameters returned from a number of fits achieved to the reduced magnetisation data for the Ni(II) crystal complex, using the ANISOFIT 2.0 [5-6] programme, with different constraints applied and different starting parameters

6.3.2.4. Magnetic Susceptibility Data

Figure 6.7 shows the magnetic susceptibility data collected for the Ni(II) complex. The data was first corrected for the paramagnetic contribution of the Ni(II) acetate tetrahydrate contaminant, and then for the diamagnetic contribution due to both the sample holder and straw and the atoms and bonding present in the Ni crystal complex itself. The paramagnetic contribution of the Ni(II) acetate tetrahydrate was calculated using the Brillouin function as detailed in section

6.3.1.2. This method gave the magnetisation per mole of Ni(II) acetate tetrahydrate. As the mass of Ni(II) acetate tetrahydrate had previously been determined through fitting of the Brillouin function to a number of hysteresis loops at various temperatures, it was possible to calculate the number of moles present in the sample. Hence the magnetic signal generated by Ni(II) acetate tetrahydrate could be determined in emu and subtracted from the total measured signal

of the whole sample. Diamagnetic contributions due to the ions and bonding present in the Ni(II) complex were calculated using Pascal's constants and applied to the experimental data [12]. The diamagnetic contribution due to the sample holder and straw was calculated as detailed in section 6.3.1.2. and subtracted from the data. The fully corrected data is displayed in Figure 6.7.

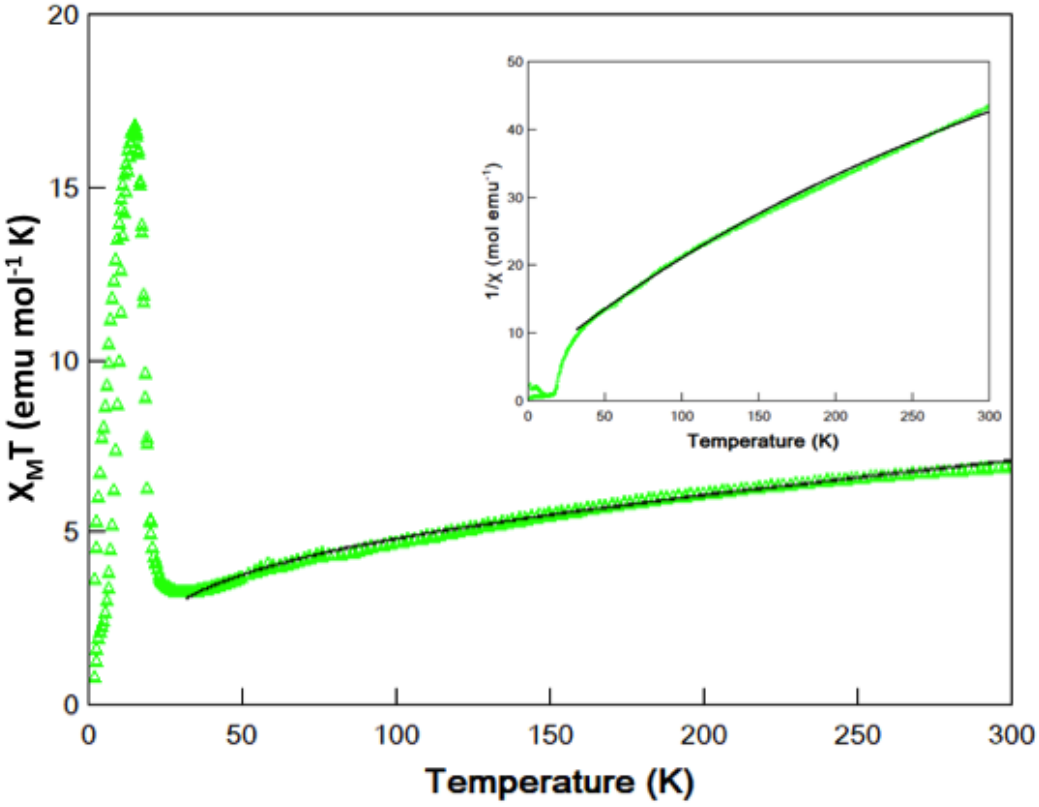

Figure 6.7: Magnetic susceptibility data collected for the Ni(II) crystal complex, plotted as a function of susceptibility and temperature, against temperature and inverse susceptibility against temperature (inset). The upper branch in the susceptibility data and lower branch in the inverse susceptibility represents the field cooled (FC) measurement and the other branch represents the zero-field cooled measurement (ZFC). The solid lines represent the fit achieved using the PHI software [4]

As detailed in section 6.3.2.3., the uncertainty in the magnetic measurements mainly results from the uncertainty in the sample mass, as the SQUID magnetometer device-related uncertainty is so small. The overall uncertainty in the nickel mass is 5 x10^{-5} g, which equates to

an uncertainty of around 4.8% in the susceptibility data. As with the plot of reduced magnetisation, error bars have been omitted from the susceptibility plots due to the density of data points, in keeping with convention in the literature.

A slight difference in the FC/ZFC curves is observed in the temperature range 2-15K suggesting remanence in the low temperature regime. This can also be observed in the inverse susceptibility data displayed in the inset of Figure 6.7. At room temperature the Ni(II) complex exhibits a X_MT value of 6.92 ± 0.33 emuKmol^{-1}, which is relatively close to the expected value of 6.00 ± 1.26 emuKmol^{-1} which corresponds to the spin only value calculated for six uncoupled Ni centres. A spin only value for the magnetic moment associated with each individual Ni centre can be calculated using the following formula;

$$\mu = (n(n+2))^{\frac{1}{2}} \qquad \textbf{Equation 6.5}$$

where n denotes the number of unpaired electrons

The orbital contribution can be ignored for the Ni complex as orbital quenching occurs in Ni ions [15]. This results in a magnetic moment per Ni ion of 2.82 ± 0.28 B.M. The X_MT for a single Ni ion could then be calculated using the following formula;

$$\chi_M T = \left(\frac{\mu}{2.828}\right)^2 \qquad \textbf{Equation 6.6}$$

Multiplying the expected X_MT value for a single Ni ion by 6 gave the value of 6.00 ± 1.26 emuKmol^{-1} for 6 uncoupled Ni(II) centres.

On cooling the Ni complex a slight decrease in the X_MT is observed until a local minimum of 3.29 ± 0.16 emuKmol^{-1} is reached at 32K. This is just marginally larger than the X_MT value of 3.00 ± 0.63 emuKmol^{-1} expected for the spins of four Ni centres facing one direction, up or down, and the remaining two spins, associated with the other two Ni centres, aligned in the opposite direction (i.e. a spin state of 2). The decrease in X_MT value with decreasing temperature would suggest the presence of antiferromagnetic interactions taking place between the Ni ions which would agree with this two Ni up (or down) and 4 Ni down (or up) alignment. A slight canting of the Ni spins in the complex could account for the slight discrepancy between the X_MT value

observed at 32K with that expected for a spin state of 2 [17]. On further cooling of the Ni complex a rapid increase in the X_MT value is observed until a maximum value of 16.70 ± 0.80 emuKmol^{-1} is achieved at 15K. Complete ferromagnetic alignment of the six nickel centres would result in a X_MT value of 25.42 ± 4.41 emuKmol^{-1}. On further cooling the X_MT value decreases rapidly, from 16.70 ± 0.16 emuKmol^{-1} at 15K to 0.81 ± 0.04 emuKmol^{-1} at 2K. Similar behaviour has been noted in the literature for other Ni(II) crystal complexes [18-19]. This low temperature susceptibility decrease can be attributed to ZFS, Zeeman effects and/or intermolecular antiferromagnetic interactions [20].

The magnetic susceptibility data for the Ni complex was fit using the PHI fitting software [4]. The programme was set to fit the Landé g-factor for each of the Ni ions (which was assumed and set equal to the same value for each Ni centre), the exchange interactions according to the schematic shown in Figure 6.6, and the intermolecular interaction. The low temperature regime data could not be fit using the previously mentioned parameters and as a result the data was fit in the temperature range of 32-300K. In order to achieve a fit to the low temperature regime data, more parameters, *i.e.* separate, anisotropic g-factors for each individual Ni centre, would need to be used and this may have resulted in over parameterisation of the fit, hence the decision to only fit to the high temperature data. As can be seen from Figure 6.7, the susceptibility curve from 32-300K seems to follow a stable trend. Additionally, from the fit to the reduced magnetisation data, we know that the rhombic ZFS parameter has a relatively large value, which is likely to be of similar magnitude to the exchange parameters between the Ni centres. As these two parameters are likely to have similar contributions it would be meaningless to fit to the curve with optimised values and as a result the rhombic and axial ZFS parameters were set to the values returned from the fit to the reduced magnetisation data. Only the exchange interactions between the Ni centres, the g-factors for the Ni ions and the intermolecular interaction were fit by the PHI programme. The g-factor was not set to the value determined by the ANISOFIT 2.0 fit to the reduced magnetisation data as the ANISOFIT 2.0 software sets a single g-factor for the whole system, whereas the PHI software sets an individual g-factor to each magnetic centre. Therefore the two values are not directly comparable.

The parameters returned by the PHI fit to the magnetic susceptibility data are displayed in Table 6.3.

Parameter	Value
Landé g factor (g)	1.85 cm^{-1}
Axial zero field splitting (D)	-2.34 cm^{-1}
Rhombic zero field splitting (E)	0.00 cm^{-1}
J1 Exchange Parameter (J1)	-2.73 cm^{-1}
J2 Exchange Parameter (J2)	-2.64 cm^{-1}
J3 Exchange Parameter (J3)	2.70 cm^{-1}
J4 Exchange Parameter (J4)	2.75 cm^{-1}
Intermolecular exchange interaction (zJ)	-1.13 cm^{-1}

Table 6.3: Parameters returned from fitting to the magnetic susceptibility data for the Ni(II) crystal complex, using the PHI [4] programme.

As predicted the magnitude of the values for the exchange parameters between the Ni(II) centres are comparable with the magnitude of the rhombic ZFS parameters, validating the decision to set the ZFS parameters to those achieved by fitting to the reduced magnetisation data rather than include them in the PHI fit. The direction of the exchange parameters means that the bonding between the Ni centres is a mixture of antiferromagnetic and ferromagnetic as shown in Figure 6.6 (b). This results in the alignment of spins as shown in Figure 6.6 (b) and would lead to a spin ground state of 2, as each Ni centre has a spin of 1, in agreement with that returned by fitting to the reduced magnetisation data. The g-value of 1.849 returned by the PHI fit is slightly smaller than the value of 1.918 returned by the ANISOFIT 2.0 fit to the reduced magnetisation data, but, as outlined earlier, this is not surprising given the different assignments of Landé g-factors of the two programmes. The small negative value returned for the intermolecular interactions indicates weak antiferromagnetic interactions between neighbouring Ni clusters. This would explain the rapid decrease in magnetic susceptibility observed below 15K.

6.3.2.5. Magnetic Hysteresis Data

Figure 6.8 shows the hysteretic data collected for the Ni complex at 4K, 5K, 6K 8K and 10K, with a maximum applied field of 20,000 Oe.

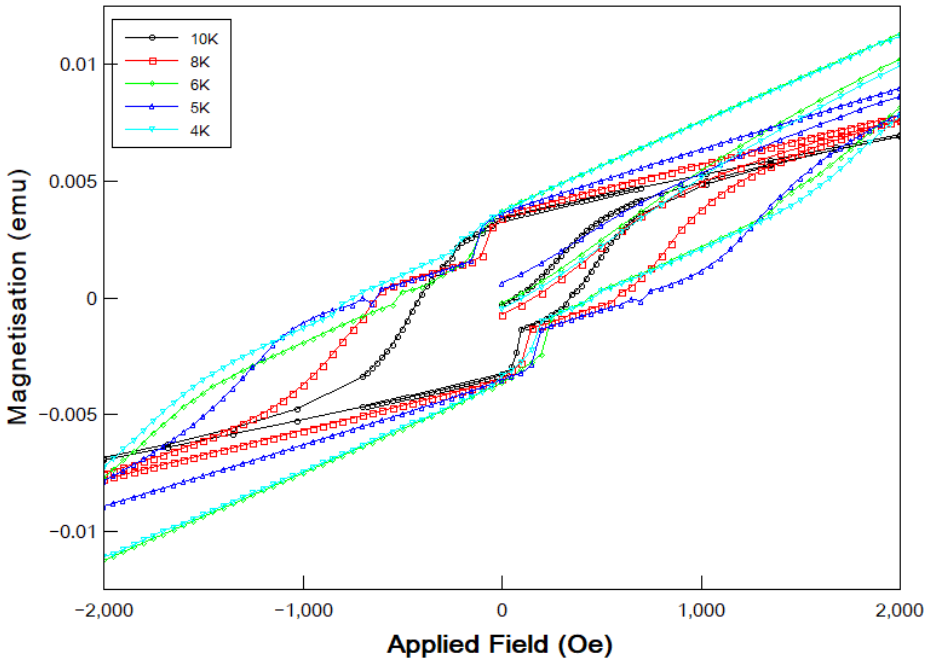

Figure 6.8: Hysteresis loops for the Ni(II) crystal complex taken at temperatures 4, 5, 6, 8, and 10K, with a maximum applied field of 20,000Oe. The applied field range of interest, -2,000 Oe – 2,000 Oe, is plotted in this figure.

The data was corrected for the paramagnetic signal of the Ni(II) acetate tetrahydrate contaminant and the diamagnetic contributions of both the sample and sample holder using the same method as in section 6.3.2.3. The experimental uncertainty in the DC field dependent magnetic data due to the uncertainty in the sample mass is around 3.6%. Error bars are omitted from the plot due to the density of data points and in keeping with the literature.

Only the data for -2000 Oe to +2000 Oe is shown in Figure 6.8 to clearly demonstrate both the stepping of the hysteresis loop and the remanence and coercivity of the sample at these temperatures. As predicted, from the fact that there is a difference observed in the FC/ZFC plots within this temperature range, all five hysteresis loops exhibit both coercivity and remanence. The coercive field and remnant magnetisation for the nickel complex at each temperature is displayed in Table 6.4.

Parameter	4K	5K	6K	8K	10K
Remnant Magnetisation (emu/mol)	560 ± 20.2	550 ± 19.8	570 ± 20.5	520 ± 1.87	510 ± 1.84
Coercive Field (Oe)	750 ± 27.0	700 ± 25.2	500 ± 18.0	600 ± 21.6	400 ± 14.4
Field at which Step in Hysteresis Loop Occurs (Oe)	200 ± 7.2	200 ± 7.2	200 ± 7.2	150 ± 5.4	75 ± 2.7

Table 6.4: Parameters derived from the magnetisation measurements for the Ni(II) crystal complex

As the temperature increases from 4K to 10K there is a general decrease in the coercive field and remnant magnetisation observed. This is as expected as the complex becomes a softer ferromagnet, whose magnetisation is easier to switch, on approaching the blocking temperature (above which the complex behaves paramagnetically).

A single step is observed in each hysteresis loop. As explained in section 6.2. steps occur in the hysteresis loops of SMM's due to macroscopic quantum tunnelling (MQT) between different states of magnetisation in the molecule [20]. If the spin ground state of the molecule was equal to six we would expect to see 6 steps in the hysteresis loops. When H=0 each of the positive M_s levels would be in alignment with its corresponding negative M_s level, and quantum tunnelling would occur. On application of an applied field the Ni spins will align, one by one with the direction of the applied field. As each Ni spin flips the positive and negative M_s levels will fall into alignment and quantum tunnelling will take place. However, as the spin ground state of the Ni complex was found to be equal to 2 the quantum tunnelling observed is more complex. As explained in section 6.3.2.1. the Ni complex is essentially comprised of two sets of three Ni centres arranged in a triangular configuration. Fitting to the susceptibility data revealed that the bonding between the Ni centres in these triangles is antiferromagnetic, resulting in an overall spin of 1. In the spin ground state the two triangles interact ferromagnetically, resulting in the spin ground state of 2. When H=0 Oe the positive and negative M_s levels are in alignment and quantum tunnelling can occur. On application of an applied field, instead of the six Ni centres flipping individually, it is proposed that each triangle acts as a spin centre and the three Ni centres comprising the triangle flip simultaneously. As the triangle flips the positive and

negative M_s levels fall into alignment and quantum tunnelling of the magnetisation can occur. As such we may expect to see two steps in the hysteresis loops, one at H = 0 Oe, when $M_s = \pm 2$, and one corresponding to the triangle flipping with the application of the applied field. However it is not particularly surprising that only one step is observed, as observing quantum tunnelling between the lowest energy M_s states is notoriously difficult and has only been achieved a couple of times in the literature [22]. Hence the observed step in the hysteresis loop is probably as a direct result of one of the triangles of three nickel centres flipping. The field at which the step in the hysteresis loop occurs for each temperature is displayed in Table 6.4. As expected, at lower temperatures a higher field is needed to flip the nickel triangle and allow for quantum tunnelling to be observed. This is because the $M_s = \pm 2$ state is more stable at lower temperatures and therefore more energy is required to move from this state to a higher energy level state.

6.3.3. Conclusions

A hexameric Ni(II) complex, $[C_2mim]_4[Ni_6(OAc)_{13}(OH)_2(H_2O)_2][OAc] \cdot H_2O$, was synthesised using a one-step ionothermal synthesis process involving the dissolution of Ni(II) acetate in the ionic liquid $[C_2mim][OAc]$. Structural analysis using single crystal XRD revealed the presence of an acetate on top of the hexameric cluster in a $\mu - \eta^2 : \eta^2$ binding mode which has not been previously reported for a crystal structure with carboxylate ligands. Magnetic susceptibility measurements carried out using SQUID magnetometry revealed the presence of remanence below 15K. Reduced magnetisation measurements showed a non-superposition of the isofield lines suggesting the presence of sizable ZFS in the complex. This was confirmed by fitting to the data, which returned a value of -2.34 cm^{-1} for the axial ZFS parameter. Fitting to the susceptibility data revealed a combination of antiferromagnetic and ferromagnetic bonding between the Ni centres resulting in a spin ground state of 2. The fact the Ni complex has a sizable negative rhombic ZFS parameter and a spin ground state greater than 0.5 suggests the complex may behave as an SMM. This is confirmed by the presence of a step in the hysteresis loops obtained for the complex. It was proposed that the single step observed was as a result of the three Ni centres, comprising each of two triangles in the complex, simultaneously acting together as a single magnetic centre. On application of an applied field the three Ni centres in each triangle flip simultaneously. As such the complex can be considered as being made up of 2 magnetic centres instead of the six expected due to the presence of 6 Ni centres in the complex. Hence we may expect to see two steps in the hysteresis loops, however the step associated with the lowest energy level ($M_s = \pm 2$) was not observed.

6.4. Trimeric Co(II) crystal complex

In the second part of this study a trimeric Co(II) compound was synthesised using the same synthesis process as was used in the previous section (6.3.) As before, the crystal structure of the complex was studied via means of XRD and the magnetic properties studied using SQUID magnetometry. Fitting of the magnetic susceptibility and reduced magnetisation data was once again possible by means of the programmes PHI and ANISOFIT 2.0 respectively.

6.4.1. Experimental

6.4.1.1. Material Synthesis

Using the same synthetic methodology as outlined in section 6.3.1.1. single crystals of the trimeric compound $[C_4mim]_2[Co_3(OAc)_8]$ were isolated. In this instance however Co(II) acetate solution was dissolved in the ionic liquid $[C_4mim][OAc]$.

6.4.1.2. Characterisation

As for the nickel crystal complex, structural characterisation of the cobalt crystals was carried out using single crystal X-ray diffraction (Panalytical X'Pert PRO) with a CuKα1 radiation source of wavelength 1.540598Å. Magnetic characterisation, including magnetic susceptibility measurements, DC field dependent measurements and reduced magnetisation measurements were carried out on powdered samples of the crystals, using a Quantum Design MPMS DC XL SQUID magnetometer. Magnetic susceptibility measurements were carried out in the temperature range 2-300K under an applied field of 500Oe. As with the Ni sample, data was collected on heating the sample after it had been cooled both with and without an applied field. The experimental data was then fitted using the PHI fitting software, using the coupling regime shown in Figure 6.11 (inset) [4]. Reduced magnetisation data was taken in the temperature range 2-10K, at applied fields of 0.5T, 2T 5T and 7T. This data was then fitted using the ANISOFIT 2.0 software [5-6]. Finally DC field dependent measurements were carried out at 2K, with a maximum field of 5T applied.

The cobalt crystals did not exhibit the same hygroscopic behaviour observed for the Ni crystals and as a result there was very little (if any) degradation of the Co crystals into Co(II) acetate tetrahydrate, on contact with the atmosphere. However, to be sure that the sample was pure, and the measured mass of the sample was accurate, an attempt was made to fit to the hysteretic

profile acquired for the Co sample at 2K, using the Brillouin function. As we believe the Co centres interact antiferromagnetically, the presence of any paramagnetic material would cause a paramagnetic response, which would swamp the weak antiferromagnetic signal of the Co crystals at low temperatures. Attempts to fit to the hysteresis data of the Co crystals were unsuccessful, meaning it is highly unlikely that there is any significant proportion of the paramagnetic Co(II) acetate tetrahydrate present in this sample. As such the measured mass of the sample could be taken as being that of only the Co crystals, and no paramagnetic corrections needed to be applied to the data, as in the case of the Ni crystals. The magnetisation data was therefore simply corrected for the diamagnetic contribution of the ions and bonds present in the Co complex, and also the sample holder and straw. The diamagnetic contribution due to the ions and bonds in the compound was calculated using Pascal's constants, to be a value of $4.645 \times 10^{-4} \pm 0.068 \times 10^{-4}$ emu/mol [7].

On this occasion a gelatine capsule was used to contain the Co samples, as their non-hygroscopic nature meant that the water content in the gelatine capsules was not an issue, as it had been for the Ni crystals. The diamagnetic correction for the gelatine capsule and straw was obtained using the same method outlined in section 6.3.1.2, for the peek capsule, and was found to be a value of $0.610 \times 10^{-4} \pm 0.009 \times 10^{-4}$ emu/mol. The fact that fits could be achieved for both the susceptibility data and reduced magnetisation data after applying only these corrections, further support the claim that the Co sample was sufficiently pure and any contamination present made an insignificant impact to the magnetisation data.

6.4.2. Results and discussion

6.4.2.1. Crystalline structure and configuration analysis

The structure of the trimeric cobalt complex was investigated using XRD and is displayed in Figure 6.9.

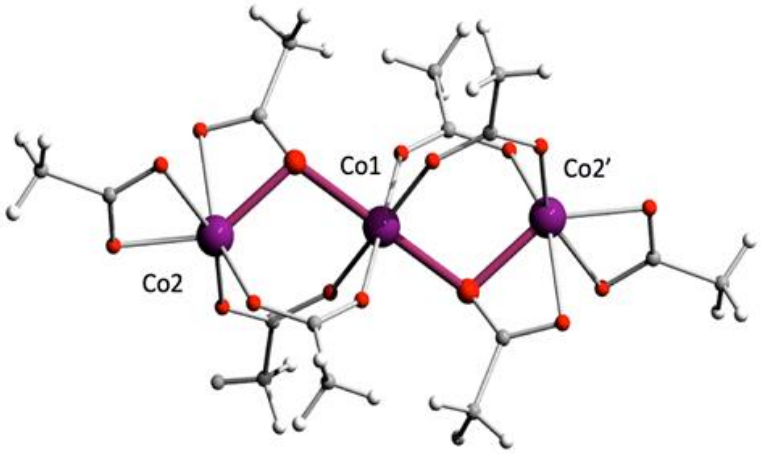

Figure 6.9: The structure of the trimeric $[Co_3(OAc)_8]^{2-}$ anion in the Co crystal complex

It can be identified from this figure that the terminal distorted octahedral Co(II) centres are located in opposite directions. The Co-Co distances from the central Co ion to the two terminal Co ions were found to be the same (3.4(2)Å). As can be seen from Figure 6.9, between the central Co ion and both terminal Co ions, there are three binding ligands present. Two binding acetates in the $\mu - \eta^1 : \eta^1$ mode are present on one side of adjacent Co centres, as well as one in the $\mu - \eta^2$ mode directly opposite. A chelating acetate is also present on each end of the trimer resulting in strongly distorted octahedral coordination of the terminal Co(II) ions.

6.4.2.2. Reduced Magnetisation Data

Figure 6.10 shows the reduced magnetisation data collected for the Co complex after the diamagnetic contributions of both the sample and sample holder had been accounted for.

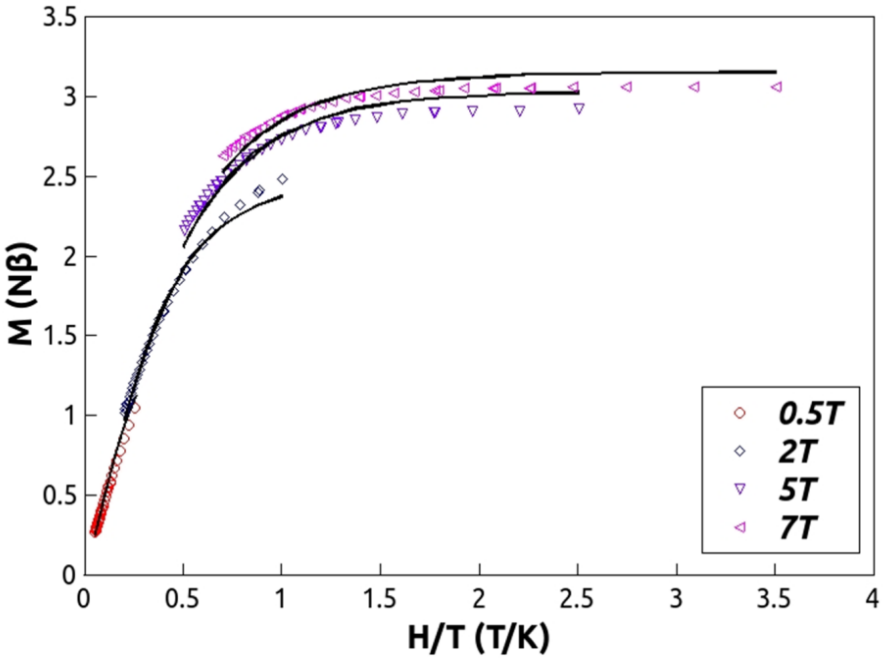

Figure 6.10: Reduced magnetisation data for the cobalt complex taken in the 2-10K temperature range at fields of 0.5, 2, 5 and 7T

As contamination of the Cobalt complex is not an issue as it was for the Ni(II) complex, the uncertainty in the sample mass is solely due to the device uncertainty in the mass measurement apparatus. This amounts to an uncertainty in the Cobalt complex mass of 2.30 $x10^{-2} \pm 5\ x10^{-6}$ g. which equates to an uncertainty of around 0.3% in the reduced magnetic measurements. Error bars have been omitted from the plots of the magnetic measurements due to the negligible size of the uncertainty and the density of data points, in keeping with convention in the literature.

It can be seen from Figure 6.10 that the reduced magnetisation saturates at a value of roughly 3.0 Nβ, suggesting a spin ground state of 1.5. As each cobalt centre has an individual spin of 1.5, this would suggest that the cobalt ions are interacting antiferromagnetically. There is an obvious non-superposition of the isofield lines observed suggesting the presence of sizable zero field splitting. This is expected as Co(II) ions possess a first order orbital moment and hence spin orbit coupling of the ground state occurs. The reduced magnetisation data was fit using the

ANISOFIT 2.0 software [5-6]. It is important to note that this software does not account for the presence of spin orbit coupling in the complex. Additionally the g-factor is assumed to be isotropic. As Co(II) ions are likely to exhibit spin orbit coupling and generally have an anisotropic g-factor it is therefore likely that the g factor returned by the fit will be skewed as a result.

The parameters returned from the fit are displayed in Table 6.5.

Parameter	**Value**
Spin ground state (S)	1.5
Landé g factor (g)	2.88 cm^{-1}
Axial zero field splitting (D)	16.66 cm^{-1}
Rhombic zero field splitting (E)	2.20 cm^{-1}
Goodness of fit (f)	0.65

Table 6.5: Parameters returned from the best fit achieved to the reduced magnetisation data for the Co(II) crystal complex, using the ANISOFIT 2.0 [5-6] programme.

A large axial zero field splitting parameter, D, is returned, as expected due to the non-superposition of the isofield lines. As explained in section 6.3.2.2., ANISOFIT 2.0 has difficulty in returning the correct sign of the D parameter. In order to best estimate what this sign should be, multiple fits were attempted, using a different initial D value each time. The D value was constrained to be both negative and positive depending on the initial value. A selection of the results are displayed in Table 6.6.

Parameter	D constrained positive, Initial Values, g=2.2, D=10, E=2	D constrained positive, Initial Values, g=2.2, D=30, E=2	D constrained negative, Initial Values, g=2.2, D=-10, E=0	D constrained negative, Initial Values, g=2.2, D=-30, E=1	D unconstrained, Initial Values, g=2.0, D=10, E=2
Landé g factor (g)	2.20	2.88	2.89	2.89	2.20
Axial zero field splitting (D)	3.45	16.66	-1.21	-1.21	3.45
Rhombic zero field splitting (E)	1.16	2.20	1.00	1.00	1.16
Goodness of fit (f)	1.56	0.65	1.77	1.77	1.56

Table 6.6: Parameters returned from a number of fits achieved to the reduced magnetisation data for the Co(II) crystal complex, using the ANISOFIT 2.0 [5-6] programme, with different constraints applied and different starting parameters

It was concluded that the sign of the D value must be positive as no reasonable optimization was obtained when the initial D factor was negative. It is essential that the condition $3|E| \leq |D|$ is satisfied. The magnitude of the axial and rhombic zero field splitting parameters returned by the fit seem to be in keeping with other similar complexes in the literature [23]. Additionally, although the g-factor may appear a little higher than expected, it is also in good agreement with g-factors reported in the literature, which have been calculated using the ANISOFIT 2.0 software for similar complexes [23]. As outlined briefly earlier, it is likely that these are quite high as ANISOFIT 2.0 does not take into account the spin orbit coupling occurring in the complex, and also treats the g-factor as isotropic when it is in fact possibly anisotropic. The value of 1.5 for the spin ground state suggests that antiferromagnetic coupling is taking place between the cobalt ions.

6.4.2.3. Magnetic Susceptibility Data

Figure 6.11 shows the magnetic susceptibility data collected for the cobalt crystal complex.

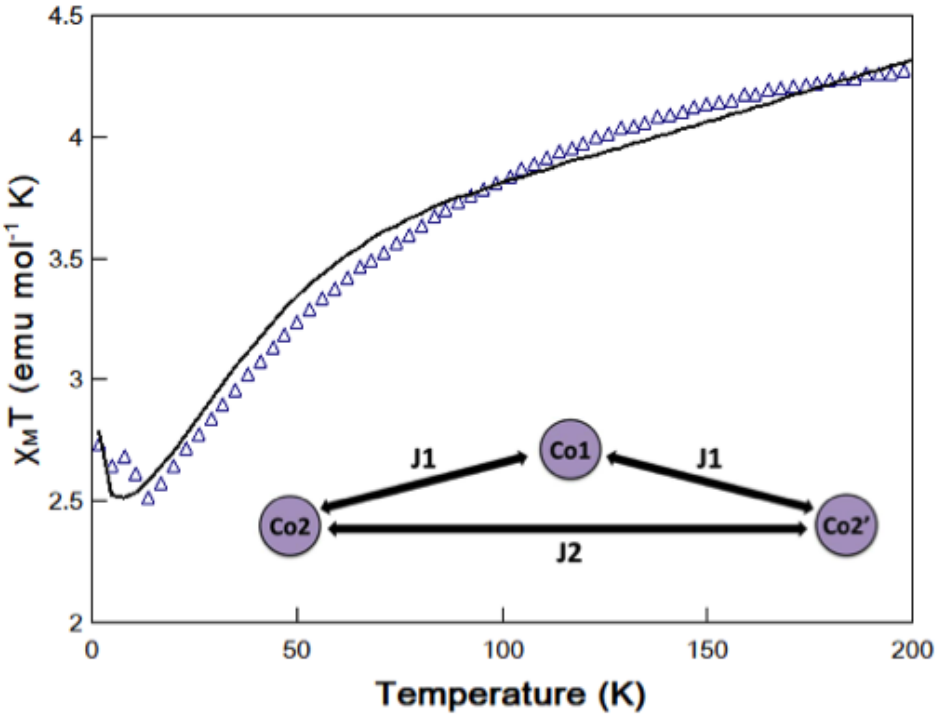

Figure 6.11: Magnetic susceptibility data collected for the Co(II) crystal complex. The solid lines represent the fit achieved using the PHI software [4]

This data was corrected for both the diamagnetic contributions of the sample and the sample holder. The uncertainty in the susceptibility data for the cobalt complex amounts to around 0.2%.

The cobalt compound starts at room temperature with a X_MT value of ≈ 4.30 ± 0.05 emu K mol^{-1}. This is smaller than the expected value of 8.4 ± 0.3 emu K mol^{-1} for three uncoupled Co centres. Due to the presence of first order orbital momentum in the cobalt ions it was not appropriate to use the spin only formula used for the Ni complex to calculate the expected X_MT value, and it was determined as follows. The g factor associated with each cobalt ion was calculated using the following formula, Equation 6.7, to be a value of 1.6 ± 0.05.

$$g = 1 + \frac{S(S+1) - L(L+1) + J(J+1)}{2J\,(J+1)}$$ **Equation 6.7**

where S is the spin quantum number, L is the orbital angular momentum quantum number and J is the total angular momentum quantum number (J = S + L).

The effective magnetic moment associated with each cobalt ion was then calculated in Bohr magnetons using the following equation, Equation 6.8.

$$\mu = g\,\{J(J+1)\}^{\frac{1}{2}}$$ **Equation 6.8**

This returned a value of 4.73 ± 0.15 B.M. The X_MT value for a single cobalt ion could then be calculated using Equation 6.6, as for the nickel complex, and the answer multiplied by three to give the expected X_MT of 8.4 ± 0.3 emuKmol^{-1} for three non-interacting cobalt centres.

On cooling of the cobalt complex the X_MT value decreases to a local minimum of 2.50 ± 0.05 emuKmol^{-1} at 14K suggesting the presence of antiferromagnetic interactions between the cobalt centres. The X_MT value expected for a spin ground state of 1.5 resulting from complete antiferromagnetic interactions between the three cobalt centres is 2.80 ± 0.09 emuKmol^{-1}. On further cooling of the cobalt complex from 14K to 2K, the X_MT value slightly increases to a value of 2.76 ± 0.05 emuKmol^{-1}. This can be attributed to ZFS, Zeeman effects and/or intermolecular interactions [20].

The magnetic susceptibility data was fit using the PHI fitting software. In principle the effect of ZFS, in systems where the magnetic anisotropy arises from first order orbital momentum, can be of the same order of magnitude as the effect of exchange coupling and so fitting the X_MT data using a Hamiltonian which accounts for both effects (plus intermolecular interactions and even on occasions anisotropy of the g factor) can be very challenging. As can be seen from Figure 6.11, the susceptibility curve collected for the Cobalt crystals follows a stable trend and as a result care must be taken not to over parameterise the fit, and make it meaningless. Additionally if the magnitudes of the exchange parameters and ZFS parameter have roughly equal contributions, it can be meaningless to fit to the curve with "optimised' values for these two contributions. As a result, when fitting to the susceptibility curve for the cobalt crystals, the zero field splitting parameters were set to the values determined from fitting to the reduced magnetisation data using the ANISOFIT 2.0 software, i.e. D = 16.7 and E = 2.2 cm^{-1}. The PHI

programme was set to only change the values of the g factors of each ion, the exchange interactions between the cobalt centres and the intermolecular interactions. This was simply to confirm that the parameters achieved from fitting to the reduced magnetisation data could also reproduce a respectable fit to the susceptibility data. The g factors were not set to the value determined from the fit to the reduced magnetisation data as the ANISOFIT 2.0 software only returns a single g factor for the whole system, where as PHI designates a g factor to each metallic ion in the complex. The two values are therefore not directly comparable. Additionally as ANISOFIT 2.0 does not account for spin orbit coupling in the system, and assumes an isotropic g-factor it is likely that the g factor returned from the reduced magnetisation fit is slightly skewed as a result.

Although PHI is able to fit both spin orbit coupling and anisotropic g-factors, it was decided not to include these parameters, as it would have resulted in over parameterisation of the system and affected the integrity of the parameters returned from the fit. As a result it is likely that the exchange interactions and g factors obtained from the fit will be slightly skewed to account for the spin orbit coupling in the system. What we are really interested in is the type of interaction (ferromagnetic or antiferromagnetic) between the cobalt centres, which the fit indicates. This is indicated by the sign of the exchange parameters returned rather than the magnitude, hence slightly skewed values as a result of the spin orbit coupling is relatively unimportant. The type of exchange interactions occurring is of interest, as it would confirm what was inferred from the ground state determined by the reduced magnetisation fit. The parameters from the PHI fit are displayed in Table 6.7 and the fit is displayed in Figure 6.11.

Parameter	**Value**
Landé g factor (g)	1.80 cm^{-1}
Axial zero field splitting (D)	16.66 cm^{-1}
Rhombic zero field splitting (E)	2.20 cm^{-1}
J1 Exchange Parameter (J1)	-32.35 cm^{-1}
J2 Exchange Parameter (J2)	-32.35 cm^{-1}
Intermolecular exchange interaction (zJ)	0.21 cm^{-1}

Table 6.7: Parameters returned from fitting to the magnetic susceptibility data for the Co(II) crystal complex, using the PHI [4] programme.

As the fit achieved is in relatively good agreement with the experimental data, we can conclude that the parameters achieved from the reduced magnetisation fit are accurate. As can be observed from Table 6.7 the value of the exchange interactions between Co1 and Co2, and Co2 and Co3, is of the same order of magnitude as that of the rhombic zero field splitting parameter. Additionally as a negative value for the exchange interactions was returned, we can conclude that the Co centres are interacting antiferromagnetically resulting in a spin ground state of 1.5, which agrees with that returned from the fit to the reduced magnetisation data. The small positive value returned for the intermolecular interaction suggests that there is also an extremely weak ferromagnetic interaction taking place between neighbouring molecules in the complex.

6.4.2.4. Magnetic Hysteresis Data

Figure 6.12 shows the hysteretic data collected for the cobalt complex when T = 2K, for a maximum applied field of 50,000 Oe.

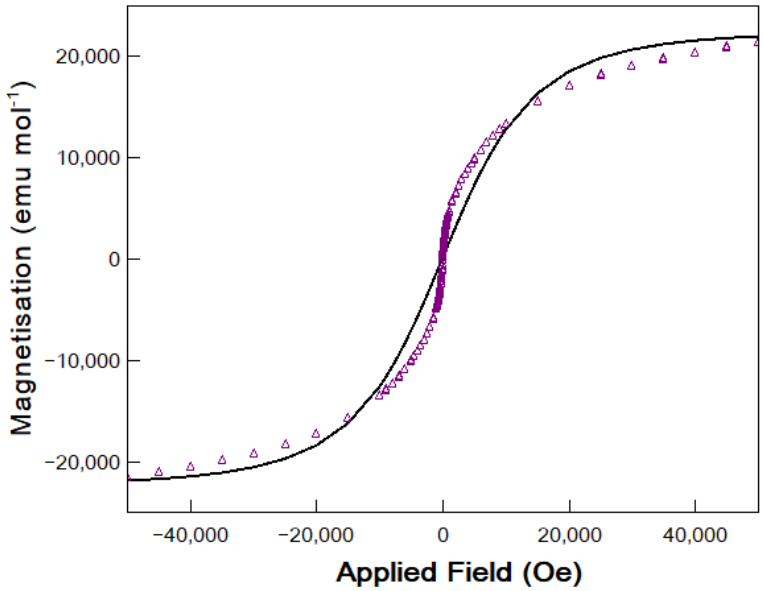

Figure 6.12: Hysteretic data collected for the Co(II) crystal complex. The solid line shows the attempted fit using the Brillouin function

The overall uncertainty in the hysteretic data was calculated as being around 0.2%, as a direct result of the uncertainty in the sample mass measurement. As can be seen from Figure 6.12, no remanence is observed in the hysteretic data for this complex. The hysteresis loop collected for the cobalt complex is akin to either a saturated paramagnetic material, or an antiferromagnetic material. According to both the fits to the susceptibility data and the reduced magnetisation data we expect the cobalt complex to be in the antiferromagnetic state at this temperature. In order to confirm that it is not in fact acting as a saturated paramagnet an attempt was made to fit to the data using the Brillouin function, solid line in Figure 6.12. A convincing fit could not be achieved, further indicating that the cobalt complex is behaving antiferromagnetically at this temperature. The saturation magnetisation for the complex was calculated to be a value of 21500 ± 43 emu/mol.

6.4.3. Conclusions

A trimeric cobalt single crystal complex, $[C_4mim][CO_3(OAc)_8]$, was synthesised using a one-step ionothermal synthesis process which involved the dissolution of Co(II) acetate into the ionic liquid $[C_4mim][OAc]$. Magnetic characterisation of the complex via SQUID magnetometry revealed that the Co(II) centres interact antiferromagnetically, resulting in the complex having a spin ground state of 1.5. Reduced magnetisation measurements suggested the presence of sizable ZFS for the complex and fitting to the data returned a large positive rhombic ZFS parameter of 16.66 cm^{-1}. Using the parameters from the fit to the reduced magnetisation data and including the exchange interaction parameters between the cobalt centres, a convincing fit to the magnetic susceptibility data could be achieved. The exchange interactions between the cobalt centres were identified as having a value of -32.35 cm^{-1}. Hysteresis data collected showed the characteristic shape of an antiferromagnet or saturated paramagnet. Attempts to fit to the hysteretic data using the Brillouin function were unsuccessful, supporting the fact that the Co centres do in fact interact antiferromagnetically.

6.5. Polymeric Mn(II) crystal complex

In the third part of this study a polymeric Mn(II) compound was synthesised using the same synthesis process as in the previous two sections (6.3. and 6.4.) As before, the crystal structure of the complex was studied via means of XRD and the magnetic properties were studied using

SQUID magnetometry. Fitting of the magnetic susceptibility was possible by means of the programme Phi, however on this occasion the reduced magnetisation data could not be fitted by the ANISOFIT 2.0 software used in the previous two sections. This was probably as a direct result of the more complex magnetic behaviour exhibited by polymeric compounds.

6.5.1. Experimental

6.5.1.1. Material Synthesis

Using the same synthetic methodology as outlined in section 6.3.1.1. but dissolving Mn (II) acetate into the ionic liquid [C_4mim][OAc], single crystals of the polymeric compound [C_4mim]{$Mn_3(OAc)_7$}$_n$ were isolated.

6.5.1.2. Characterisation

As for both the Ni and Co complexes structural characterisation was carried out on the Mn crystals by means of single crystal X-ray diffraction, (Panalytical X'Pert PRO) with a CuKα1 radiation source of wavelength 1.540598Å, and magnetic characterisation was carried out using a Quantum Design MPMS DC XL SQUID magnetometer. Magnetic susceptibility measurements were carried out under an applied field of 500Oe in the temperature range 2K-300K, and reduced magnetisation measurements were carried out in the temperature range 2-4K, at applied field strengths of 4, 5, 6, and 7T. DC field dependent measurements were carried out at 10K with a maximum applied field of 50000 Oe. The Mn crystals did not exhibit the same extent of hygroscopic behaviour as the Ni compound however if exposed to a significant amount of moisture a degradation to Mn(II) acetate tetrahydrate, was in fact observed. As such the same precautions were taken to prevent extended exposure to the atmosphere, as were for the Ni complex; such as sample preparations and transfer into a sealed sample holder taking place in a fume cupboard, and sealing the lid of the sample holder using vacuum grease. A peek capsule was used to contain the sample, as initial experiments using gelatine capsules, showed the Mn samples to draw moisture from the capsule and undergo degradation. As with the Ni(II) complex it was impossible to completely prevent to Mn complex from undergoing some form of degradation to Mn(II) acetate tetrahydrate and therefore the measured sample mass did not accurately represent the mass of the Mn(II) crystal complex present. As Mn(II) acetate tetrahydrate is paramagnetic it was possible to fit to the hysteresis data for the sample at low temperatures using the Brillouin function in order to estimate the mass of Mn(II) acetate

tetrahydrate. The same process was used as for the Ni complex and is described in detail in section 6.3.1.2. All experimental data is corrected for the paramagnetic signal from the Mn(II) acetate tetrahydrate contaminant, and the Mn(II) crystal complex sample mass is corrected by subtracting the calculated mass of the Mn(II) acetate tetrahydrate from the measured sample mass. Diamagnetic contributions for the ions and bonds present in the Mn compound were calculated using Pascal's constants to be a value of $4.645 \times 10^{-4} \pm 0.068 \times 10^{-4}$ emu/mol [12]. This along with the diamagnetic correction for the straw and peek capsule, as calculated in section 6.3.1.2, was applied to all the magnetisation data.

6.5.2. Results and discussion

6.5.2.1. Crystalline structure and configuration analysis

The polymeric structure of the Mn(II) complex was found to occur in repeating units which were comprised of five Mn(II) centres, Figure 6.13. Each repeating unit consisted of a zigzag chain formed by three Mn(II) ions in a line and two different distorted octahedral manganese centres. The Mn-Mn distance was found to be consistent throughout each repeating unit and measured 3.4(2)Å. As with the Co(II) complex, two binding acetates in the $\mu - \eta^1 : \eta^1$ mode were found to be present on one side of each set of adjacent Mn centres as well as one in the $\mu - \eta^2$ mode, directly opposite.

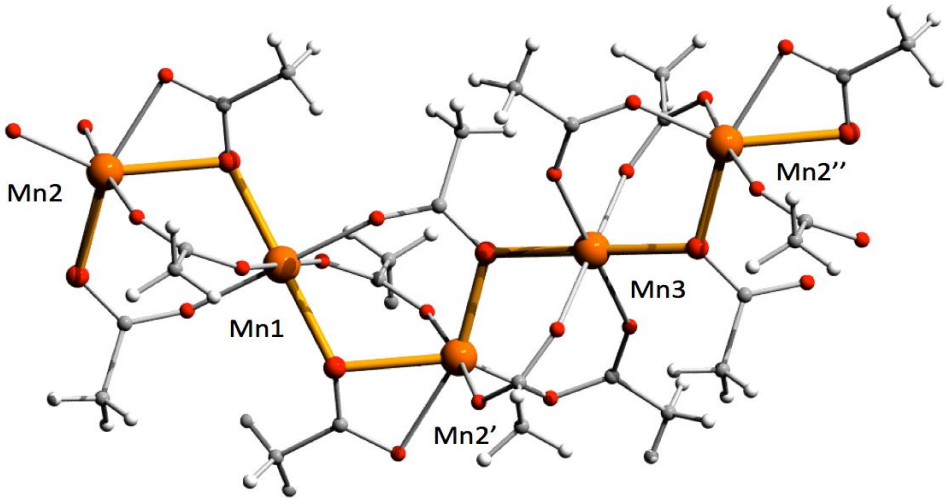

Figure 6.13: The structure of the polymeric $\{Mn_3(OAc)_7\}_n$ anion in the Mn crystal complex

6.5.2.2. Reduced Magnetisation Data

Figure 6.14 shows the reduced magnetisation data collected for the Mn complex at applied fields of 4, 5, 6 and 7T, in the temperature range 2 - 4K.

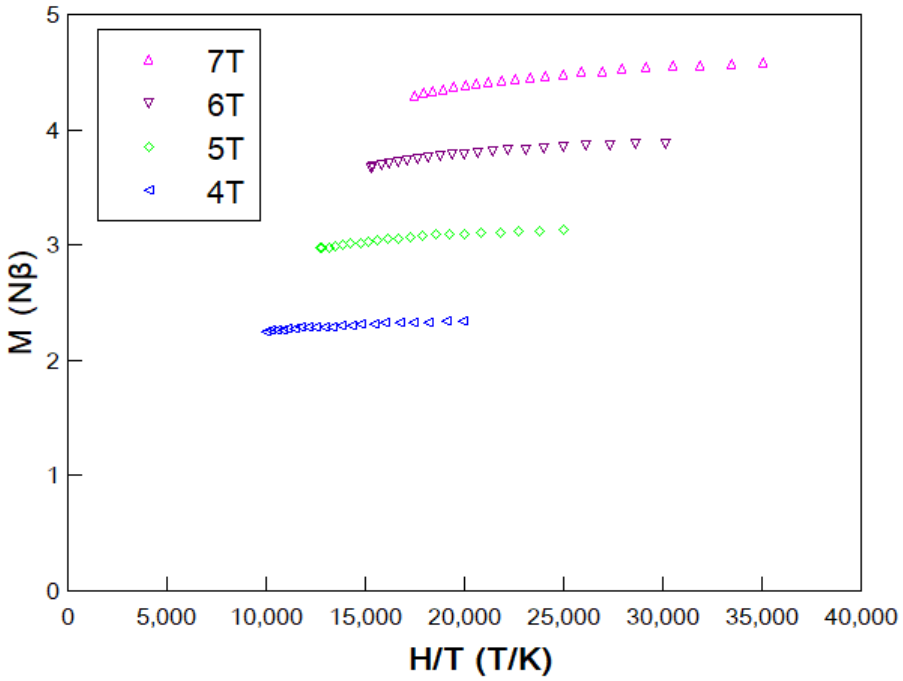

Figure 6.14: Reduced magnetisation data for the manganese complex taken in the 2-4K temperature range at fields of 4, 5, 6 and 7T

Diamagnetic corrections for the sample and sample holder were calculated as for the Ni and Co complexes and applied to the experimental data. The paramagnetic signal of the Mn(II) acetate tetrahydrate contaminant was calculated using the same method as for the Ni complex, detailed in section 6.3.2.2. As for the Nickel and Cobalt complexes, experimental uncertainty in the measurement of the sample mass is the biggest contributor to the overall uncertainty in the magnetic measurements. Similarly to the Nickel complex, this uncertainty is heightened as for the Nickel complex, due to the contamination of the sample measured and subsequent corrections made, as detailed in section 6.3.2.2. The overall uncertainty in the manganate mass is 5 x10^{-5} g, which equates to an uncertainty of around 5% at the lower end of the temperature range, 2K, and 1% at the higher end of the temperature range, 4K, in the reduced magnetic measurements. As with the previous magnetic measurement, error bars have been omitted

from the plots of the magnetic measurements due to the density of data points, in keeping with convention in the literature.

As can be seen in Figure 6.14, there is a very obvious non-superposition of the isofield lines suggesting a large extent of ZFS in the complex. At 7T a saturation value of 4.58 Nβ is achieved. Where no ZFS is present in a complex, the reduced magnetisation data should saturate at a value equivalent to gS, where g is the landé g factor and S is the spin ground state of the complex. For a complex with considerable ZFS it can be difficult to determine the exact value of saturation as with an increased applied field an increased saturation value is observed, up to a certain point. It is likely the value of 4.58 Nβ obtained at 7T is slightly smaller than the actual saturation value for the complex. As such it is possible that the saturation value for the complex could actually be around 5, suggesting a spin ground state of 2.5, which would correspond to antiferromagnetic bonding between the Mn centres. An attempt was made to fit to the reduced magnetisation data using the ANISOFIT 2.0 software but a convincing fit could not be achieved. This is probably due to the polymeric nature of the Mn complex resulting in too complex a magnetic response to be fit using the relatively simplistic Hamiltonian employed by the ANISOFIT 2.0 software. As such values for the ZFS parameters could not be found and no quantitative conclusions could be drawn from the reduced magnetisation data for the Mn complex.

6.5.2.3. Magnetic Susceptibility Data

Figure 6.15 shows the magnetic susceptibility data collected for the Mn(II) crystal complex under an applied field of 500Oe in the temperature range 2K-300K.

This data was corrected for the paramagnetic signal of the Mn(II) acetate contaminant and the diamagnetic contribution due to the sample and sample holder using the same method as for the Ni(II) complex which is detailed in section 6.3.2.3. The uncertainty in the susceptibility data for the manganese complex due to the uncertainty in the sample mass amounts to around 1.0%.

The FC/ZFC plots follow the same general pattern, however a slight deviance in the data points of the two plots is observed below 34K. This can be clearly seen in the inset of Figure 6.15 in which the susceptibility is displayed as inverse susceptibility against temperature (see below).

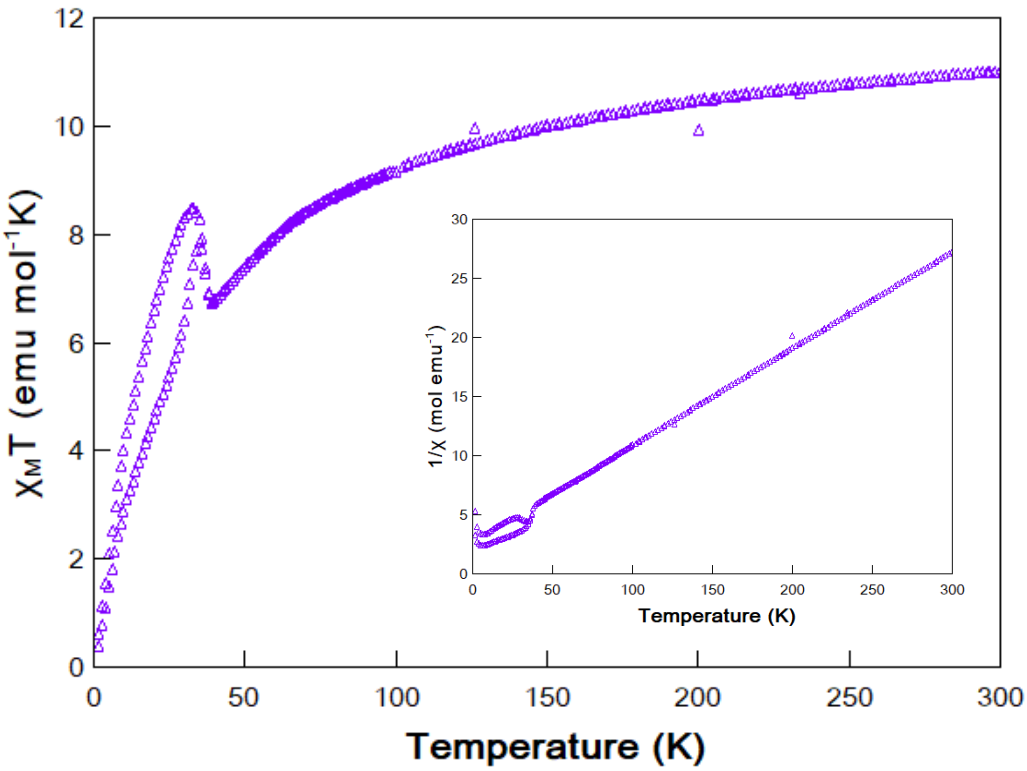

Figure 6.15: Magnetic susceptibility data collected for the Mn(II) crystal complex, plotted as a function of susceptibility and temperature, against temperature and inverse susceptibility against temperature (inset). The upper branch in the susceptibility data and lower branch in the inverse susceptibility represents the field cooled (FC) measurement and the other branch represents the zero-field cooled measurement (ZFC).

The difference in the FC/ZFC plots would suggest that the Mn(II) complex exhibits remanence in the low temperature regime. At room temperature the Mn(II) complex exhibits a $X_M T$ value of 11.00 ± 1.10 emuKmol^{-1}, which is roughly equivalent to the spin only value of 12.9 ± 2.24 emuKmol^{-1} calculated for three uncoupled Mn(II) centres. As Mn(II) ions do not exhibit first order orbital momentum due to orbital quenching, the spin only $X_M T$ values can be calculated using the same method employed for the Ni(II) complex outlined in section 6.3.2.3. As the Mn(II) complex is polymeric, unlike both the Ni(II) and Co(II) complexes, it is much more difficult to predict what is happening from the magnetic data. However qualitatively we can say that the overall decrease in $X_M T$ value observed with decreasing temperature is likely due to antiferromagnetic interactions between the Mn(II) centres. The $X_M T$ value is observed to decrease steadily from 300K until a value of 6.87 ± 0.69 emuKmol^{-1} is reached at 88K. Below this a rapid increase in the $X_M T$ value of both the FC and ZFC plots is observed until a value of

8.47 ± 0.84 emuKmol^{-1} is achieved for the FC plot at 32K, and a value of 7.70 ± 0.77 emuKmol^{-1} is achieved for the ZFC plot at 34K. It is at 34K that we first observed a considerable difference in the X_MT values of the FC/ZFC plots. The X_MT values of both plots continue to decrease with temperature below 32K for the FC plot and 34K for the ZFC plot. The fact that the complex appears to exhibit remanence may suggest that the antiferromagnetic bonding between the Mn(II) centres is incomplete, resulting in canting of the Mn(II) spins.

Unfortunately it was not possible to fit the magnetic susceptibility data using the PHI software. This is probably due to the more complex polymeric structure of the Mn complex in comparison to the isolated units of the Ni and Co complexes. As a result only qualitative analysis of the susceptibility data could be carried out.

6.5.2.4. Magnetic Hysteresis Data

Hysteretic data was collected for the Mn sample at 10K, with a maximum applied field of 50000 Oe. The data was corrected for the paramagnetic Mn(II) acetate tetrahydrate contaminant and the diamagnetic contribution of the sample and sample holder, using the same method as outlined for the nickel sample in section 6.3.2.3. The overall uncertainty in the hysteretic data was calculated as being around 0.9%, as a direct result of the uncertainty in the sample mass measurement.

Figure 6.16 shows the hysteresis data collected at 10K, for the applied field range of -50000 Oe to + 50000 Oe, and the inset shows the same magnetisation data for the zoomed in field range of -1000 Oe to +1000 Oe.

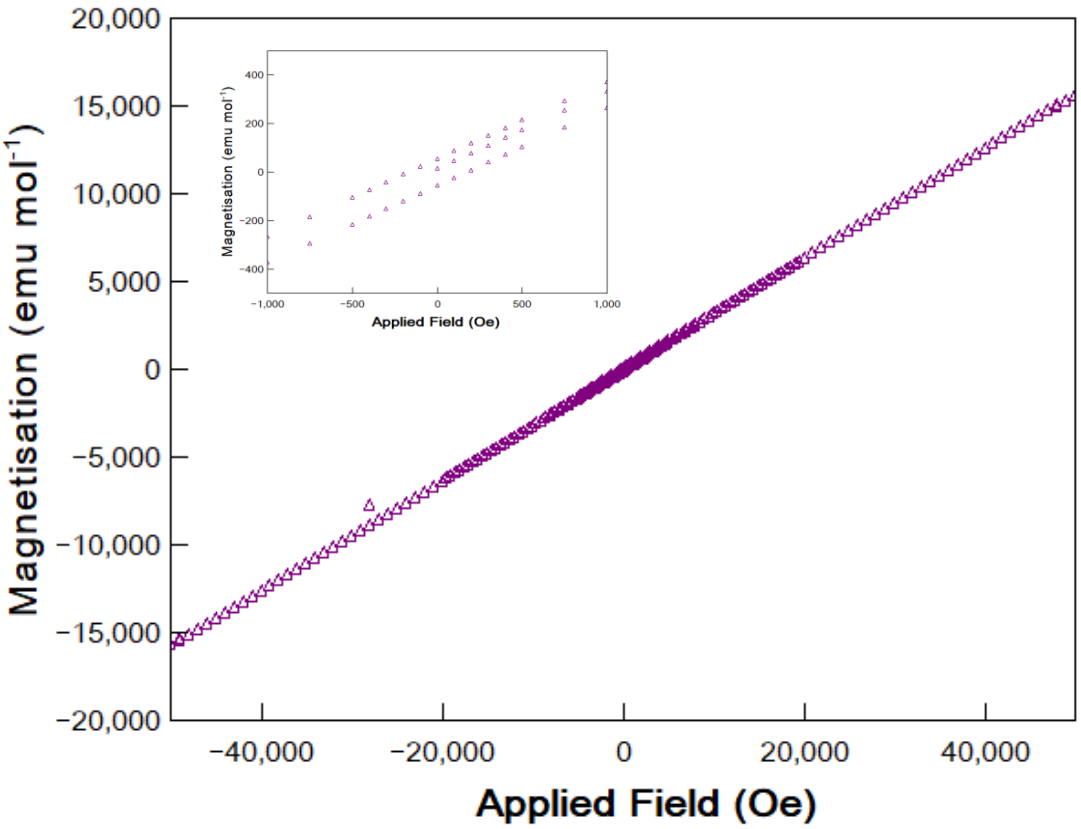

Figure 6.16: Hysteresis loop for the Mn(II) crystal complex taken at 10K, with a maximum applied field of 50000Oe. The inset shows a zoomed section of the loop from -1000Oe - +1000Oe.

As can be seen from Figure 6.16 a field of 50000 Oe is not large enough to fully saturate the Mn complex and therefore a value for the saturation magnetisation cannot be achieved. As can be seen from the inset of Figure 6.16 the Mn complex exhibits a small amount of remanence and coercivity at this temperature. This is consistent with the observation that the FC/ZFC plots are different at this temperature. As detailed in sections 6.5.2.2. and 6.5.2.3 we suspect that the Mn centres are interacting antiferromagnetically. The fact that a very small amount of remanence and coercivity is observed is probably as a result of incomplete antiferromagnetic interactions between the Mn centres, causing canting of the Mn spins. In this case it was not deemed necessary to fit to the data using the Brillouin function, as in the case of the cobalt complex, to confirm that the complex is not behaving paramagnetically. This was due to the coercivity and remanence observed which would not be possible for a paramagnet to exhibit.

6.5.3. Conclusions

A polymeric Mn(II) complex, $[C_4mim]\{Mn_3(OAc)_7\}_n$ was synthesised using a one-step ionothermal synthesis process involving the dissolution of Mn(II) acetate into the ionic liquid $[C_4mim][OAc]$. Qualitative analysis of magnetic measurements taken for the sample using SQUID magnetometry suggested the presence of antiferromagnetic coupling between the Mn(II) centres. Reduced magnetisation data showed a non-superposition of the isofield lines indicating the presence of sizable ZFS. The presence of remanence below 32K was identified in magnetic susceptibility measurements and confirmed in magnetic hysteresis measurements taken at 10K. This suggested that the antiferromagnetic coupling between the Mn(II) centres was incomplete and canting of the Mn(II) spins in this complex had subsequently taken place.

References

[1] Pedersen, K. S., Bendix, J., and Clérac, R., "Single-molecule magnet engineering: building-block approaches", (2014), *Chemical Communications*, Vol **50**, 4396-4415

[2] Freudenmann, D., Wolf, S., Wolff, M., and Feldmann, C., "Ionic liquids: new perspectives for inorganic synthesis?", (2011), *Angew Chem Int Edit*, Vol **50**, 11050-11060

[3] Ríos, A. P., Irabien, A., Hollmann, F., and Fernández, F. J. H., "Ionic Liquids: Green Solvents for Chemical Processing", (2013), *Journal of Chemistry*, Vol **2013**, 402172

[4] Chilton, N.F., Anderson, R. P., Turner, L.D., Soncini, A., and Murray, K.S., "PHI: A Powerful New Program for the Analysis of Anistropic Monomeric and Exchange-Coupled Polynuclear d- and f-block Complexes", (2013) *Journal Computational Chemistry,* Vol **34**, 1164-1175.

[5] Banci, L., Bertini, I., Bren, K.L., Cremonini, M.A., Gray, H.B., Luchinat, C., Turano, P., "The use of pseudocontact shifts to refine solution structures of paramagnetic metalloproteins, Met8oAla cyano-cytochrome c as an example", (1996), *Journal Biological Inorganic Chemistry*, Vol **1**, **2**, 117-126

[6] Banci, L., Bertini, I., Huber, J. G., Luchinat, C., Rosato, A., "Partial Orientation of Oxidized and Reduced Cytochrome b_5 at High Magnetic Fields: Magnetic Susceptibility Anisotropy Contributions and Consequences for Protein Solution Structure Determination", (1998), *Journal of the American Chemical Society*, **120**, **49**, 12903-12909

[7] Aukauloo, A., Ottenwaelder, X., Ruiz, R., Journau, Y., Pei, Y., Riviere, E., and Munoz, C., "Rational design of homo and hetero hexanuclear coordination compounds: syntheses and

magnetic properties of $[Cu_2^{11}M_4^{11}]$ (M = Cu, Ni) Species and the crystal structure of $\{[Cu(tmen)(H_2O)]_2[Cu(tmen)]_2[Cu_2L](H_2O)\}(ClO_4)_4 \cdot H_2O$", (2000), *European Journal of Inorganic Chemistry*, Vol **2000**, 5, 951-957

[8] Chien, C. H., Change, J. C., Yeh, C. Y., Lee, G. H., Fang, J. M., Song, Y., and Peng, S, M., "Weak antiferromagnetic coupling for novel linear hexanuclear nickel (II) string complexes (Ni_6^{12+}) and partial metal-metal bonds in their one-electron reduction products (Ni_6^{11+})", (2006), *Dalton Transactions*, Vol **26**, 3249-3256

[9] Liu, S. Z., Wang, S. N., Cao, F., Fu, H. Y., Li, D. C., and Dou, J. M., "Crystallization condition-controlled assembly of oxygen-bridged tetranuclear and hexanuclear Ni(II) clusters: syntheses, structures and properties", (2012), *RSC Advances*, Vol 2, 1310-1313

[10] Coey, J. M. D., "Magnetism and Magnetic Materials", (2010), *Cambridge University Press*, 109-111

[11] Stamatatos, T.C., Escuer, A., Abboud, K. A., Raptopoulou, C. P., Perlepes, S. P., and Cristou, G., "Unusual structural types in Nickel cluser chemistry from the use of pyridyl oximes: Ni_5, $N_{12}Na_2$ and Ni_{14} clusters", (2008), *Inorganic Chemistry*, **47**, 11825-11838

[12] Bain, G.A. and Berry, J.F., "Diamagnetic Corrections and Pascal's Constants", (2008), *Journal of Chemical Education*, Vol. **85**. **4**

[13] Martinez-Lillo, J., Dolan, N., Brechin, E.K., "A family of cationic oxime-based hexametallic manganese(III) single-molecule magnets", (2014), *Dalton Press,* **43,** 4408 – 4414

[14] Gerloch, M., "Spin-orbit coupling in "tetrahedral" nickel (II) compexes; An anomaly", (2016), *Polyhedron*, Vol **120**, 205-207

[15] Bagai, R., and Christou, G., "The Drosophila of single-molecule magnetism $[Mn_{12}O_{12}(O_2CR)_{16}(H_2O)_4]$", (2008), *Chemical Society Reviews*, Vol **38**, 1011-1026

[16] Langenberg, A., Hirsch, K., Lawicki, A., Zamudio-Bayer, V., Niemeyer, M., Chmiela, P., Langbehn, B., Terasaki, A., Issendorff, B., and Lau, J. T., "Spin and orbital magnetic moments of size-selected iron, colbalt, and nickel clusters and their link to the bulk phase diagrams", (2014), *Physical Reviews B*, **90**, 184420

[17] Mossin, S., Weihe, H., Sorensen, H. O., Lima, N., and Sessoli, R., "Rationisation of weak ferromagnetism in manganese (III) chains: the relation between structure and ordering phenomena", (2004), *Dalton Transactions*, 4, 632-639

[18] Ferguson, A., Schmidtmann, M., Brechin, E. K., and Maurrie, M., "Bis-tris propoane as a new multidentate ligand for nickel- and colbalt- based spin clusters", (2011), *Dalton Transactions*, Vol **40**, 334

[19] Aromi, G., Parsons, S., Wersdorfer, W., Brechin, E. K., and McInnes, E. J. L., "Synthesis, structure and magnetic properties of a decametallic Ni single-molecule magnet", (2005), *Chemical Communications*, Vol **40**, 5038-5040

[20] Moushi, E. E., Masello, A., Wernsdorfer, W., Nastopoulos, V., Christou, G., and Tasiopoulos, A. J., "A Mn_{15} single-molecule magnet consisting of a supertetrahedron incorporated in a loop", (2010), *Dalton Transactions*, Vol **39**, 4978-4985

[21] Friedman, R., and Sarachik, "Macroscopic measurement of resonant magnetisation tunnelling in high-spin molecules", (1996), *Physical Review Letters*, Vol **79**, 6031

[22] Christou, G., Gatteschi, D., Hendrickson, N., and Sessoli, R., "Single Molecule Magnets", (2000), *MRS Bulletin*, Vol **25**, 11, 66-71

[23] Peng, Y., Bodenstein, T., Fink, K., Mereacre, V., Anson, C. E., and Powell, A. K., "Magnetic anistotropy of a Co11 single ion magnet with distorted trigonal prismatic coordination: theory and experiment", (2016), *Physical Chemistry Chemical Physics*, Vol **18**, 30135

Chapter 7

Conclusions and Future Work

SQUID magnetometry was shown throughout this thesis as a useful tool for magnetic characterization on bulk, nano- and atomic scales. Its ability to measure materials of different state, structure and composition was highlighted through the three distinct studies conducted in this thesis. Some of the experimental considerations and limitations of the device were also detailed.

The effect of changes in the composition and crystal structure of lanthanum manganate magnetic nanoparticles were studied in detail in Chapter 4. It was shown that doping this material with ions of a larger atomic radius than that of the La^{3+} ion resulted in an enhanced magnetic heating effect, whereas doping with ions with a smaller radius resulted in reduced magnetic heating. Additionally the magnetic heating exhibited by the material was shown to increase with increasing dopant concentration until a maximum heating was achieved for $La_{65}Sr_{35}MnO_{3.}$ This material showed promise as a potential mediator in mild hyperthermia treatment, with maximum heating of 46.7°C and an SAR of 56 Wg_{Mn}^{-1} observed. Finally studies into the effects of microwave heating during the synthesis process showed that this approach resulted in MNPs with improved crystallinity and enhanced magnetic properties. A positive linear relationship between the microwave power setting used (50, 100 and 200W) and the

specific absorption rate (37.7, 56.6 and 57.5 Wg^{-1}) and magnetic susceptibility of the material was also observed.

There are a number of additional experimental studies, which could add to the research completed in this thesis and contribute to a greater understanding of the doped lanthanum manganate MNPs. As detailed in Chapter 4, the SQUID magnetometer magnetic measurements were completed under a DC field whereas the magnetic heating experiments were completed under an AC field. As hyperthermia treatment requires an AC field, and to allow for direct comparison with the heating experiments it would be interesting to conduct the magnetic measurements under an AC field where modulating the frequency of the field and it's magnitude could be of particular interest. There are a number of instruments commercially available, which could be used to conduct these measurements such as vibrating sample magnetometers (VSM) and AC SQUID susceptibility magnetometers. As discussed in Chapter 3 VSM's operate in a wide range of temperatures (1.6K-1,273K) and can typically generate fields of around 10^{-7}T [1-2], making them suitable for magnetic measurements for comparison with the magnetic heating data. One addition experimental consideration, which must be taken into account if using VSM for these experiments, is how to contain the powered sample. This is typically resolved in the literature by setting the powder into some form of sample holder, which is then inserted into the VSM [3]. Similarly to the VSM, AC susceptibility magnetometers are commercially operational in the desired temperature (1.8-700K) and field ranges (0-7T), for future studies in this area [4-5]. Powdered samples can be contained in the same manner as for a DC SQUID magnetometer as discussed in this thesis. In contrast to the VSM, AC SQUID magnetometers are a much more sensitive device, with the ability to achieve resolutions of 10^{-17}T [4, 6] or better, in comparison a commercially available VSM which can achieve resolution of 10^{-7}T [1], making them slightly more appealing for future measurements in this area.

The DC magnetic measurements displayed in Chapter 4 showed hysteresis, which is an undesirable quality in potential mediators of hyperthermia treatment, as previous discussed. It was not conclusively determined what the cause of this magnetic behaviour was with the work presented here, however it was postulated that the MNPs may have been too large to exist as single domain particles. Due to agglomeration of the particles it was also difficult to obtain an accurate measurement of mean particle size. In future, it would be interesting to delve deeper into the domain structure of these particles. A promising method of research would be to conduct transmission electron microscopy on the particles. Such experiments are already widely reported in the literature and would provide a more detailed insight into the physical structure of the particles and additionally, provide information on the domain structure of the particles [7-8]. From this information more conclusive comparisons could be made between the

physical qualities of the particles and the observed magnetic behaviour, this could potentially providing more insight into the correlations between dopant size, quantity and synthesis process on the magnetocaloric effect exhibited by the MNPs.

Finally it would be interesting to investigate how the magnetic heating exhibited by the MNPs would manifest in a biological environment. In vivo (or mimicking environment) studies of the MNPs would be essential in order to further investigate these materials as potential mediators of magnetic hyperthermia treatment.

In Chapter 5, bulk magnetic characterization was conducted on a family of monomeric lanthanide ionic liquids. All samples were shown to exhibit paramagnetic behaviour and fitting to the data using the Curie-Weiss relationship returned magnetic moments for each sample consistent with those reported in the literature. Two dimeric ionic liquids (Dy and Nd), were also synthesized and their magnetic properties characterized. These samples both exhibited anti ferromagnetic coupling between neighbouring ions in the 0-100K temperature range.

Whilst in this thesis we experienced difficulty in obtaining reproducible results for the dimeric ionic liquids, this is a novel synthesis process and was iteratively improved on during the course of the study. Further improvements have been made since the experiments herein were conducted and are reported in the paper by Nockermann et al, paving the way for further studies of similar materials [9].

As detailed in Chapter 2, in recent years ionic liquids have garnered much interest in the evolving field of chemical synthesis. This is predominately due to the shift away from using conventional solvents, in a bid to practice 'greener' chemistry. Ionic liquids are of particular interest due to their low vapour pressure and non-volatile nature [10]. Additional refinement of the material synthesis and characterization processes of ionic liquids, such as that detailed in reference 9, is vital for providing a firm bedrock for future development of this higher desirable field.

Finally in Chapter 6, the magnetization of three magnetic crystals on the atomic scale were investigated. The three distinct magnetic crystals were synthesized using the same process utilizing the 1-methyl-3-ethylimidazolium ionic liquid. All three samples showed non-superposition of the isofield lines in the reduced magnetization measurements, suggesting the presence of sizable zero field splitting. This was confirmed for the Ni(II) and Co(II) crystal complexes by fitting to the magnetic susceptibility data. Axial field splitting parameters of -2.34cm^{-1} and 16.66 cm^{-1} were calculated for the Ni(II) and Co(II) complexes respectively. Fitting to magnetic data collected for the Mn(II) magnetic data was not achievable due to the more

complex behaviour exhibited by the polymeric complex. Of particular notability was that fact that stepping of the hysteresis loop of the Ni(II) complex was observed in the temperature range 1.8-10K. This coupled with the fact that a spin ground state of 2 was calculated for this material suggests that this complex may exhibit single molecule magnetic behaviour.

As detailed in Chapter 6, additional complications in the synthesis process arose due to the hygroscopic nature of the crystal complexes. Although the synthesis process was conducted in a fume cupboard, transportation of the complexes across research facilities and sample preparation for measurement in the SQUID magnetometer meant the complexes were not always contained in an inert environment. Ideally all sample prep will be conducted in a fume cupboard, including preparation for the magnetic measurements (i.e. fixing sample holder onto drinking straw and SQUID transport tube). This should help prevent any degradation of the complexes and reduce the experimental uncertainty due to the sample purity. Additionally, following synthesis of the magnetic crystals, extended X-ray absorption fine structure (EXAFS) experiments would be beneficial to determine if there is any of the precursor ionic liquid left in the sample and if so what quantity.

An attractive potential use case for materials such as those explored in Chapter 6 is in the field of magnetic storage, where molecule sized magnetic bits would yield highly desirable storage densities. While this is an immature area of research measurements of the relaxation time would provide insight into the stable storage of information coded in this molecules. As a result, we would like to conduct AC susceptibility measurements in future, in order to confirm the relaxation time for each complex, as detailed in section 2.6.3.

Due to the promise shown by this synthesis method in producing unique magnetic crystals with interesting properties, there is vast potential to create other new materials using different metallic ions. Research is currently ongoing to realize this potential.

References

[1] Lake Shore Cyrotronics, Inc., “7400-S Series VSM Specificiations”, (2018), https://www.lakeshore.com/products/Vibrating-Sample-Magnetometer/7400-S-Series-VSM/pages/Specifications.aspx, (accessed 21/10/2018)

[2] Cryogenic Limited, “Vibrating sample magnetometer (VSM)”, (2012), https://www.cryogenic.co.uk/products/vibrating-sample-magnetometer-vsm (accessed 21/10/2018)

[3] Hang Zong, B., “Magnetic characterization of powder samples from the magnetocaloric compound series Mn5-xFexSi3”, (2016), Thesis submitted to Aachen University of Applied Sciences

[4] Fagaly, R.L., “Superconducting quantum interference device instruments and applications”, (2006), Review of scientific instruments, Vol 77, 10, 101101

[5] Bendanta, S., Petracic, O., Aderholz, M., and Kleeman, W., “A sample holder design for high temperature measurements in superconducting quantum interference device magnetometers”, (2005) Review of scientific instruments, Vol 76, 083910

[6] Martínez-Pérez, M. J., and Koelle, D., “NanoSQUIDs: Basics & recent advances”, (2017), Physical sciences reviews, Vol 2, 8

[7] Chen, Y., Wang., Liu, L., Lu, M., Cao, J., and Wang, T., “LSMO nanoparticles coated by hyaluronic acid for magnetic hyperthermia”, (2016), Nanoscale Research Letters, Vol 11, 538

[8] Soleymani, M., and Edrissi, M., “Heating ability and biocompatibility study of silica-coated magnetic nanoparticles as heating mediators for magnetic hyperthermia and magnetically triggered drug delivery systems”, (2015), Bulletin Material Science, Vol 38, 6, 1633-1638

[9] Nockemann, P., Felton, S., Esien, K., McCourt, E., and Zhenyu, L., “Designing dimeric lanthanide (111)-containing ionic liquids”, (2018), Angewandte Chemie International Edition

[10] Olivier-Bourbigou, H., Magna, L., and Morvan, D., “Ionic liquids and catalysis: Recent progress from knowledge to applications”, (2010), Applied Catalysis A: General, Vol 373, 1-2